Springer Series in
GEOMECHANICS & GEOENGINEERING

Lyesse Laloui
Alessio Ferrari (Eds.)

Multiphysical Testing of Soils and Shales

Springer

Springer Series in Geomechanics and Geoengineering

For further volumes:
http://www.springer.com/series/8069

Lyesse Laloui and Alessio Ferrari (Eds.)

Multiphysical Testing of Soils and Shales

Springer

Editors
Prof. Dr. Lyesse Laloui
EPFL ENAC IIC LMS
Lausanne
Switzerland

Dr. Alessio Ferrari
EPFL ENAC IIC LMS
Lausanne
Switzerland

ISSN 1866-8755 e-ISSN 1866-8763
ISBN 978-3-642-32491-8 e-ISBN 978-3-642-32492-5
DOI 10.1007/978-3-642-32492-5
Springer Heidelberg New York Dordrecht London

Library of Congress Control Number: 2012943951

Printed on acid-free paper

Springer is part of Springer Science+Business Media (www.springer.com)

Preface

Significant advancements in the experimental analysis of soils and shales have been achieved over the last several decades. Fundamental issues have been solved, and important achievements have been made in specific areas, including the development of multiphase testing facilities for non-isothermal conditions and the characterisation of the microstructural arrangement of complex geomaterials. This outstanding progress has led to improvements in the theoretical development of geomechanical theories, such as the constitutive modelling of multiphysical and multiscale processes, as well as important engineering applications.

This book is a compilation of the contributions to the international workshop, "Advances in Multiphysical Testing of Soils and Shales," held at the Swiss Federal Institute of Technology in Lausanne (EPFL) on September 3-5, 2012, under the auspices of the Technical Committee 101 of the International Society for Soil Mechanics and Geotechnical Engineering. The present text focuses on recent advances in a variety of laboratory facilities and techniques for the analysis of the behaviour of geomaterials and aims to provide readers with an overview of modern trends in experimental geomechanics, including testing materials in variably saturated conditions, non-isothermal experiments, micro-scale investigations and image analysis techniques, advances in the assessment of compressibility and time-dependent behaviour, analysis of shale behaviour and experiments on treated and weathered soils. Six theme lecture papers from leading researchers in experimental geomechanics are also included.

We would like to express our thanks to all of the authors and theme lecturers for their outstanding contributions. We are especially grateful to Valentina Favero, Ali Seiphoori and Alice Di Donna for assistance with the preparation of this book.

September 2012
Lausanne, Switzerland

Lyesse Laloui
Alessio Ferrari

Contents

Theme Lectures

Testing in Variably Saturated Conditions

Testing in Non-isothermal Conditions

Micro-scale Investigations and Image Analysis Techniques

Compressibility, Strength and Time-Dependent Investigations

Experimental Analyses of Shales Behaviour

Treated and Weathered Geomaterials

Theme Lectures

Recent Advances in Experimental Modelling of Unsaturated Soil Behaviour over a Whole Range of Paths and Modes of Deformation

Laureano R. Hoyos

University of Texas at Arlington, Arlington, Texas 76019, U.S.A.
lhoyos@uta.edu

Abstract. The last few decades have been an era of intensive and sustained experimental efforts that has defined the threshold of our understanding of unsaturated soil behavior. The adoption of matric suction, $(u_a - u_w)$, and the excess of total stress over air pressure, that is, net normal stress, $(\sigma - u_a)$, as the relevant stress state variables, has facilitated the investigation of key features of unsaturated soil behavior via the axis-translation technique. It is the relative success of this technique that has prompted researchers in the discipline to devote countless hours to fine-tuning myriad details of existing and standardized soil testing devices, and hence keep the focus of their efforts on expanding their testing capabilities. The present Theme Lecturer's paper summarizes some of the most recent advances in experimental modeling of unsaturated soil behavior, over a whole range of suction-controlled paths and modes of deformation, accomplished at the University of Texas at Arlington. Its main sections are devoted to describing the test protocols and analyzing the key results from a series of suction-controlled resonant column, bender elements, biaxial (plane strain), true triaxial (cubical), and ring shear (large displacement) testing programs successfully conducted on compacted samples of sandy soils.

1 Background and Scope

The vast majority of geotechnical infrastructure in the world, which is normally made of compacted soil or rests on unsaturated ground, is also subjected to a wide range of deformations. Calculations of elastic settlements experienced by shallow foundations, for instance, require a good estimation of soil stiffness at relatively small strains. Analyses of natural/man-made earth slopes, highway embankments, earth retaining systems, and soil bearing capacity, on the other hand, require good estimations of soil's shear strength, from peak to residual, under biaxial, triaxial, or multiaxial stress states.

The last few decades have been an era of intensive and sustained experimental efforts that has defined the threshold of our understanding of unsaturated soil behavior. The adoption of matric suction, $(u_a - u_w)$, and the excess of total stress over the air pressure, that is, net normal stress, $(\sigma - u_a)$, as the relevant stress state variables, has facilitated the experimental investigation of essential and crucial

L. Laloui and A. Ferrari (Eds.): Multiphysical Testing of Soils and Shales, SSGG, pp. 3–20.
springerlink.com

features of unsaturated soil behavior via the axis-translation technique (Hilf 1956, Fredlund and Rahardjo 1993). It is the relative success of this technique that has prompted researchers in the discipline to devote countless hours to fine-tuning myriad details of existing and standardized soil testing devices, and hence keep the focus of their efforts on expanding their testing capabilities.

The present Theme Lecturer's paper summarizes some of the most recent advances in experimental modeling of unsaturated soil behavior, over a whole range of suction-controlled paths and/or modes of deformation, accomplished at the University of Texas at Arlington. The following sections are devoted to describing the test protocols and analyzing the key results from a series of suction-controlled resonant column, bender elements, biaxial (plane strain), true triaxial (cubical), and ring shear (large displacement) testing programs successfully conducted on compacted samples of sandy soils.

2 Resonant Column and Bender Element Testing on Unsaturated Soil

Small-strain stiffness of soils, such as shear modulus and material damping, play a fundamental role in the design/analysis of unsaturated earth structures subjected to static/non-static loading. Most conventional soil testing techniques, however, cannot capture this small-strain behavior and, hence, vastly underestimate the true soil stiffness. Several efforts have been reported since the early 1980's to study the effects of capillarity and saturation on small-strain stiffness of unsaturated soils via resonant column (RC) or bender element (BE) testing, including Brull (1980), Wu et al. (1984), Qian et al. (1991), Marinho et al. (1995), Picornell and Nazarian (1998), Cabarkapa et al. (1998), Cho and Santamarina (2001), Mancuso et al. (2002), Inci et al. (2003), Kim et al. (2003), Mendoza et al. (2005), Cabarkapa and Cuccovillo (2006), Vassallo et al. (2006), Sawangsuriya et al. (2008, 2009), Ng et al. (2009), and Khosravi et al. (2010).

The bender element technique has proved a viable way to investigate unsaturated soil stiffness at very small strains. However, there is a great need for assessing the suitability of this technique, particularly for unsaturated soils, as compared to more fully-standardized procedures, such as the resonant column and simple shear test methods. This paper introduces a suction-controlled proximitor-based resonant column device that features self-contained bender elements for simultaneous testing of soils under both techniques. Particular attention is devoted to the effects of matric suction over the frequency response curves, free-vibration decay curves, cyclic hysteretic stress-strain loops, and material damping of sandy soil.

The model THS-100 resonant column cell features a reinforced acrylic chamber of 1000 kPa confining pressure capacity. The bottom pedestal, for samples of 70-mm diameter, features a full set of 5-bar HAEV ceramics as well as one bender element crystal (receiver) for shear-wave velocity readings: Fig. 1(a). The top cap features a full set of coarse porous stones, for uniform pore-air pressure application, and also one bender element transmitter. An electrical servo motor actuator is used for the application of torsional loads with +/- 23.3 kN-m (peak) capacity, and

300-Hz frequency range. The input torque is measured in pfs (percent of full scale) units, with 100 pfs equivalent to a 10 kN-m torque. Mounted on an internal floating frame to allow for large vertical deformations, the actuator includes a servo amplifier for closed-loop control of torsional loads, and one proximitor mounting acting as the internal angular displacement transducer: Fig. 1(b). The scope of the present work, however, is limited to the small-strain (linear or low-amplitude) stiffness response. Thereby, a 1-pfs input torque (0.1 kN-m) was adopted for all RC tests. A model PCP-15U pressure panel is used for direct control of pore-air pressure u_a through the top cap, with dual pressure regulators/gauges for precise measurement and control of matric suction, $s = u_a$ ($u_w = 0$).

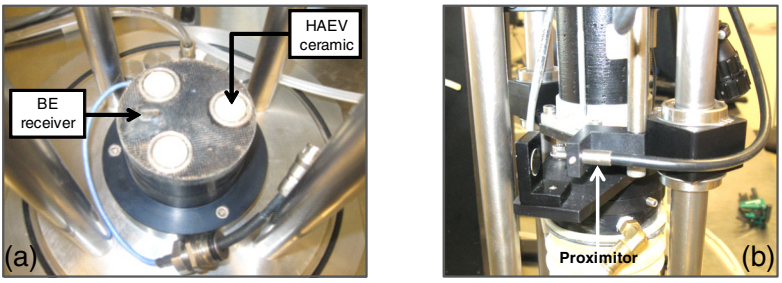

Fig. 1 THS-100 resonant column cell: (a) bottom pedestal, (b) proximitor mounting.

The soil used in this work classifies as silty sand (SM) according to the USCS: 70% sand and 30% silt. The coarse fraction has particle sizes between 0.5-1.2 mm. The passing No. 40 sieve fraction has liquid limit, LL = 26.4%, and plastic limit, PL = 22.2%. Samples were statically compacted into a 70-mm diameter, 130-mm height, compaction split mold via a triaxial loading frame. Samples were prepared in three lifts, at a constant displacement rate of 1.0 mm/min, to a target void ratio, e = 1.0, and dry unit weight, $\gamma_d = 13.13$ kN/m^3. The initial water content of 26% corresponds to an average degree of saturation of 72% and initial matric suction of 20 kPa, according to the soil-water retention curve (Hoyos et al. 2011a).

A series of RC and BE tests were simultaneously conducted on identically prepared samples of SM soil. Each sample was tested under matric suction, s = 50, 100, 200, or 400 kPa, achieved via axis-translation, and four different net confining pressures, $(p - u_a) = 50$, 100, 200, and 400 kPa. The soil was first isotropically compressed to a target confining pressure, p = 50 kPa. The pore-air pressure u_a was then gradually increased (soil drying) to the pre-established value of suction, while the net confining pressure was kept constant at 50 kPa by simultaneous and equal increases of the external confinement.

Pore-air pressure u_a was maintained constant until no further change in water volume from within the soil (less than 0.035 ml/day) was observed, at which point the pore-fluids equalization stage was considered complete. A 36-hr equalization time (1.5 days) was found suitable for all suction states. Equalization stage was finally followed by a constant-suction ramped consolidation to the target values of

net confining pressure. All RC tests were conducted by sweeping the entire input-torque frequency scale until obtaining a thorough frequency response curve, typically between 50 and 250 Hz. The peak torsional vibration was then completely cut off in order to record the free-vibration logarithmic decay curve.

Fig. 2(a) shows a full set of frequency response curves obtained from four SM soil samples tested at matric suctions, s = 50, 100, 200, and 400 kPa, respectively, under same net confining pressure, $(p - u_a) = 50$ kPa. It can be readily noticed the critical influence that matric suction has over the resonant frequency of the soil column, with a considerable increase in resonant frequency for s = 400 kPa. The maximum (peak) shear strain γ_{max} induced by the 0.1 kN-m torque, however, decreases with increasing suction. Similar trends were observed for other combinations of stress variables $(p - u_a)$ and $(u_a - u_w)$.

Fig. 2(b) shows the free-vibration logarithmic decay curves from two SM soil samples tested at matric suctions, s = 50 kPa (dotted line) and 400 kPa (solid line), respectively, under same net confining pressure, $(p - u_a) = 50$ kPa. It is observed that the initial peak shear strain at time zero (t = 0), i.e., as soon as the torsional vibration was completely cut off, is lower at higher suction states, in agreement with results in Fig. 2(a). Both decay curves appear to be fully attenuated after 0.08 seconds of free vibration. Since the first peak amplitude is lower for matric suction s = 400 kPa, this is indicative of lower material damping at higher suction values, which further highlights the increase in rigidity of the soil skeleton (i.e., effective stress) with increasing matric suction, as shown in Fig. 2(a).

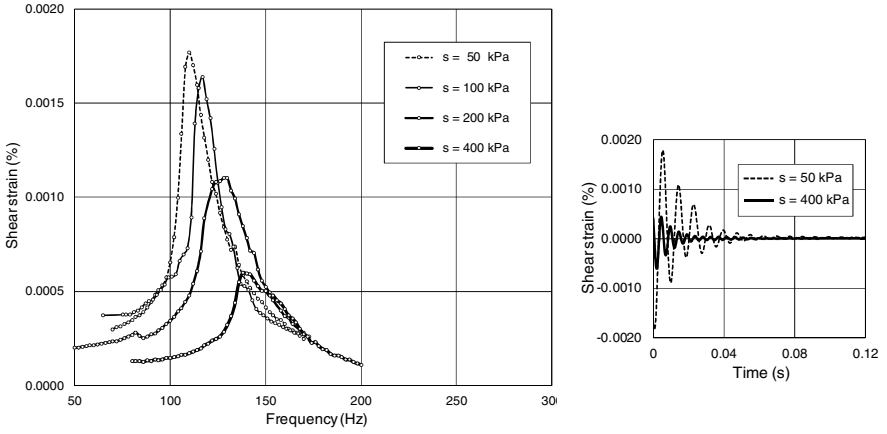

Fig. 2 Dynamic response of SM soil: (a) frequency response curves, (b) decay curves.

The variation of small-strain shear modulus G_{max} (from RC tests) with matric suction, for different net confining pressures, is shown in Fig. 3(a), where the influence of suction is readily manifested. The solid and dotted lines represent best-fit power regression functions of the form, $G_{max} = A(u_a - u_w)^B$. Constant A represents the value of G_{max} (MPa) at suction, $(u_a - u_w) = 1$ kPa; while constant B is the slope of the best-fit curve, which represents how susceptible soil stiffness is

to changes in matric suction. Slope B is observed to remain virtually constant, which might form the basis for the eventual introduction of a unified three-dimensional framework for small-strain stiffness of unsaturated soils, similar to that postulated for peak shear strength (Fredlund et al. 1978). The comparison of all experimental values of G_{max} from both resonant column (RC) and bender element (BE) tests is shown in Fig. 3(b). The bender element technique is observed to yield G_{max} values reasonably close to those assessed from resonant column testing.

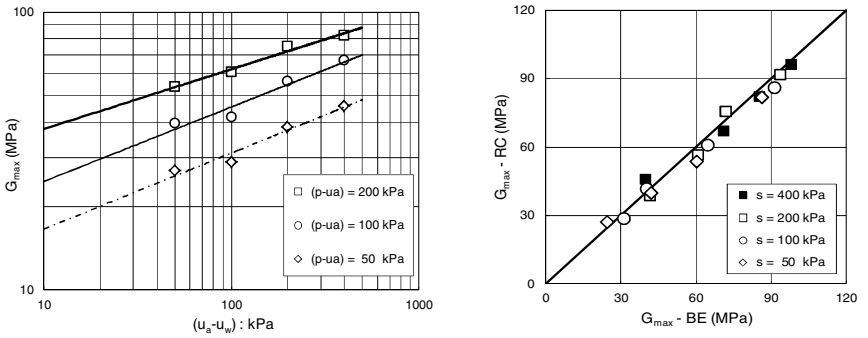

Fig. 3 Stiffness response of SM soil: (a) resonant column, (b) bender elements.

The variation of small-strain damping ratio D_{min} (from RC free-vibration decay curves) with matric suction, for different net confining pressures, is shown in Fig. 4(a). The trends confirm those in Fig. 3(a), with lower damping (higher stiffness) at higher suctions. Data have also been best-fitted by power regression functions, $D_{min} = C(u_a - u_w)^D$, in which the slope D also remains virtually constant. Fig. 2(a) shows that the half-power points, i.e. frequencies on each side of the frequency response curves corresponding to a shear strain of $0.707(\gamma_{max})$, become less apparent as suction increases. Thereby, assessment of damping using half-power bandwidth method appears to become less reliable at higher suction values.

The main focus of this work has been on small-strain stiffness of unsaturated soil. Cyclic behavior of soils, however, is nonlinear and hysteretic; consequently, the shear modulus and material damping are heavily strain dependent. Fig. 4(b) shows the cyclic hysteretic stress-strain loops from two SM soil samples subjected to a cyclic 6-pfs input torque (0.6 kN-m) at suctions, s = 50 kPa (thinner trace) and 200 kPa (thicker trace), respectively, under same net confining pressure, $(p - u_a)$ = 200 kPa. Equivalent viscous damping could also be evaluated from the area enclosed by the cyclic hysteretic loops. Therefore, the loops further substantiate the trends shown in Fig. 4(a), including smaller areas enclosed by the cyclic hysteretic loops, and lower shear strains induced by same cyclic shear stress, with increasing matric suction.

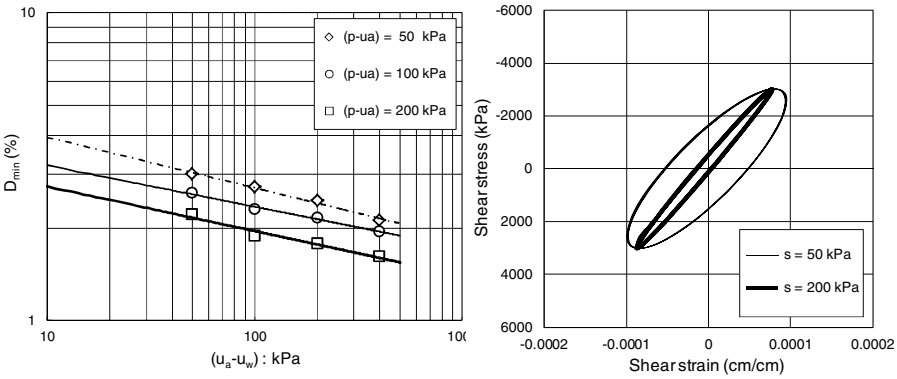

Fig. 4 Damping response of SM soil: (a) resonant column, (b) cyclic stress-strain loops.

3 Plane Strain Testing on Unsaturated Soil

The engineering response of crucial geotechnical infrastructure, including earth dams and tunnelling, may be best modeled using plane strain analyses, given the particular geometries, stress paths, and boundary conditions that such geosystems normally feature or undergo in the field. Biaxial devices allow for direct testing of soils under truly plane strain conditions, facilitating a more accurate assessment of strength parameters and shear banding phenomena under these conditions (Wood 1958, Vardoulakis and Goldscheider 1981, Vardoulakis and Graf 1985, Drescher et al. 1990, Alshibli et al. 2004). Recent attempts at testing unsaturated soils under suction-controlled plane strain conditions have been reported by Schanz and Alabdullah (2007), and Fauziah and Nikraz (2008). The respective devices, however, offered plenty of room for further refinement and elaboration.

In this summary paper, a novel suction-controlled biaxial apparatus suitable for unsaturated soil testing via axis-translation technique is briefly introduced. Its core system is similar to the original Vardoulakis type of biaxial device (Vardoulakis and Goldscheider 1981). Originally manufactured at the University of the Andes, Colombia (Ruiz 2003), the system has been further refined for suction-controlled testing at the University of Texas at Arlington.

Fig. 5 shows the reference coordinate system and photographs of both the core system of the apparatus and a typical compacted sample trimmed to final dimensions, d_{1o} = 90 mm, d_{2o} = 60 mm, and d_{3o} = 30 mm. The upper loading platen is made of very light material (Nylon 66) to minimize the initial seating pressure on the soil, while pore-air pressure u_a is supplied to the soil pores through one coarse porous stone. Plane strain condition is imposed on the soil by means of two 8-mm thick stainless steel rigid walls, which prevent the soil from deforming along the intermediate principal axis. Stainless steel tie rods, tightly secured onto the walls, prevent them from bending during shearing. A bottom pedestal receives an HAEV ceramic while resting directly on a U-shaped base frame, which couples the pedestal and the lateral rigid walls to a sliding table. The sliding table is a model NKL

6-110 Schneeberger type of table, which provides an additional degree of freedom to naturally expedite the formation of the failure surface during shearing. The horizontal displacement of the table is recorded by an LVDT affixed to the base plate of the apparatus. Therefore, initiation of shear band formation or a failure surface can be readily detected by the motion of the sliding table.

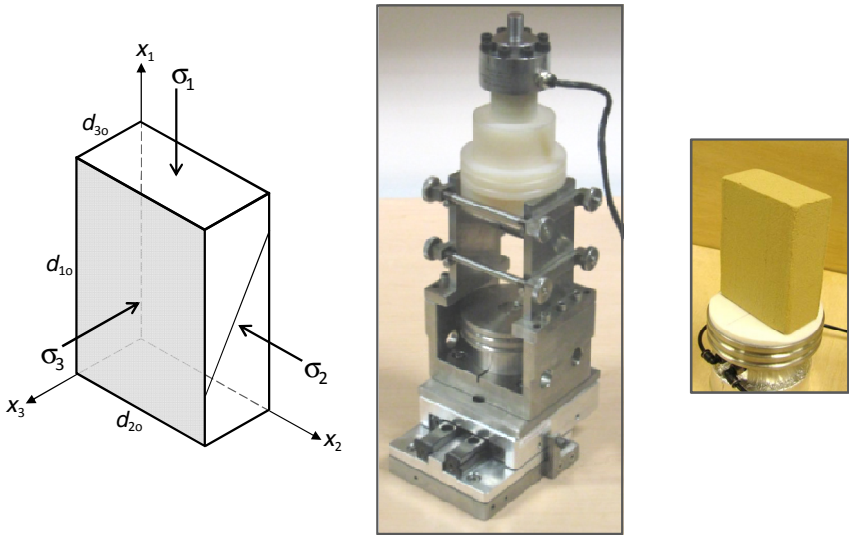

Fig. 5 Reference coordinate system, core system of biaxial apparatus, and typical sample.

Photographs of the partly and fully assembled systems are shown in Fig. 6. The fully assembled system is placed inside a reinforced acrylic chamber of 1700 kPa confining pressure capacity. The axial stress is applied by means of an MTS Universal Machine with 1 MN axial load capacity and suitable for stress or strain controlled schemes. Axial displacement of the soil is measured by an LVDT while the lateral displacements in the minor principal direction are measured by Microstrain DVRTs (Differential Variable Reluctance Transducers) attached to each one of the tie rods. A model LCM203-50kN Omega pressure cell is used for vertical pressure readings in the upper loading platen. In addition, three model 13 AL322CV Sensotec miniature load cells are installed right underneath the bottom pedestal. With this particular arrangement, the applied axial stresses can be simultaneously measured in the upper and lower sides of the prismatic sample. Therefore, any friction developed between the lateral rigid walls and the soil can be readily quantified.

The intermediate principal stress generated against the rigid walls is also measured by Sensotec type pressure cells installed on each of the walls. Readings from these cells, along with measurements of displacement in the remaining two principal axes, allow for a thorough definition of stress/strain tensors during suction-controlled plane strain shearing. A model PCP-15U pressure panel is used for suction control using axis-translation. A detailed description of the initial calibration process, using a neoprene spring rubber block, is given by Cruz et al. (2011).

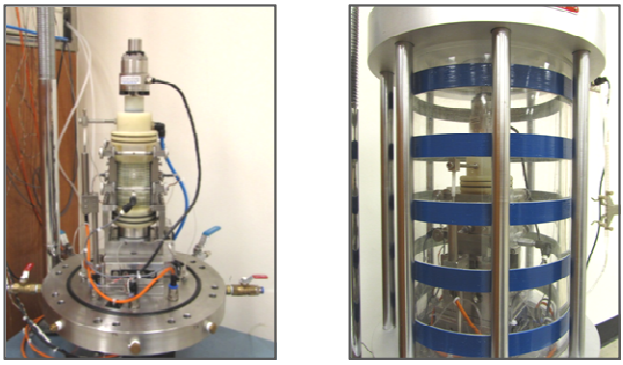

Fig. 6 Photographs of partly and fully assembled suction-controlled biaxial apparatus.

The material used in this work is an artificially mixed soil that classifies as silty sand (SM) according to the USCS: 75% silty sand and 25% kaolin. The kaolin fraction has liquid limit, LL = 57.1%, and plastic limit, PL = 45.8%. A slurry is first prepared with initial water content about twice its liquid limit, LL = 25.3% (1500 g of dry sand-kaolin soil thoroughly mixed with deaired-deionized water). A biaxial specimen is prepared by uniaxial consolidation of the slurry into a custom-made acrylic mold of 80 x 80 mm section and 200 mm height. The slurry is consolidated to final dimensions of 80 x 80 x 135 mm via 12.5, 25, 50, 100, 200, and 400 kPa load increments, yielding an average saturated unit weight, γ_{sat} = 20 kN/m^3. Finally, the compacted sample is gently removed from the acrylic mold, from which two specimens are trimmed for plane strain testing (Fig. 5).

Two identically prepared samples of SM soil were tested at matric suctions, s = 50 kPa and 100 kPa, respectively, under same net confining pressure, $(\sigma_3 - u_a)$ = 150 kPa. The axis-translation technique was implemented via a 15.87 mm diameter, 3-bar HAEV ceramic at the bottom pedestal. The suitable pore-fluids equalization time was found to be 144 hrs (6 days). Upon completion of the pore-fluids equalization stage, the soil was sheared at a constant vertical deformation rate of 0.004 mm/min (4.4×10^{-5}% strain/min), low enough to prevent sudden increases in pore pressures during shearing (Fredlund and Rahardjo 1993).

The stress-strain response of SM soil from both suction-controlled plane strain tests are shown in Fig. 7. In both cases, peak strength is observed to be followed by a sharp drop in stress until an apparent residual state is attained by the soil. The results corroborate the important role played by matric suction in the stress-strain-strength response of unsaturated soils under plane strain conditions. Photographs of failed samples are also embedded in Fig. 7. A fully developed failure surface, making a 65^o angle with the horizontal, can be readily identified from the sample failed under constant matric suction, s = 100 kPa. A relatively less inclined failure surface, making a 61^o angle, is observed for the sample failed under matric suction, s = 50 kPa; thus substantiating the observed stress-strain response curves.

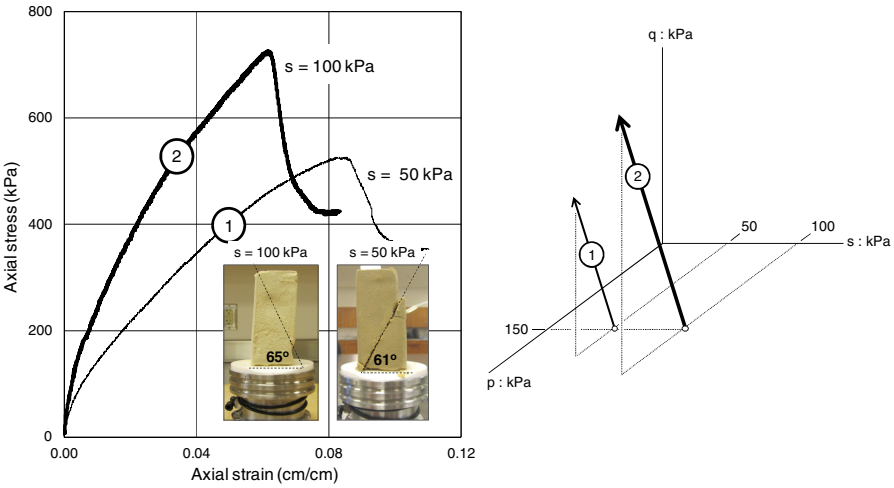

Fig. 7 Plane strain response of SM soil under matric suctions, s = 50 kPa and 100 kPa.

4 True Triaxial Testing on Unsaturated Soil

Pavement subgrades and shallow foundation soils, well above ground-water table, may be rather often subjected to three-dimensional stress gradients from changes in the stress state variables, $(\sigma_{ij} - u_a\delta_{ij})$ and $(u_a - u_w)\delta_{ij}$, as shown in Fig. 8. In these cases, the accurate prediction of the engineering performance of these geosystems requires that the constitutive relations be valid for all principal stress paths that are likely to be experienced in the field. It is in this context that a suction-controlled true triaxial (cubical) cell, facilitating a wider range of multiaxial stress paths not achievable in a conventional cylindrical cell, plays a fundamental role.

Previous efforts to investigate unsaturated soil behavior under constant-suction multiaxial loading have been reported by Hoyos and Macari (2001), Matsuoka et al. (2002), and Hoyos et al. (2008). All of these devices, however, presented some important limitations, including highly corrosive frames, use of hydraulic oil as pressurizing fluid, use of rigid loading platens, and suction control via negative pore-water pressure. This paper introduces a fully servo/suction-controlled true triaxial apparatus suitable for testing cubical, 7.62 cm (3 in) side, samples via axis-translation. The apparatus is aimed at overcoming all of the above limitations, thus yielding a considerably enhanced performance. The new cell is an upgraded, more elaborate version of the one introduced by Hoyos et al. (2008).

The apparatus is a mixed-boundary type of cell, with the sample seating on top of a 5-bar HAEV ceramic and between five flexible membranes on the remaining sides of the cube. It consists mainly of a stainless steel frame, featuring six pressure cavities to accommodate one top and four lateral latex membranes, and one cubical base aluminum piece at the bottom assembly to receive the HAEV ceramic and four coarse porous stones: Fig. 9(a). The sample is gently slid in through one of the lateral cavities of the frame, with the membranes acting as the pressure seals

between the wall assemblies and the frame, thus transmitting the water-based hydraulic pressure to the top and four lateral faces of the soil: Fig. 9(b).

External hydraulic pressure is generated by a computer-driven, model PCP-5000-UNSAT pressure control panel, with independent control of major, intermediate, and minor principal stress: Fig. 9(c) – left panel. A computer-driven, model PVC-100-UNSAT pressure-volume control system maintains a constant pore-air pressure u_a through the porous stones at the bottom of the sample: Fig. 9(c) – right panel. In both panels, model DC-750-5000 Macro Sensors hydraulic pistons are used for measurements of positive (compression) and negative (extension) deformations of the sample in all three principal directions. A more detailed account, including assessment of suitable loading rate, is presented by Hoyos et al. (2010).

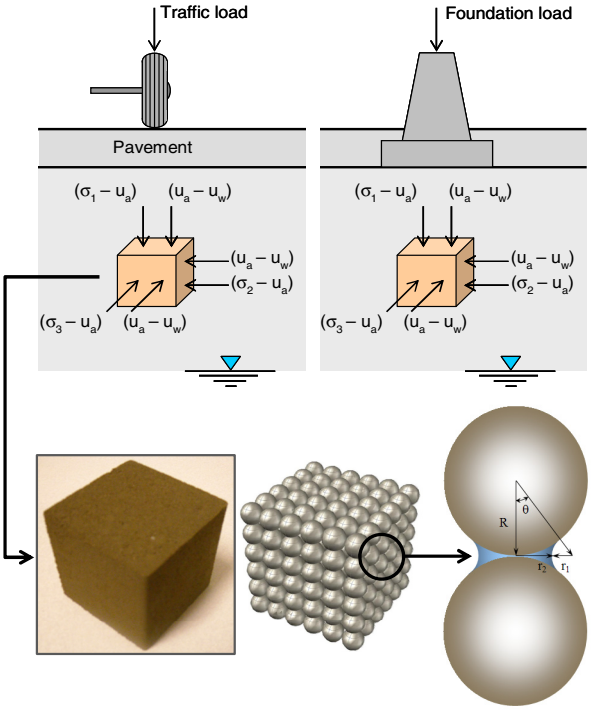

Fig. 8 Unsaturated geotechnical infrastructure subjected to multiaxial stress states.

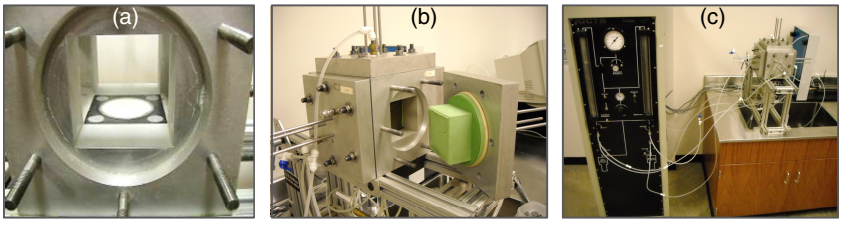

Fig. 9 True triaxial system: (a) core frame, (b) wall assemblies, (c) main cell and panels.

The material used in this work classifies as clayey sand (SP-SC) according to the USCS: 70% poorly-graded sand and 30% low-plasticity clay. More details, including soil-water retention curve, are presented by Hoyos et al. (2011b). Samples were statically compacted into a custom-made stainless steel cubical mold via a triaxial loading frame. The loose soil-water mixture was compressed in one single lift at a constant displacement rate of 1.0 mm/min, initial water content, w = 11%, and to a target dry unit weight, γ_d = 15.34 kN/m^3. Statically compacted samples yielded an average specific volume, v = 1.72 (= 1 + e), and average degree of saturation, S = 37.5%, which corresponds to an initial suction of about 50 kPa.

A comprehensive series of suction-controlled conventional triaxial compression (CTC) and triaxial compression (TC) tests was accomplished on identically prepared samples of SP-SC soil: Fig. 10(a). Tests were conducted at constant matric suctions, s = 50, 100, or 200 kPa; and initial net mean stresses, p = 50, 100, or 200 kPa. A 120-hr equalization time (5 days) was found suitable for all induced matric suctions. During suction-controlled shearing stage, the sample was imposed a deviator-stress loading rate of 8 kPa/hr, until it was readily apparent that the soil had reached peak strength. Best-fitting critical state lines (CSL) from all CTC/TC tests are shown in Fig. 10(b). Matric suction is observed to have a marked influence on the final positioning of the critical state lines; however, the slope M(s) of all critical state lines remains virtually constant, in agreement with the framework postulated by the original Barcelona Basic Model (Alonso et al. 1990).

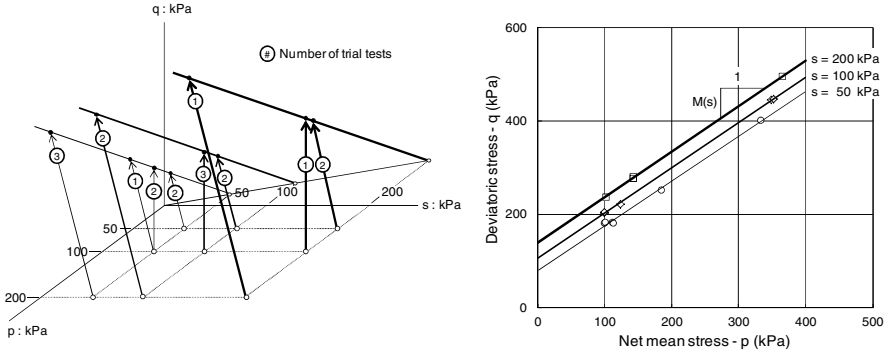

Fig. 10 Suction-controlled stress paths and critical state lines from axisymmetric shearing.

Results from a suction-controlled simple shear (SS) test conducted at constant matric suction, s = 200 kPa, and constant net mean stress, p = 100 kPa, are shown in Figs. 11(a)-(b). During SS testing, the major principal stress is monotonically increased, the minor principal stress is simultaneously decreased in the same magnitude, and the intermediate principal stress is kept constant. Consequently, the major principal strain is observed to be compressive (+), the minor principal strain expansive (–), and the intermediate principal strain virtually negligible.

Peak strength values from a series of suction-controlled TC, TE, and SS tests, all conducted under same net mean stress, p = 100 kPa, were used to identify the

failure envelopes in the octahedral plane: Fig. 11(c). It can be readily observed the marked effect that matric suction has over the size and positioning of the failure loci, with a significant expansion for s = 200 kPa. Although the scope of this work did not contemplate a comparison of suction-controlled test data from true (cubical) and conventional (cylindrical) triaxial systems, previous works have reported an acceptable degree of consistency between the two testing methods, including Matsuoka et al. (2002), and Reis et al. (2011).

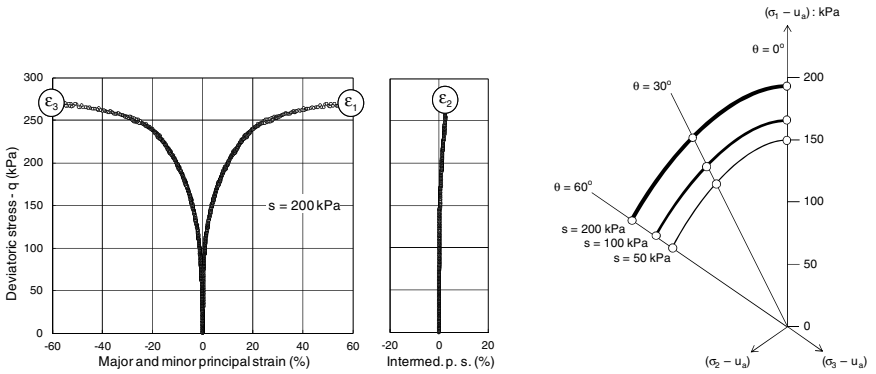

Fig. 11 General response of SP-SC soil from suction-controlled true triaxial stress paths.

5 Ring Shear Testing on Unsaturated Soil

Assessment of residual shear strength properties of unsaturated soils, at relatively low net normal stresses and matric suction states, is of critical importance in slope stability analyses that involve potentially shallow failures triggered by rainfall at relatively high degrees of saturation; particularly, natural slopes in fissured rocks with unsaturated clayey and silty fills, or shallow fissured landslides that can also be activated by wetting. However, very limited experimental evidence is available of the nature of unsaturated soil behavior under large deformations as the soil is being subjected to controlled-suction conditions.

Recent efforts by Infante Sedano et al. (2007), and Merchán et al. (2011), have mainly focused on adapting existing Bromhead-type devices (Bromhead 1979) for unsaturated soil testing using vapor-transfer or axis-translation technique. Despite their crucial findings, which demonstrated the key role played by soil suction, further efforts have yet to be undertaken with the aim of generating a thorough set of residual failure envelopes at relatively low suction values.

This paper introduces a fully servo/suction-controlled ring shear apparatus suitable for testing ring-shaped samples of unsaturated soil using axis-translation; including vertical loads up to 8000 N, monotonic torque up to 113 N-m, and three main modules: (1) Main cell with pneumatic actuator for normal loads, and electromechanical rotary actuator for torque loads; (2) DAS with data reduction software for normal/shear stresses, and average linear/angular displacements; and (3) Model PCP-15U pressure panel for suction control via axis-translation.

The bottom annular platen receives a full set of 5-bar HAEV ceramics: Fig. 12(a). The 15-mm (0.59-in) thick sample is statically compacted into the bottom annular platen: Fig. 12(b). The platen is gently transferred to the RS frame and tightly secured onto the base plate: Fig. 12(c). The vertical load shaft is brought up via a servo controller and the upper annular platen affixed to the top of the piston shaft: Fig. 12(c). A sitting load of 25 N is applied to bring the upper platen in full contact with the top surface of the soil.

All drainage and flushing lines are filled with de-aired water and flushed several times to eliminate the trapped air in the whole system. The main RS cell is then set into place, and a top cover plate securely affixed to the main cell: Fig. 12(d). A pore-air pressure u_a line, from the PCP-15U panel, is connected to the cover plate via a quick connector. The soil is subjected to a suction-controlled multi-stage ring shear testing scheme, using the $s = u_a$ testing concept ($u_w = 0$). Finally, the induced shear surface is thoroughly examined via microscopic digital imaging.

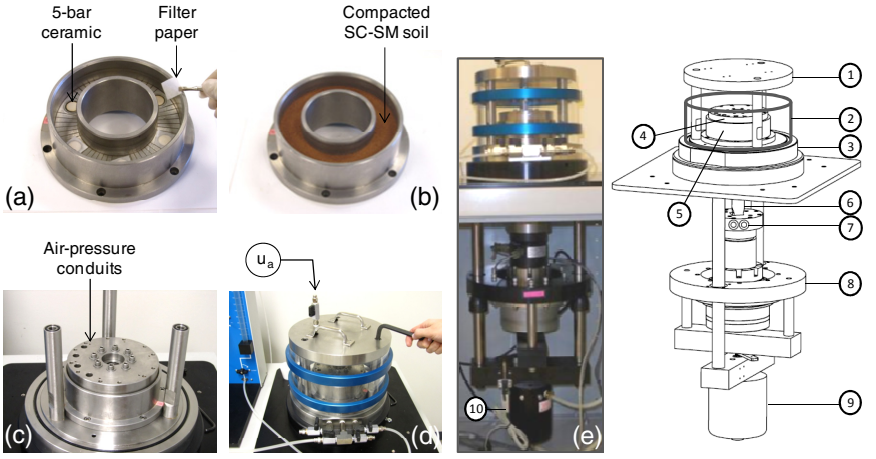

Fig. 12 Suction-controlled RS apparatus: General assembly and torque application system.

Fig. 12(e) shows an isometric view of the main cell and servo-controlled axial load and torque application systems: 1 – Top cover plate; 2 – Confining cell; 3 – Bottom base plate; 4 – Rotary upper annular platen; 5 – Fixed lower annular platen; 6 – Vertical load shaft; 7 – Combined axial force and torque transducers (Tovey Engineering); 8 – Electromechanical rotary actuator (Harmonic Drive Sys.) for torque application; 9 – Pneumatic actuator (MB Marsh Bellofram) for axial loads; 10 – LVDT for soil vertical deformation. A detailed description of its full development, including calibration, is given by Hoyos et al. (2011c).

The soil used in this work classifies as silty clayey sand (SC-SM) according to the USCS: 60% sand, 34.05% silt, and 5.95% clay. The fine-grained fraction has LL = 26.4% and PI = 6.2%. SC-SM soil was selected because of its poor gradation and relatively low plasticity, thus minimizing the required pore-fluids equalization time. Fine-grained material was also expected to prevent significant wall-friction

effects during shearing. All samples were statically compacted into the lower annular platen to a target dry unit weight of 95% of $\gamma_{d\text{-}max}$ (= 1.33 g/cm^3).

The first stage of a multi-stage suction-controlled RS test involved bringing the soil to initial net normal stress, $(\sigma_n - u_a)$ = 25 kPa, and matric suction, s = 0, 25, 50, or 100 kPa. The time required for consolidation-equalization ranged from 72-120 hrs (3-5 days). All tests were performed by following a multi-stage scheme in which residual strength assessments were made at 3 or more net normal stresses, $(\sigma_n - u_a)$ = 25, 50, 75, 100, or 200 kPa. A constant rotational speed of 0.023°/min (equivalent horizontal displacement rate of 0.025 mm/min) was adopted.

Fig. 13(a) shows the shear stress vs. horizontal displacement response, during first shearing stage, at suctions, s = 0, 25, 50, and 100 kPa. All samples exhibit an increase in shear stress up to a peak value, followed by a gradual decrease until residual state is attained: the peak is clearly more pronounced at higher suctions. A considerable increase in residual shear strength is also observed for s = 100 kPa.

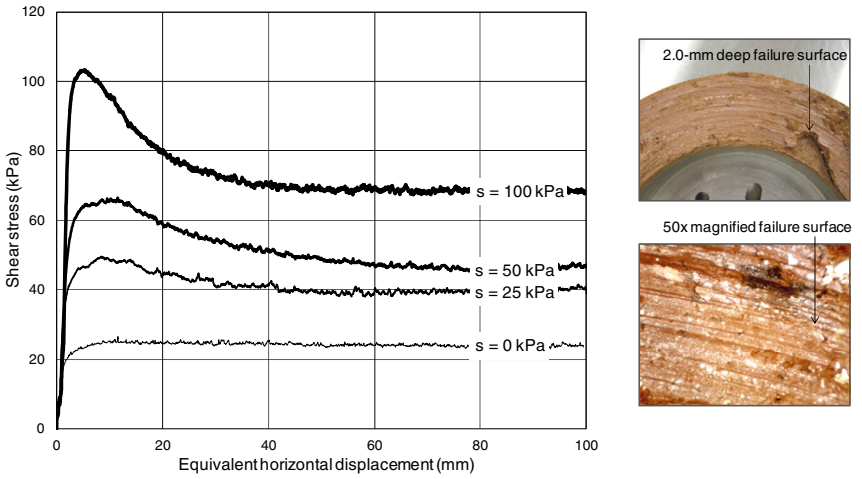

Fig. 13 General response of SC-SM soil from suction-controlled ring shear testing.

A typical failure surface is shown in Fig. 13(b) – top. The failure plane was induced within the thickness of the sheared sample, about 2.0-mm deep. A microscopic digital image of the induced failure is also shown in Fig. 13(b) – bottom, which is characterized by a polished and bright surface, thus indicating the development of slickensides along which residual strength is measured.

Fig. 14(a) shows the effect of net normal stress on residual failure envelopes. Results show a high nonlinearity with respect to matric suction. This nonlinearity of the residual failure envelopes increases with increasing net normal stress. There also appears to be a direct correspondence between the nonlinear nature of the envelopes (threshold value of suction beyond which they become nonlinear) and the air-entry value of the very SC-SM soil, as assessed from its SWRC in Fig. 14(b).

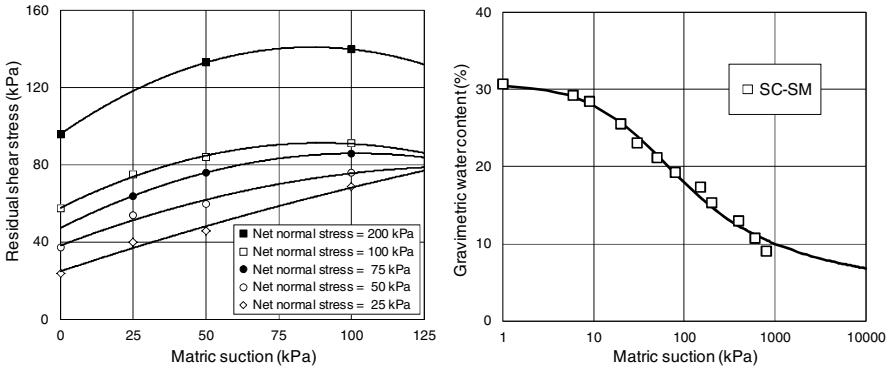

Fig. 14 Contrast of residual failure envelopes against SWRC of compacted SC-SM soil.

6 Closing Remarks

Civil engineers all around the world, vividly aware of the thousands of tragic losses from natural disasters every year, are increasingly recognizing that unsaturated soil research may provide more robust analytical tools and safer design guidelines for critical geotechnical infrastructure; thereby, they are increasingly exhorting researchers and state agencies to act accordingly to realize that potential. This adds new urgency to a longstanding search for new testing methodologies that are more suitable for modeling the engineering response of unsaturated soils. The devices described in this paper, and the corresponding experimental protocols, offer the unlimited potential to advance our understanding of unsaturated soil behavior under general stress states, therefore facilitating the incorporation of more reliable material properties into existing design models for geosystems made of compacted soil or resting on unsaturated ground. However, the most exciting prospect of all is that the future experimental series will reveal something completely unanticipated, opening new vistas on the fascinating nature of unsaturated soil behavior.

Acknowledgements. The research efforts summarized in this document have been supported by the National Science Foundation, Arlington, Virginia; and COLCIENCIAS, Bogotá, Colombia. This support is gratefully acknowledged. The author would also like to acknowledge the contributions from his current and former graduate students, Eduardo Suescún, William Douglas, J. Andrés Cruz, Diego Pérez-Ruiz, and Claudia Velosa; and research collaborators, Anand Puppala and Arcesio Lizcano. Any findings, conclusions, or recommendations expressed in this material are those of the author and do not necessarily reflect the views of NSF or COLCIENCIAS.

References

Alonso, E.E., Gens, A., Josa, A.: A constitutive model for partially saturated soils. Géotechnique 40(3), 405–430 (1990)

Alshibli, K.A., Godbold, D.L., Hoffman, K.: The Louisiana plane strain apparatus for soil testing. Geotechnical Testing Journal, ASTM 27(4), 337–346 (2004)

Bromhead, E.N.: A simple ring shear apparatus. Ground Engineering 12(5), 40–44 (1979)

Brull, A.: Caracteristiques mécaniques des sols de fondation de chaussées en fonction de leur état d'humidité et de compacité. In: Proc. of Int. Conference on Soil Compaction, Paris, vol. 1, pp. 113–118 (1980)

Cabarkapa, Z., Cuccovillo, T.: Automated triaxial apparatus for testing unsaturated soils. Geotechnical Testing Journal 29(1), 1–9 (2006)

Cabarkapa, Z., Cuccovillo, T., Gunn, M.: A new triaxial apparatus for testing unsaturated soils. In: Proc. of Second Int. Conference on Unsaturated Soils, Beijing, China, vol. 2, pp. 194–195 (1998)

Cho, G.C., Santamarina, J.C.: Unsaturated particulate materials: Particle-level studies. Journal of Geotechnical and Geoenv. Engineering, ASCE 127(1), 84–96 (2001)

Cruz, J.A., Hoyos, L.R., Lizcano, A.: A novel suction-controlled biaxial apparatus for unsaturated soils. In: Jotisankasa, A., Sawangsuriya, A., Soralump, S., Mairaing, W. (eds.) Proc. of 5th Asia-Pacific Conference on Unsaturated Soils: Theory and Practice 2011, Pattaya, Thailand, November 14-16, vol. 1, pp. 233–237. Kasetsart University (2011)

Drescher, A., Vardoulakis, I., Han, C.: A biaxial apparatus for testing soils. Geotechnical Testing Journal, ASTM 13, 226–234 (1990)

Fauziah, M., Nikraz, H.R.: The behaviour of unsaturated compacted clay under plane strain condition. In: Geo-Environment and Landscape Evolution III, Proc. of 3rd Int. Conference on Evolution, Monitoring, Simulation, Management and Remediation of the Geological Environment and Landscape, New Forest, UK, pp. 77–85 (June 2008)

Fredlund, D.G., Rahardjo, H.: Soil Mechanics for Unsaturated Soils. John Wiley & Sons (1993)

Fredlund, D.G., Morgenstern, N.R., Widger, R.A.: The shear strength of unsaturated soils. Canadian Geotechnical Journal 15, 313–321 (1978)

Hilf, J.W.: An investigation of pore water pressure in compacted cohesive soils. Tech. Memo. No. 654, U.S. Department of Interior, Bureau of Reclamation, Design and Construction Division, Denver, CO (1956)

Hoyos, L.R., Suescún, E.A., Puppala, A.J.: Small-strain stiffness of unsaturated soils using a suction-controlled resonant column device with bender elements. In: Han, J., Alzamora, D.E. (eds.) Advances in Geotechnical Engineering, GSP 211, Geo-Institute of ASCE, Proc. of Geo-Frontiers 2011, Dallas, Texas, March 13-16, pp. 4313–4322 (2011a)

Hoyos, L.R., Pérez-Ruiz, D.D., Puppala, A.J.: Constitutive behavior of compacted clayey sand using a refined suction-controlled cubical test cell. In: Han, J., Alzamora, D.E. (eds.) Advances in Geotechnical Engineering, GSP 211, Geo-Institute of ASCE, Proc. of Geo-Frontiers 2011, Dallas, Texas, March 13-16, pp. 4303–4312 (2011b)

Hoyos, L.R., Velosa, C.L., Puppala, A.J.: A servo/suction-controlled ring shear apparatus for unsaturated soils: Development, performance and preliminary results. Geotechnical Testing Journal, ASTM 34(5), 413–423 (2011c)

Hoyos, L.R., Pérez-Ruiz, D.D., Puppala, A.J.: Modeling unsaturated soil behavior under multiaxial stress paths using a refined suction-controlled cubical test cell. In: Hoyos, L.R., Zhang, X., Puppala, A.J. (eds.) Experimental and Applied Modeling of Unsaturated Soils, GSP 202, Geo-Institute of ASCE, Proc. of GeoShanghai 2010, Shanghai, China, June 3-5, pp. 40–47 (2010)

Hoyos, L.R., Laikram, A., Puppala, A.J.: A novel suction-controlled true triaxial apparatus for unsaturated soils. In: Toll, D.G., Augarde, C.E., Gallipoli, D., Wheeler, S.J. (eds.) Proc. of First European Conference on Unsaturated Soils: Advances in Geo-Engineering, Durham, U.K., July 2-4, pp. 83–88. CRC Press (2008)

Hoyos, L.R., Macari, E.J.: Development of a stress/suction-controlled true triaxial testing device for unsaturated soils. Geotechnical Testing Journal, ASTM 24(1), 5–13 (2001)

Inci, G., Yesiller, N., Kagawa, T.: Experimental investigation of dynamic response of compacted clayey soils. Geotechnical Testing Journal, ASTM 26(2), 125–141 (2003)

Infante Sedano, J.A., Vanapalli, S.K., Garga, V.K.: Modified ring shear apparatus for unsaturated soil testing. Geotechnical Testing Journal, ASTM 30(1), 1–9 (2007)

Khosravi, A., Ghayoomi, M., McCartney, J., Ko, H.Y.: Impact of effective stress on the dynamic shear modulus of unsaturated sand. In: Fratta, D., Puppala, A.J., Muhunthan, B. (eds.) Advances in Analysis, Modeling & Design, GSP 199, Geo-Institute of ASCE, Proc. of GeoFlorida 2010, West Palm Beach, Florida, February 20-24, pp. 410–449 (2010)

Kim, D.S., Seo, W.S., Kim, M.J.: Deformation characteristics of soils with variations of capillary pressure and water content. Soils and Foundations 43(4), 71–79 (2003)

Mancuso, C., Vassallo, R., d'Onofrio, A.: Small strain behavior of a silty sand in controlled-suction resonant column-torsional shear tests. Canadian Geotechnical Journal 39, 22–31 (2002)

Marinho, F.A.M., Chandler, R.J., Crilly, M.S.: Stiffness measurements on unsaturated high plasticity clay using bender elements. In: Alonso, E.E., Delage, P. (eds.) Proc. of First Int. Conference on Unsaturated Soils, Paris, France, September 6-8, vol. 2, pp. 535–539 (1995)

Matsuoka, H., Sun, D.A., Kogane, A., Fukuzawa, N., Ichihara, W.: Stress-strain behaviour of unsaturated soil in true triaxial tests. Canadian Geotechnical Journal 39, 608–619 (2002)

Mendoza, C.E., Colmenares, J.E., Merchán, V.E.: Stiffness of an unsaturated compacted clayey soil at very small strains. In: Tarantino, A., Romero, E., Cui, Y.J. (eds.) Proc. of Int. Symposium on Advanced Experimental Unsaturated Soil Mechanics, Trento, Italy, June 27-29, pp. 199–204. Balkema (2005)

Merchán, V., Romero, E., Vaunat, J.: An adapted ring shear apparatus for testing partly saturated soils in the high suction range. Geotechnical Testing Journal, ASTM 34(5), 433–444 (2011)

Ng, C.W.W., Xu, J., Yung, S.Y.: Effects of imbibition-drainage and stress ratio on anisotropic stiffness of an unsaturated soil at very small strains. Canadian Geotechnical Journal 46, 1062–1076 (2009)

Picornell, M., Nazarian, S.: Effects of soil suction on low-strain shear modulus of soils. In: Proc. of Second Int. Conference on Unsaturated Soils, Beijing, China, August 27-30, vol. 1, pp. 102–107 (1998)

Qian, X., Gray, D.H., Woods, R.D.: Resonant column tests on partially saturated sands. Geotechnical Testing Journal, ASTM 14(3), 266–275 (1991)

Reis, R.M., de Azevedo, R.F., Botelho, B.S., Vilar, O.M.: Performance of a cubical triaxial apparatus for testing saturated and unsaturated soils. Geotechnical Testing Journal, ASTM 34(3), 177–185 (2011)

Ruiz, W.: Diseño de un aparato biaxial. Proyecto de grado de Magíster en Ingeniería Civil, Universidad de los Andes, Bogotá, Colombia (2003)

Sawangsuriya, A., Edil, T.B., Bosscher, P.J.: Modulus-suction-moisture relationship for compacted soils in postcompaction state. Journal of Geotechnical and Geoenv. Engineering, ASCE 135(10), 1390–1403 (2009)

Sawangsuriya, A., Edil, T.B., Bosscher, P.J.: Modulus-suction-moisture relationship for compacted soils. Canadian Geotechnical Journal 45, 973–983 (2008)

Schanz, T., Alabdullah, J.: Testing unsaturated soil for plane strain conditions: A new double wall biaxial device. In: Experimental Unsaturated Soil Mechanics, pp. 169–178. Springer (2007)

Vardoulakis, I., Graf, B.: Calibration of constitutive models for granular materials using data from biaxial experiments. Géotechnique 35(3), 299–317 (1985)

Vardoulakis, I., Goldscheider, M.: Biaxial apparatus for testing shear bands in soils. In: Proc. of 10th Int. Conference on Soil Mechanics and Foundation Engineering, Stockolm, vol. 4, pp. 819–824 (1981)

Vassallo, R., Mancuso, C., Vinale, F.: Effects of net stress and suction history on small strain stiffness of a compacted clayey silt. Canadian Geotechnical Journal 44, 447–462 (2006)

Wood, C.C.: Shear strength and volume change characteristics of compacted soil under conditions of plane strain. Ph.D. dissertation, University of London, UK (1958)

Wu, S., Gray, D.H., Richart Jr., F.E.: Capillary effects on dynamic modulus of sands and silts. Journal of Geotechnical Engineering, ASCE 110(9), 1188–1203 (1984)

Desiccation Cracking in Clayey Soils: Mechanisms and Modelling

Jayantha Kodikara[1] and Susanga Costa[2]

[1] Department of Civil Engineering, Monash University, Australia
Jayantha.Kodikara@monash.edu
[2] School of Applied Sciences and Engineering, Monash University Gippsland Campus, Australia

Abstract. This paper presents a summary of the work undertaken on desiccation cracking in soils with special reference to the work undertaken by the authors and co-workers at Monash University. All areas of historical field observations, laboratory modelling and identified mechanisms are discussed briefly. Analytical and numerical approaches for modelling of the desiccation cracking and process are discussed. Cohesive crack approach is presented as a viable approach for modelling of desiccation cracking and fracture evolution catering for consistency change of soil during desiccation. It is highlighted that both tensile strength and crack opening displacement increases, thereby increasing the fracture energy of the soil as the moisture content reduces. This modelling approach can be extended to model wetting/drying cycles and to model crack dynamics. Associated moisture transfer modelling also needs to be advanced for a complete solution.

1 Introduction

Desiccation cracking in soil has been a challenging puzzle for researchers for decades. The presence of cracking in clay soils can significantly alter its mechanical, hydrological, physico-chemical and thermal properties, commonly in an undesirable fashion. Therefore, this problem has been a stumbling block in numerous disciplines such as geotechnical engineering, geo-environmental engineering, transport engineering, mining and resource engineering, agricultural engineering and soil science. Some specific applications within these disciplines where desiccation cracking is significant are shown in Table 1.

Despite soil cracking has been a major issue in a range of applications and a theme of research for decades, its advancement in comparison to our capability of modeling shear failure of the soil matrix as a continuum is limited. Over the last decade or so, there has been a substantial research effort directed around the world to study and model the desiccation induced shrinkage cracking in soils. One reason for this is due to the increase in the importance of ground/atmosphere modeling especially related to climate change effects in a range of field applications and the need for safe solid and nuclear waste management technologies. The other reason is the recognition that there is a significant knowledge gap in this particular area.

L. Laloui and A. Ferrari (Eds.): Multiphysical Testing of Soils and Shales, SSGG, pp. 21–32.
springerlink.com

Table 1 Summary of how desiccation cracking influence field applications

Discipline	Application
Geotechnical Engineering	• Slopes – There is significant evidence that cracking at the crest area of the slopes trigger the initiation of slope failure (Take 2003) • Flood dykes – Progressive failures that take place in UK's extensive dyke system (extending up to 35,000 km with an annual maintenance budget of £450 million) are triggered commonly by desiccation cracking that takes place in the downstream slope, subsequently providing seepage paths and block uplifting during flooding (Dyer 2009). Canal systems also suffer from desiccation cracking induced distress. • Dams – Embankment dams experience internal erosion leading to piping failures, which accounts for about 50% dam failures and accidents. Potential erosion pathways are assisted by cracks formed by desiccation above phreatic surface, differential settlement, hydraulic fracturing and earthquakes (Foster et al. 2000)
Geo-environmental Engineering	• Compacted clay landfill liners and covers and Geosynthetic clay liners – Thermally induced or evaporation induced desiccation and differential settlement induced cracking of these components in modern waste landfills is a major issue providing unwanted pathways for escape of leachate and gas (Daniel and Wu 1993; Zhou and Rowe 2003) • Deep nuclear waste isolation – Bentonite buffer zones can undergo thermal drying, shrinkage and cracking near the waste package (Park et al. 2001)
Transport Engineering	• Cracking in road pavements – Reactive soil induced cracking in road bases is a major problem and inure substantial annual maintenance costs worldwide (Chakrabarti et al. 2002; Lytton et al. 1976)
Mining and Resources Engineering	• Mine tailings managements – Cracking in mine tailings influences its drying rates and stability (Morris et al. 1992) and induce changes in the permeability creating environmental consequences because of the potential pollutant generation on infiltration (Rodriguez et al. 2007)
Agricultural Engineering / Soil Science/Geology	• Fracture of soils is important consideration in tillage and water and chemical usage in agricultural engineering (Chertkov 2002; Ahmad 1996) • In irrigated lands cracks allows the water and solutes to flow rapidly through the soil bypassing the dry root zone, thus leading to water and nutrient shortage for crops (Bronswijk 1991) • Formation of fissures and gilgai formation in soil has been a subject of research in soil and geo-science (Kodikara et al. 2002)
Materials Engineering	• Cracking and warping (or curling) cause problems in many coating and material elaboration processes that are based on the drying of colloidal suspensions (Pauchard et al. 1999)
Planetary Sciences	• Formation of giant polygons on Earth and Mars, and evidence of presence of water (El Marry et al. 2012)

2 Experiments and Mechanisms

Work has been carried out on fracture mechanics since the early twentieth century. The history of investigation of desiccation cracks in geo-engineering related areas also dates back in the same period. For example, studies of Kindle (1917) are one of the earliest works found in literature on this topic. In early stages, most of the

work in geoengineering was predominantly on the qualitative behaviour of cracking. Later, the quantitative behaviour, cracking mechanism and modelling became more pronounced.

2.1 Experiments

The involvement of highly non-linear material behaviour that vary with the environmental factors such as temperature, cyclic wetting and drying and relative humidity makes the study of cracking complicated. Though a substantial quantity of data are presented in literature on both small scale laboratory experiments and large scale field investigations, most of them do not give sufficient detailed information to explain the process completely. Significant disagreements can be found in these reported data in relation to crack spacing, crack width and crack depth. Kodikara et al. (2002) reviewed the field and laboratory evidence on clay cracking and presented a synthesis of mechanisms applicable to heavy clays, drawing knowledge from a number of disciplines, in particular from Soil Science.

Early work on experimental modelling of desiccation cracking of soils was mostly on rectangular boxes. While these tests provided valuable qualitative data, the results were far too complex for detailed analysis or numerical modelling. Nahlawi and Kodikara (2006) (originally Nahlawi 2004) first introduced undertaking tests in long moulds where cracks are controlled to develop parallel to longitudinal directions. This approach was subsequently followed by a number of researchers for experimental and numerical modelling (e.g. Peron et al. 2009a), and have led more insights into fracture behaviour (e.g. Kodikara and Choi 2006; Peron et al. 2009a). Table 2 summarises main categories of experimental work on desiccation cracking.

Other forms of experimentation were undertaken to determine the material properties governing the fracture process. These include tensile strength measurements, which included direct (e.g. Nahlawi et al. 2004; Wang et al. 2007; Lakshmikantha 2009) and indirect (e.g. Konrad and Ayad 1997; Harrison et al. 1994) tests. Linear Elastic Fracture Mechanics (LEFM) was commonly assumed with determination of fracture toughness (e.g. Wang 2007; Lakshmikantha 2009; Costa 2009; Konrad and Ayad 1997). Importance of considering elasto plastic nature of soil during fracture was highlighted by some researchers (Hallet and Newson, 2005). Numerical work undertaken on this topic has been mainly based on the linear elastic fracture mechanics (LEFM) principles, which utilized fracture toughness, mostly in Mode I cracking (Fang 1994; Lakshmikantha et al., 2008). More recently, Amarasiri and Kodikara (2011) advocated the use of cohesive crack model for soils highlighting that this model is applicable for the full range of soil consistencies during desiccation. Amarasiri et al. (2011) presented techniques to derive cohesive crack properties for Mode I cracking from compacted clay beams. All these tests were performed with external loading. Therefore, on one hand, their relevance to desiccation cracking needed to be explained and, on the other hand, soft materials with high moisture contents could not be tested since they could not be formed into beams or cylinders easily. However, Costa (2009)

Table 2 Seminal experimental work on desiccation cracking

Test type	Reference	Material / investigated parameters
Rectangular tests	• Corte and Higashi (1960)	• Bloomington till – drying tests with different base materials, densities, thicknesses, and gravel inclusions. More details also see Kodikara et al. (2000).
	• Miller et al. (1998)	• clay landfill liner models – wet-dry cycles, crack intensity factor was introduced.
	• Yesiller et al. (2000)	• three compacted clay liner materials – wet-dry cycles, crack intensity factor, effect of fine content, suction
	• Lakshmikantha et al. (2006)	• Silty clay – specimen size, aspect ratio, specimen thickness
Circular tests	• Kindle (1917)	• mud – desiccation rate, effect of salinity, influence of composition of mud on cracks
	• Groisman and Kaplan (1994)	• coffee-water mixtures - effect of layer thickness and basal restrains
	• Toramaru and Matsumoto (2004)	• starch-water mixture – desiccation rate, columnar joint formation
	• Costa et al. (2012) (originally Costa 2009)	• starch/clay/fine sand – layer thickness, desiccation rate, crack initiation and flaw distribution, fracture energy
Long mould tests	• Nahlawi and Kodikara (2006) (originally Nahlawi 2004)	• Werribee clay – cracking water content, evolution of cracking pattern, desiccation rate, crack spacing to depth ratio
	• Peron et al. (2009a)	• silt and clay – shrinkage strain, water content and suction
Long mould tests with image analysis	• Costa et al. (2008) (originally Costa 2009)	• Werribee clay – slurry and compacted conditions, shrinkage strain development, restrained and free basal conditions, crack initiation, strain isochrones patterns
Field experiments of clay cracking	• Konrad and Ayad (1997), Philip et al. (2002)	• Saint Alban clay – Konrad and Ayad investigated cracking and patterns in field cell in soft clay. Philip et al. undertook field tests on landfill liners.

(also in Costa and Kodikara 2012) developed a restrained ring test and presented a way to compute fracture energy in the form of 'J-integral' using image analysis during desiccation.

2.2 Mechanisms

On the basis of the various tests undertaken (some listed in Table 2), governing mechanisms of desiccation are identified as follows. The primary requirement for formation of desiccation cracks is restrained shrinkage leading to tensile stress development exceeding the tensile strength. If the drying soil body can be considered free of any restraints, the full potential shrinkage free from cracks

would develop, which would be a function of drying environment and soil properties. The restraints against free shrinkage can be internal, external or a combination of the two. Internal constraints are usually due to soil structure such as differing soil fabric units and moisture gradient. Displacement boundary conditions and interface friction can be regarded as external constraints.

Crack initiation is a major consideration in shrinkage crack modeling. It is, therefore, important to have a good understanding of the mechanisms behind the crack initiation. There appears to be two major controls in crack initiation during soil desiccation. First, the control that arises due to generated tensile stress distribution as a result of restraining of free shrinkage strain in the soil. According to this control, the cracks should initiate at the midpoint of the drying soil mass (with free edges), where the stresses are likely to be maximum. Nahlawi and Kodikara (2006) observed this behaviour in relation to desiccation of long thin layers of soil, where with time, sequential subdivision of the long soil layer took place, starting from a first crack close to the middle of the layer.

In most circular and rectangular experiments cracks do not initiate at the exact positions where the tensile stress is considered to be maximum theoretically. This behavior is due to the second control coming from the influence of flaws in crack initiation. However, their activation will be influenced by the tensile stress at those locations. These flaws could be either imperfections such as micro-cracks, inclusions such as air bubbles or large stiff particles and large pores that can desaturate rather quickly. Some researchers have indicated that cracking water content coincides with the air-entry value of the drying material. However, this statement needs to be carefully considered since drying soft near-saturated soil (such as slurry soil) desaturate at very high suctions (sometimes over 1000 kPa) but they can crack at very low suctions, for instance less than 10 kPa (Costa 2009). This behavior arises because the fracture initiates due to the failure of the water-phase locally at the tip of the flaws (or local air entry of larger pores) while the soil matrix remains predominantly saturated (Shin and Santamarina, 2011). In other words, during drying of wet soft soils under restraints, the soil effective stress is normally compressive and it is the water stress that is negative making the total stress tensile. In contrast, when soil water characteristics or shrinkage tests are undertaken, normally cracking is avoided providing mostly free shrinkage and, therefore, pore sizes becomes progressively small (for shrinking soils) allowing them to sustain higher suctions and therefore air entry is substantially delayed.

Fig. 1 illustrates this combined influence of stress and flaws. According to the fracture mechanics, the tensile stress that is needed to activate a flaw is inversely proportional to the square root of the flaw size. Hence, it is possible for cracks to occur at locations away from the points where the tensile stress is maximum, if flaws at those locations are sufficiently large to get activated by the prevailing tensile stress.

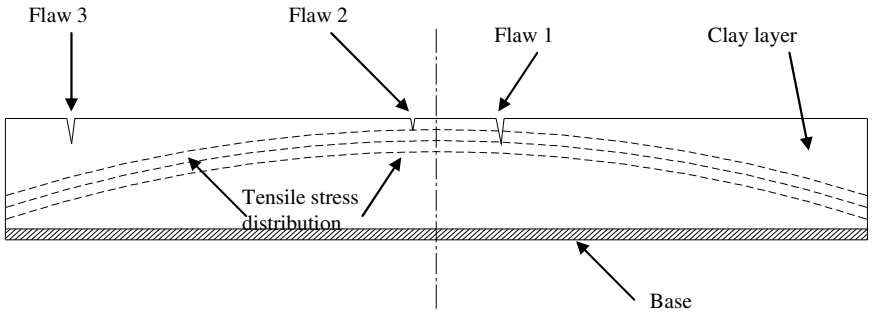

Fig. 1 Effect of flaws on crack initiation using hoop stress distribution in circular test (Costa et al. 2012)

The evolution and propagation of shrinkage cracks cannot be categorized as pure orthogonal or pure non-orthogonal (e.g. hexagonal) patterns. Generally, non-orthogonal patterns seem to occur when the "effective" thickness of the drying soil is small, which leads to high concentration of strain energy in comparison to fracture energy required for crack propagation (Corte and Higashi 1960; Costa et al. 2012). Under these conditions, fractures tend to occur predominantly simultaneously with optimum crack configuration to dissipate energy. Costa et al. (2012) highlighted that this "effective length", which holds most of the suction caused by drying, scales with $D/\dot{E}$, where D is the moisture diffusion coefficient (L^2/T) and $\dot{E}$ (is the rate of evaporationL/T) from surface. Therefore, the effective thickness can become small either when D is small, as for clay, (and) or $\dot{E}$ is large, as in fast drying. The final state of the crack pattern can be a mixture of orthogonal, non-orthogonal, simultaneous and sequential cracks (see Nahlawi and Kodikara (2006) for definitions). However in clay cracking, sequential, orthogonal cracks significantly dominate the final pattern. Costa et al. (2012) extensively discussed the factors that lead to evolution of these two crack patterns.

3 Analytical and Numerical Modelling

Table 3 summarises seminal analytical and numerical modelling undertaken on desiccation cracking to date. The overall work is presented in three categories: systems approach, tensile stress failure approach and fracture mechanics approach. In the following description, some recent developments of desiccation cracking are outlined.

Table 3 Seminal numerical work on desiccation cracking

Approach	Description
Systems approaches e.g. Bronswijk (1988), Abu-Hejleh and Znidarcic (1995)	These models usually take into account the water removal and associated volume change. The crack volume is considered through geometric relations without considering detailed mechanics of fracture.
Tensile stress failure approach e.g. Morris et al. (1992), Kodikara and Choi (2006), Peron et al. (2009b), Amarasiri et al. (2010),	Morris et al. presented analytical equations to compute crack depths under Ko conditions, which lead to tensile stresses. The point where tensile stress reaches tensile strength was considered as the depth of cracking. Kodikara and Choi (2006) developed a simplified analytical model for desiccation cracking of long layers of soil accounting for basal restraints and tensile failure. These models assume linear elastic soil behaviour although significant non-linear effects were taken into account by Kodikara and Choi in an approximate incremental way. Peron et al. (2009b) modelled the desiccation process using distinct element method and indicated that this method has promise capturing some essential behaviour. Amarasiri et al. (2010) modelled numerically the evolution of desiccation cracking in a thin long layer using a hybrid distinct element and continuum method. They included the significant non-linear effects of desiccation including suction development and soil stiffening using an incrementally non-linear elastic approach.
Fracture mechanics approaches e.g. Lachenbruch (1961), Morris et al. (1992), Ayad et al. (1997), Amarasiri and Kodikara (2011).	Early work on shrinkage induced cracking using fracture mechanics was introduced by Lachenbruch (1961). Morris et al. presented 1-D analytical solutions using LEFM to predict crack depths. Ayad et al. (1997) applied LEFM approach to model a field experiment. However, they were unable to model crack spacing rationally. More recently, Amarasiri and Kodikara (2011) introduced cohesive crack approach to incorporate fracture energy and significant non-linearity present during desiccation.

Conventional unsaturated soil mechanics dictate that suction is used as the state variable for stress analysis (e.g. Morris et al. 1992). However, more recently researchers have found that it is more convenient to use (gravimetric) moisture content as a governing state variable for desiccation modelling (e.g. Kodikara and Choi 2006; Peron et al. 2009a). In this approach, the stress increment due to desiccation $d\sigma_{ij}$ can be expressed as:

$$d\sigma_{ij} = D_{ijkl}(d\varepsilon_{kl} - d\varepsilon_{kl}^{sh}) \tag{1}$$

where, D_{ijkl} is the tangent stiffness matrix, $d\varepsilon_{kl}$ is the observed strain increment, $d\varepsilon_{kl}^{sh}$ is the general 'free' shrinkage increment. Assuming free shrinkage to be isotropic, $d\varepsilon_{kl}^{sh} = d\varepsilon^{sh}\delta_{kl}$, where $\delta_{kl}$is Kronecker delta. As a simplification, if non-linear elastic constitutive behaviour is assumed, Equation (1) can be simplified as:

$$d\sigma_{ij} = D_{ijkl}d\varepsilon_{kl} - 3Kd\varepsilon^{sh}\delta_{kl} \tag{2}$$

where, K is the tangent bulk modulus. The free shrinkage strain is related moisture decrement (or increment in swelling) as $d\varepsilon^{sh} = \alpha de_w$, where e_w is the moisture ratio defined as wG_s, where w is the gravimetric moisture content G_s is the soil specific gravity. The parameter α is known as the hydric constant similar to thermal shrinkage coefficient. However, α may not be a constant and may depend on the drying/wetting history and stress level. Under 1-D conditions, relevance of α can be derived as follows. In homogeneous volumetric modelling, the state variables are void ratio (e), moisture ratio (e_w), net stress (σ) and suction (s). Out of these, two variables can be considered independent (Gould et al. 2011; Kodikara, 2012). Taking σ as a function of e and e_w:

$$d\sigma = \left(\frac{\partial\sigma}{\partial e}\right)_{e_w} de + \left(\frac{\partial\sigma}{\partial e_w}\right)_{e} de_w \tag{3}$$

From cyclic formula,

$$\left(\frac{\partial\sigma}{\partial e_w}\right)_{e} = -\frac{\left(\frac{\partial\sigma}{\partial e_w}\right)_{\sigma}}{\left(\frac{\partial e}{\partial\sigma}\right)_{e_w}} \tag{4}$$

Substituting Eq. (4) in (3) and rearranging gives:

$$d\sigma = \left(\frac{\partial\sigma}{\partial e}\right)_{e_w} \left(de - \left(\frac{\partial e}{\partial e_w}\right)_{\sigma} de_w\right) \tag{5}$$

Using $\left(\frac{\partial e}{\partial e_w}\right)_{\sigma} = \alpha$ and $\left(\frac{\partial\sigma}{\partial e}\right)_{e_w} = K$, Eq. (5) can be expressed as:

$$d\sigma = K(de - \alpha de_w) \tag{6}$$

It is evident that Eq. (6) is 1-D or isotropic representation of Eq. (1), and the hydric coefficient α will be function of both σ and e. The relationship of α to the shrinkage curve can be obtained as $\alpha = \alpha^*/(1 + e_o)$, where α^* is the gradient of the shrinkage curve defined as the gradient of e vs. e_w curve at constant σ (Kodikara, 2012).

In incremental analysis, Eq. (2) can be modified as $d\sigma_{ij} + 3Kd\varepsilon^{sh}\delta_{kl} = D_{ijkl}d\varepsilon_{kl}$, and solved for actual deformations subject to boundary conditions in 2 or 3D conditions. The first author used this approach both in soil shrinkage (e.g. Kodikara et al. 2004; Amarasiri et al. 2011; Amarasiri and Kodikara 2011) and swelling analysis (Rajeev and Kodikara 2011).

For post-fracture modelling, three approaches have been used in the past, namely, tensile failure, LEFM and cohesive crack approach. The LEFM approach has not been used to model fracture evolution except for fracture depth prediction in an approximate way (Konrad and Ayad 1997). More recently the first author (with co-workers) introduced cohesive model as a versatile technique for desiccation and load-induced fracture modelling (e.g. Amarasiri and Kodikara, 2011). A brief description of this approach is presented here.

The cohesive crack concept was first introduced into material fracture by Dugdale (1960) and Barenblatt (1962). The basic premise of the cohesive crack method is that, when a crack opens and the two cracked surfaces move apart, the

normal stress across the crack surface drops gradually from the tensile strength (σ_t) of the material to zero at crack opening displacement, u_c. The area within the curve represents the fracture energy. In addition to fracture energy, it also allows the inclusion of energy dissipated in softening or plasticity in the material immediately adjacent to the advancing crack in the numerical model. Unlike for LEFM, the cohesive crack method can be used even where no initial crack is present, since fracture initiation is governed by tensile failure.

Fig. 2 shows some typical cohesive laws that have been proposed. These include Dugdale's (path ABB'), rectangular (path ABC), triangular (path AD), bilinear (path AFE) and exponential (path AGE) softening laws, which have been used in the past for modelling fracture of different materials. After significant trialing, Amarasiri et al. (2011) back-figured cohesive laws applicable to a clay with high shrink swell potential (Werribee clay) and indicated that triangular (path AD) can adequately describe the cohesive laws applicable to that soil. They indicated that σ_t and u_c both increased with decreasing moisture content. Furthermore, they formulated the unloading and re-loading mechanics since some cracks may close when multiple cracks form and propagate. In general sense, the same method could be extended to model drying and wetting cycles, but currently no data on cohesive behavior are available, under these conditions.

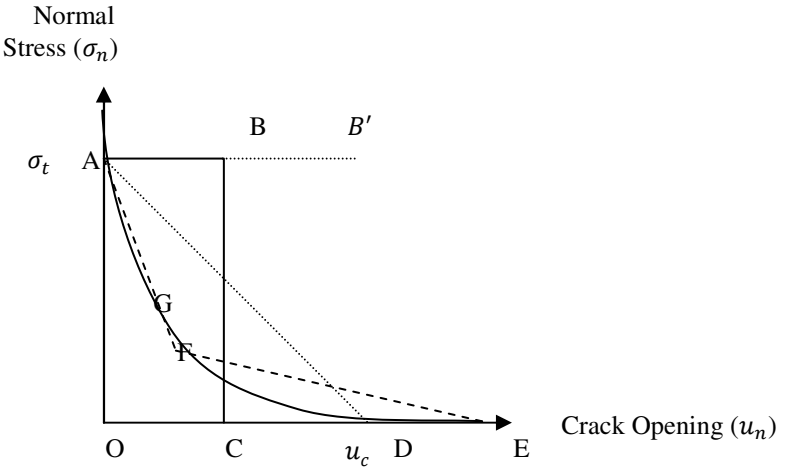

Fig. 2 Typical cohesive crack laws

4 Concluding Remarks

This paper presented a summary of the work undertaken on desiccation cracking in soils with special reference to the work undertaken by the authors and co-workers at Monash University. All areas of historical field observations, laboratory modelling and identified mechanisms were discussed briefly, and the authors apologise if reference to any of the work is missed. Analytical and numerical

approaches for modelling of the desiccation cracking and process were discussed. Cohesive crack approach was presented as a viable approach for modelling of desiccation cracking and fracture evolution catering for consistency change of soil during desiccation. It was highlighted that both tensile strength and crack opening displacement increases, thereby increasing the fracture energy of the soil as the moisture content reduces. This modelling approach can be extended to model wetting/drying cycles and associated cracking. Associated moisture transfer modelling needs to be advanced for a complete solution.

Acknowledgement. Financial support received from the Australian Research Council's Discovery Scheme is gratefully acknowledged.

References

Abu-Hejleh, A.N., Znidarcic, D.: Desiccation theory for soft cohesive soils. J. Geotech. Engrg. 121, 493–503 (1995)

Ahamad, N.: Occurrence of distribution of Vertisols. In: Ahmad, N., Mermut, A. (eds.) Vertisols and Technologies for their Management, Development in Soil Science, vol. 24, pp. 1–41 (1996)

Amarasiri, A., Kodikara, J., Costa, S.: Numerical Modelling of Desiccation Cracking. International Journal for Numerical and Analytical Methods in Geomechanics 48, 336–340 (2010)

Amarasiri, A.L., Costa, S., Kodikara, J.: Determination of cohesive properties of Mode I fracture from compacted clay beams. Canadian Geotechnical Journal 48(8), 1163–1173 (2011)

Amarasiri, A.L., Kodikara, J.K.: Numerical modelling of desiccation cracking using cohesive crack method. International Journal of Geomechanics GM (2011) 1943-5622.0000192

Ayad, R., Konrad, J.M., Soulié, M.: Desiccation of a sensitive clay: application of the model CRACK. Canadian Geotechnical Journal 34, 943–951 (1997)

Barenblatt, G.I.: The mathematical theory of equilibrium of cracks in brittle fracture. Adv. Appl. Mech. 7, 55–129 (1962)

Bronswijk, J.J.B.: Modeling of water balance, cracking and subsidence of clay soils. Journal of Hydrology 97, 199–212 (1988)

Bronswijk, J.J.B.: Relation between vertical soil movements and water content changes in cracking clays. Soil Sci. Soc. Am. J. 55, 1220–1226 (1991)

Chakrabarti, S., Kodikara, J.K., Pardo, L.: Overview of pavement performance in Australia. Road Transport and Research 11(3), 3–16 (2002)

Chertkov, V.Y.: Modelling cracking stages of saturated soils as they dry and shrink. Eur J. Soil Sci. 53, 105–118 (2002)

Corte, A., Higashi, A.: Experimental research on desiccation cracks in soil. Research Report, U. S. Army Snow Ice and Permafrost Research Establishment, Illinois, USA (1960)

Costa, S.: Study of desiccation cracking and fracture properties of clay soils. PhD Dissertation, Monash University (2009)

Costa, S., Kodikara, J.: Evaluation of J-integral for clay soils using a new ring test. Goetechnical Testing Journal (January 2012) (accepted for publication)

Costa, S., Kodikara, J., Shannon, B.: Salient Factors Controlling Desiccation Cracking in Laboratory Experiments. Geotechnique (2012) (accepted for publication)

Costa, S., Kodikara, J., Thusyanthan, N.I.: Modelling of desiccation crack development in clay soils. In: Proc. 12th International Conference of IACMAG, Goa, India, pp. 1099–1107 (2008)

Daniel, D.E., Wu, Y.K.: Compacted Clay Liners and Covers for Arid Sites. Journal of Geotechnical Engineering 119(2), 223–237 (1993)

Dugdale, D.S.: Yielding of steel sheets containing slits. J. Mech. Phys. Solids 8, 100–108 (1960)

Dyer, M., Utill, S., Zielinski, M.: Field study of desiccation fissuring of flood embankments. Water Management 162, 221–232 (2009)

El Marry, M.R., Kodikara, J., Wijesooriya, S., Markiewics, W.J., Thomas, N.: Desiccation mechanism for formation of giant polygons on earth and intermediate-sized polygons on Mars: Results from a pre-fracture model. Earth and Planetary Sci. Letters 323-324, 19–26 (2012)

Fang, H.Y.: Cracking and fracture behavior of soil. Fracture Mechanics Applied to Geotechnical Engineering. ASCE, Geotechnical Special Publication 43, 102–117 (1994)

Foster, M.A., Fell, R., Spannagle, M.: The statistics of embankment dam failures and accidents. Canadian Geotechnical Journal 37(5), 1000–1024 (2000)

Gould, S., Pathmanathan, R., Kodikara, J., Zhao, X.-L., Burn, S., Marlow, S.: A void ratio-water content-net model for environmentally stabilised expansive soils. Canadian Geotechnical Journal 48(6), 867–877 (2011)

Groisman, A., Kaplan, E.: An experimental study of cracking induced by desiccation. Europhysics Letters 25(6), 415–420 (1994)

Hallet, P.D., Newson, T.A.: Describing soil crack formation using elastic - plastic fracture mechanics. European Journal of Soil Science 56, 31–38 (2005)

Harison, J.A., Hardin, B.O., Mahboub, K.: Fracture toughness of compacted cohesive soils using ring test. Journal of Geotechnical Engineering 120(5), 872–891 (1994)

Kindle, E.M.: Some factors affecting the development of mud cracks. The Journal of Geology 25(2), 135–144 (1917)

Kodikara, J.K.: New framework for volumetric constitutive behaviour of compacted unsaturated soils. Canadian Geotechnical Journal (to appear, 2012)

Kodikara, J., Barbour, S.L., Fredlund, D.G.: Structure development in surficial heavy clay soils: A synthesis of mechanisms. Australian Geomechnics 37(3), 25–40 (2002)

Kodikara, J.K., Barbaour, S.L., Fredlund, D.G.: Desiccation cracking of soil layers. In: Proceedings of the Asian Conference in Unsaturated Soils, UNSAT ASIA, Singapore, pp. 693–698 (2000)

Kodikara, J.K., Choi, X.: A simplified analytical model for desiccation cracking of clay layers in laboratory tests. In: Miller, G.A., Zapata, C.E., Houston, S.L., Fredlund, D.G. (eds.) Proc. Fourth International Conference on Unsaturated Soils, vol. 2, pp. 2558–2567. ASCE Geotechnical Special Publication 147 (2006)

Kodikara, J.K., Nahlawi, H., Bouazza, A.: Modelling of curling in desiccating clay. Canadian Geotechnical Journal 41, 560–566 (2004)

Konrad, J.M., Ayad, R.: An idealized framework for the analysis of cohesive soils undergoing desiccation. Canadian Geotechnical Journal 34, 477–488 (1997)

Lachenbruch, A.H.: Depth and spacing of tension cracks. J. Geophysical Research 66(12), 4273–4292 (1961)

Lakshmikantha, M.R.: Experimental and theoretical analysis of cracking in drying soils. PhD Dissertation. Universitat Politecnica De Catalunya (2009)

Lakshmikantha, M.R., Prat, P.C., Ladesma, A.: An experimental study of cracking mechanisms in drying soils. In: Proc. 5th International Conference on Environmental Geotechnics, pp. 533–540. Thomas Telford, London (2006)

Lakshmikantha, M.R., Prat, P.C., Tapia, J., Ledesma, A.: Effect of moisture content on tensile strength and fracture toughness of a silty soil. In: Toll, et al. (eds.) Proc. of First European Conference on Unsaturated Soils, E-UNSAT, Durham, UK, pp. 405–409 (2008)

Lytton, R.L., Boggess, R.L., Spotts, J.W.: Characteristics of expansive clay roughness of pavements. Transport Research Record, TRB, Washington, D.C., pp. 9–23 (1976)

Miller, C.J., Mi, H., Yesiller, N.: Experimental analysis of desiccation crack propagation in clay liners. Journal of the American Water Resources Association 34(3), 677–686 (1998)

Morris, P.H., Graham, J., Williams, D.J.: Cracking in drying soils. Canadian Geotechnical Journal 29, 263–277 (1992)

Muller, G.: Experimental simulation of basalt columns. Journal of Volcanology and Geothermal Research 86, 93–96 (1998)

Nahlawi, H.: Behaviour of reactive soil during desiccation. Masters Thesis, Monash University, Australia (2004)

Nahlawi, H., Chakrabarti, S., Kodikara, J.: A Direct Tensile Strength Testing Method for Unsaturated Geomaterials. Geotechnical Testing Journal 27(4), 1–6 (2004)

Nahlawi, H., Kodikara, J.K.: Laboratory experiments on desiccation cracking of thin soil layers. Geotechnical and Geological Engineering 24, 1641–1664 (2006)

Park, J.W., Chang, K., Kim, C.L.: Numerical simulations of the moisture movement in unsaturated bentonite under a thermal gradient. J. of Korean Nuclear Society 33(1), 62–72 (2001)

Pauchard, L., Parisse, F., Allain, C.: Influence of salt content on crack patterns formed through colloidal suspension desiccation. Physical Review E 59(3), 3737–3740 (1999)

Peron, H., Delenne, J.Y., Laloui, L., El Youssoufi, M.S.: Discrete element modelling of drying shrinkage and cracking of soils. Computers and Geotechnics 36, 61–69 (2009b)

Peron, H., Hueckel, T., Laloui, L., Hu, L.B.: Fundamentals of desiccation cracking of fine-grained soils: experimental characterisation and mechanisms identification. Canadian Geotechnical Journal 46, 1177–1201 (2009a)

Philip, L.K., Shimell, H., Hewitt, P.J., Ellard, H.T.: A field-based test cell examining clay desiccation in landfill liners. Quarterly Journal of Engineering Geology and Hydrogeology 35, 345–354 (2002)

Rajeev, P., Kodikara, J.: Numerical analysis of an experimental pipe buried in swelling soil. Computers and Geotechnics 38(7), 897–904 (2011)

Rodriguez, R., Sanchez, M., Ledesma, A., Lloret, A.: Experimental and numerical analysis of desiccation of a mining waste. Canadian Geotechnical Journal 44, 644–658 (2007)

Shin, H., Santamarina, J.C.: Desiccation cracks in saturated fine-grained soils: particle level phenomena and effective stress analysis. Géotechnique 61(11), 961–972 (2011)

Take, W.A.: The influence of seasonal moisture cycles on clay slopes. PhD dissertation, Cambridge University (2003)

Toramaru, A., Matsumoto, T.: Columnar joint morphology and cooling rate: A starch-water mixture experiment. J. Geophysical Research 109, B02205 (2004)

Wang, J.-J., Zhu, J.-G., Chiu, C.F., Zhang, H.: Experimental study on fracture toughness and tensile strength of a clay. Engineering Geology 94(1-2), 65–75 (2007)

Yesiller, N., Miller, C.J., Inci, G., Yaldo, K.: Desiccation and cracking behaviour of three compacted landfill liner soils. Engineering Geology 57, 105–121 (2000)

Zhou, Y., Rowe, R.K.: Development of a technique for modelling clay liner desiccation. Int. J. Numer. Anal. Meth. Geomech. 27, 473–493 (2003)

Triaxial Testing of Unsaturated Soils

E.C. Leong, T.T. Nyunt, and H. Rahardjo

School of Civil & Environmental Engineering,
Nanyang Technological University, Singapore
cecleong@ntu.edu.sg

Abstract. This paper highlights the key features of triaxial testing of unsaturated soils. The modifications to a conventional triaxial apparatus and the test procedures for various unsaturated soil triaxial tests are described. Test results for an undisturbed residual soil tested under consolidated undrained (CU) and constant water content (CW) conditions at three different strain rates are presented. The test results showed that ϕ^b is not a constant, but decreases as matric suction is increased. The shear strength envelopes obtained from CU and CW tests at the three different strain rates are similar.

1 Introduction

The difference between behavior of saturated and unsaturated soils lies in the existence of suction in unsaturated soils. Soil suction has two main components matric suction and osmotic suction (solute suction). Often, osmotic suction does not feature in the constitutive relationships for unsaturated soils whereas matric suction is always a permanent fixture. Katte and Blight (2012) showed that changes in osmotic suction do not affect shear strength of a soil. Matric suction is pore-water pressure when referenced to air pressure. Edil et al. (1981) and Fredlund and Rahardjo (1993) showed that matric suction is the fundamental suction component that controls mechanical behavior of unsaturated soils. There are two ways to impose matric suction onto a soil specimen: (1) to use the axis-translation technique (Hilf 1956) or (2) to use the osmotic technique via a semi-permeable membrane. Due to the inherent difficulties in the osmotic technique, the axis-translation technique is often used in the triaxial apparatus. Using the axis-translation technique, the conventional triaxial apparatus for saturated soil tests can be easily modified for unsaturated soil testing by inclusion of pore-air pressure control.

This paper examines triaxial testing of unsaturated soils using the axis-translation technique for controlling of matric suction. Issues relating to the triaxial apparatus, test procedures and interpretation of test results are discussed. A series of triaxial test results for an unsaturated residual soil is also presented and discussed.

L. Laloui and A. Ferrari (Eds.): Multiphysical Testing of Soils and Shales, SSGG, pp. 33–44.
springerlink.com

2 Triaxial Apparatus and Test Procedures

In testing unsaturated soil specimens, modifications have to be made to the conventional triaxial apparatus to apply/control matric suction and special considerations must be made for measurement of volume change. Similar to saturated soil triaxial testing, several different types of triaxial tests can be performed.

2.1 Application of Matric Suction

The simplest modification that can be incorporated into a conventional triaxial apparatus is to replace the bottom porous disk with a high air entry (HAE) ceramic disk. However the HAE disk will need to be sealed to the bottom platen such that any fluid movement will only be through the HAE disk. A water channel is usually etched into the platen so that the HAE disk does not experienced flexure cracks during air pressure application (Leong et al. 2004a). Possible configurations of etched water channels are shown in Fig. 1. A properly sealed HAE disk when fully saturated will only allow water to pass through but not air until its air entry value is exceeded. This effectively limits the maximum matric suction at which the soil specimen can be tested to 1500 kPa as this is the upper limit of currently available HAE disk. As the triaxial test duration for unsaturated soils tends to be much longer than saturated soils, air diffusion through the HAE disk and reappearing as air bubbles in the water volume below the HAE disk may be a problem. Flushing the air bubbles in the water volume may be facilitated if a spiral groove is etched into the bottom platen as illustrated in Fig. 1b.

The above arrangement may be improved with simultaneous application of pore-air and pore-water pressures at both the top and bottom platens. This can be achieved by having both coarse porous stone and HAE disks in both top and bottom platens. Possible arrangements of the filter elements are illustrated in Fig. 2.

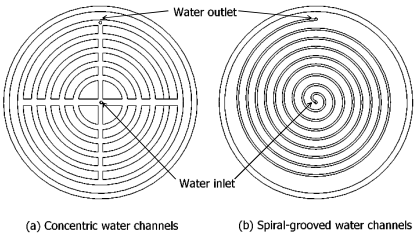

Fig. 1 Etched water channels in platen.

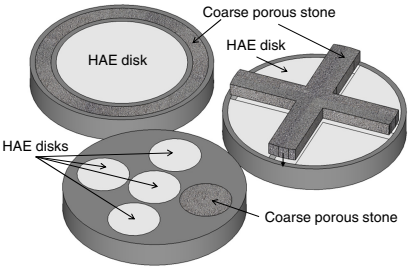

Fig. 2 Possible arrangement of high air entry (HAE) disk and coarse porous stone on the same platen.

2.2 Volume Change Measurement

Unlike saturated soil triaxial testing, the presence of air makes volume measurement of an unsaturated soil specimen difficult. This is further compounded by the fact that unsaturated soil is usually stiffer and has smaller volume changes. Laloui et al. (2006) had categorized volume change measurement of unsaturated soil specimen into three categories: (i) Cell liquid measurement; (ii) Direct air-volume and water-volume measurements, and (iii) Direct measurements on the specimen.

In cell liquid measurement technique, the volume of the confining liquid moving in and out of the triaxial cell is measured. This technique is affected by compressibility of the cell wall, volume expansion of the confining fluid to temperature, adsorption of water by the cell wall and accuracy of volume measurement.

These problems can be overcome by adopting a double-walled cell (e.g. Wheeler 1988), correcting volume expansion of the confining fluid due to temperature fluctuations (Leong et al. 2004b), minimizing the liquid volume using an inner cylinder (e.g. Bishop and Donald 1961, Aversa and Nicotera 2002, Toyota et al. 2001), using wall materials that are more resistant to water adsorption and adopting accurate liquid volume measurement such as high accuracy differential pressure transducer, respectively.

In direct air-volume and water-volume measurements, the volumes of air and water draining from the soil specimen are measured separately. This is possible when both air and water phases are continuous which in reality does not occur at the same time. As air volume is severely affected by pressure and temperature, correction of air volume to a standard pressure and temperature is needed.

For direct measurements, local displacement transducers mounted on the specimen (e.g. Leong et al. 2011), non-contact transducers such as proximity transducers (e.g. Fredlund and Rahardjo 1993, Leong et al. 2006), laser techniques (e.g. Romero et al. 1997) or digital imaging technique may be used. However volume is estimated from the measurements which may translate to error of the order of the volume change in unsaturated soils.

2.3 Test Procedures

There are several unsaturated soil tests that can be conducted using the triaxial apparatus: Consolidated drained test, constant water content test, consolidated undrained test with pore-pressure measurements and undrained test.

For the consolidated drained (CD) test, the soil specimen is first consolidated to the net confining pressure and matric suction. The soil specimen is then sheared at a slow rate where net confining pressure ($\sigma_3 - u_a$), pore-air (u_a) and pore-water (u_w) pressures and hence matric suction ($u_a - u_w$), are maintained constant. This test is also commonly known as constant suction (CS) test. For the constant water (CW) test, the soil specimen is first consolidated to the net confining pressure and matric suction similar to the consolidated drained test. The soil specimen is then sheared where net confining pressure and pore-air pressure are maintained constant but pore-water pressure is undrained. The pore-water pressure can be measured but accuracy of the pore-water pressure measurement will depend on the

pore-water pressure system to be free from diffused air and the response time to be unaffected by the HAE disk. For the consolidated undrained (CU) test, the soil specimen is first consolidated to the net confining pressure and matric suction similar to the consolidated drained test. The soil specimen is then sheared under undrained conditions with respect to the air and water phases. The pore-air and pore-water pressures are measured during shearing. However, it is difficult to maintain fully undrained condition for the air phase as air may diffuse through the pore water, the rubber membrane and water in the HAE disk. For the undrained test, the soil specimen is sheared at its initial water content and matric suction. Either unconfined or confined compression test may be performed. For the unconfined compression (UC) test, the soil specimen is sheared at a high strain rate typically 1.2 mm/min until failure to maintain undrained conditions. The pore pressures are usually not measured during the test. Similar to the saturated soil unconfined compression test, the undrained shear strength is taken as half of the unconfined compressive strength. For confined compression (undrained) test, a confining pressure is applied to the unsaturated soil specimen. The undrained shear strength of the soil increases as confining pressure is increased due to a reduction in soil specimen's volume. The matric suction of the soil decreases with an increase in degree of saturation and the undrained shear strength approaches that of a saturated soil specimen. A summary of the triaxial tests for unsaturated soils is shown in Table 1.

Table 1 Different triaxial tests for unsaturated soils.

Test method	Consolidation			Shearing			Stress analysis
	σ_3	u_a	u_w	σ_3	u_a	u_w	
CD/CS	Applied	Applied	Applied	Maintained	Maintained	Maintained	SSV*
CW	Applied	Applied	Applied	Maintained	Maintained	Measured	SSV
CU	Applied	Applied	Applied	Maintained	Measured	Measured	SSV
UC	No	No	No	-	-	-	Total
Undrained	No	No	No	Applied	-	-	Total

*SSV – Stress state variables

For triaxial testing of unsaturated soils, the three commonly performed tests are the constant suction (CS) test, the constant water content (CW) test and the consolidated undrained (CU) test. The simplest way of interpretation of the CS, CW and CU tests is to use the extended Mohr-Coulomb shear strength equation (Fredlund et al. 1978):

$$\tau = c' + (\sigma - u_a)\tan\phi' + (u_a - u_w)\tan\phi^b \quad (1)$$

where τ is shear strength, c' is the effective cohesion, σ is the normal stress, u_a is pore-air pressure, u_w is pore-water pressure, ϕ' is effective friction angle, ϕ^b is the angle describing the rate of increase in shear strength due to matric suction. The angle ϕ^b is not a constant and generally decreases as matric suction decreases.

Using Eq. 1, the stress paths for the CS, CU and CW tests are shown in Fig. 3. For simplicity, ϕ^b is assumed to be constant in Fig. 3.

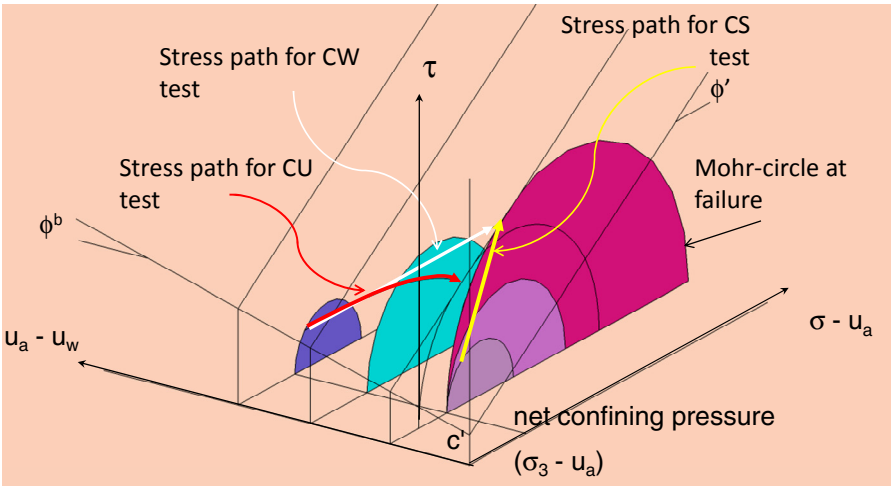

Fig. 3 Stress paths for CS, CU and CW tests.

3 Test Programme

A test programme was set up to study the shear strength of unsaturated residual soils from Bukit Timah Granite formation of Singapore. Undisturbed residual soil samples were obtained using Mazier samplers. Quantification of the shear strength behavior of unsaturated soils requires a number of identical soil specimens to be tested. Residual soil samples are seldom homogeneous and this poses a challenge to the test programme. Furthermore, CS test requires the soil specimen to be sheared at very slow strain rates thus increasing the duration of each test. To overcome these difficulties, multi-stage shearing test using cyclic loading procedure as described by Ho and Fredlund (1982) was adopted in the test programme. The triaxial tests performed were CW and CU tests. Different shearing rates were used to investigate the effect of shearing rate on shear strength of the unsaturated residual soils.

3.1 Triaxial Apparatus Set-Up

The triaxial apparatus used is shown schematically in Fig. 4. Air pressure is supplied via a coarse porous stone in the top platen and pore-water pressure is controlled by a digital pressure volume pressure controller (DPVC) through a 5-bar HAE ceramic disk in the bottom platen. The modified triaxial apparatus is equipped with a 3 kN submersible load cell, a pair of local displacement transducers (LDT) for measurement range of 0 – 0.4 mm (details can be found in

Leong et al. 2011), an internal submersible linear variable transformer (LVDT) with measurement range of ±2.5 mm, an external LVDT for axial strain measurements at large strain levels (range = ±15 mm) and a pair of proximeter transducers for radial strain measurements (range = ±1.5 mm).

3.2 Properties of Soil Tested

The residual soil specimens tested were from depths of 2 to 3 m. The average initial water content and the average void ratio of the undisturbed residual soil sample were 42% and 1.3, respectively. The residual soil was classified as silt with low plasticity (ML) according to USCS with LL=45% and PL=30%. The sand and fines content of the residual soils were 45% and 55%, respectively. Table 2 summarizes the basic properties of the residual soils. The effective shear strength parameters of the saturated residual soil obtained from CU test are c' = 10 kPa and $\phi' = 33^o$.

3.3 Test Procedures

Soil specimens of 50 mm diameter and 100 mm height were trimmed from 70 mm diameter undisturbed Mazier residual soil samples. The trimmed specimen was placed on the base pedestal of the triaxial apparatus fitted with a 5-bar high air entry ceramic disk. The specimen was then enclosed in a rubber membrane and the top cap fitted with a coarse porous disk was lowered onto the specimen. The triaxial apparatus's top cap was rigidly connected to the piston. After securing the rubber membrane on the top cap and the pedestal with O-rings, local displacement transducers (LDT) were attached to the specimen for axial strain measurements and proximity sensors were positioned for radial strain measurements. The specimens were saturated in the triaxial cell prior to consolidation to ensure that the specimen starts from a fully saturated condition. Full saturation was assumed when pore-water pressure parameter B measured was greater than 0.96 (Head 1980). After saturation, the soil specimens were isotropically consolidated to the in situ effective confining pressure and subsequently at the required net confining pressure (σ_3-u_a) and matric suction (u_a-u_w) via the axis-translation technique. For the application of matric suction, a constant air pressure of 450 kPa was supplied at the top of the soil specimen through a porous disk and water pressure was controlled via a digital pressure volume controller (DPVC) through a 5-bar high air entry ceramic disk. The amount of water flowing out of the soil specimen during matric suction equalization was monitored via the DPVC. Matric suction equalization was assumed to have been completed when the amount of water flowing out of the soil specimen had become negligible. The soil specimens were tested under two different test conditions: consolidated undrained test (CU) and constant water content test (CW). Multi-stage shearing test was carried out under net confining pressure of 50 kPa in four stages at initial matric suctions of 50 kPa, 100 kPa, 200 kPa and 400 kPa. Matric suction was applied by reducing the pore-water pressure while the pore-air pressure was maintained at 450 kPa. At the end of each matric suction equalization stage, the specimen was sheared until failure was imminent

and then unloaded before imposing the next required matric suction. Three different strain rates (0.5 mm/min, 0.1 mm/min and 0.006 mm/min) were used. In CU test, both pore-air and pore-water pressures were not allowed to drain during shearing. In CW test, air was allowed to drain freely, but, pore-water pressure was undrained during shearing. The variations of pore-air and pore-water pressures during shearing were recorded. At the end of the test, water content was measured to obtain the variation of water content with respect to the applied matric suction.

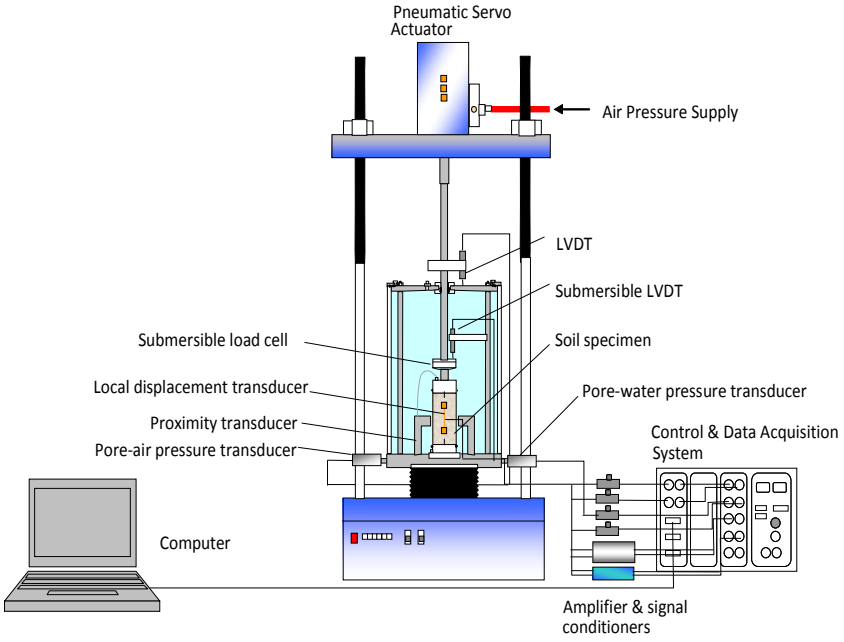

Fig. 4 Modified triaxial test set-up (from Leong et al. 2006)

Table 2 Summary of basic properties of undisturbed residual soil.

Soil properties	Value
Depth (m)	2.0-3.0
Liquid limit (%)	45
Plastic limit (%)	30
Plasticity index (%)	15
Sand (%)	45
Silt (%)	35
Clay (%)	20
Specific gravity	2.74
Unified Soil Classification System (USCS)	ML (Low plasticity silt)

3.4 Test Results and Discussion

The deviator stress and matric suction versus axial strain relationships are shown in Figs. 5 and 6 for the CU and CW tests, respectively. Figs. 5 and 6 show that the deviator stress increased significantly with the increase in initial matric suction. Matric suction decreased with axial strain and reached a constant value near the failure strain. Generally, the deviator stress versus axial strain relationship at slow strain rate was observed to be stiffer than that at faster strain rate in both CU and CW tests.

For CU tests, pore-water pressure increased with axial strain for all the tests. However, different behaviors of pore-air pressure changes with axial strain were observed during shearing. For the specimen tested at strain rate of 0.5 mm/min, pore-air pressure increased during shearing for all shearing stages at different initial matric suctions. For the specimen tested at strain rate of 0.1 mm/min, no change in pore-air pressure was measured during shearing. For the specimen tested at strain rate of 0.006 mm/min, pore-air pressure decreased with axial strain. This is because when the specimen was sheared under undrained pore pressures condition at a slow strain rate, pore-air could diffuse into pore-water and as a result, decreasing pore-air pressure was measured during shearing.

For CW tests, pore-water pressure increased with axial strain while pore-air pressure was maintained constant with during shearing. Difference in pore-pressure conditions gave different trends in the variations of matric suction with axial strain for CU and CW tests (Figs. 5 and 6). The variation of matric suction with axial strain at different strain rates showed similar trend for each type of test except for the test at initial matric suction of 400 kPa.

Using $\phi' = 33^{o}$, the total cohesion intercepts for the CU and CW tests at different strain rates were obtained as illustrated in Fig. 7 for the tests at strain rate of 0.5 mm/min. The total cohesion intercepts obtained from CU and CW tests were plotted against matric suctions at failure in Fig. 8. Fig. 8 shows that the total cohesion intercepts fall within a narrow band indicating that the CU and CW tests gave similar relationships with matric suctions for the three strain rates. The relationship of total cohesion intercept with matric suction is the shear strength envelope on the zero net confining pressure plane. The shear strength envelope on the zero net confining pressure plane gives the relationship of ϕ^b with matric suction. Fig. 8 shows that ϕ^b is not a constant. The angle ϕ^b is approximately equal to ϕ' at low matric suctions and reduces as matric suction increases.

The strains measured using the LDT and proximity transducers are not discussed due to space constraint.

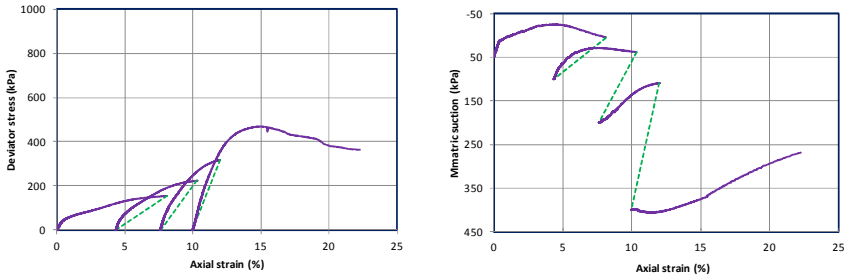

(a) Strain rate = 0.5 mm/min

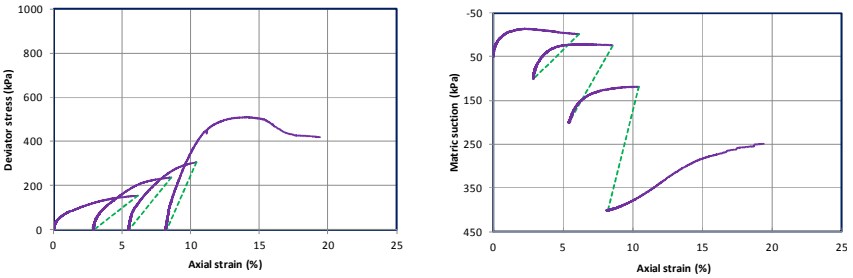

(b) Strain rate = 0.1 mm/min

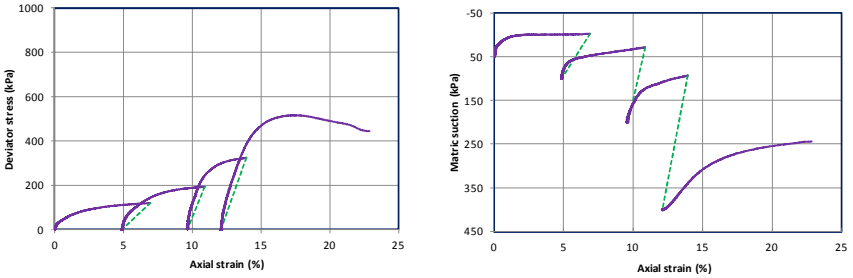

(c) Strain rate = 0.006 mm/min

Fig. 5 Variation of deviator stress and matric suction with axial strain for CU test.

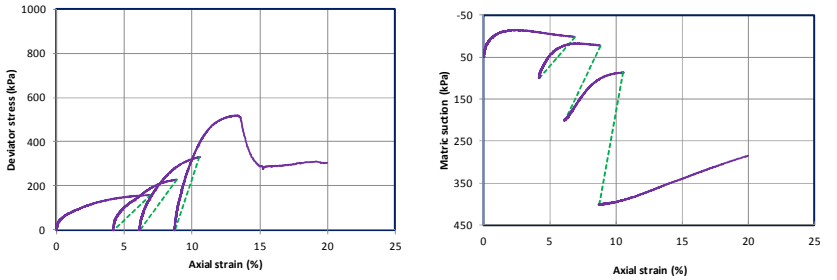

(a) Strain rate = 0.5 mm/min

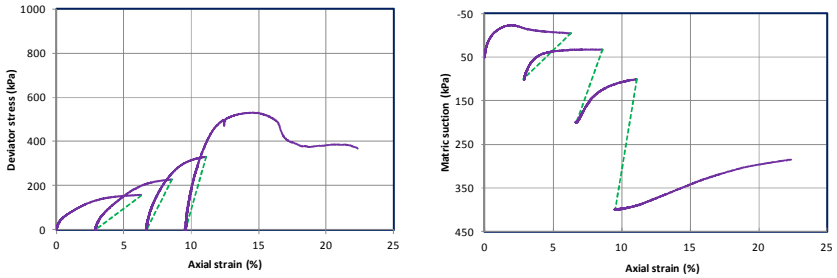

(b) Strain rate = 0.1 mm/min

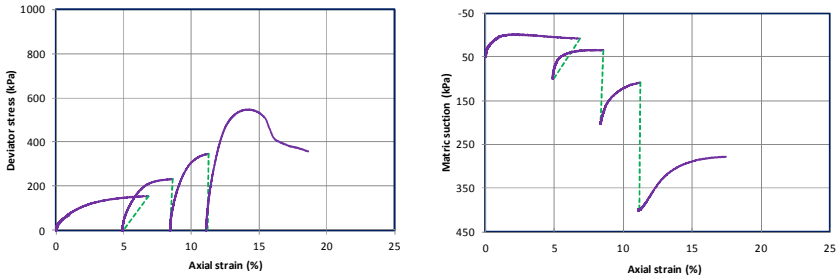

(c) Strain rate = 0.006 mm/min

Fig. 6 Variation of deviator stress and matric suction with axial strain for CW test.

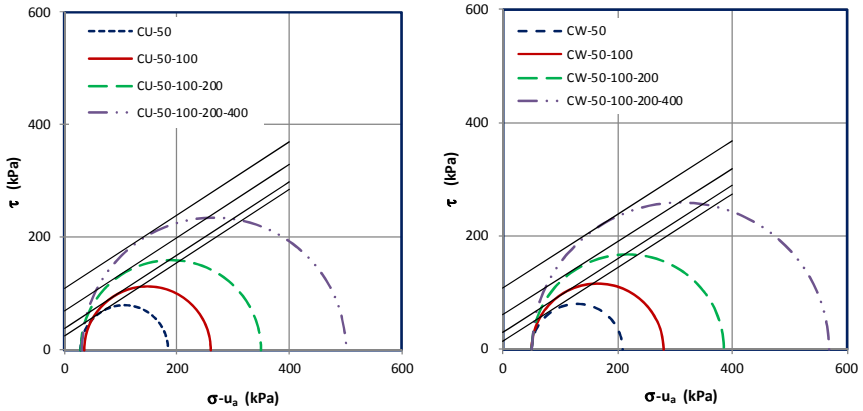

(a) CU test (b) CW test

Fig. 7 Interpretation of for CU and CW tests at strain rate of 0.5 mm/min.

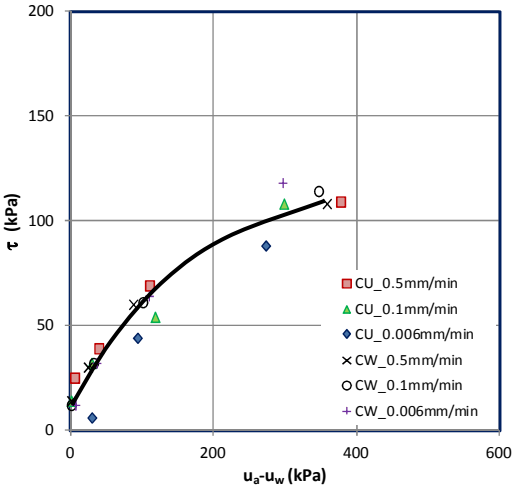

Fig. 8 Shear strength envelope on the zero net confining pressure plane.

4 Conclusion

Key modifications of the triaxial apparatus were highlighted. Different types of triaxial tests for unsaturated soils and their interpretation were discussed. Consolidated undrained (CU) and constant water content (CW) test results for an undisturbed residual soil were presented. The test results showed that ϕ^b is not a constant and decreases as matric suction is increased. The shear strength envelopes obtained from CU and CW tests are similar. Usually CW test is preferred as

the test results for the CU test showed some discrepancies in the measurement of air pressure due to diffusion of air during the test.

Acknowledgments. The financial support from Defence Science and Technology Agency and Ministry of Education (RGM 8/05) is gratefully acknowledged. The second author acknowledges the research scholarship from Nanyang Technological University.

References

Aversa, S., Nicotera, M.V.: A triaxial and oedometer apparatus for testing unsaturated soils. Geotechnical Testing J. 25(1), 3–15 (2002)

Bishop, A.W., Donald, I.B.: The experimental study of partly saturated soil in triaxial apparatus. In: Proc. 5th Int. Conf. on Soil Mechanics and Foundation Engineering, vol. 1/3, pp. 13–21 (1961)

Edil, T.B., Motan, S.E., Toha, F.X.: Mechanical behavior and testing methods of unsaturated soils. In: Yong, R.N., Townsend, F.C. (eds.) Laboratory Shear Strength of Soil. ASTM STP 740, pp. 114–129 (1981)

Fredlund, D.G., Morgenstern, N.R., Widger, R.A.: The shear strength of unsaturated soils. Canadian Geotechnical J. 15(3), 313–321 (1978)

Fredlund, D.G., Rahardjo, H.: Soil Mechanics for Unsaturated Soils. John Wiley, New York (1993)

Head, K.H.: Manual of Soil Laboratory Testing, Effective Stress Tests. Pentech Press (1980)

Hilf, J.W.: An investigation of pore-water pressure in compacted cohesive soils. Technical Memo 654, U.S. Dept of the Interior, Bureau of Reclamation, Design and Construction Div., Denver, Colorado (1956)

Ho, D.Y.F., Fredlund, D.G.: A multistage triaxial test for unsaturated soils. Geotechnical Testing J. 5(1), 18–25 (1982)

Katte, V., Blight, G.E.: The roles of surface tension and solute suction in the strength of unsaturated soils. In: Unsat 2012, Int. Conf. on Unsaturated Soils, Naples, Italy, p. 5 (2012)

Laloui, L., Péron, H., Geiser, F., Rifa'i, A., Vulliet, L.: Advances in volume measurement in unsaturated soil triaxial tests. Soils and Foundations 46(3), 341–349 (2006)

Leong, E.C., Tripathy, S., Rahardjo, H.: A modified pressure plate apparatus. Geotechnical Testing J. 27(3), 322–331 (2004a)

Leong, E.C., Agus, S.S., Rahardjo, H.: Volume change measurement of soil specimen in triaxial test. Geotechnical Testing J. 27(1), 47–56 (2004b)

Leong, E.C., Cahyadi, J., Rahardjo, H.: Stiffness of a compacted residual soil. In: Proc. 4th Int. Conf. on Unsaturated Soils, pp. 1168–1180. Geotechnical Special Publication 147 (2006)

Leong, E.C., Nyunt, T.T., Low, K.S.: Local displacement transducer with Anderson loop. Geotechnical Testing J. 34(6), 676–684 (2011)

Romero, E., Facio, J.A., Lloret, A., Gens, A., Alonso, E.E.: A new suction and temperature controlled triaxial apparatus. In: Proc. 14th Int. Conf. on Soil Mechanics and Geotechnical Engineering, Hamburg, Germany, vol. 1, pp. 185–188. Balkema

Toyota, H., Sakai, N., Nishimura, T.: Effects of stress history due to unsaturation and drainage conditions on shear properties of unsaturated cohesive soil. Soils and Foundations 41(1), 13–24 (2001)

Wheeler, S.J.: The undrained shear strength of soils containing large gas bubbles. Geotechnique 38, 399–413 (1988)

Undrained Shear of Plastic Soils under Suction

Fernando A.M. Marinho

University of São Paulo, São Paulo, Brazil
fmarinho@usp.br

Abstract. From the very beginning of the soil mechanics the interest for understanding the role of the pore water pressure is evident. In fact, the role of pore water pressure has been investigated even earlier by the agronomic sciences, which prepared a strong base for us. It has been a challenger to bring to practice the entire framework that has been developed for unsaturated soils. The primary purpose of this paper is to discuss undrained shear the behaviour of plastic soils, when the pore water pressure is negative and even under tension, in order to establish a relation between some fundamental characteristics of the soils with the undrained shear strength for plastic soils, and in particular for a residual compacted soil. Data from different type of soils are presented and specifically from a residual soil. Results from triaxial tests demonstrate that suction developed by unloading and by drying the specimen may produce different effects on the undrained shear strength. The results also indicate that the undrained shear test in unsaturated soils can be a valuable tool to bring theory into practice.

1 Introduction

"A number of years ago the author became impressed with the perplexing character of the problems which the behaviour of sand and clay soils presents to the engineer." This statement is at the first paragraph of the Terzaghi's paper published in 1925. In his paper Terzaghi discuss the shrinkage phenomena stating that "the only difference between the artificial compression and the natural shrinkage is that compression under load can be carried as far as we want, while in shrinkage due to evaporation a point is reached beyond which the volume of the clay remains constant." Terzaghi also mentioned that the shrinkage process is similar to mechanical compression up to plasticity limit. Fifty years later Bishop et al (1975) pointed out the fact that the unconfined compression strength is lower than the strengths obtained at higher confining pressures at the same water content. In this case the authors are dealing with reconstitute saturated soils. It is well known that the ratio between undrained shear strength of normally consolidated plastic soils in saturated state and its effective consolidation pressure ($S_u/p`$) is approximately constant and does not change significantly with the soil plasticity (e.g. Bishop et al, 1975, Mesri, 1975, Jamiolkowski et al, 1985). Reliable undrained shear test in undisturbed sample implies that the mean effective stress remains in the sample,

L. Laloui and A. Ferrari (Eds.): Multiphysical Testing of Soils and Shales, SSGG, pp. 45–55.
springerlink.com

under the "responsibility" of the pore water. During sampling the unloading process will generate negative pore water pressure that can be sustained by the soil. Depending on the soil type and its state, the maximum negative pore water pressure that a soil can sustain can be as high as 3MPa (e.g Bishop et al, 1975). That maximum negative pressure is named the air entry pressure of the soil. There is a link between the air entry pressure and the point where the consequence (for instance void ratio) of mechanical pressure differs from negative pore water pressure generated by evaporation, mentioned previously.

The water content of a saturated plastic soil is directly related to its void ratio and hence to its undrained shear strength. For plastic soils the liquidity index is an useful tool to infer soil consistency. It may be related to plastic limit (e.g. Wood, 1990) or to optimum water content in the case of compacted soil as suggested by Lerouiel et al. (1992). It is clear that the undrained shear strength and the liquidity index of reconstituted or remoulded saturated soils are consistently correlated (e.g., Skempton and Northey, 1952; Houston and Mitchell, 1969; Burland, 1990; Wood, 1990; Terzaghi et al., 1996, among others). The behaviour of plastic soils at an unsaturated state can also be interpreted using liquidity index, since when a compacted soil undergoes drying or wetting, a change in its unsaturated undrained shear strength is also observed. (e.g. Lerouiel et al., 1992; Marinho & Oliveira, 2012). However, the role of suction as mentioned by Terzaghi and investigated by Bishop may vary significantly according to the soil type and its state. This papers intend to present some considerations about the suction generation in plastic soils undergoing drying or generated by an unloading process, with the objective of establishing a relation between some fundamental characteristics of the soils and the undrained shear strength for plastic soils, in particular for a residual compacted soil.

2 The Atterberg Limits

The arbitrary definition of water contents that limit the plastic behaviour of soils has been very useful and at the same time creating controversy. The use of the Atterberg limits in practice has gone beyond the expectation. As mentioned by Schofield (2005) these limits "...become the most frequently performed and least understood of all soil mechanics tests..." The liquid limit test is, in fact, an undrained shear test. And the relation between water content and the number of blows in the Casagrande's apparatus is associated to S_u. Croney and Coleman (1954) went beyond that and measured the suction after the groove closes in Casagrande apparatus; presenting a state called by them as continuously disturbed state. Croney and Coleman (1961) suggested a relationship between unconfined strength and continuously disturbed suction for highly plastic soils.

Going back to the basics, it is important to call attention for the physical relation that exists between the plastic and liquid limits and the void ratio. The maximum and minimum void ratio, usually defined for non-plastic materials, can also be idealised for plastic soil at the liquid and plastic limits, respectively. This very fundamental fact leads us to conclude that the undrained shear strength should increase from the liquid limit to the plastic limit. However, the behaviour of the soil

for water content close or below plastic limit is not clear since the soil is likely to be unsaturated when drying or compacted.

The relationship between plastic limit and the optimum water content suggests, as can be seen in Figure 1, that the plastic limit is slightly higher than the optimum water content. For compacted soils the knowledge of the suction value at optimum water content can be valuable for the prediction of pore water pressure development during loading. The suction at optimum water content, depicted in Figure 1b although present some variability suggest that the suction range between 50 kPa and 500 kPa.

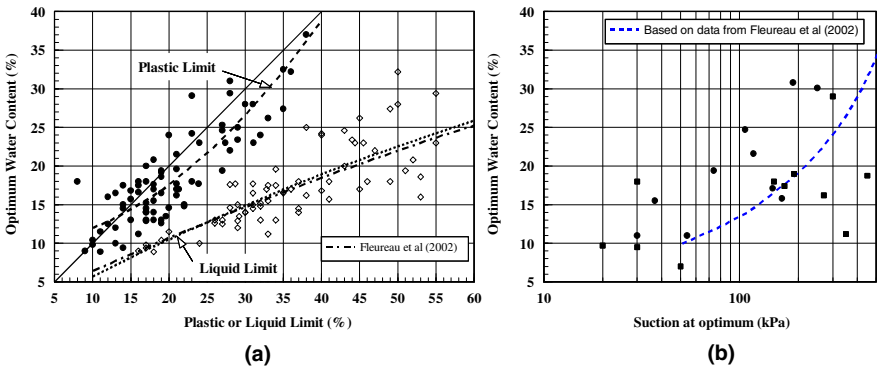

Fig. 1 Relation between Atterberg Limits, suction and optimum water content.

3 Shrinkage Behaviour

As mentioned before the drying behaviour of a plastic soil can be similar to consolidation provided the soil remains saturated. Results obtained with a residual soil remoulded at a water content above its liquid limit (from slurry), shows that during the drying process the water evaporated is equal to the volume change, as can be seen in Figure 2 (star symbol). Data from specimens compacted at different water content and wetted after compaction are also shown in Figure 2 (data from Oliveira, 2004). When compacted the soil may remain at constant degree of saturation up to a point where air enters the pores with more profusion (general air entry point, GAE). The air entry point refers to the desaturation point specifically. When compacted below optimum the sample starts from a lower degree of saturation and its ability to contract is reduced. The water content at which the GAE occurs depends on its initial state. It can be seen in Figure 2 the drying curve of the same soil compacted at optimum but confined up to 300 kPa before undergo drying, showing a reduction in the water content at the GAE. The numbers, close to symbols in the Figure 2 are the value the suction measured using filter paper technique. Bearing in mind that for high suction the filter paper technique will measure total suction, regardless it is in contact or not with the soil (e.g. Marinho and

Silva Gomes, 2012). The increase in the suction value associated to the GAE of each sample tested can be observed. As reference the plastic and liquid limit are indicated as well as the optimum water content of the soil. For this soil the difference between the optimum water content and the plastic limit is about 9%.

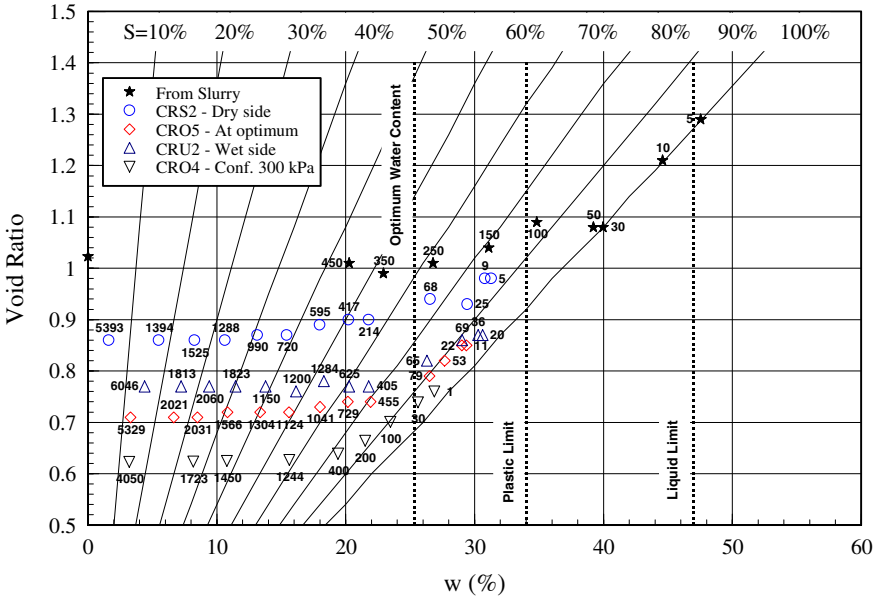

Fig. 2 Drying curves for compacted residual soil (Oliveira, 2005)

The observation made by Terzaghi (1925) regarding the range of full efficiency of the suction in producing the same effect of the effective stress is confirmed for the residual soil, but only when it is remoulded from slurry. The increase in the undrained shear strength from liquid limit to plastic limit is associated with the saturated condition. Below the plastic limit and close to optimum water content the unsaturated condition create difficulties for normalization of the behaviour.

4 The SWRC

The air entry pressure of a soil depends of the soil type and its structure which is reflected in its ability to shrink. Figure 3 presents the soil water retention curve (SWRC) for pure London clay and London clay mixed with fine sand (Marinho, 1994). It is also show the SWRC of a compacted residual soil. Points marked with a start symbol are the plastic limit (w_p) of the soils. The full circles plotted on the SWRC lines of Figure 3 indicate the range of GAE suction observed. It can be observed that the lower the plastic limit, lower is the suction at the GAE. From the suction at the plastic limit to the suction at GAE the soil remains with a degree of

saturation above 80%. For the residual soil the $w_{p,}$ indicated by an arrow in Figure 3, is associated to a suction which is approximately four hundred times lower than the suction at the GAE.

When a soil is subjected to an effective stress in the field, the unloading due to undrained sampling will necessarily generate suction. If the *in situ* average effective stress is above the air entry pressure, the soil will not be able to hold the effective stress transferred to the pore water. The relation between air entry pressure and maximum effective or total stress previously applied is not clear.

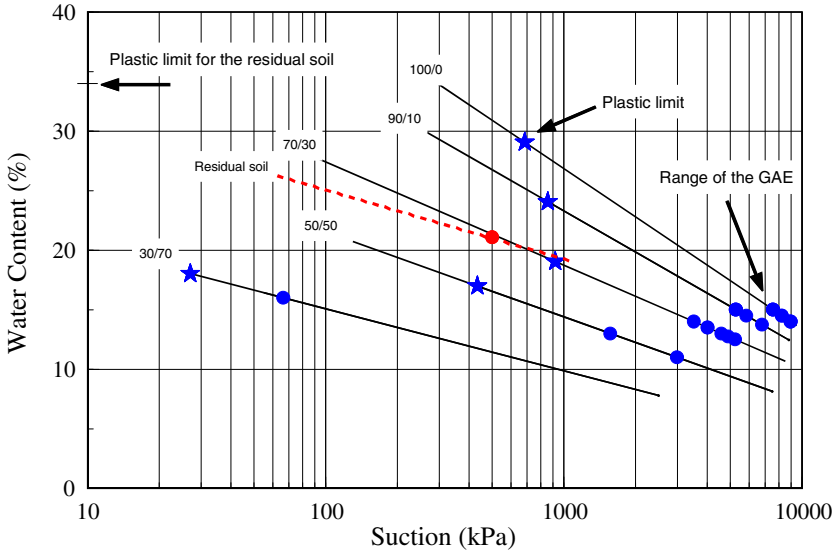

Fig. 3 Soil water retention curve and its air entry points for mixture of London clay and sand and residual soil (modified from Marinho, 1994).

The drying behaviour of compacted soil specimens depends on its initial water content. The SWRC, in particular the air entry suction, is not significantly affected by the compaction energy (e.g. Marinho and Stuermer, 2000). Figure 4 presents the relationship between degree of saturation, water content and suction for a statically compacted London clay. The specimens were compacted at different void ratio and at different initial water content. It can be observed that the reduction in the degree of saturation is slower for specimens initially compacted with S > 80%.The suction at the GAE point depends not only on the initial degree of saturation but also on the initial void ratio. Analysing the specimen LCST8 shown in Figure 4 is clear that the soil remain almost at the same degree of saturation during the drying process. At the same time the specimen change its volume in approximately 28% before reach the GAE.

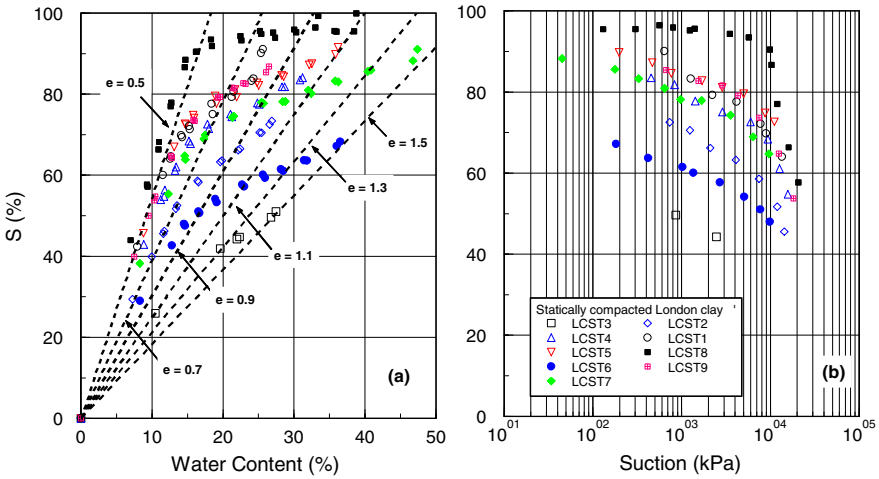

Fig. 4 Interrelated relationships between degree of saturation, water content and suction (Marinho and Chandler, 1994).

Consider a specimen of reconstitute saturated plastic soil during drying with an initial void ratio (e_{sl}). It will reduce its void ratio until it reaches a point where the soil desaturates (probably before the shrinkage limit and after the plastic limit). At that point the soil will have a suction equivalent to that void ratio (e_{sh}). Any specimen prepared under saturated condition between e_{sl} and e_{sh} should not change its air entry suction. The only way to change it is to apply mechanical pressure in order to bring the specimen to a void ratio lower than e_{sh}.

At this point it is important to make a distinction between air entry due to drying and the maximum suction the soil can sustain when unloaded. It seems that this will depend on the soil compressibility. The actual value of the undrained shear strength should depend on the ability of the soil to hold the *in situ* stress (negative pore pressure generated) and also on its volume change during unloading.

5 Undrained Shear Strength

The undrained shear strength is an important parameter for a great number of geotechnical engineering designs (e.g. embankments in general, foundations and slopes). When dealing with saturated soils the initial pore water pressure of an undisturbed specimen is in general negative or close to zero. The nature of this negative pressure is the unloading process due to the undrained sampling process. The quality of the undisturbed sample depends on the ability of the soil water to sustain negative pressure. In this case the soil does not have negative pore water pressure in the field. The suction generated due to sampling from a saturated soil can be given by the following expression (Skempton, 1961, see also Chandler et al., 1993):

$$Suction = \sigma_v'[K_o - A_s(K_o - 1)] \quad (1)$$

where:

σ_v' is the vertical effective stress
K_o is the coefficient of earth pressure at rest
A_s is the pore pressure coefficient for sampling.

When dealing with unsaturated soils the undrained shear strength is in general drained to air, although it is a constant water content test as a usual undrained shear test. For unsaturated soils the suction is generated during compaction or it is induced by seasonal variation of water content due to meteorological conditions of the site. The loading and unloading of the soil in the field and the sampling process are important aspects to be investigated, in particular when it is possible to measure suction directly, during the tests.

In order to evaluate the effect of unloading on the undrained shear strength four tests were performed using a residual soil of gneiss, compacted at optimum water content using normal Proctor energy. In two of the tests the specimen were consolidated under a confining pressure of 300 kPa and then sheared under undrained condition (i.e. initial confining effective stress of 300 kPa). The others two testes the specimens, prepared in the same manner, were also consolidated to 300 kPa but unloaded under undrained condition. The unloading of the specimen induced a suction of about 160 kPa in one test and 140 kPa in the other. The suction was measured using a high capacity tensiometer. The high capacity tensiometer used has a resolution of about 15 kPa. The lower suction value measured after unloading was expected since the air entry pressure of the soil is about 100kPa. The pore water pressure development during loading and unloading of the same residual soil was investigated by Marinho et al (2003).

The results of the four triaxial undrained tests are presented in Figure 4. For the tests presented in Figure 4a the rate of shear was 0.05 mm/min and for the tests shown in Figure 4b the rate of shear was 0.3 mm/min.

The test performed at a slower rate did not shown the behaviour observed by Bishop et al (1975) where the soil behave as a brittle material when under suction. However, the test done using a higher rate of shear presented a tendency for a more brittle behaviour. The change in suction followed this tendency. The difference in behaviour in relation to Bishop's test can be due to the type of soil and also due to the level of stress tested. For the test performed at a confining stress of 300 kPa no difference was observed suggesting that the rate of shear had only effect on the specimen under suction.

The measurement of suction during the test indicated a rapid reduction in suction during the test, in particular for the test performed with a lower rate of shear, showing a small tendency to increase suction at failure. Similarly the specimen tested under effective stress of 300 kPa presented a decrease in pore water pressure at failure.

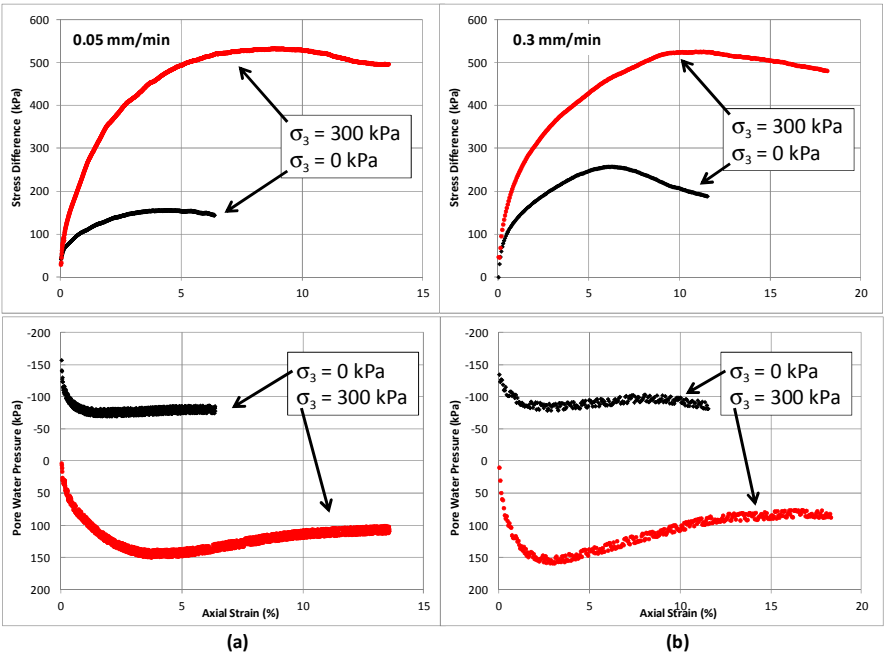

Fig. 5 Results of the undrained shear test performed in residual soil under confining pressure of 300 kPa and under unconfined condition after unloading.

Oliveira (2004) presented data from unconfined undrained shear test performed using the same compacted residual soil. These results are presented in Figure 5 along with the data obtained from the tests shown in Figure 4. The tests were performed under a shear rate of 0.3 mm/min. The specimens were statically compacted at optimum water content and at maximum dry density. Before testing the specimens were allowed to dry or to wet under controlled condition in order to cover a range of water content. When compacted at optimum water content the residual soil tested undergo a small swelling when wetted, and some contraction when dried. The change in void ratio due to reduction in water content is, in part, responsible for the increase in undrained shear strength ($S_{u\text{-}unsat}$). Even for the same void ratio the $S_{u\text{-}unsat}$ increase, due to suction up to a certain value.

In Figure 5a the relation between S_u and suction is presented showing an increase in the undrained shear strength up to a suction of approximately 1MPa. The results obtained with the specimens tested under 300 kPa of effective stress presented the same maximum level of strength reached by the unsaturated specimens. When comparing the S_u obtained from tests performed after unloading from 300 kPa of confining pressure (under suction generated by the unloading process), with the tests done by Oliveira (2004) a reasonable agreement is observed in terms of suction. These results suggested that the suction generated by drying and by unloading has the same effect on the undrained shear strength.

In Figure 5b, the undrained shear strengths are presented as function of void ratio prior shear. The results obtained by Oliveira (2004) indicate an increase of S_u up to a void ratio of the order of 0.6, for specimen undergoing drying. When comparing that data with the results obtained with the specimen under suction due to the unloading one can observe a shift of the tendency to the left. This is suggesting that the void ratio did not play the same role as for saturated soils. It seems that the increase in suction due to drying not only induce a lower void ratio for the same suction, but also gave different undrained shear strength for the same void ratio.

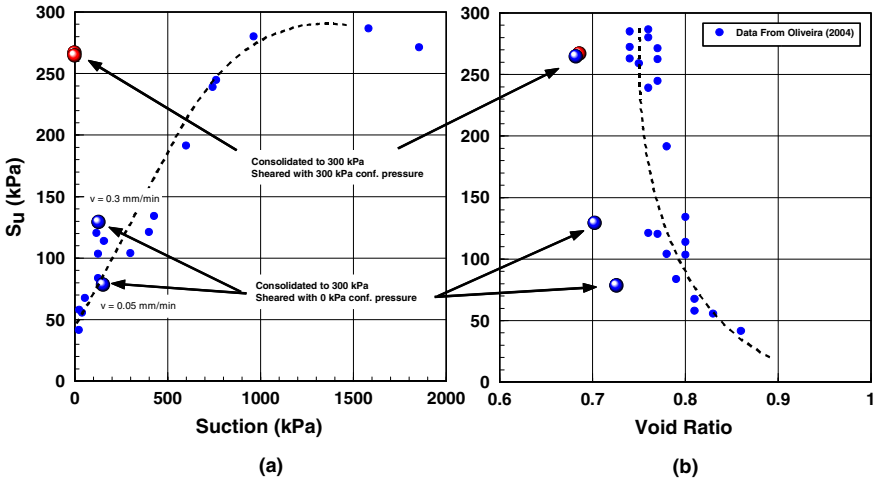

Fig. 6 Relation between undrained shear, suction and void ratio for a residual soil.

It should be point out that the void ratios for unloading tests were calculated considering that the soil remains saturated. If air appears into the specimen after unloading, implying a volume change, the void ratio should be higher than the one calculated. The relation between void ration and S_u differ since the drying process is not able to induce a void ratio below the void ratio associated to the shrinkage limit (e_{sh}). The drying behaviour may also generate phenomena that are particular features of residual soil, associated to its complex physical chemical characteristics that are activated during drying, and need further investigation.

6 Final Considerations and Conclusions

The ability to measure negative pore water pressure during triaxial test is well established among researcher. However, it is not of common use by the industry. Unsaturated shear tests performed using high capacity tensiometer can bring to practice many important concepts of unsaturated soil mechanics, while further development is required to simplify its use.

At a specific suction the void ratio may differ according to the process of suction generation. At the same water content the soil may have different void ratio depending whether it was consolidated mechanically or by drying. The use of the shrinkage curve and SWRC are useful for interpreting the soil behaviour.

The unloading from a known effective stress did not generate a suction equivalent to the average initial effective stress in saturated specimens of residual soil. This behaviour was observed for the level of stress applied and for state of the specimens of the soil tested.

The development of suction due to drying induces different response of the soil in terms of void ratio in relation to mechanical loading, as expected. However,the undrained shear strength correlates well with the initial suction (prior shear), regardless the process of suction generation (drying or unloading).

Acknowledgements. The author would like to acknowledge the support of the FAPESP (Research Support Foundation of the State of São Paulo, Brazil) and the CNPq (The National Council for Scientific and Technological Development).

References

Bishop, A.W., Kumapley, N.K., El-Ruwayih, A.: The influence of pore-water tension on the strength of clay. Philosophical Transactions of The Royal Society of London Series A: Mathematical and Physical Sciences 278(1286), 511–554 (1975)

Chandler, R.J., Crilly, M.S., Montgomery-Smith, G.: A low-cost method of assessing clay desiccation for low-rise buildings. In: Proc. Institution of Civil Engineers, Civ. Engng., vol. 92, pp. 82–89 (1992)

Croney, D., Coleman, J.D.: Pore pressure and suction in soil. In: Pore Pressure and Suction in Soils, pp. 31–37. Butterworth, London (1961)

Croney, D., Coleman, J.D.: Soil structure in relation to soil suction (pF). Journal of Soil Science. London 5, 75–84 (1954)

Jamiolkowsi, M., Ladd, C.C., Germaine, J., Lancellotta, R.: New developments in field & lab testing of soils. In: Proc. 11th ICSMFE (1), San Francisco, pp. 57–154 (1985)

Leroueil, S., Le Bihan, J.P., Bouchard, R.: Remarks on the design of clay liners used in lagoons as hydraulic barriers. Canadian Geotechnical Journal 29, 512–515 (1992)

Marinho, F.A.M., Chandler, R.J.: On the relationship between suction and degree of saturation of soils. In: 2nd Brazilian Symposium on Unsaturated Soils, Recife, vol. 1, pp. 37–44 (1994)

Marinho, F.A.M., Oliveira, O.M.: Unconfined Shear Strength of Compacted Unsaturated Plastic Soils. In: Proceedings of the Institution of Civil Engineers, vol. 165(GE2), pp. 97–106 (2012), doi: http://dx.doi.org/10.1680/geng10.00027

Marinho, F.A.M., Silva Gomes, J.E.: The Effect of Contact on the Filter Paper Method for Measuring Soil Suction. Geotechnical Testing Journal 35 (2012)

Marinho, F.A.M., Standing, J., Kuwagima, R.M.: Soil Suction Development under Isotropic Loading and Unloading in a Compacted Residual Soil. Soils and Rocks 26(2), 115–128 (2003)

Marinho, F.A.M., Stuermer, M.M.: The Influence of the Compaction Energy on the SWSC of a Residual Soil. Advances in Unsaturated Geotechnics Geo-Denver, Denver 99 125-141ASCE (2000)

Mesri, G.: New Design Procedure for Stability of Soft Clays. Journal of the Geotechnical Engineering Division, ASCE 101, GT4, 409–412 (1975)

Oliveira, O.M.: Study on the Shear Strength of a Unsaturated Compacted Residual Soil. DSc thesis, University of São Paulo, Brazil (2004) (in Portuguese)

Schofield, A.: Disturbed Soil Properties and Geotechnical Design, p. 142. Thomas Telford (2005)

Skempton, A.W.: Horizontal Stress in an Over-Consolidated Eocene Clay. In: Proceddings of the 5th International Conference on Soil Mechanics and Foundation Engineering, Paris, vol. 1, pp. 351–357 (1961)

Terzaghi, K.: Principles of soil mechanics: I – Phenomena of cohesion of clay. Engineering News-Record 95(13) (1925)

Advances in the Testing of the Hydro-mechanical Behaviour of Shales

Alessio Ferrari and Lyesse Laloui

Swiss Federal Institute of Technology, Lausanne, EPFL, Switzerland
{alessio.ferrari,lyesse.laloui}@epfl.ch

Abstract. The paper presents some of the advanced experimental techniques and apparatuses that have been developed by the authors for testing the hydro-mechanical behaviour of shales. A methodology established for the analysis of the water retention behaviour in non-isochoric conditions is introduced; the method allows for the determination of the main drying and wetting paths in addition to the volume change response upon total suction variations. A high-pressure oedometric cell is then presented; the apparatus allows for the analysis of the transition from the pre-yield behaviour to the normally consolidated state. The analysis of the settlement versus time curves yields information on the permeability of the material as a function of the void ratio. The test results are illustrated for two Mesozoic shales from the northern region of Switzerland, namely, the Opalinus Clay from Mont Terri and the so called "Brown Dogger" from the Schlattingen site in the Molasse Basin.

1 Introduction

The geomechanical behaviour of shales is quickly becoming one of the most important issues in modern geomechanics, largely driven by the nuclear waste geological storage and petroleum industries (i.e., the extraction of gas shale and the sequestration of CO_2). In any such application, a deep understanding of the hydro-mechanical behaviour of the involved materials is of primary significance. The water retention mechanisms play a major role in either fluid trapping due to the capillary forces present in low permeability formations or in the resaturation of shale formations after ventilation, as in the case of deep geological repositories. The swelling/shrinkage of shale is related to suction, or the degree of saturation variations. The mechanical properties and the permeability are of primary importance in determining the production capacity of gas shale reservoirs. In reference to the mentioned issues, this paper presents the advanced experimental techniques and apparatuses that have been recently developed by the authors for testing the hydro-mechanical behaviour of shales. A methodology for obtaining the water retention properties of shales is presented first. A high-pressure oedometric apparatus is then introduced. Selected test results are presented for two shales from the northern region of Switzerland.

L. Laloui and A. Ferrari (Eds.): Multiphysical Testing of Soils and Shales, SSGG, pp. 57–68.
springerlink.com

2 Tested Shales

Test results are presented for two shales from the northern region of Switzerland: the Opalinus Clay sample was obtained from the Mont Terri Underground Laboratory and the "Brown Dogger", from a deep geothermal well (depth of 766.67 and 778.30 m) near the village of Schlattingen in the Molasse Basin. The tested Opalinus Clay (OPA) was recovered in the Gallery 98 of the Mont Terri URL from the shaly facies, consisting of dark grey silty, calcarerous shales with a typical clay content of 55-60%, 25-30% carbonate, 5-10 % quartz and 10-15% biodetritus. The core samples of "Brown Dogger" (BD) originated from the Varians- and Parkinsoni-Würtembergica beds (Bathonian/Bajocian age), consisting of silty to clay-rich marls with a clay content of 25-45%, 30-50% carbonate and 20-25% quartz.

The results of the geotechnical identification of the cores are reported in Table 1, which presents the particle density (ρ_s), the bulk density (ρ), the water content (w), the void ratio (e), the degree of saturation (S_r) and the Atterberg limits (the liquid limit w_L and the plastic limit w_P). The grain size distributions reported in Figure 1.a were obtained by sedimentation analysis. The material was first crushed using a grinder, and the fraction passing the ASTM No. 35 sieve (with an aperture diameter d = 500 μm) was selected. The crushed material was placed in distilled water along with a dispersing agent and was then shaken overnight. As seen in the figure, the obtained curves are situated on the left side of the maximum dimension of the selected material; this observation confirms that the material did not present particles with a diameter larger than the maximum dimension of the crushed blocks, and it validates the selected procedure for preparation of the sedimentation analysis. The OPA and the BD core samples were classified as CM (sandy clay) and CL-ML (silty clay with sand), respectively.

Synthetic waters aiming to reproduce the in-situ pore water composition were used throughout the tests (Pearson 1998; Mäder 2011). The osmotic suctions of the synthetic waters used were measured by a dew-point psychrometer and resulted in values of 0.9 MPa for the BD and 1.2 MPa for the OPA.

Mercury Intrusion Porosimetry (MIP) was used to determine the pore size density function of the selected cores. The MIP technique includes the forced penetration of mercury into a sample and the measurement of the intruded volume of mercury as a function of the applied pressure. The required pressure is inversely proportional to the size of the progressively filled pores.

Table 1 Geotechnical characterization of the tested shales.

Shale	ρ_s (Mg/m^3)	ρ (Mg/m^3)	w (%)	e (-)	S_r (%)	w_L (%)	w_P (%)
OPA	2.74	2.46	6.9	0.21	92	38	23
BD	2.72	2.55	2.7 - 3.5	0.09 - 0.11	78 - 92	25 - 29	23

To minimise the effects of shrinkage during drying, the MIP tests were carried out on freeze-dried samples, which was achieved by sublimation inside a vacuum chamber at 0 mbar and -50°C for 24 hours. The tests were carried out using a Thermo Electron Corporation MIP apparatus composed of two operating units: a low pressure (max. pressure 100 kPa) and a high pressure (max. pressure 400 MPa) unit. The results of the MIP tests are depicted in Figure 1.b in terms of the pore size density function (PSD), which is the derivative of the cumulated intruded void ratio with respect to the logarithm of the entrance pore diameter.

The total cumulated void ratios obtained with the MIP tests were 0.13 and 0.074 for the OPA and the BD sample, respectively. A comparison of the void ratio values reported in Table 1 demonstrates that not the overall porosity was intruded and therefore investigated with the MIP tests; this limit can be related to pores on the surface of the samples that were filled with mercury before the pressure increments started and to the smallest pores that required higher pressures to be intruded (minimum pore diameter that could be intruded with the used apparatus was 3.8 nm). The PSD functions were found to be unimodal for both tested shales, showing pore modes at approximately 20 nm and 15 nm for the OPA and the BD samples, respectively.

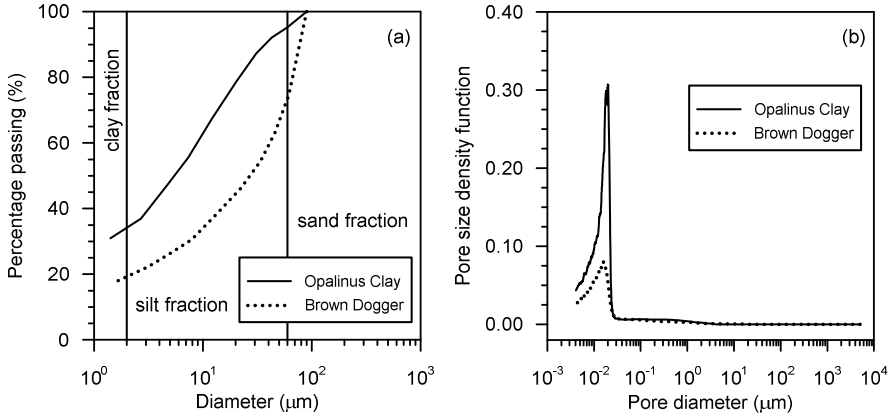

Fig. 1 Grain size distribution (a) and pore size density function (b) of the tested shales.

3 Water Retention Behaviour

The strength and stiffness of shales are significantly influenced by the degree of saturation or alternatively by the suction (among others, see: Valès et al. 2004; Ramos da Silva et al. 2008). Changes in the degree of saturation are common in several engineering applications, including the drying and re-imbibition of host rock formations for waste repositories and the two-phase flow in shale gas

reservoirs. Despite the recognised impact of suction on shale behaviour, few experimental tests have been carried out to evaluate the water retention properties of shales (e.g., Ramos da Silva et al. 2008; Muñoz 2007; Zhang et al. 2007).

This section describes the experimental methodology established to analyse the water retention behaviour of shales under unstressed conditions. The methodology involves the direct control of the shale water content and the subsequent measurement of the suction at equilibrium by a psychrometer. To compute the degree of saturation, the volume is measured for each equilibrated state.

The imposed water content is applied differently for the wetting and drying paths. Slices measuring 7 – 8 mm in height are initially obtained from the shale core. To obtain the main drying paths, the core slices are initially wetted by placing them in a sealed-glass jar on filter papers, which in turn are placed on a porous stone filled by synthetic water (corresponding to the in situ water composition). At this stage, the slices are wetted by capillary action, allowing for volume changes. The weight evolution over time is measured to assess the equilibration. Nearly two weeks are required for the slices to equalise. The wetted slices are then divided in small parts measuring approximately 20 x 20 x 8 mm^3. Each part is placed in a desiccator and dried for the amount of time necessary to achieve the desired water content of that particular part. After the drying step, the parts are packed for at least three days to allow for the internal redistribution of water. When the main wetting paths are sought, the core slices are initially placed in a desiccator containing silica gel and left to dry for approximately three weeks (applied total suction of approximately 270 MPa) until no significant change in their weight can be detected. The slices are then cut in pieces and a certain amount of synthetic water is added to each part to obtain the target water content. Each part is placed in a hermetic container for one week to allow for the internal redistribution of water. The total suction of each specimen is measured using a WP4c dewpoint psychrometer (Leong et al. 2003; Cardoso et al. 2007). The psychrometer used gives indirect measures of the total suction of a sample by reading the relative humidity established by the sample in a closed environment. The chilled-mirror dew point technique is used to measure the relative humidity. The total suction is then obtained by the psychrometric law (Thomson, 1871) which relates the relative humidity (RH) and the absolute temperature (T) to the total suction (ψ):

$$\psi = -\frac{\rho_w RT}{M_w} \ln(RH),$$

where R is the universal gas constant and ρ_w and M_w are the density and the molecular mass of water, respectively.

A fluid displacement technique is used to measure the volume of each tested specimen after equalisation. The technique uses pycnometers filled with kerdane, which is used for its immiscibility with water and its ability to invade the air-filled pore spaces in the surface without affecting the soil structure (Peron et al. 2007).

The water retention behaviour of the OPA and the BD core samples are reported in Figures 2 and 3, respectively. The results are depicted in terms of the water content, the void ratio and the degree of saturation versus the total suction. Each point represents a measurement average of three specimens, each of which followed an identical drying/wetting path. The initial state of each sample is also depicted. Both materials had an initial degree of saturation close to one, which is in agreement with the fact that both materials were reported to be saturated in situ. The initial state was found for both materials along the main drying paths as a consequence of the coring process and the exposure to atmosphere before preservation.

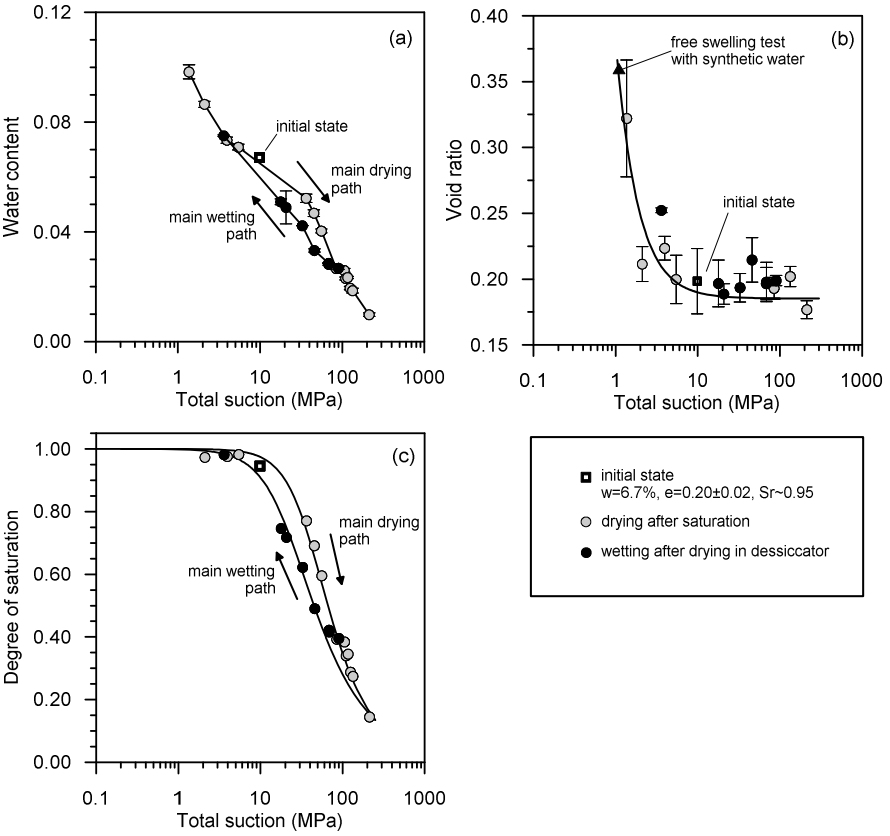

Fig. 2 Water retention behaviour of the Opalinus Clay core sample: the water content (a), the void ratio (b) and the degree of saturation (c) as a function of the total suction.

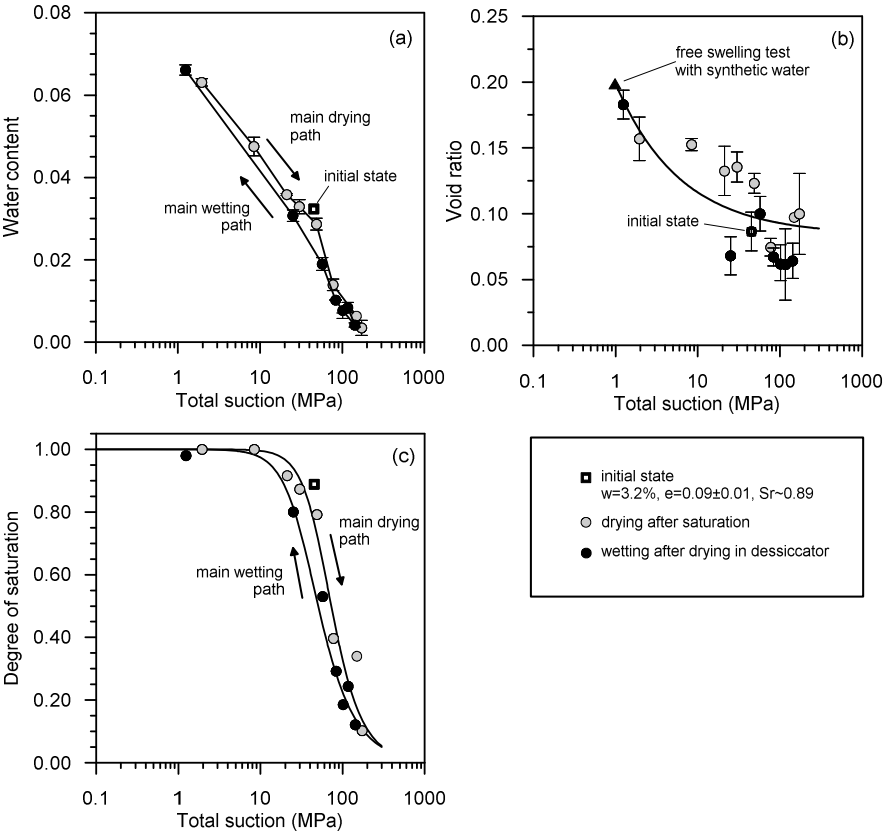

Fig. 3 Water retention behaviour of the Brown Dogger core sample: the water content (a), the void ratio (b) and the degree of saturation as a function of the total suction.

The main drying and wetting paths are well distinguished, and hysteresis zones can be observed. The evolution of the void ratios with the total suction (Figures 2.a and 2.b) showed that the porosity changes are more significant for the lowest range suction variations. The void ratios of the lowest measured suctions were in very good agreement with the results of the free swelling tests carried out with the same synthetic waters used for determining the water retention curves. The shrinkage limits (assumed to be defined by $\Delta e/\Delta\psi < 0.1$ %) were identified at suction values of approximately 10 MPa for the OPA and 15 MPa for the BD. The corresponding water content values read along the main drying paths were 6.4% and 4.0% for the OPA and the BD, respectively. The data were fitted with the following incremental expression:

$$\dot{e} = -\frac{\dot{\psi}}{K_{ref}}\left(\frac{\psi_{ref}}{\psi}\right)^{m}(1+e_0),$$

in which K_{ref}, ψ_{ref} and m are the fitting parameters. The obtained values of the parameters are reported in Table 2. The retention curves, in terms of the degree of saturation, are depicted in Figures 2.c and 3.c. The experimental points were fitted using a van Genuchten's expression (1980):

$$S_r = \left(1+\left(\frac{\psi}{P}\right)^{n}\right)^{\left(\frac{1}{n}-1\right)},$$

where P and n are the fitting parameters; the obtained values are reported in Table 2. The curves show an air entry value (gas entry pressure) of approximately 13 MPa for the OPA core sample and 22 MPa for the BD core sample (the values computed for a degree of saturation of 95%). The higher air entry value of the BD core sample is in agreement with the lower porosity (Table 1).

Table 2 The fitting parameters for the water retention behaviour.

Shale	K_{ref} (MPa)	ψ_{ref} (MPa)	m (-)	n (-)		P (MPa)	
				wetting	drying	wetting	drying
OPA	14.6	1.32	2.63	1.82	2.1	22.0	41.0
BD	22.0	0.98	1.55	2.4	2.8	35.9	57.2

4 High-Pressure Oedometric Tests

A multi-purpose oedometric cell was developed to analyse the hydro-mechanical behaviour of the geomaterials at high confining stresses. The device allows for the performance of tests in non-isothermal and controlled suction conditions. This section focuses on the use of the device for testing the volume change behaviour of shales in saturated conditions. The layout of the apparatus used is depicted in Figure 4.

The cell is designed to hold cylindrical samples (12.5 mm in height and 35 mm in diameter). The oedometer cell is inserted into a rigid stainless steel frame. The loading ram is positioned in the lower part of the system to prevent the specimen from being loaded before the test starts. The vertical load is applied by a hydraulic jack connected to a volume/pressure controller. The relationship between the controller pressure and the vertical stress on the specimen was assessed through a calibration step, which took into account the friction developed within the system (Salager et al. 2010). The maximum vertical stress that can be imposed on the

specimen is 100 MPa. The volumetric strains are measured by three LVDTs (with a resolution of 1 μm), which are fixed to the frame and are in contact with the loading ram. The tests can be performed in incremental loads, in a constant loading rate mode or in a constant vertical strain rate mode. Two pore water pressure controllers are used to control the pore water pressure at the bottom and top basis and to measure the volume changes of the pore water.

The following procedure was developed and systematically applied to obtain the specimens for the oedometric tests. A slice with a thickness of approximately 20 mm was sawed without unpacking the core to minimise the sample disturbance. The diameter of the slice was then progressively reduced to obtain a disk with a diameter slightly larger than the final confining ring. The final re-coring step was performed with a hydraulic press. Finally, the lower and upper faces were smoothed using sand paper to obtain parallel and planar surfaces.

The results are presented for the tests performed by incremental loading, which attained a maximum vertical stress equal to 30 MPa and 100 MPa for the OPA and the BD, respectively. The high level of applied vertical stress was required to observe the transition from the over- to the normally consolidated state of each material. The specimens were initially saturated in isochoric conditions by applying a back pressure in the range of 20 – 50 kPa, and the developed swelling pressure was measured. Afterward, two loading-unloading cycles were performed in stages, allowing for the complete dissipation of the excess pore water pressure (drained conditions).

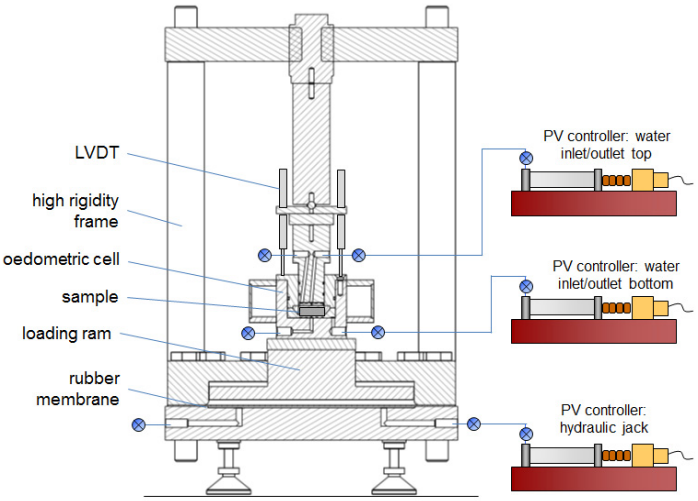

Fig. 4 A diagram of the high-pressure oedometric cell used to perform the tests in saturated conditions.

To analyse the settlement versus time curve for each loading increment, an analytical solution was developed that considers the time requested by the controller for applying the target pressure, the deformation of the apparatus, the primary consolidation settlement for a non-instantaneous loading and the secondary consolidation (Manca et al. 2012). Figures 5 and 6 report the total settlements of the OPA and the BD, respectively, which are measured at the end of each loading step and corrected in light of the deformation of the apparatus, in terms of the volumetric strain versus the vertical effective stress. The figures also depict the volumetric strain relative to the end of the primary consolidation. The difference between the total and the end-of-primary strains is associated with the secondary consolidation component. The average computed coefficients of secondary compression were 0.0006 for the OPA and 0.0004 for the BD. The end-of-primary strains are used to compute the compression and the swelling indexes and to assess the vertical effective yield stresses (Figures 5 and 6). The oedometric modulus (E_{oed}) and the coefficient of consolidation (c_v) as a function of the applied vertical effective stress are depicted in Figure 7. A systematic higher rigidity of the BD versus that of the OPA was registered; this observation was consistent with a lower initial void ratio (Table 1).

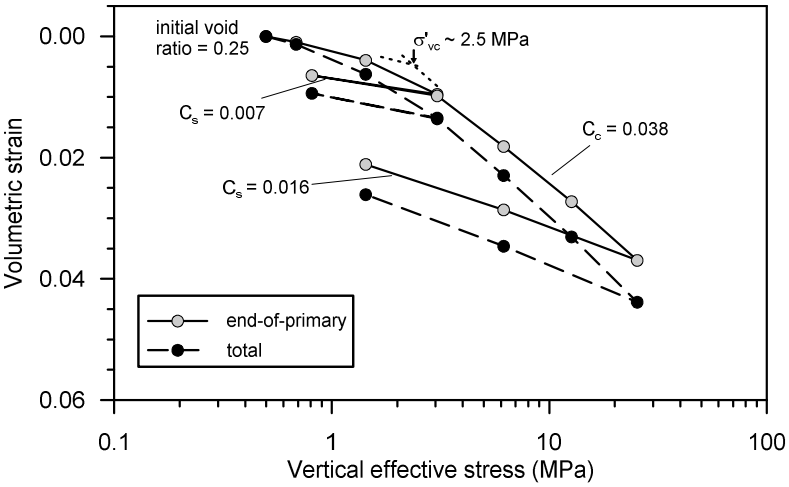

Fig. 5 Results of the oedometric test on the Opalinus Clay: the volumetric strain computed in light of the total settlement and the end-of-primary consolidation settlement

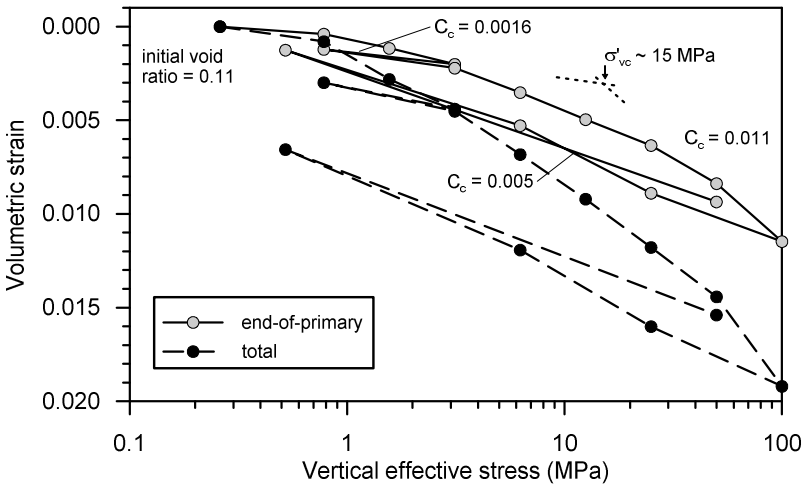

Fig. 6 Results of the oedometric test on the Brown Dogger: the volumetric strain computed in light of the total settlement and the end-of-primary consolidation settlement

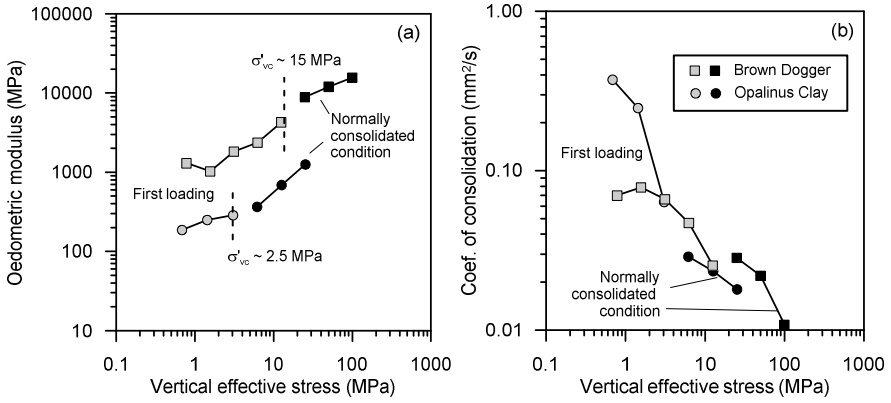

Fig. 7 The oedometric modulus (a) and the coefficient of consolidation (b), each as a function of the vertical effective stress computed from the analysis of the settlement versus time curves.

Finally, the coefficient of permeability (K) was back-calculated for each load increment using the definition of the coefficient of consolidation:

$$K = \frac{c_v \gamma_w}{E_{oed}},$$

where γ_w is the specific weight of water. The computed values for both materials are reported in Figure 8 as a function of the void ratio. The obtained trends are in very good agreement with the results of constant head permeability tests that have

been reported by other authors (Horseman et al. 2007; Romero et al. 2012). This agreement shows that, when the end-of-primary consolidation and the coefficient of consolidation are properly computed, high-pressure oedometric tests can be used to gather information on the permeability of the tested shales within a significant range of porosity.

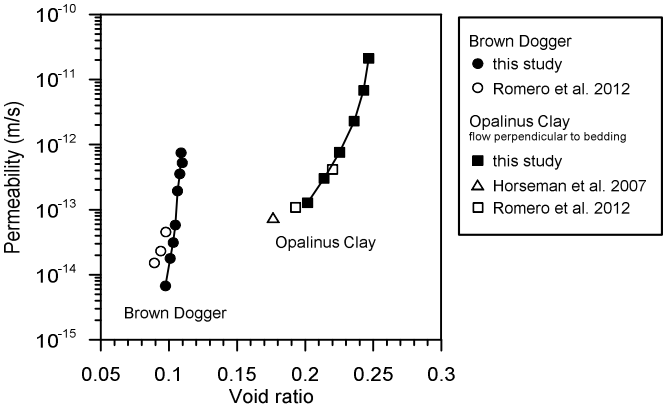

Fig. 8 The coefficient of permeability as a function of the void ratio computed from the analysis of the settlement versus time curves and compared with other available data.

5 Closing Remarks

The paper presents experimental techniques that have been developed for analysis of the water retention behaviour and the volumetric response of shales at high confining stress levels. Selected experimental results for two shales from the northern region of Switzerland are presented and discussed.

The low porosity of the tested shales (with principal pore modes in the range of 15 - 20 nm) required the consideration of a wide range of suction to observe the significant variations in the degree of saturation. The procedure adopted for the analyses of the water retention behaviour of shales consisted of controlling the water content by the addition of synthetic water or by the dehydration of the material in a desiccator; additionally, the procedure involved the measurement of total suction by a dew-point psychrometer. The method is suitable for describing the water retention behaviour along the main drying and wetting paths and for highlighting the hysteretic behaviours of retention curve. The systematic measurement of volume changes along the wetting and drying paths allowed for the computation of the degree of saturation and for the assessment of the shrinkage limit of each material.

A new high-pressure oedometric cell was introduced to analyse the transition from the over- to the normally consolidated state of shales. Attainment of a vertical effective stress in the range of 30 – 100 MPa was needed to measure the yield vertical stress. Analysis of the settlement versus time curves yielded information on the consolidation parameters and the permeability at various stress levels and void ratios.

Acknowledgments. The authors acknowledge the Swiss National Cooperative for the Disposal of Radioactive Waste (NAGRA) for supporting these research activities. The authors would like to acknowledge the research assistants, Donatella Manca and Paul Witteveen, for their help with the experimental work.

References

Cardoso, R., Romero, E., Lima, A., Ferrari, A.: A comparative study of soil suction measurement using two different high-range psychrometers. In: Schanz, T. (ed.) 2nd Int. Conf. on Mech. of Unsat. Soils, Weimar, Germany, pp. 79–93. Springer, Berlin (2007)

Horseman, S.T., Harrington, J.F., Noy, D.J.: Swelling and osmotic flow in a potential host rock. Physics and Chemistry of the Earth, Parts A/B/C 32(1-7), 408–420 (2007)

Leong, E.-C., Tripathy, S., Rahardjo, H.: Total suction measurement of unsaturated soils with a device using the chilled-mirror dew point technique. Géotechnique 53(2), 173–182 (2003)

Mäder, U.: Recipe and preparation of a simplified artificial pore water for Opalinus Clay and Brown Dogger. NAGRA AN 11-159 (2011)

Manca, D., Ferrari, A., Laloui, L.: Analysis of 1D high-pressure consolidation tests considering time dependent loading (in prep., 2012)

Muñoz, J.J.: Thermo-hydro-mechanical analysis of soft rockapplication to a large scale heating test and large scale ventilation test. PhD dissertation, Universitat Politècnica de Catalunya, Spain (2007)

Pearson, F.J.: Opalinus Clay experimental water: A1 Type, Version 980318. PSI Internal report TM-44-98-07, Paul Scherrer Institut, Villigen PSI, Switzerland (1998)

Peron, H., Hueckel, T., Laloui, L.: An improved volume measurement for determining soil water retention curves. Geotechnical Testing Journal 30(1), 1–8 (2007)

Ramos Da Silva, M., Schroeder, C., Verbrugge, J.-C.: Unsaturated rock mechanics applied to a low porosity shale. Engineering Geology 97, 42–52 (2008)

Romero, E., Senger, R., Marschall, P.: Air Injection Laboratory Experiments on Opalinus Clay. Experimental techniques, Results and Analyses. In: 3rd EAGE Shale Workshop, Barcelona, January 23-25 (2012)

Salager, S., Ferrari, A., Laloui, L.: New experimental tools for the characterization of highly overconsolidated clayey materials in unsaturated conditions. In: Laloui, L. (ed.) Mechanics of Unsaturated Geomaterials, pp. 113–126. John Wiley & Sons (2010)

Thomson, W.: On the equilibrium of vapour at a curved surface of liquid. Phil. Mag. 42, 448–452 (1871)

Valès, F., Nguyen Minh, D., Gharbi, H., Rejeb, A.: Experimental study of the influence of the degree of saturation on physical and mechanical properties in Tournemire shale (France). Applied Clay Science 26(1-4), 197–207 (2004)

van Genuchten, M.T.: A closed-form equation for predicting the hydraulic conductivity of unsaturated soils. Soil Sci. Soc. Am. J. 44, 892–898 (1980)

Zhang, C.-L., Rothfuchs, T., Su, K., Hoteit, N.: Experimental study of the thermohydro-mechanical behaviour of indurated clays. Physics and Chemistry of the Earth 32(8-14), 957–965 (2007)

Air Tests on Low-Permeability Claystone Formations. Experimental Results and Simulations

Enrique Romero[1,*], Rainer Senger[2], Paul Marschall[3], and Rodrigo Gómez[1]

[1] Department of Geotechnical Engineering and Geosciences,
Universitat Politècnica de Catalunya, Barcelona, Spain
{Enrique.romero-morales,rodrigo.gomez}@upc.edu
[2] Intera Inc., Swiss Branch Ennetbaden, Switzerland
[3] Nagra, Science and Technology, Switzerland
Paul.Marschall@nagra.ch

Abstract. The paper presents the results of an experimental investigation aimed at characterising the water and air permeability properties of low-permeability claystone formations from a Mesozoic sequence in Northern Switzerland. The experiments, besides providing quantitative data to calibrate hydraulic and two-phase flow properties, intend to analyse the phenomena and processes, which control the percolation of air through an initially water saturated claystone. Fast controlled-volume rate air injection experiments were performed in a triaxial cell, testing a total of four rock samples under isotropic stress state conditions at different initial porosity and at two sample orientations (flow parallel and orthogonal to bedding planes). Simulation results showed a good agreement between the measured pressures at the injection and outflow sides of the sample using a standard two-phase flow simulation code.

1 Introduction

Understanding the phenomena and processes associated with the release of gases from the disposal systems of a geological repository for radioactive waste is one of the key issues in the assessment of repository performance and is the focus of this research. If the gas production rate (generated by the anaerobic corrosion of the steel canisters and microbial degradation of organic material) exceeds the rate of diffusion of gas in the pore-water, gas pressure will increase and migrate through the engineered barrier system and into the surrounding host rock. The actual gas migration mechanisms may entail standard two-phase flow conditions (partially displacing water) or more complex mechanisms involving coupled two-phase geomechanical and possibly geochemical phenomena–in all cases, preferential gas pathways will develop taking advantage of the material heterogeneity and anisotropy, rock discontinuities or interfaces.

* Corresponding author.

L. Laloui and A. Ferrari (Eds.): Multiphysical Testing of Soils and Shales, SSGG, pp. 69–83.
springerlink.com

These gas transport mechanisms are sensitive to the stress state (two-phase flow affected by porosity changes and pathway transmissivity sensitive to fracture aperture variations; see for instance, Olivella & Alonso 2008). Within this context, laboratory scale experiments under controlled pneumatic, hydraulic and mechanical boundary conditions are important to provide data to develop and validate theoretical frameworks and predictive tools. Some issues of concern under which gas breakthrough processes occur are associated with the following aspects–to cite but a few of them–: a) the effects of the stress state; b) the initial porosity; c) the volume change behaviour during gas injection (changes in gas and liquid pressures and their impact on porosity changes); d) the role played by the orientations of rock discontinuities and their spatial variability; e) the influence of the gas injection rate; f) if interstitial liquid displacements (specimen desaturation) occur during these extreme processes; g) if mechanical degradation issues (microfracturing processes) are occurring during the creation of pathways; h) time-dependent effects on breakthrough pressures; and i) temperature effects.

Despite its importance, information at laboratory scale on gas pressure-induced pathways and breakthrough pressures in geological barriers under controlled gas volume rate injection, controlled stress state and orientation of rock discontinuities is rather scarce (see for instance, Hildenbrand *et al.* 2002, Arnedo *et al.* 2008, and more recently Romero *et al.* 2009, 2010 and 2012). Previous tests performed by Horseman *et al.* (1999) and Harrington & Horseman (2003) evidenced that no measurable water displacements occurred inside the specimen, despite the fact that the observed breakthrough pressures appeared to be higher than the air-entry pressure of the material.

To this aim, an experimental study was conducted on rock samples from two Mesozoic formations, considered as candidate host rocks in the Swiss programme for deep geological disposal of radioactive waste, namely the Opalinus Clay (OPA) and the so-called 'Brown Dogger', a clay-rich sequence of the Upper Dogger unit. The samples were retrieved at two different and contrasting depths ('shallow' and 'deep', respectively), and a test programme was launched using controlled volume-rate gas injection experiments on a high-pressure triaxial cell (isotropic stress states). The experiments, besides providing quantitative data for model validation (applicability of two-phase flow models) and parameter estimation (calibration of hydraulic and two-phase flow properties), intend to analyse the influence of the stress state under isotropic conditions, the initial porosity and anisotropic flow conditions (flows parallel and normal to bedding) on gas breakthrough processes.

2 Materials Used in the Research

At Mont Terri Underground Rock Laboratory in the Jura Mountains of Northwestern Switzerland an undisturbed OPA (Jurassic claystone) core sample was

recovered from the shaly facies, approximately 300 m depth below ground (core BHA-8/1; MI-niche). A single barrel dry-drilling technique was used and immediately after core recovery, the rock sample was cast in epoxy resin for safe preservation during shipment. Sample preparation at the laboratory took place under dry conditions (pre-cut with a band saw and then prepared with a lathe) by subcoring the specimen at two orientations with respect to bedding to match a circular cross-section of 50 mm in diameter and a maximum height of 25 mm. Two other core samples were retrieved from a deep geothermal well near the village of Schlattingen in the Molasse Basin of North-eastern Switzerland (Canton Thurgau). The first core was recovered from a clay-rich sequence at a depth of around 776.5 m bg, called 'Brown Dogger' (Parkinsoni-Würtembergica strata of the Upper Dogger). The second core was taken from the Opalinus Clay formation at a depth of 879.9 m bg. The cores were recovered with a double core barrel using a NaCl drilling mud. After on-site core documentation, the samples were cast immediately in epoxy resin for save preservation during shipment. In what follows, these samples are identified as 'shallow sample' (300 m depth OPA) and 'deep samples' (776.5 m depth 'Brown Dogger' and 879.9 m depth OPA). A synthetic pore-water was used for the saturation of both samples. Initial conditions of the claystone samples are summarised in Table 1.

Table 1 Range of initial conditions of shallow (300 m) and deep (776.5 and 879.9 m, respectively) samples

Property	Value
Density	2.34 - 2.38 Mg/m^3* 2.51 - 2.53 Mg/m^3+
Density of solids	2.70 Mg/m^3* 2.69 Mg/m^3+
Dry density	2.20 - 2.23 Mg/m^3* 2.41- 2.43 Mg/m^3+
Void ratio	0.21 - 0.23* 0.11 - 0.12+
Porosity	0.17 - 0.19* 0.10 - 0.11+
Water content	6.6 - 6.9%* 4.3 - 4.7%+
Degree of saturation (ρ_w=1 Mg/m^3)	77 - 88%* 100%+
Total suction	15 MPa* 4 MPa++
Dominant pore mode (MIP)	23 nm* 16 nm++
Air-entry value (MIP)	13 MPa* 18 MPa++
van Genuchten p_0 (Fig. 2)	18 MPa* 27 MPa++
Liquid limit	(38 ± 5)%*
Plastic limit	(23 ± 2)%*

* 'Shallow sample' (300 m depth OPA)
+ 'Deep samples' (776.5 m depth 'Brown Dogger'; 879.9 m depth OPA)
++ 'Deep sample' 879.9 m depth OPA

Mercury intrusion porosimetry tests were carried out on both freeze-dried materials to characterise their porosity network (Romero & Simms 2008). Figure 1 (on the left) shows the cumulative intruded pore volume normalised by solid volume (intruded void ratio) plotted against the entrance pore size ('shallow sample' and 'deep sample' 879.9 m depth OPA). There is some deviation from the initial void ratio (refer to Table 1), due to the limited capacity of the porosimeter to enter the smallest pores (non-intruded porosity). Other useful information that can be obtained from the MIP test is the pore size density function (right plot in Figure 1), defined as: $f(\log x) = -\mathrm{d}e/\mathrm{d}(\log x)$, where x represents the entrance pore size. The density function obtained from MIP displays one dominant pore mode at approximately 23 nm for the 'shallow sample' and slightly lower at 16 nm for the 'deep sample'. The pore network description of the 'deep sample' was complemented by nitrogen adsorption tests. The pore size distribution was estimated following the Barrett, Joyner and Halenda (BJH) method using the desorption information (Webb & Orr 1997). A wider range of pore sizes is covered when using this complementary information. Maximum intruded void ratio was 0.116 (left plot in Figure 1), equivalent to the value indicated in Table 1. The complementary pore-size density function obtained by BJH is plotted in Figure 1 (on the right), which identifies another dominant pore mode at around 3-4 nm.

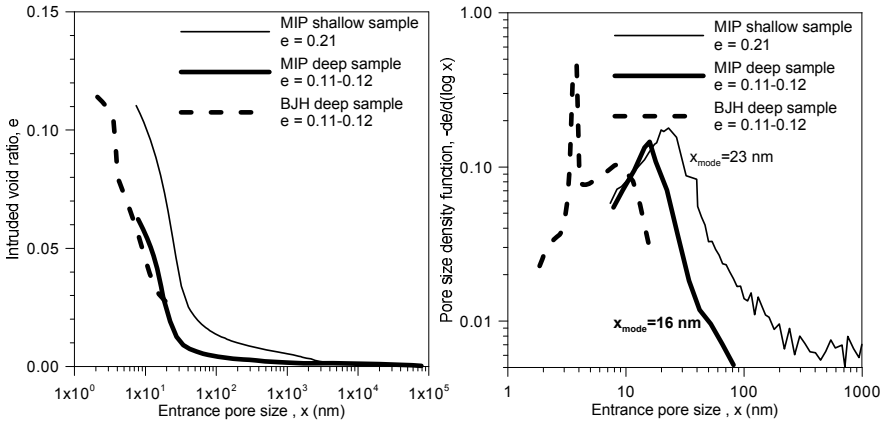

Fig. 1 Pore size distribution results. Left: Cumulated intruded void ratio. Right: Pore size density functions with dominant pore modes. 'Deep sample' corresponds to 879.9 m depth OPA

A dew point psychrometer (Cardoso *et al*. 2007) was used to obtain the water retention curves in the total suction range from 1 to 100 MPa ('shallow sample' and 'deep sample' 879.9 m depth OPA). The specimens were wetted or dried in steps starting from the initial condition, stored for one day for equalisation, weighed and the relative humidity of the air surrounding the soil measured. Pore size distribution results were also used to determine the relationship between suction and degree of saturation, as well as the air entry value corresponding to the

dominant pore mode. The injection of non-wetting mercury was assumed to be equivalent to the ejection of water by the non-wetting front advance of air (drying branch) for the same diameter of pores being intruded. Figure 2 shows the estimated water retention curve based on MIP data, together with psychrometric measurements. The air entry value AEV corresponding to the dominant pore mode can be determined from Laplace's equation. Table 1 reports these AEVs for the different samples. The consistent experimental results were fitted to van Genuchten's equation (1980). Fitted parameters and the equation used are presented in the figure, in which a constant n=1.67 has been considered for both samples. Different values of parameter p_0 –associated with the air-entry value– were fitted, which correctly matches the trend indicated by the AEV values indicated in Table 1.

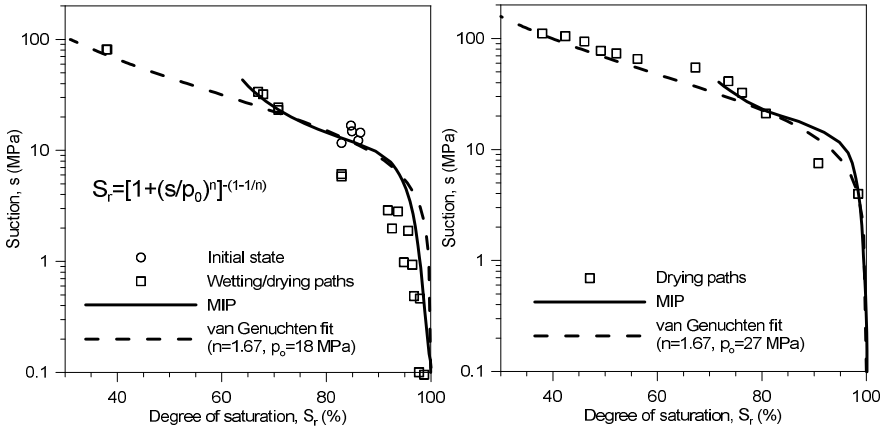

Fig. 2 Water retention information using psychrometer and mercury intrusion results. Left: OPA 'shallow sample' (300 m). Right: OPA 'deep sample' (879.9 m)

3 Experimental Study Performed

An instrumented high-pressure triaxial cell was used, which was specifically designed to apply isotropic/anisotropic stress states up to a maximum of 40 MPa, while injecting air at controlled volume rate. Figure 3 shows a scheme of the triaxial cell jointly with the test set-up. The axial deformation of low-height specimens –confined by several neoprene membranes and aluminium foils– is registered with an external linear variable differential transformer (LVDT in the figure). Each cap of the triaxial cell has inlet and outlet lines, prepared for gas and liquid connections. The equipment uses four automatic pressure / volume controllers (P/V in the figure), two for gas (injection and extraction at downstream point), and two for water, which can be used in combination (for example, air injection and water pressure at downstream, which is the setup used in the present investigation). The gas injection pressure / volume controller has a maximum range of 20 MPa

(maximum volume 500 mL), and is able to control volume rates between 10^{-4} mL/min and 100 mL/min (volume resolution < 5 mm^3). The 2 MPa P/V controllers for air and water at downstream present a volumetric resolution of 1 mm^3 (pressure resolution 1 kPa).

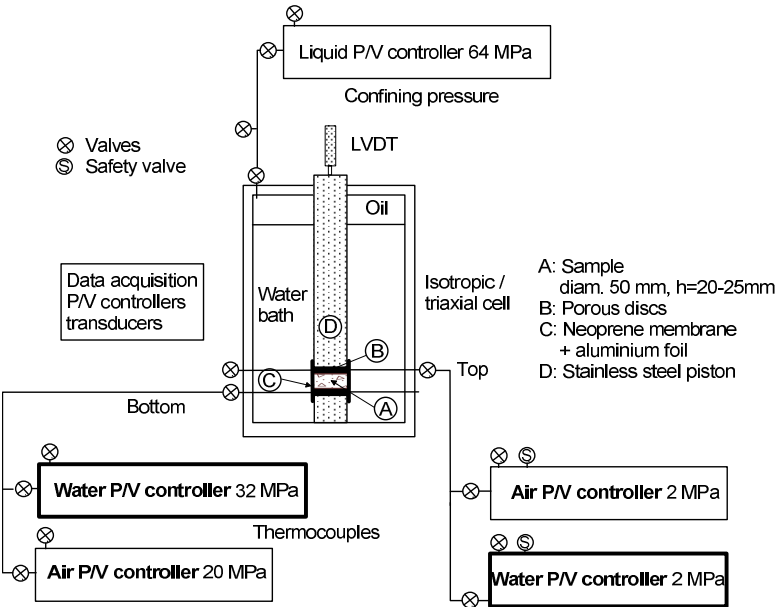

Fig. 3 Scheme of the air injection and water permeability setup with high-pressure triaxial cell and four pressure/volume controllers (two for air and two for water)

Before the air injection tests, saturation of the samples under two orientations (flows parallel and orthogonal to bedding) was ensured and water permeability measured using different hydraulic gradients at different isotropic confining stresses. Figure 4 displays a scheme of this test A, in which upstream / downstream volume changes and axial deformation are recorded during these hydraulic tests. This information allows approximately plotting water permeability as a function of void ratio in these low-height samples. Controlled-gradient conditions were maintained for around two/three weeks to ensure approx. equivalent inflow and outflow liquid volume rates (stationary flow conditions).

For the air injection tests (test B in Fig. 4), the upstream water line was rapidly drained to inject air pressure at 0.5 MPa and the recovery system maintained with water at 0.5 MPa to better ensure sample saturation. The sample was let to equalise at an initial pore water pressure of 0.5 MPa and at the target total stress (between 15 and 19 MPa). Fast air injection started under controlled volume rates (typically at 100 mL/min) from an initial value of 3 MPa. After reaching maximum air pressure (lower than the confining stress), the upstream piston was

stopped and air pressure was let to decay at constant volume. Fitting the constant mass system for different injection periods allowed estimating the initial injection volume of air (injection piston and air lines). Pressure deviations from the perfect gas law for a constant mass system in the injection point allowed estimating the injected mass of air and mass inflow rates into the sample. Information on outflow rates was recorded and used to define the breakthrough pressures.

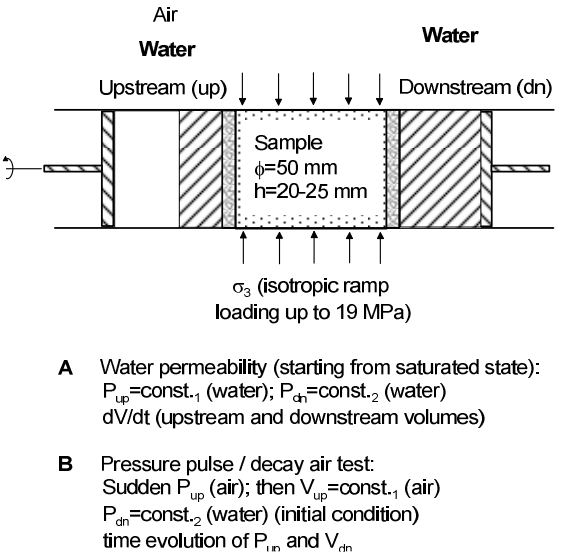

Fig. 4 Type of tests followed during controlled-gradient water permeability tests and fast air injection tests followed by recovery period at constant volume

4 Experimental Results and Simulations Performed

Figure 5 presents the water permeability results for shallow and deep samples (300 m depth OPA, 776.5 m depth 'Brown Dogger' and 879.9 m depth OPA). 'Shallow sample' data is separated in water permeability with flow orthogonal and parallel to bedding planes, which display clear anisotropic features. As shown in the figure, for constant void ratio, the anisotropy ratio $K_{II}/K_{\perp}$ (ratio of intrinsic permeability parallel to flow to intrinsic permeability orthogonal to flow) is in the range 3 to 5. Only water permeability with flow orthogonal to bedding has been measured for 'deep samples'. Furthermore, clear evidence is also shown for the important dependency of water permeability on void ratio. This measured dependency has been fitted to the exponential equations indicated in the figure. Different void ratios were attained as a consequence of mean effective stress changes induced by

the different hydraulic gradients (pore-water pressures) and isotropic total stresses applied. The deeper samples, which presented smaller void ratios (refer to Table 1), consistently displayed lower water permeability values.

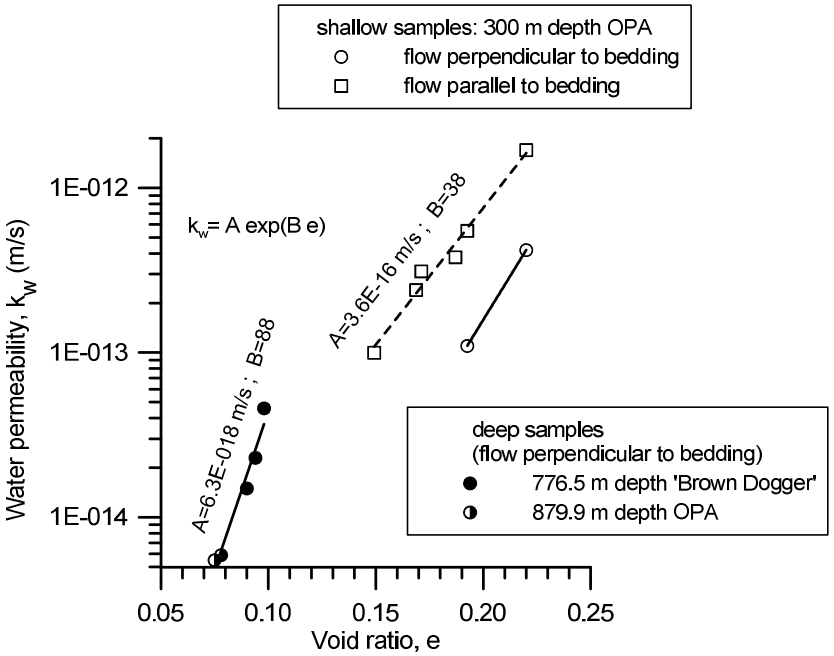

Fig. 5 Water permeability dependency on void ratio and orientation effects for the different samples

Figures 6 and 7 show the time evolution of air injection pressure during fast controlled volume-rate tests (100 mL/min) at 15 MPa isotropic confining stress on 'shallow samples' under different orientations (flow parallel and orthogonal to bedding). V_0 in the figure represents the initial injection volume of air (injection piston and air lines). As observed in the figure, the injection pressure was able to increase up to 12 and 13 MPa (depending on the test), followed by a shut-in and recovery period at constant volume. For the flow parallel to bedding (Fig. 7), outflow response was immediately observed after shut-in corresponding to a sudden drop in the injection pressure, followed by a subsequent gradual decline. For the flow orthogonal to bedding, the injection pressure remained initially flat and the outflow response was significantly delayed indicating also anisotropy during air permeability tests. After the apparent air breakthrough process corresponding to an increase in the outflow pressure, the injection pressure showed a steep decline. The constant downstream pressure condition of 0.5 MPa was not possible to maintain due to the high outflow volume rates detected (the downstream pressure increased until reaching 2 MPa, where a constant pressure was again prescribed by

the pressure release valve). The pressure pulse decay information was used to estimate the evolution of the air permeability along the process. With regard to the axial displacement response (negative axial displacement corresponds to expansion), the samples at constant isotropic total stress displayed quasi-reversible features with expansion at the early fast air injection stage and progressive compression towards approximately the initial volume on air pressure dissipation. As a first approximation, this behavioural feature at constant isotropic total stress has been associated with pore pressure changes inducing constitutive (effective) stress variations: pore pressure increase inducing mean effective stress decrease (and thus expansion), followed by compression due to mean effective stress increase (pore pressure dissipation stage). Further studies are currently being undertaken to compare these volume changes related to pore pressure variations at constant total stress during air injection/dissipation to volume changes induced by total (isotropic) stress changes under constant pore pressure.

Figure 8 presents the equivalent results for the low-permeability 'deep sample' (776.5 m depth 'Brown Dogger'). In this case, the injection pressure essentially remained flat in the recovery stage at constant volume without appreciable outflow volume detected (the outflow pressure remained at 0.5 MPa). The material response during air injection tests was thus very sensitive to void ratio, following an equivalent behavioural picture to that observed during water permeability tests.

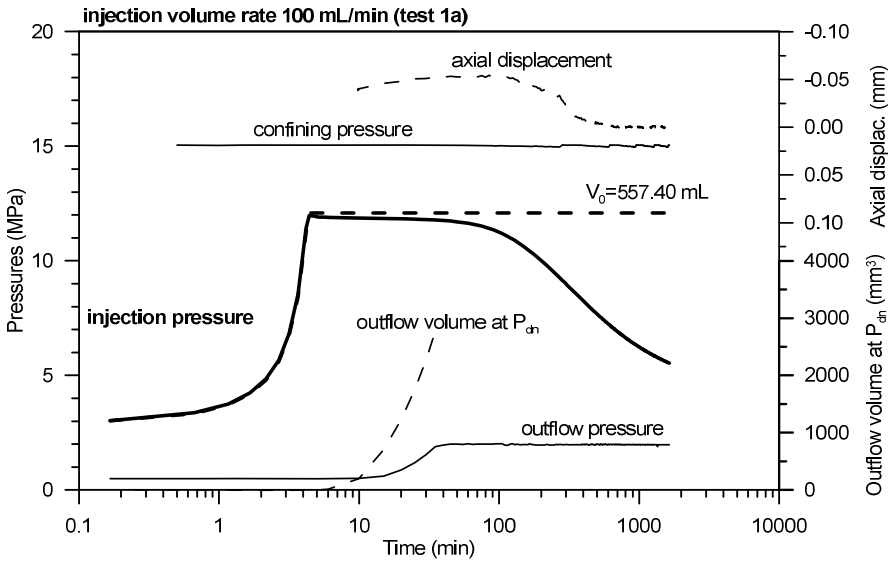

Fig. 6 Measured time evolution of pressures at the injection and outflow sides together with outflow volume and axial displacements. 'Shallow sample' with bedding plane orientation orthogonal to flow

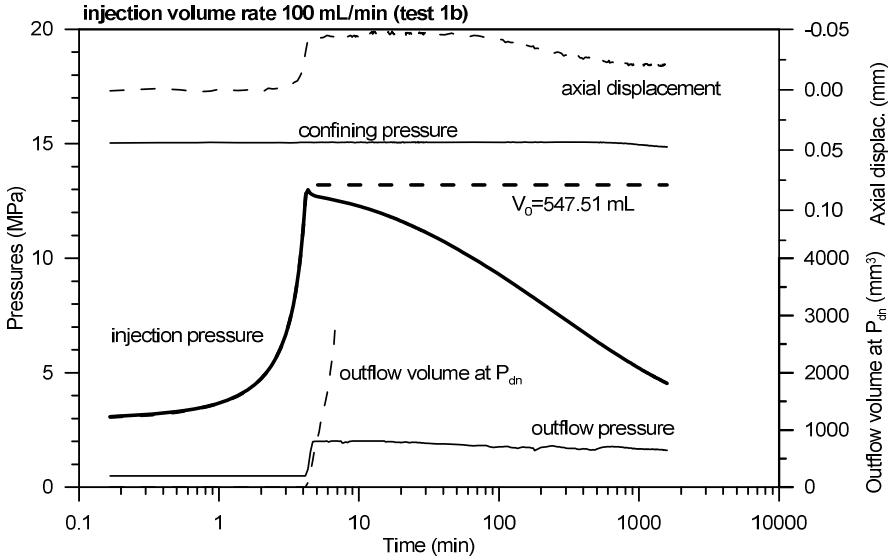

Fig. 7 Measured time evolution of pressures at the injection and outflow sides together with outflow volume and axial displacements. 'Shallow sample' with bedding plane orientation parallel to flow

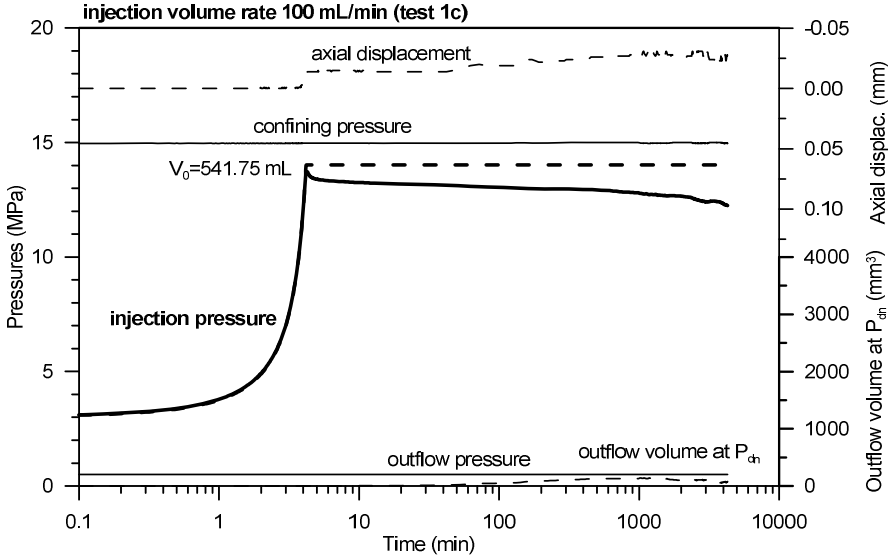

Fig. 8 Measured time evolution of pressures at the injection and outflow sides together with outflow volume and axial displacements. 'Deep sample' (776.5 m depth 'Brown Dogger')

To help with the interpretation of the results and for the investigation of the measured responses in terms of injection and outflow pressures, as well as outflow volumes, numerical models were developed implementing the geometry of the shallow OPA core and the corresponding boundary conditions on the injection and outflow sides. For the analyses, standard two-phase flow processes were considered in the numerical model in an attempt to reproduce the observed measurements. The two-phase flow code TOUGH2 (Pruess *et al.* 1999) was used, which takes into account fluid flow in both liquid and gas phases occurring under pressure, viscous, and gravity forces according to Darcy's law. Pressures in the liquid and gaseous phases are related by the capillary pressure functions and interference between the phases is represented by relative permeability functions. The code considers binary diffusion in the gas phase, and diffusion of dissolved gas in the liquid phase. The air injection through a solid piston at constant rate was implemented by injecting water into an air filled injection chamber element connected to the elements representing the clay sample. This implementation may affect the actual air volume injected, as small amount of air can dissolved in the injection water, which could affect the maximum pressure (a correction was considered to account for this effect).The volume of the initially air-filled injection element was fixed at 557.4 mL (Fig. 6) and 547.41 mL (Fig. 7). The outflow pressure was set constant at 2 MPa after the air breakthrough process and the activation of the pressure release valve.

Standard two-phase flow model parameters van Genuchten / Mualem were calibrated based on the experimental data reported in Figures 2 and 5, as well as by inverse modelling of the air injection / outflow responses using the ITOUGH2 code (Finsterle 2007). Results of the numerical modelling are shown in Figure 9 for the air injection experiment carried out on the shallow OPA sample with bedding plane orientation orthogonal to flow. The initial injection pressure evolution is reasonably well reproduced, indicating a slight decline after shut-in that is not observed in the experimental data. Nevertheless, the simulated air pressures after air breakthrough remained higher than the measured ones at late times, indicating that the air permeability in the model is too low. The outflow pressure response – i.e., after air breakthrough– is also well reproduced. Some of the estimated two-flow phase parameters used in the simulation are reported in the figure. The estimated intrinsic permeability is higher compared to the results from the water tests (Fig. 5), whereas the estimated van Genuchten parameter p_0 is lower than the one fitted from the retention data shown in Figure 2 (on the left). Figure 10 displays simulation results of the air injection test performed on the 'shallow sample' with bedding plane orientation parallel to flow. Again, the simulated pressure responses for the injection and outflow sides indicate an overall good agreement with the measured response. Similar to the case with flow perpendicular to bedding, the estimated intrinsic permeability is higher compared to the results reported from the water permeability tests (a slightly higher p_0 parameter is obtained from this inverse simulation, but still below the value indicated in Fig. 2 on the left).

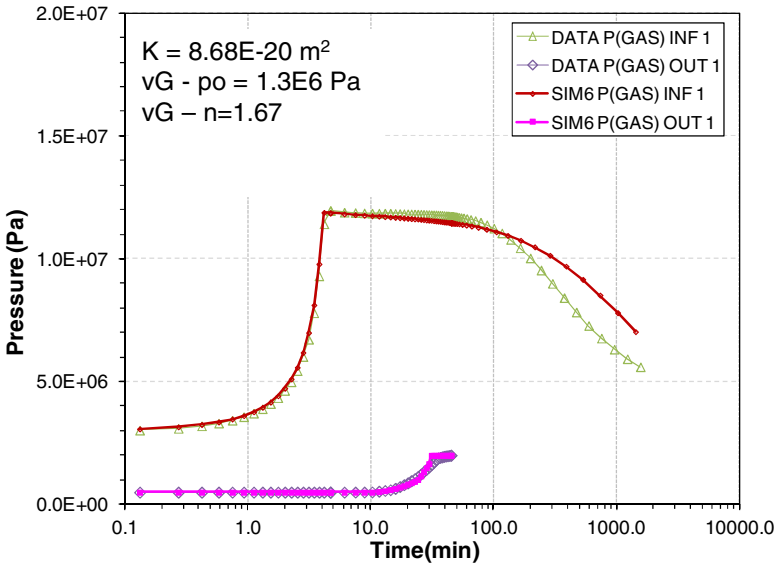

Fig. 9 Simulation (sim) and measured (data) results in terms of injection pressure and outflow pressure for 'shallow sample' with bedding plane orientation orthogonal to flow

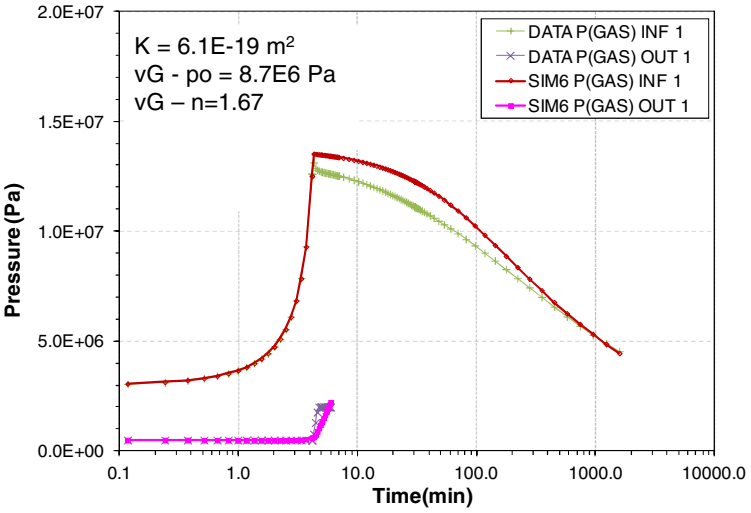

Fig. 10 Simulation (sim) and measured (data) results in terms of injection pressure and outflow pressure for 'shallow sample' with bedding plane orientation parallel to flow

The initial calibration could not reproduce well the measured pressure response at late times of the test with flow orthogonal to bedding planes even with a high air permeability. In addition, the two-phase flow parameters were not fully consistent with the complementary experimental results from the retention curves. These results suggest a change in properties or a non-linear behaviour in intrinsic permeability and corresponding two-phase flow properties. In a second analysis step, the measured relationships between pore compressibility and void ratio and the corresponding changes in intrinsic permeability were implemented in TOUGH2. In a first approximation, a linear relationship between pore compressibility and porosity was used by Senger *et al.* (2012), supported by experimental results, which allowed introducing the coupling between compressibility, porosity, permeability and capillary pressure. A fitted log-linear relationship between measured porosity and permeability at the different mean total stresses was derived by Senger *et al.* (2012), and the change in capillary pressure with permeability was represented by the Leverett function (Leverett 1941). With these changes, the simulations significantly improved the fit of the observed responses of both tests with flow parallel and perpendicular to bedding. However, more detailed model calibrations and sensitivity analyses are currently being conducted to better understand the two-phase flow mechanisms in these low-permeability argillaceous materials.

5 Conclusions

The paper describes the experimental setup and procedures for air permeability tests performed in an instrumented high-pressure triaxial cell, which was specifically designed to apply isotropic stress states, while injecting air at controlled-volume rate up to a maximum pressure of 20 MPa. A series of controlled-gradient water tests and fast controlled-volume rate air injection tests followed by pressure pulse decay stages were run to calibrate hydraulic and two-phase flow properties at different sample orientations (flows parallel and orthogonal to bedding) and different initial porosities. The study was performed on clay-rich rocks of the Upper and Middle Dogger Unit ('Brown Dogger' and Opalinus Clay, respectively), representing candidate host formation for a geological repository for radioactive waste in Switzerland. The specimens were taken from depth ranging from around 300 m to 870 m below ground.

The water and air permeability experiments revealed some important hydro-mechanical characteristics of the claystone samples. Thus, the intrinsic permeability (as measured in water flow tests) exhibits an anisotropy ratio $K_{II}/K_{\perp}$ (ratio of intrinsic permeability parallel to flow to intrinsic permeability orthogonal to flow) in the range 3 to 5 at constant void ratio. Furthermore, clear evidence is also shown for the important dependency of water permeability with void ratio and thus constitutive stress (coupling between pore compressibility and effective stress). The deeper samples, which presented smaller void ratios (refer to Table 1), consistently display lower water permeability values. The equivalent behavioural picture has been also observed during air injection tests, in which the material response is also sensitive to void ratio (the injection pressure on 'deep sample' essentially remained flat in the recovery stage at constant volume without

appreciable outflow volume detected) and displays clear anisotropy features (significant air transport observed at pressures below confining stress and with flow parallel to bedding planes in 'shallow sample').

Another important observation is the axial displacement of the test samples in response to the increase in gas pressure, suggesting a marked dependency of volumetric strain on the constitutive stress changes during air injection/dissipation tests. The samples display quasi-reversible features with expansion at the early fast air injection stage in response to mean effective stress decrease, and progressive compression towards approximately the initial volume on air pressure dissipation (mean effective stress increase). Further studies are currently being undertaken to analyse these features and their implications on changes in the air transport properties.

The analysis using standard two-phase flow model provided insight into the overall air flow mechanisms and showed a good agreement between the measured pressures at the injection and outflow sides of the sample. However, no consistent parameter set could be determined, in agreement with the complementary characterisation tests performed on the material, which can be attributed to the compressibility of the sample and the resulting non-linear phenomena (changes in porosity along the sample). Changes in porosity associated with changes in constitutive stress and corresponding changes in intrinsic permeability have not been considered in the present study. Numerical analyses are currently being performed (Senger *et al*. 2012) that include the coupled changes in porosity and intrinsic permeability under changing stress states (i.e., the coupling between pore compressibility, porosity, intrinsic permeability and capillary pressure).

Acknowledgements. The authors acknowledge the financial support provided by NAGRA (Nationale Genossenschaft für die Lagerung radioaktiver Abfälle, Switzerland) through different research projects with International Centre for Numerical Methods in Engineering (Spain).

References

Arnedo, D., Alonso, E.E., Olivella, S., Romero, E.: Gas injection tests on sand/bentonite mixtures in the laboratory. Experimental results and numerical modelling. Physics and Chemistry of the Earth 33, S237–S247 (2008)

Cardoso, R., Romero, E., Lima, A., Ferrari, A.: A comparative study of soil suction measurement using two different high-range psychrometers. In: Proc. 2nd Int. Conf. Mechanics of Unsaturated Soils, Experimental Unsaturated Soil Mechanics, Proceedings in Physics, Weimar, Germany, March 7-9, pp. 79–93. Springer, Berlin (2007)

Finsterle, S.: ITOUGH2 User's Guide, Report LBNL-40040, Lawrence Berkeley National Laboratory, Berkeley, CA, USA (2007)

Harrington, J.F., Horseman, S.T.: Gas migration in KBS-3 buffer bentonite. Sensitivity of test parameters to experimental boundary conditions. SKB Technical Report TR-03-02, Stockholm, Sweden (2003)

Hildenbrand, A., Schlömer, S., Krooss, B.M.: Gas breakthrough experiments on fine-grained sedimentary rocks. Geofluids 2, 3–23 (2002)

Horseman, S.T., Harrington, J.F., Sellin, P.: Gas migration in clay barriers. Engineering Geology 54, 139–149 (1999)

Leverett, M.C.: Capillary behaviour in porous solids. Transactions of the AIME (142), 159–172 (1941)

Olivella, S., Alonso, E.E.: Gas flow through clay barriers. Géotechnique 58(3), 157–176 (2008)

Pruess, K., Oldenburg, C., Moridis, G.: TOUGH2 User's Guide, Version 2.0, Lawrence Berkeley National Laboratory, LBNL-43134 (1999)

Romero, E., Simms, P.H.: Microstructure investigation in unsaturated soils: A review with special attention to contribution of mercury intrusion porosimetry and environmental scanning electron microscopy. Geotechnical and Geological Engineering 26(6), 705–727 (2008), doi:10.1007/s10706-008-9204-5

Romero, E., Alonso, E.E., Marshall, P., Arnedo, D., De Gracia, M.: Gas injection laboratory experiments on Opalinus clay. Experimental set-up and preliminary results. In: 2nd International Conference on Fault & Top Seals, From Pore to Basin Scale, Montpellier, France, September 21-24, European Association of Geoscientists & Engineers (2009) Poster presentation

Romero, E., Arnedo, D., Gómez, R., Alonso, E.E., Marschall, P.: Gas injection laboratory experiments on Opalinus clay (preliminary results). Book of abstracts Clays in Natural and Engineered Barriers for Radioactive Waste Confinement. In: 4th International Meeting Andra (France), in cooperation with Nagra (Switzerland), Ondraf/Niras (Belgium) and SKB (Sweden), Nantes, France, March 29-April 1, vol. O/05/4, pp. 113–114 (2010)

Romero, E., Senger, R., Marschall, P.: Air Injection laboratory experiments on Opalinus clay. Experimental techniques, results and analyses. In: Proceedings Shale Workshop EAGE Conferences, Barcelona, Spain, January 23-25, vol. C07, pp. 96–100 (2012)

Senger, R., Romero, E., Ferrari, A., Marschall, P.: Characterization of gas flow through low-permeability claystone. Laboratory experiments and two-phase flow analyses. Extended abstract submitted to Clays in Natural and Engineered Barriers for Radioactive Waste Confinement. In: 4th International Meeting Andra (France), Montpellier, France, October 22-25 (2012)

van Genuchten, M.T.: A closed-form equation for predicting the hydraulic conductivity of unsaturated soils. Soil Science Society of America Journal 44(5), 892–898 (1980)

Webb, P.A., Orr, C.: Analytical methods in fine particle technology. Micromeritics Instrument Corp., Norcross (1997)

Testing in Variably Saturated Conditions

Influence of Hydraulic Hysteresis on the Resilient Behavior of a Natural Compacted Sand

Xuan Nam Ho, Hossein Nowamooz, Cyrille Chazallon, and Bernard Migault

Laboratoire de Génie de la Conception (LGéCo), Insa de Strasbourg,
24 Boulevard de la Victoire, 67084 Strasbourg Cedex, France
hossein.nowamooz@insa-strasbourg.fr

Abstract. This paper presents the influence of the unsaturated state (suction) and especially the different hydraulic behaviour during the wetting and drying cycles (hysteresis phenomenon) on the resilient behavior, of unbound granular materials for roads. First, the Soil Water Retention Curve (SWRC) of a compacted clayey sand will be obtained for both wetting and drying paths. These experimental results were then completed by a series of repeated load triaxial tests at a range of water content between 8% and 11% on both wetting and drying paths. Finally, the experimental results were simulated using the modified Boyce model. Generally, it can be stated that the hydraulic hysteresis phenomenon plays an important role on the mechanical modelling of the resilient behaviour.

1 Introduction

Low traffic pavements with a thin bituminous surfacing, granular base and sub-base layers represent approximately 60% of the road network in France. In these pavements, permanent deformations of the unbound layers and of the soil represent the main causes of distress that lead to rutting of the pavement surface.

Repeated load triaxial tests (RLTT) are commonly used to establish the mechanical characteristics of granular materials and are used to describe either the resilient behavior (Gomes Correia, 1999; Nowamooz et al., 2011) or permanent deformation accumulation (Habibalah and Chazallon, 2005).

The behavior of unbound granular materials in roads is generally studied in the unsaturated state and the influence of water content on the mechanical behaviour is very important. The variation of water content with suction is generally represented by a SWRC in unsaturated soil mechanics. The water content of a soil decreases with suction during drying process, while the water content increases when the suction decreases following a wetting path because of the hysteresis phenomenon in the unsaturated soils.

The purpose of this paper is to study the effect of hydraulic hysteresis in unsaturated soils based on triaxial tests performed with a natural compacted sand.

L. Laloui and A. Ferrari (Eds.): Multiphysical Testing of Soils and Shales, SSGG, pp. 87–92.
springerlink.com

2 Soil Water Retention Curve

The Miscillac sand is a clayey sand, used as subgrade soil in low traffic pavements. It is sensitive to moisture, and it's in situ elastic modulus typically varies between 50 and 100 MPa. It contains 7.5% fines (fraction 0 / 80 microns). The optimum of the normal proctor compaction is w_{opt} = 9% and ρ_d = 2.06 g/cm^3.

In this study, for the wetting path, the samples were prepared at a water content ranging from 8% to 11%. For the drying path, the samples initially saturated at a water content of 12.3%, were dried in the ambient temperature (20°) during different periods to reach the desired water content ranging between 8% to 11%.

To determine the SWRC, two methods were used: the filter paper method (ASTM, 1995) and the tensiometer method (ISO 11275, 2004). Various empirical equations have been suggested to describe the SWRC (Brooks and Corey, 1964; Van Genuchten, 1980; Fredlund and Xing, 1994). The Fig. 1 shows the fitted drying and wetting curves using the Brooks and Corey model.

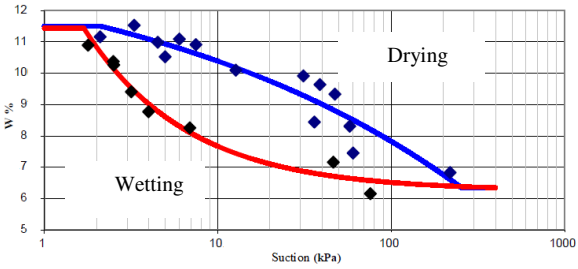

Fig. 1 SWRC for the Miscillac sand fitted by the Brooks and Corey model

3 Repeated Load Triaxial Tests

In this section, 8 triaxial tests were performed on the samples prepared in the wetting and drying paths with a water content between 8% to 11%. The RLTT were conducted with a variable confining pressure, where both the axial load and the confining pressure are cycled. The cylindrical samples compacted with vibrating hammer method (NF P 13286-4) present a diameter of 150 mm and a height of 300 mm. The samples were first subjected to conditioning, which consists of applying 5000 loading cycles at a frequency of 1 Hz, to stabilize the permanent deformations. The cyclic stress path during the conditioning q/p = 3 correspond to (Δp, Δq) = (23.33 kPa, 69.99 kPa) with an initial stress state (p_0, q_0) equals to (10 kPa, 0 kPa), where p is the mean normal stress and q is the deviatoric stress. For a triaxial test, p and q are defined by:

$$p = \frac{\sigma_1 + 2.\sigma_3}{3} \; ; \; q = \sigma_1 - \sigma_3 \tag{1}$$

where σ_1 and σ_3 are the vertical and the radial stress.

At the end of the conditioning phase, the resilient behavior was studied with series of 100 cycles applied on different stress paths ($\Delta q/\Delta p$) and different maximum stress levels (p_{max}, q_{max}) at a frequency of 0.1 Hz. Four stress paths were studied ($\Delta q/\Delta p$ = 0; 1; 2; 3) with two stress levels for each stress path (30 and 60 kPa). For each load phase, the last cycle was used to determine the resilient behavior. The soil resilient behavior is generally presented by the volumetric strain (ε_v) and the deviatoric strain (ε_q) variations with the normal mean stress (p). These deformations can be related to the axial strain (ε_1) and the radial strain (ε_3) :

$$\varepsilon_q = \frac{2(\varepsilon_1 - \varepsilon_3)}{3} \; ; \; \varepsilon_v = \varepsilon_1 + 2\varepsilon_3 \tag{2}$$

Fig. 2, 3 show the evolution ε_v, ε_q with p for the water content of 9% for both wetting and drying paths. The following remarks can be done on these results:

- The loading and unloading cycles present a different resilient behaviour for all the applied stress paths.
- The deviatoric strains are positive for the loading paths in q/p = 1, 2 and 3, negative for the loading path in q/p = 0. On the other hand, the volumetric strains become negative only for q/p = 3. It can be stated that ε_q increases while ε_v decreases with the ratio q/p increases.
- The samples prepared on the wetting path show a higher volumetric strains compared to these prepared on the drying path. The hysteresis phenomenon will slightly influence the deviatoric strains.

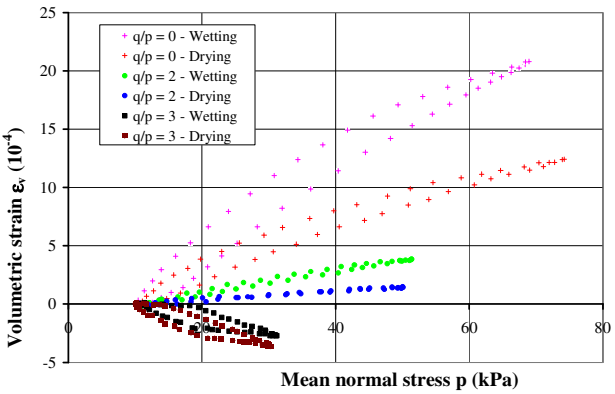

Fig. 2 Evolution of the volumetric strain with the mean normal stress and the stress paths

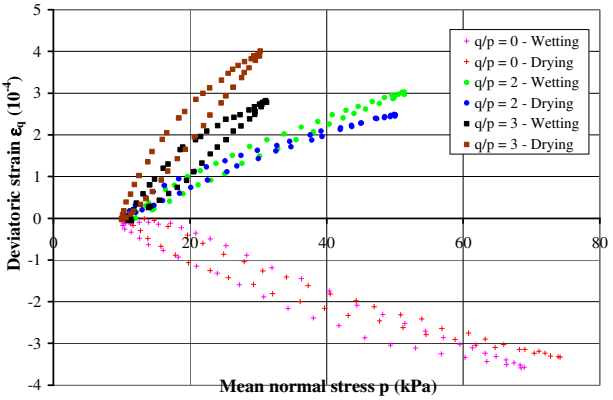

Fig. 3 Evolution of the deviatoric strain with the mean normal stress and the stress paths

4 Modelling

Boyce (1980) presented some basis for the stress-dependent modeling of the resilient response of cyclically loaded unbound granular materials. Hornych (Hornych et al., 1998) modified this model for the nonlinear elastic orthotropic behavior. The volumetric strain and the deviatoric strain can be obtained:

$$\varepsilon_v = \frac{p^{*n}}{p_a^{n-1}}\left[\frac{\gamma+2}{3.K_a}+\frac{n-1}{18.G_a}.(\gamma+2).\left(\frac{q^*}{p^*}\right)^2+\frac{\gamma-1}{3.K_a}\frac{q^*}{p^*}\right] \tag{3}$$

$$\varepsilon_q = \frac{2}{3}.\frac{p^{*n}}{p_a^{n-1}}\left[\frac{\gamma-1}{3.K_a}+\frac{n-1}{18.G_a}.(\gamma-1).\left(\frac{q^*}{p^*}\right)^2+\frac{2.\gamma+1}{6.K_a}\frac{q^*}{p^*}\right] \tag{4}$$

where p_a is the atmospheric pressure (p_a = 100 kPa) ; p* and q* are the mean stress and the deviatoric stress:

$$p^* = \frac{\gamma.\sigma_1+2.\sigma_3}{3} \;;\; q^* = \gamma.\sigma_1-\sigma_3 \tag{5}$$

K_a, G_a, n, γ are the model parameters. These model parameters were fitted by the least square method based on the following equation:

$$S_{\min} = \frac{\sum\left(\varepsilon_v - f\left(p^*,q\right)\right)^2}{\sum\left(\varepsilon_v - m_v\right)^2}+\frac{\sum\left(\varepsilon_q - g\left(p^*,q\right)\right)^2}{\sum\left(\varepsilon_q - m_q\right)^2} \tag{6}$$

where f(p*, q), g(p*, q) are the equations (3) and (4); m_v, m_q are the average values of the experimental volumetric and deviatoric elastic strains. The correlation coefficient is expressed by:

$$C_{correl} = 1-\sqrt{\frac{S_{\min}}{2}} \tag{7}$$

The experimental results were simulated by the modified Boyce model. The variation of the K_a, G_a, n and γ parameters with the water content for both wetting and drying paths are presented in Table 1 as well as Fig. 4.

Table 1 The Boyce model parameter

w, %	Δq/Δp	Wetting path				C_{correl}	Drying path				C_{correl}
		K_a	G_a	n	γ		K_a	G_a	n	γ	
8	0, 1, 2, 3	29.84	33.73	0.65	0.61	0.430	36.47	32.11	0.45	0.41	0.782
9	0, 1, 2, 3	25.04	34.76	0.85	0.63	0.700	27.96	35.49	0.44	0.46	0.702
10	0, 1, 2, 3	31.06	31.28	0.74	0.77	0.422	43.95	21.37	0.88	0.56	0.657
11	0, 1, 2, 3	34.04	20.76	0.79	0.48	0.528	24.12	13.45	0.79	0.51	0.425
Average values		**29.99**	**31.89**	**0.76**	**0.65**		**33.05**	**25.61**	**0.64**	**0.49**	

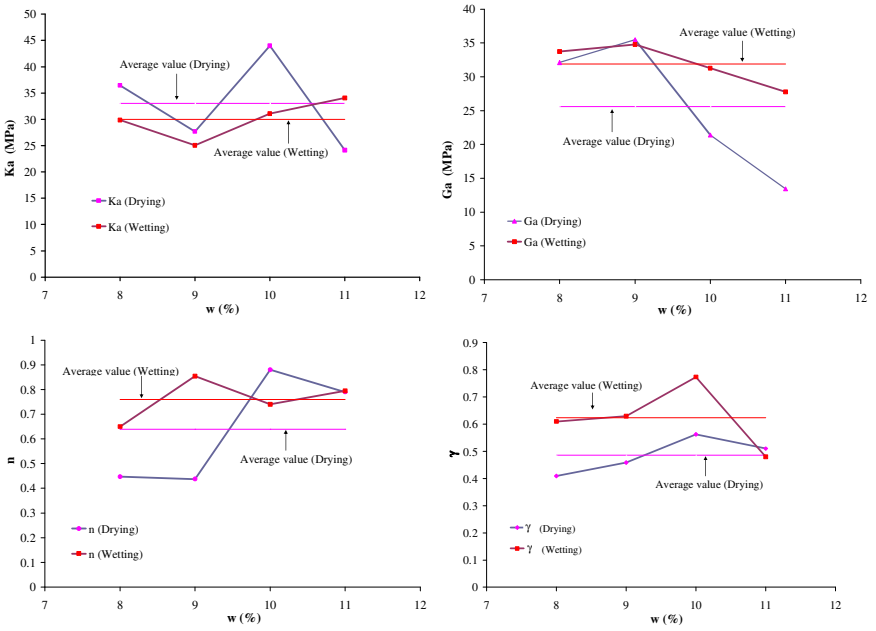

Fig. 4 Evolution of the parameters K_a, G_a, n and γ with the water content

The following remarks can be made on these results:

- On the drying path, the parameters K_a, G_a, n rise and fall considerably with the water content increase, while for this model on the wetting path, the water content has less influence on the parameters and less deviation from the average value.
- The average values of parameters G_a, n and γ are higher for the wetting path. On the other hand, the K_a average value is higher for the drying path.

5 Conclusion

This paper investigates the influence of hydraulic hysteresis on the cyclic resilient behavior of Missillac sand. The RLTT results confirm that the hydraulic hysteresis play an important role on the stress-strain characteristic, and the samples prepared on the wetting path show a higher volumetric strains comparing to these prepared on the drying path and the hysteresis phenomenon will slightly influence the deviatoric strains. The experimental results were simulated by the modified Boyce model. It can be stated that the hysteresis phenomenon influences all the model parameters (K_a, G_a, n and γ).

Acknowledgements. This work was funded by the European Commission Initiative INTERREG IV A,Upper Rhin Programme (Project B20, TEM3).

References

ASTM D 52980-094, Standard test method for measurement of soil potential (suction) using filter paper 4(09), 154 –159 (1995)

Boyce, J.R.: A nonlinear model for the elastic behaviour of granular materials under repeated loading. In: International Symposium on Soils Under Cyclic and Transient Loading, Swansea, pp. 285–294 (1980)

Brooks, R.H., Corey, A.T.: Hydraulic properties of Porous Medium. Hydrology paper No.3. Civ. Eng. Dep., Colorado State Univ., Fort Colins, Colo (1964)

Fredlund, D.G., Xing, A.: Equations for the Soil-Water Characteristic Curve. Canadian Geotechnical Journal 31, 521–532 (1994)

Gomes Correia, A.: Unbound Granular Materials – Laboratory testing. In-situ testing and modelling. A.A. Balkema, Rotterdam (1999)

Habibalah, T., Chazallon, C.: An elastoplastic model based on the shakedown concept for flexible pavements unbound granular materials. International Journal for Numerical and Analytical Methods in Geomechanics 29, 577–596 (2005)

Hornych, P., Kazai, A., Piau, J.M.: Study of the resilient behaviour of unbound 529 granular material. In: Proceedings 5th Conference on Bearing Capacity of 530 Roads and Airfields, Trondheim, vol. 3, pp. 1277–1287 (1998)

ISO 11275, Soil quality - Determination of unsaturated hydraulic conductivity and water - retention characteristic – Wind's evaporation method (2004)

NF P 13286-4 , Unbound and hydraulically bound mixtures- Part 4: Test methods for laboratory reference density and water content – Vibrating hammer, p. 23 (2003)

Nowamooz, H., Chazallon, C., Arsenie, M.I., Hornych, P., Masrouri, F.: Unsaturated resilient behavior of a natural compacted sand. Journal of Computers and Geotechnics 38(4), 491–503 (2011)

Van Genuchten, M.T.H.: A closed-form equation for predicting the hydraulic conductivity of unsaturated soils. Soil Science Society American Journal 44, 892–898 (1980)

Monotonic Simple Shear Response of Fine Grained Silts under Different Saturation Condition

F. Daliri[1] and D.H. Basu[2]

[1] Department of Civil and Environmental Engineering, Carleton University, Ottawa, Canada
fdaliri@connect.carleton.ca
[2] Department of Civil and Environmental Engineering, University of British Columbia, Vancouver, Canada

Abstract. Simple shear test is a specialized laboratory test to determine shear strength parameters of soils. Most of simple shear devices do not have capacity to measure pore water. Alternatively, constant volume test has been employed to simulate the truly undrained condition. Due to the fact that identical response of saturated constant volume test and undrained test was previously proved, there is a belief among geotechnical engineers indicating that the response of constant volume dry test is identical to undrained response. The applicability of constant volume test for partial saturated fine grained materials is of significant importance. This paper aims to investigate the similarity of the response of constant volume dry or partial saturated tests to the response of constant volume saturated test and therefore undrained simple shear tests. It was found that the responses of constant volume dry and partial saturated specimen at same void ratio are identical to the response of saturated constant volume test.

1 Introduction

Laboratory shear tests are generally used in many soil investigations to determine the shear strength parameters of a soil. The purpose of laboratory shear testing is to simulate the in-situ field condition in an element test. Triaxial tests (compression and extension), direct simple shear test and hollow cylinder tests can be used in laboratory shear tests to simulate different field conditions. Although triaxial and hollow cylinder tests represent the stress-strain relationships more distinctively, direct shear tests (DST) are widely employed because of its simplicity and quickness. Bjerrum and Landva (1966) introduced an initial procedure for direct simple shear test. In simple shear device, the specimen is initially consolidated under one-dimensional vertical load followed by a horizontal shear loading (Dyvik et al., 1987). Direct simple shear tests are typically performed to determine the soil strength parameters of a potential failure surface which are more or less horizontal (Dyvik et al., 1987; Prevost and Høeg 1970).

L. Laloui and A. Ferrari (Eds.): Multiphysical Testing of Soils and Shales, SSGG, pp. 93–98.
springerlink.com

Several researchers have used simple shear devices over the years: Peacock & Seed (1968), Casagrande (1976), Ansell & Brown (1978) and Sidey et al. (1978), and these generally fall within two types: i) Norwegian Geotechnical Institute (NGI) and ii) Cambridge university simple shear devices (Bjerrum & Landva, 1966; Prevost & Høeg 1970; Dyvik et al., 1987).

However, in both types, samples experience a displacement boundary condition such that the lateral displacement is assumed to be zero ($\varepsilon_x = 0$). In this case, when an angular shear distortion is applied under constant volume, the side of the sample stretches (Prevost and Høeg 1970).

In order to achieve truly undrained condition, the shear device should measure back pressure and pore water pressure. Several of the direct simple shear devices are not able to measure pore water pressure. Thus, due to difficulties in prevention of drainage in the simple shear devices, constant volume test was alternatively proposed to simulate the truly undrained condition, which is more convenient than real undrained test with pore water pressure measurement (Bjerrum & Landva, 1966). Since the simple shear device does not allow lateral deformation ($\varepsilon_x = 0$), only height should be kept constant to achieve constant volume condition. The constant height condition can be applied by clamping the top and bottom loading caps against vertical movement. In a constant volume test, it is assumed that the decrease (or increase) of vertical stress in a constant volume simple shear test is essentially identical to the increase (or decrease) of excess pore water pressure that would have measured in an undrained simple shear test conducted on the saturated specimen (Bjerrum & Landva, 1966; Finn et al. 1978; Dyvik et al. 1987). Dyvik et al. (1987) designed a chamber for NGI simple shear device that enables performing a truly undrained test with pore water pressure measurement. They performed four parallel undrained and constant volume simple shear tests on consolidated Drammen clay to verify the validity of the assumption. Comparing the responses of undrained and constant volume tests, Dyvik et al. (1987) reached the following conclusion: "The assumption that the change in applied vertical stress is equal to the pore pressure which would have developed in an undrained test is valid. This conclusion applies to saturated soils". Likewise, this assumption had been previously verified in triaxial test by Berre (1983) and summarized by Vucetic & Lacasse (1983).

As discussed in the previous paragraph, the assumption of identical response of undrained test and constant volume test was verified for saturated soil. However, there is a belief among geotechnical engineers indicating that identical response of undrained test and saturated constant volume tests can be gained even in dry constant volume test (Daliri et al., 2011). In other words, the response of constant volume dry test is identical to the response of undrained test at same fabric, loading condition and relative density. Thus, if the equality of the response of constant volume dry test and constant volume saturated test under same condition is verified, it can be essentially developed to equality of the response of constant volume dry test and undrained test. While the monotonic and cyclic response of saturated sands and clays have been the topic of extensive research during the past

50 years, the behaviour of silty materials especially in unsaturated condition have been considered only from 1990s. The strength parameters of fine grained soils are typically used in design of mine tailings facilities, landfills, surface foundations, etc.

This paper aims to i) verify the similarity of the response of constant volume dry test and constant volume saturated test and ii) investigate the effect of degree of saturation on the response of constant volume tests in silty materials.

2 Material

The material used in this study was silt-sized spherical glass micro-beads. The particle size distribution, as determined by the hydrometer method (ASTM D422) and soil water characteristics curve (SWCC) are presented in Figure 1. The specific gravity of the material is 2.48. Liquid Limit (LL) and Plastic Limit (PL) were obtained 19 % and 13% respectively. The color of material is white. Saturated hydraulic conductivity of this material was obtained 1.7×10^{-6} m/s.

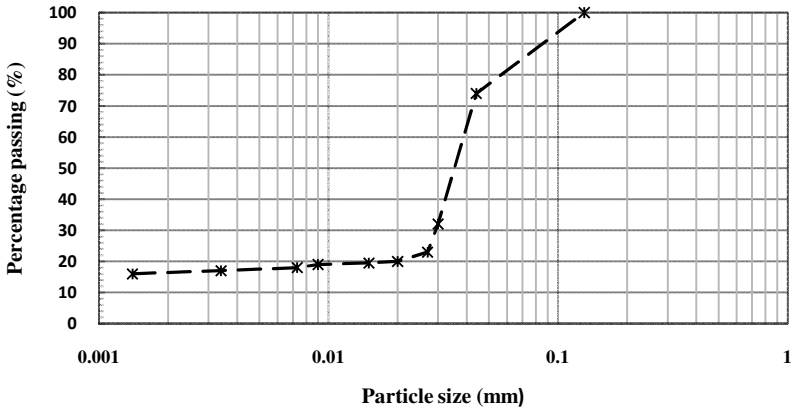

Fig. 1 Grain Size Distribution of the material

3 Test Equipment and Methodology

The apparatus employed in this study was a NGI type simple device. In the apparatus, the sample is surrounded and fixed by a steel wire reinforced rubber membrane in order to minimize the lateral deformation. The constant volume condition is obtained during shear loading by keeping the height of the sample constant using a clamping mechanism.

In order to investigate the influence of degree of saturation on the response of constant volume tests, samples with different degrees of saturation (from saturated $S_r = 1$ to dry $S_r = 0$) should be prepared under similar conditions i.e. density, fabric and consolidation pressures. The air pluviation method was selected for dry samples. To compare the partial saturated and saturated responses with dry sample responses, a method of saturation was adopted in this study. According to this method, the sample that was supposed to be partially or fully saturated was prepared initially as a dry sample with the same void ratio of the dry sample using air pluviation method. The prepared sample was placed under simple shear device and slowly saturated using a reservoir of water. The water in the reservoir was adjusted to be one or two centimeter higher (depending on the grain size of the sample) than the top of the sample in the simple shear device. This adjustment resulted in hydraulic gradient equal to 0.4 ~ 0.8. Thus, a very slow flow is circulated from the bottom to the top of the sample. The reason for applying upward direction of the flow was that the water was moved in opposite of gravity; Therefore, the height (void ratio) and fabric of the specimen were not affected by the flow of water through the specimen. The height of the sample was monitored during the test and the maximum height change was obtained 0.014 mm, which could not make a tangible change in void ratio. Water went out from the top of the sample was collected in a container and once the collected water was around 400 mL, the sample was assumed to be reasonably saturated and the drainage valve was closed and the height was fixed to be ready for a constant volume test. For partial saturated samples, the dry sample was saturated to reach appropriate water content (degree of saturation). As a result, responses of constant volume tests with same fabric, density and consolidation pressure but different degrees of saturation are comparable in this method.

4 Results

Silty materials were air pluiviated, partially saturated using the water reservoir and consolidated to 50 kPa effective consolidation pressure. It was attempted to investigate the effect of increasing degree of saturation (from $S_r = 0\%$ to $S_r = 73\%$) on monotonic response of constant volume tests under constant void ratios (i.e. 0.66, 0.7, 0.78). Some complementary tests were also prepared in other void ratios (e.g. 0.65, 0.67, 0.74) in order to accurately calculate the phase transformation and failure lines. Figure 2 presents the monotonic response of specimens at same water contents (W= 10%; S_r= 30-37%) but different void ratios (densities) consolidated to the same stress level. It is clear that with decreasing void ratio (increasing density) from $e_c = 0.78$ to $e_c = 0.66$, the dilative response increases significantly.

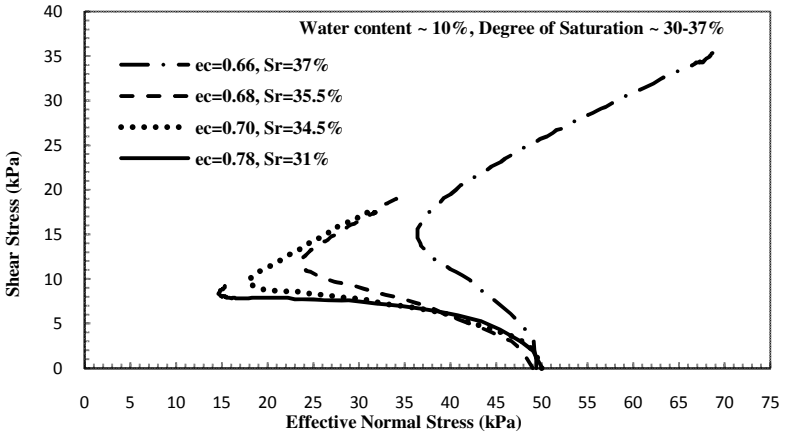

Fig. 2 Monotonic response of constant volume test at 10% water content but different void ratios

Same tests were also performed for W= 20%, 14% and dry tests. Figure 3 presents the comparison of monotonic response of constant volume tests at same void ratio (e_c = 0.78) but different degrees of saturation. It is clear that all samples exhibit limited liquefaction response with a mild peak at this void ratio. It is also presented that with increasing degree of saturation from S_r = 0% to S_r = 73% there is no tangible change in the response. Therefore, the degree of saturation is ineffective to the response of constant volume tests at e_c = 0.78. Consequently, the response of dried constant volume test, partial saturated and saturated test at same void ratio would be identical for the silty material. It should be noted that even though matric suction is produced in this silty material at Sr < 1, the effect of suction is negligible and not influential since the matric suction values are not high based on SWCC of the material.

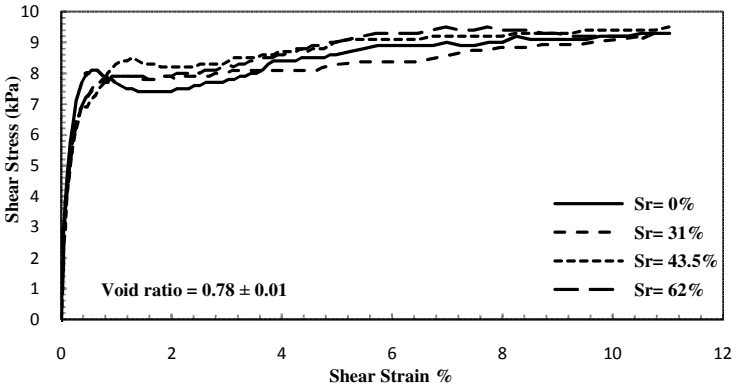

Fig. 3 Monotonic response of constant volume test at 10% water content but different void ratio

5 Conclusion

Constant volume simple shear tests were performed on a silty material at different degrees of saturation in order to investigate: i) whether the responses of constant volume dry or partial saturated tests are identical to the response of constant volume saturated test and therefore undrained simple shear test, ii) the effect of degree of saturation on monotonic response of constant volume tests. Based on the results of performed experiments, the followings can be concluded:

- The monotonic response of dry constant volume simple shear test at same relative density and fabric is identical to the response of saturated constant volume test and therefore undrained test for silty materials.
- Under constant density (void ratio) condition, degree of saturation does not affect the response of constant volume tests performed on fine grained soils that generate low values of suction during desiccation.

References

Ansell, P., Brown, S.F.: A cyclic simple shear apparatus for dry granular materials. Geotechnical Testing Journal, ASTM 1(2), 82–92 (1978)

Berre, T.: Triaxial testing at the Norwegian Geotechnical Institute. Geotechnical Testing Journal, ASTM 5(1-2), 3–17 (1982)

Bjerrum, L., Landva, A.: Direct simple-shear tests on a Norwegian quick clay. Geotechnique 16(1), 1–20 (1966)

Casagrande, A.: Liquefaction and cyclic deformation of sands. A critical review. Harvard Soil Mechanics. Serial No. 88 (1976)

Daliri, F., Simms, P., Sivathayalan, S.: A comparison of different laboratory techniques to simulate stress and moisture history of hard rock mine tailings. In: Proceedings of Tailings and Mine Waste 2011 Conference, Vancouver, B.C., Canada, pp. 165–173 (2011)

Dyvik, R., Berre, T., Lacasse, S., Raadim, B.: Comparison of truly undrained and constant volume direct simple shear tests. Geotechnique 37(1), 3–10 (1987)

Finn, W.D.L., Vaid, Y.P., Bhatia, S.K.: Constant volume simple shear testing. In: Proc. 2nd International Conference on Microzonation for Safer Construction Research and Application, San Francisco, CA, pp. 839–851 (1978)

Prevost, J.H., HØeg, K.: Effective stress-strain- strength model for soils. Journal of Geotechnical Engineering Div., ASCE. 101(GT3), 259–278 (1975)

Peacock, W.H., Seed, H.B.: Sand liquefaction under cyclic loading simple shear conditions. Journal of Soil Mechanics and Foundations Div. American Society of Civil Engineers 94, SM3, 689–708 (1968)

Sidey, R., Strom, J.A., Pyke, R.M.: Discussion on Measurement of dynamic soil properties. In: Proceeding of Conference of Earthquake Engineering and Soil Dynamic, Pasadena III, pp. 1478–1481 (1978)

Vucetic, M., Lacasse, S.: Specimen size effect in simple shear test: closure. Journal of Geotechnical Engineering Division, American Society of Civil Engineers 110 (GT4), 447–453 (1983)

Effect of Loading and Suction History on Time Dependent Deformation of Crushed Granular Aggregates

Enrique Romero, Clara Alvarado, and Eduardo E. Alonso

Universitat Politècnica de Catalunya, Barcelona, Spain
{Enrique.romero-morales,eduardo.alonso}@upc.edu

Abstract. The paper presents the results of an experimental investigation aimed at evaluating the time-dependent compressibility of a coarse crushed quartzitic slate, focusing on the effects of the previous loading and hydraulic history. Long-term and large diameter compression tests under oedometer conditions were performed at different relative humidity (total suctions) and vertical stresses but following different loading and hydraulic paths. A finding is that pre-compressing at increasing overconsolidation ratios or pre-soaking the crushed material at constant and elevated stresses leads to the progressive vanishing of long-term deformations.

1 Introduction

Rockfill mechanical behaviour is very sensitive to the action of water, which is of particular concern during the design and performance stage of rockfill and zoned dams. These structures also exhibit long term deformations, which tend to depend linearly on the logarithm of time as indicated by field records (see for instance; Oldecop & Alonso 2007). Breakage of rock particles and crack propagation are the main underlying physical mechanisms that explain these phenomena, which depend on the strength of individual particles, the grain size distribution and shape of particles, the stress level and the relative humidity prevailing at the rockfill voids–or alternatively the activity of the liquid filling these voids–(Oldecop & Alonso 2001, Romero *et al*. 2005).

The paper specifically explores the time-dependent compressibility, focusing on the effects of the previous hydraulic and loading history–as considered, for instance, by the overconsolidation ratio OCR–on rockfill delayed deformations. A crushed quartzitic slate was tested at constant relative humidity–or total suction–and at different OCR values in special large diameter oedometer cells. The dependency of creep deformation on OCR is by no means an academic issue. In fact, it has practical application, since the long term settlements could be controlled by pre-conditioning techniques (pre-compression or pre-soaking technique at constant and elevated stresses).

L. Laloui and A. Ferrari (Eds.): Multiphysical Testing of Soils and Shales, SSGG, pp. 99–104.
springerlink.com

2 Material Used in the Research

Crushed quartzitic Cambric slate from the Pancrudo River outcrop (Aragón, Spain) and used to build the zoned earth and rockfill Lechago Dam was tested. The behaviour of this material has been studied by several authors (see for instance; Oldecop & Alonso 2001, Chávez & Alonso 2003, Chávez *et al*. 2009). Some properties of the rock material are summarised in Table 1. The material obtained in the quarry was further crushed and sieved. The maximum particle size was fixed at 40 mm (before compaction: 10% passing 10-mm sieve and coefficient of uniformity 2.9). The water retention curve of the material along a drying path is shown in Figure 1.

Table 1 Properties of the quartzitic slate

Property	Value
Uniaxial compression strength*	14.2-31.9 MPa
Density of solids*	2.75 Mg/m^3
Water absorption*	1.36%
Porosity*	6.3-11.8%
Slake durability (5th cycle) (ASTM D4644)**	96.5%
Flakiness index	19%

* Oldecop & Alonso 2001, Chávez & Alonso 2003; ** Standard test method for slake durability of shales and similar weak rocks

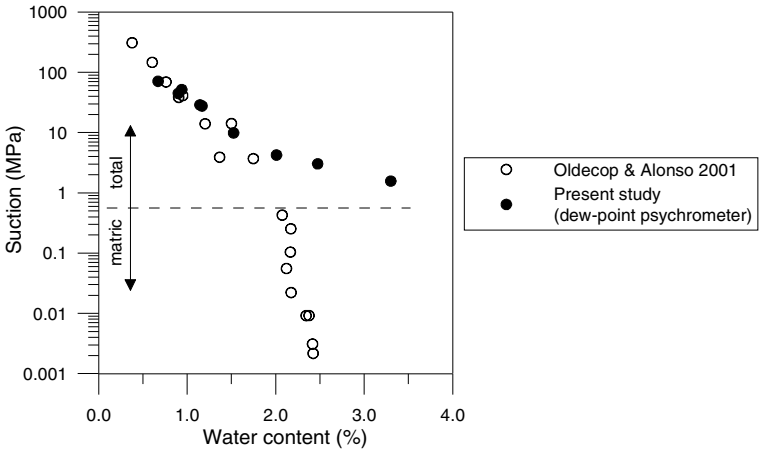

Fig. 1 Retention curve along a drying path for crushed quartzitic slate.

3 Experimental Program

An oedometer test program was carried out in a large diameter cell (300 mm in diameter and approx. 200 mm high). The crushed slate was statically compacted in four layers inside the oedometer ring at a void ratio e_0=0.55±0.03 and water con-tent around w=1% in equilibrium with the relative humidity prevailing at laboratory conditions (approx. 30%). Pre-compression tests involved loading-unloading at saturated state and at constant relative humidity of the air (75% and 30%) to induce different overconsolidation ratios, as described in Table 2. Pre-soaking tests were associated with soaking and drying paths at a constant vertical stress of 1 MPa. During soaking, compression (collapse) strains developed due to important particle breakage at the stress level tested. On subsequent drying to the target total suction–varying between 160 MPa and 39 MPa and controlled by vapour transfer–, the material was at an overconsolidated state that was hydraulically induced.

Table 2 Description of the pre-compression test program performed

Ref.	Wetting stage	Total suction	Stress applied in long term tests
1	Water at 0.05MPa	0	NC: 0.1; 0.5 and 1 MPa*
			OC: 1.0; 0.87; 0.67 and 0.25 MPa**
2	Vapour	39 MPa	NC: 0.1; 0.5 and 1 MPa*
			OC: 1.0; 0.87; 0.67 and 0.25 MPa**
3	Vapour	160 MPa	NC: 0.1; 0.5 and 1 MPa*
			OC: 1.0; 0.87; 0.67 and 0.25 MPa**

*Normally consolidates state. **Overconsolidated states with OCR between 1 and 4.

4 Experimental Results

The evolution of the vertical strain along a loading-unloading path under saturated conditions (ref. 1 in Table 2) is shown in Figure 2 (on the left). A step loading approach was followed with maximum load duration of 72 hours for overconsolidated states (unloading stages after pre-compression) and 24 hours for normally consolidated conditions (loading stages). The time evolution of the volume change response under saturated and normally consolidated conditions is presented in the same Figure 2 on the right, in which a larger time-dependent compressibility is observed at higher vertical stresses (the different loading steps are indicated in the figure).

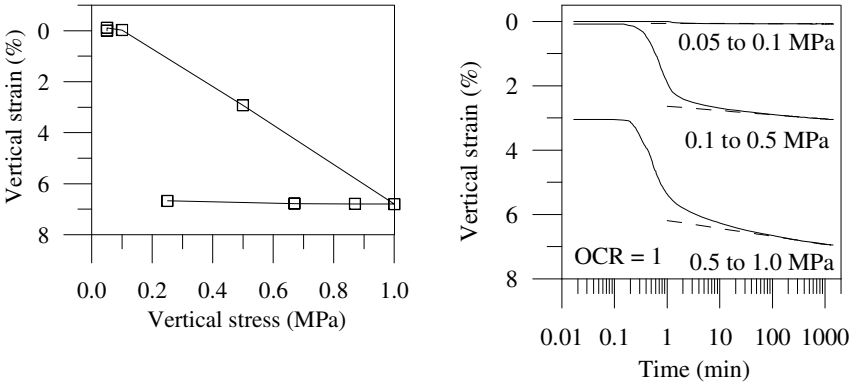

Fig. 2 Volume change results under saturated conditions along a loading-unloading path (on the left). Time evolution of vertical strain in normally consolidated and saturated samples (on the right).

The slope of the vertical strain (ε_v) – log time curves previously presented provides information for the determination of the secondary (time-dependent) compressibility index according to the following equation, which was calculated for elapsed times since load application larger than the reference t_r=100 min

$$C_\alpha = \frac{\Delta\varepsilon_v(1+e_o)}{\Delta \log t} = -\frac{\Delta e}{\Delta \log t} \tag{1}$$

The time dependent compressibility index under normally consolidated conditions $C_{\alpha NC}$ and at different total suctions (refer to Table 2) are plotted in Figure 3 (on the left) as a function of the vertical stress σ_v applied, in which the dependency on total suction is readily observed. An equivalent behavioural response was presented by Oldecop & Alonso (2007), in which samples in dry environments displayed nearly null index, consistent with the low crack propagation velocity obtained from the stress corrosion curves at low relative humidity values and with the conceptual model proposed by Oldecop & Alonso (2001). In addition, the compressibility indexes tend to level off at high vertical stresses (usually between 1 and 2 MPa, as shown by Oldecop & Alonso 2007). To limit maximum levelling out, the following empirical expression was used to fit experimental data (Fig. 3, on the left) with parameter a, which as a first approximation can depend on total suction

$$C_{\alpha NC} = a\,\sigma_v \Big/ \left(1\,\text{MPa} + \sigma_v\right) \tag{2}$$

On regarding the time dependent compressibility index under overconsolidated states obtained during the unloading stages and after pre-compression, Figure 3 (on the right) presents its evolution with OCR. An important reduction in the secondary compressibility was detected at OCR>1, which follows a behavioural

response similar to soils (see for instance, Alonso *et al.* 2000). The variation of C_α / $C_{\alpha NC}$ for different OCR values was described by the following empirical equation, where α and β are constant parameters that allow reproducing the measured data (α=0 and β=15 are used to plot the curves in Fig. 3, on the right)

$$C_\alpha / C_{\alpha NC} = (1-\alpha)\,\mathrm{e}^{-\beta(OCR-1)} + \alpha \tag{3}$$

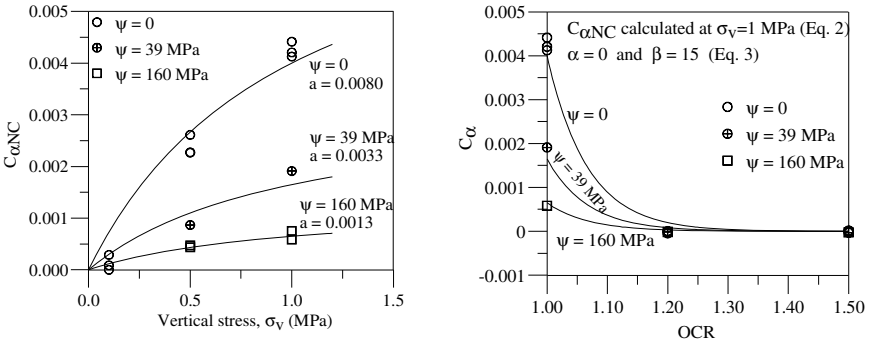

Fig. 3 Time-dependent compressibility index of normally consolidated samples against vertical stress for different constant total suctions (on the left). Time-dependent compressibility index against OCR for different constant total suctions (on the right).

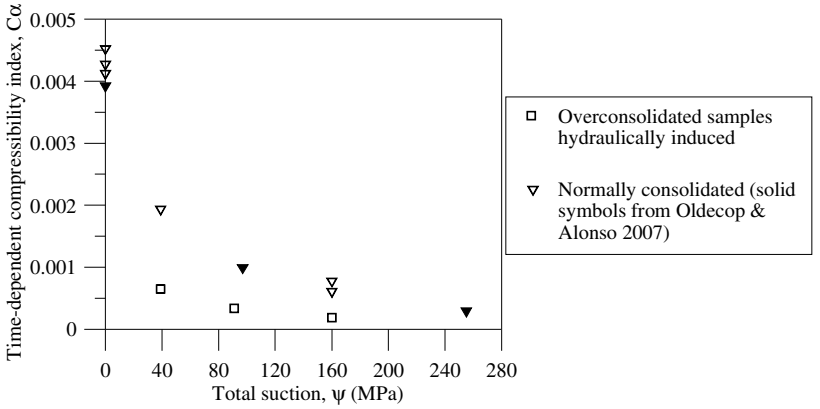

Fig. 4 Time-dependent compressibility index against total suction at a constant vertical stress of 1 MPa. Normally consolidated samples and overconsolidated samples after undergoing the soaking-drying paths at 1 MPa.

The time dependent compressibility index at constant vertical stress 1 MPa and at different total suctions under normally consolidated states and after undergoing the soaking and drying paths –that induced overconsolidated states–, is plotted in Figure 4. Again, some reduction in the time dependent compressibility index is detected in the overconsolidated samples (samples previously subjected to

soaking-drying), which presents a consistent and equivalent behavioural response to the pre-compression tests.

5 Conclusions

A crushed quartzitic slate, used in previous investigations on rockfill behaviour, was tested to study the effects of the previous loading and the hydraulic history on material delayed deformations. Typical tests involved loading-unloading samples at constant relative humidity–or total suction–and at different OCRs, as well as soaking-drying paths at constant and elevated stress, which were performed in special large diameter oedometer cells (300 mm in diameter). A finding is that pre-loading the crushed slate at increasing OCRs leads to the progressive vanishing of creep deformations, following a behavioural response similar to soils. An equivalent response was observed at overconsolidated states after the soaking-drying paths. The reduction has practical applications, since the long term settlements of rockfill materials could be controlled by pre-compression and pre-soaking technique at elevated stress. If at each point of the rockfill embankment an OCR=1.1 is ensured by pre-loading, a reduction to 22% of the normally consolidated long-term settlement would be expected.

Acknowledgements. The financial support given by the Universidad de Carabobo (Venezuela) to the second author is greatly acknowledged.

References

Alonso, E.E., Gens, A., Lloret, A.: Precompression design for secondary settlement reduction. Géotechnique 50(6), 645–656 (2000)

Chávez, C., Alonso, E.E.: A constitutive model for crushed granular aggregates which includes suction effects. Soils and Foundations 43(4), 215–227 (2003)

Chávez, C., Romero, E., Alonso, E.E.: A rockfill triaxial cell with suction control. Geotech. Testing J. 32(3), 219–231 (2009)

Oldecop, L.A., Alonso, E.E.: A model for rockfill compressibility. Géotechnique 51(2), 127–139 (2001)

Oldecop, L.A., Alonso, E.E.: Theoretical investigation of the time-dependent behaviour of rockfill. Géotechnique 57(3), 289–301 (2007)

Romero, E., Alonso, E.E., Hueso, O.: Effect of water composition on rockfill compressibility. In: Proc. 16th Int. Conf. on Soil Mechanics and Geotechnical Engineering, Osaka, September 12-16, vol. 3, pp. 1913–1916. Millpress, Rotterdam (2005)

Ultrasonic Testing of Unsaturated Soils

Z.Y. Cheng and E.C. Leong

School of Civil and Environmental Engineering,
Nanyang Technological University, Singapore
CHEN0474@e.ntu.edu.sg, cecleong@ntu.edu.sg

Abstract. Proliferation of ultrasonic testing equipment has made measurements of compression and shear wave velocities in the laboratory more accessible. However, these equipment may have different operating frequency range, type and arrangement of piezoelectric crystals, and coupling of the piezoelectric crystals to the platens. This paper investigates the effect of frequency on wave velocity of unsaturated soil with various degrees of saturation. While the trend relating wave velocity to specimen's degree of saturation is well known, the effect of frequency still remains largely unclear despite various analytical derivations. Even though various experiments conducted using ultrasonic platens have shown velocity to increase with frequency, experiments conducted in this study showed otherwise. Fast Fourier Transform (FFT) of the receiver's signal for compression wave showed that frequency of the receiver's signal does not vary with the frequency of the signal supplied to the transmitter.

1 Introduction

Compression (P) and shear (S) waves have long been used in geotechnical engineering to determine essential soil properties such as small-strain Young's modulus (E_{max}) and shear modulus (G_{max}). However, P and S wave velocities (V_p and V_s) from in-situ seismic surveys are not comparable with those obtained from laboratory ultrasonic tests due to difference in excitation frequency. Winkler et al. (1995) and Mavko et al. (1994) found V_p to be frequency dependent. Emerson et al. (2006) suggested that V_p can be scaled from its low to high frequency value using Equation (1) by Biot and Equation (2) by Geertsma et al. (1961).

$$\frac{V_{p\infty}}{V_{p0}} = \sqrt{\frac{[n\omega + n^2(\beta-2) - n^3(\beta-1)][\beta(1-n)+n]}{\omega\beta n(1-n) + n^2(\omega-1)}} \tag{1}$$

$$V_p^2 = \frac{V_{p\infty}^4 + V_{p0}^4 (f_c/f)^2}{V_{p\infty}^2 + V_{p0}^2 (f_c/f)^2} \tag{2}$$

where $V_{P\infty}$ and V_{P0} are V_p at high and low frequencies, respectively, ω is the tortuosity, β is the ratio of density of solids and density of fluid, i.e., ρ_s/ρ_f, n is the porosity, f is frequency and f_c is the characteristic frequency. Despite numerous theoretical derivations, little experimental work has been done to investigate

L. Laloui and A. Ferrari (Eds.): Multiphysical Testing of Soils and Shales, SSGG, pp. 105–110.
springerlink.com

the variation of wave velocities with frequency. In this paper, experiments were conducted using a pair of ultrasonic platens to observe the effect of varying excitation frequency on V_p and V_s for unsaturated sand.

2 Experimental Setup and Test Procedures

2.1 Soil Properties

The soil tested is Changi reclamation sand which consists mainly of uniform medium grains with minute amount of sea shells. Prior to the experiment, the sand is sieved through sieve No. 8 (2.36 mm) to remove large sea shells. The basic soil properties are tabulated in Table 1. Grain size distribution of the sand is shown in Fig. 1.

Table 1 Basic Properties of Changi Reclamation Sand

Soil Classification (ASTM D-2487)	SP
G_s	2.66
$_{d.min}$ (g/cm^3)	1.444
$_{d.max}$ (g/cm^3)	1.728
e_{max}	0.842
e_{min}	0.539

2.2 Wave Measurement Using Ultrasonic Platens

The experimental setup is shown in Fig. 2. The top and bottom platens were GCTS ultrasonic platens. Details of the platens can be found in Leong et al. (2004). However instead of using the GCTS standard set-up, the piezoelectric crystals in the transmitter platen were excited using a function generator and amplifier. The signal at the receiver platen was recorded using a digital oscilloscope. A porous disk and a 1 bar high-air entry ceramic disk were fixed on the top and bottom platens, respectively. The sand was first compacted moist to a relative density of 70% in a metal split mould. The specimen was then transferred to the triaxial cell. A rubber membrane was placed over the specimen. The top platen was then placed on top of the specimen and secured with O-rings. Saturation was performed at an effective confining pressure of 10 kPa by applying a confining pressure of 210 kPa and back pressure of 200 kPa using a GDS digital pressure volume controller (DPVC). A small suction was applied at the pressure line which was connected to the top platen. During saturation, V_p was recorded. Saturation continued until the following conditions were met (1) V_p remains constant; (2) No air bubbles were observed in the air pressure line; (3) Increase in water level in the flushing pot; and (4) Skempton's pore pressure parameter, $B > 0.95$.

Upon saturation, the top platen's pressure line was connected to an air pressure system at 250 kPa. The specimen was then consolidated at a net normal stress (σ-u_a) of 10 kPa and the amount of water that drained out was monitored using the DPVC. Matric suction was applied by reducing the pore-water pressure (u_w) while maintaining the pore-air pressure (u_a) at 250 kPa. Values of V_p and V_s were measured at equilibrium matric suctions of 0, 0.5, 1.0, 1.5, 2.0, 3.0 and 5.0 kPa. At each matric suction, V_p and V_s were obtained by exciting the ultrasonic platen at frequencies of 10, 20, 50, 100 and 200 kHz. Upon completion, the whole specimen was dried in the oven for water content determination. The water contents at various matric suctions were back-calculated from the final water content and the soil-water characteristic curve (SWCC) of the sand is shown in Fig 3.

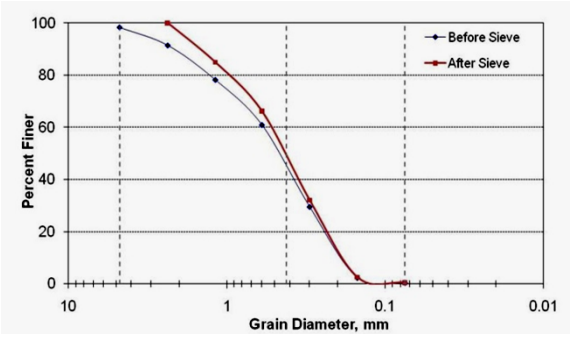

Fig. 1 Grain size distribution of Changi reclamation sand

3 Results and Discussions

Values of V_p and V_s obtained from the experiments are plotted with degree of saturation and frequency in Figs. 4 and 5, respectively. The value of V_p shows a linear decrease with increase in degree of saturation until about 88% and then a sharp increase as degree of saturation approaches 100%. The value of V_s increases slightly as degree of saturation increases and remains constant after degree of saturation of about 40%. The value of V_s does not vary significantly with changes in frequency except the discrepancy for one data point (Fig. 5b). In contrast, V_p shows a dependency on the excitation frequency but the trend is different at high degree of saturation (See S_r=88.53%. in Fig. 4b). The increase in V_p in the frequency zone shaded in Figure 4b is most likely attributed to the air phase not being continuous at S_r=88.53%. This phenomenon will be investigated in the future. At the lower degrees of saturation (12.7% and 13.7%), the trend of V_p with excitation frequency is similar to that obtained by Emerson et al. (2006) which is reproduced in Fig. 6. The characteristic frequency f for the sand was observed to be about 14 kHz.

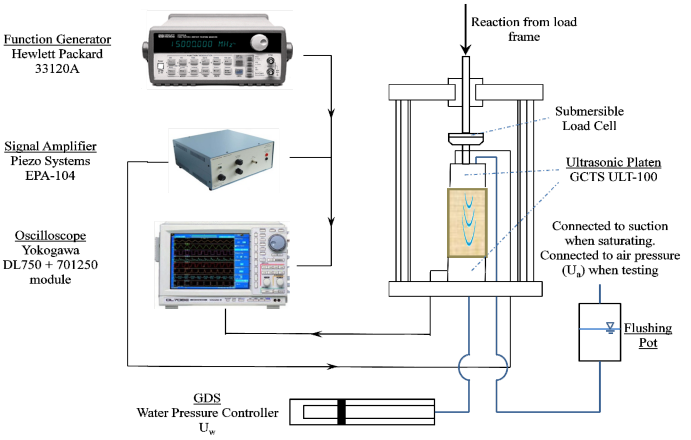

Fig. 2 Experimental setup of ultrasonic test system

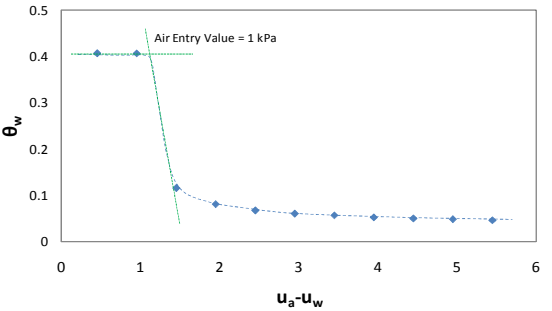

Fig. 3 SWCC for Changi reclamation sand

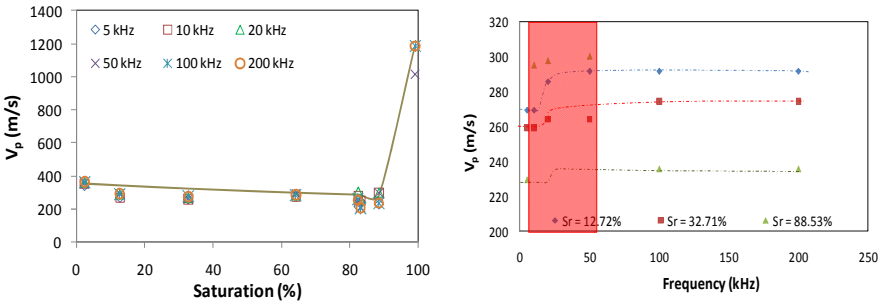

Fig. 4 (a) V_p with saturation and (b) V_p with frequency

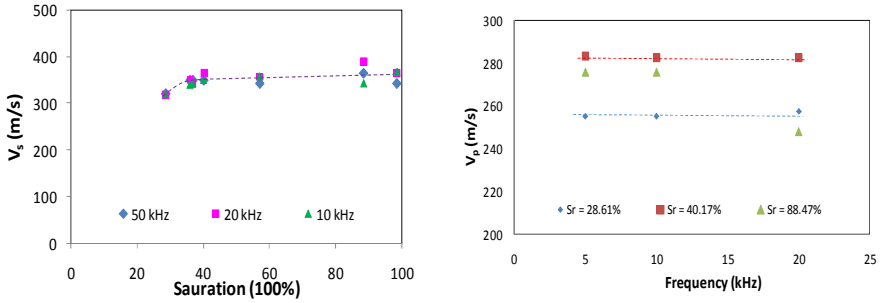

Fig. 5 (a) V_s with saturation and (b) V_s with frequency

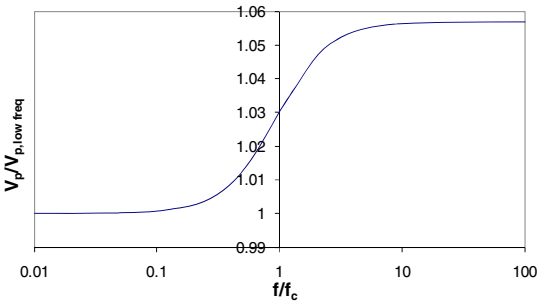

Fig. 6 Evolution of V_p with frequency for Houston sand

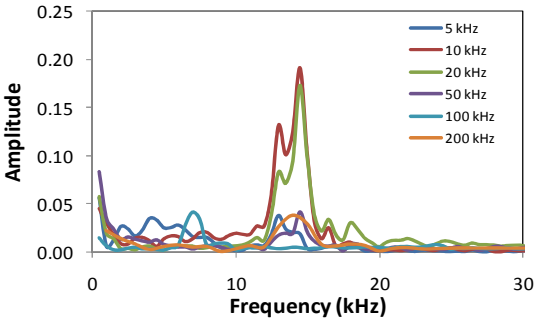

Fig. 7 FFT of Vp receiver's signal for various excitation frequency (S_r = 32.71%).

Fast Fourier Transform (FFT) of the receiver signals for V_p at various excitation frequencies showed that the signals have similar dominant frequency at around 14 kHz (Fig. 7). This would mean that despite using different excitation frequencies, the receiver signal's frequency remained the same. The results are surprising as it appears that the transmitter piezoelectric crystals vibrate at the same frequency regardless of the excitation frequency. Therefore the veracity of

Fig. 4b is questionable. More research is needed to quantify the behaviour of ultrasonic platens.

4 Conclusion

Ultrasonic velocity test results have been presented for sand at different degrees of saturation. The effect of degree of saturation on V_p becomes important only near saturation while the effect of degree of saturation on V_s is small. The effect of excitation frequency on V_s is small whereas for V_p it seems that a trend similar to that observed in the literature was obtained. However, Fast Fourier Transform of the receiver signals showed that the dominant frequency is similar regardless of the excitation frequency. More experiments should be performed to better characterise the ultrasonic platen. Numerical simulation can also be performed to better understand the propagation of waves through a multi-phase setup.

Acknowledgments. The first author is a receipient of the Nanyang President Graduate Scholarship.

References

Emerson, M., Foray, P.: Laboratory P-wave measurements in dry and saturated sand. Acta Geotechnica 1(3), 167–177 (2006)

Geertsma, J., Smit, D.: Some aspects of elastic wave propagation in fluid saturated porous solids. Geophysics 26(2), 169–181 (1961)

Leong, E.C., Yeo, S.H., Rahardjo, H.: Measurement of wave velocities and attenuation using an ultrasonic test system. Can. Geotech. J. 41(5), 844–860 (2004)

Mavko, G., Nolen-Hoeksema, R.: Estimating seismic velocities at ultrasonic frequencies in partially saturated rocks. Geophysics 59(2), 252–258 (1994)

Winkler, K.W., Murphy III, W.F.: Acoustic Velocity and Attenuation in Porous Rocks: Rock Physics and Phase Relations. A Handbook of Physical Constants. American Geophysical Union (1995)

Factors Influencing Water Retention Characteristics of Granular Materials

Gilbert J. Kasangaki[1], Gabriela M. Medero[1], and Jin Y. Ooi[2]

[1] Institute for Infrastructure and Environment, Heriot-Watt University, UK
G.Medero@hw.ac.uk
[2] Institute for Infrastructure and Environment, University of Edinburgh, UK

Abstract. Numerous theoretical and experimental attempts have been made to study the influence of moisture on the behaviour of granular materials and to correlate the measured behaviour to the physical properties of the material whilst recognising the effect of its constituent particle properties. At present there seems to be no clear understanding on how these factors individually and collectively influence the unsaturated behaviour. One common approach has been to compare different materials on the basis of particle size and plasticity characteristics but ignore other factors controlling the inter-particle forces such as particle shape, particle interstices and asperities and physico-chemical phenomena. This paper describes an attempt to investigate the effect of particle size on the drying and wetting water retention characteristics for spherical glass beads. Distilled water and spherical glass beads were chosen to provide simple and well defined wet granular assemblies where the observed response can be attributed to purely glass-glass and glass-water interaction without the presence of other complex inter-particle interactions often present in unsaturated soils. The water retention curves were established for 0.09-0.15mm and 0.25-0.50mm particle sizes of similar-material glass beads. The results show that particle-water interaction alone can produce the hysteretic water retention characteristics with particle size significantly affecting the air- and water-entry values and also the wetting maximum water content. In addition, features of the water retention curve often observed in soils were well captured with glass beads.

1 Introduction

Wet granular materials such as unsaturated soils or wet and sticky industrial bulk solids present many challenging problems. They often exhibit complex behaviour that cannot be easily predicted using classical theories. Numerous theoretical and experimental attempts have been made to study the influence of moisture on the behaviour of granular materials and to correlate the measured behaviour to the physical properties of the material whilst recognising the effect of its constituent particle properties. At present there seems to be no clear understanding of how these factors individually and collectively influence the unsaturated behaviour.

L. Laloui and A. Ferrari (Eds.): Multiphysical Testing of Soils and Shales, SSGG, pp. 111–116.
springerlink.com

In this paper emphasis is on the importance of recognising the factors that affect the water retention characteristics of granular materials.

Many studies have been conducted to determine the water retention behaviour using the relationship between water content and suction. Yang et al. (2004) used five different soils to study factors affecting the water retention characteristics of soils. Their findings are supported by those of Kawajiri et al. (2010) and Houston et al. (2006) who made similar attempts. Samples in which fine cohesive particles were present exhibited higher water retention capacity and bigger hysteresis loop compared to relatively clean materials.

In these studies and many others, soils were grouped and compared on the basis of either particle size (e.g. Yang et al., 2004) or plasticity characteristics (e.g. Houston et al., 2006) whilst ignoring other factors controlling the inter-particle forces such as particle shape, particle interstices and asperities and physico-chemical phenomena. Recognising the importance of these properties of the constituent particles would give an improved understanding on how these factors individually or collectively influence the unsaturated behaviour. It is therefore not be surprising that theories based on one type of soil cannot satisfactorily work for another (e.g. in Leverett, 1940).

This paper describes a scientific attempt to isolate and investigate the effect of particle size on the drying and wetting water retention characteristics for spherical glass beads using a pressure plate. Spherical glass beads with distilled water were chosen to provide simple and well defined wet granular assemblies where the observed response can be attributed to purely glass-glass and glass-water interaction without the presence of other complex inter-particle interactions often present in unsaturated soils. The results show that many pertinent features of the water retention curve (WRC) such as the dependence of the hysteresis loop on particle size observed for soils in previous studies are well captured with this deliberately simple material. Comparing theses typical soil characteristics can provide a useful insight into how each of the constituent properties affects the material behaviour.

2 Test Materials and Sample Preparation

Glass beads of high sphericity (89% roundness) from Sigmund Lindner in two size ranges of 0.25-0.50mm and 0.09-0.15mm were used. These are hereafter referred to as Type 1 and Type 2 glass beads respectively. Type 1 beads had the following physical properties: specific gravity: 2.5; D_{10}: 0.29mm; D_{30}: 0.33mm; D_{50}: 0.35mm; D_{60}: 0.36mm (D_X denote particle size for which X% are finer). Apart from the same specific gravity, these properties were not precisely known for the type 2 beads as all the beads were in a narrow range of particle size bound by the two smallest available standard sieves. Samples were prepared directly on a saturated 1500kPa air-entry ceramic disk in 38.6mm diameter and 10.5mm height moulds. All the samples were prepared using oven dried material. Careful tamping was deployed on each sample to achieve the desired initial void ratio of 0.55 corresponding to 88% relative density. The samples were then saturated prior to

starting the determination of the drying path of WRC. A total of 43 samples were tested altogether.

3 Experimental Programme

3.1 Water Retention Curve

The WRC tests were carried out using a pressure plate equipment manufactured by Soilmoisture Equipment Corporation. The pressure plate was fitted with 1500kPa air-entry ceramic plate. Both the drying and wetting curves were determined using the axis translation technique (Hilf, 1956). The imposed air pressure and water pressure were measured using transducers accurate to 1.0kPa. Water pressures less that 1.0kPa were controlled taking advantage of the hydrostatic pressure head in the connecting water tube.

After imposing the desired pressure, each sample was allowed sufficient time to achieve equilibrium. The equilibrating time was carefully investigated and taken to be when the sample water content change was not more than 0.1% in 24hours. The time to reach equilibrium was found to be a function of matric suction. Typically, the samples took about 7 days to approach equilibrium at 2kPa while only about 4 days were necessary at 30kPa. The dependence of equilibrium on matric suction notwithstanding, equilibrium was considered at 7 days in all the tests. After equilibrium, water content was determined by oven drying at 105^{o}C.

3.2 Liquid Bridge Observation

Besides measuring equilibrium water content at different matric suctions, microscopic observations were made at a magnification of 205±5 using Dino-Lite digital microscope in an attempt to observe the interaction of the water with the beads under varying degree of matric suction can be observed. Images were taken at the time of measuring the water content. Not to lose significant moisture due to evaporation, the time spent taking out the sample for water content and images was kept very short, typically about 3minutes.

4 Results and Discussion

Figure 1 shows the WRCs for the glass beads. The corresponding retention characteristics and the van Genutchen (1980) equation fitting parameters are summarized in Table 1. The features of water retention curves observed in soils have generally been well captured and were found to be well described by the van Genutchen equation. Regardless of the particle size, increasing matric suction of sample from saturation was not immediately accompanied by any significant change in water content, suctions up to about the air-entry value. Within this saturated capillary regime, the surface tension of water prevents air from entering into the sample voids. The micrographs taken of the sample of Type 1 glass beads

at condition marked "A" in Fig. 1 (see Fig. 2a) within this saturation regime corroborates with this observation. The image shows that all the voids are filled with water with the glass beads completely submerged. As can be seen in Fig. 1 and Table 1, the air-entry value, ψ_a for samples of small-sized particles is greater than the one for large-sized particles.

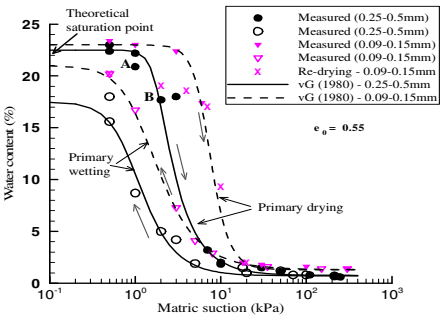

Fig. 1 Water retention curves for the tested glass beads.

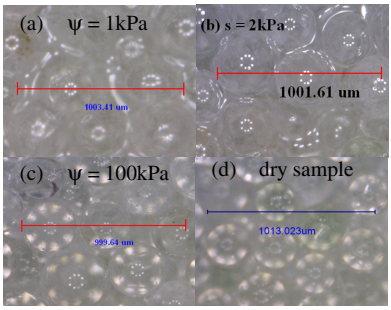

Fig. 2 Microscopic image (X200) of the formation of liquid bridges at different suctions on drying path of Type 1 beads (white spots are due to light reflection during imaging).

After the air-entry value, further increase in matric suction resulted in significant decrease in water content per unit change in suction. The rate of change was influenced by the particle size (Fig. 1). The steep slopes of the curves in this funicular bridge zone imply a considerable increase in drainage of water from the samples. Micrograph (Fig. 2b) taken of Type 1 sample at the condition "B" in Fig. 1 shows that much of the water drained out of the sample within this zone and the beads became even clearer. When water is sufficiently drained from the sample, any remaining liquid water becomes disconnected and localized at inter-particle contacts. In this pendular bridge regime, characterized by the residual matric suction ψ_r and residual water content θ_r, the matric suction is only due to the menisci water and higher energy is necessary to remove any further liquid from the voids. Further increase in matric suction beyond the residual value was followed by negligibly small changes in water content (~0.003%/kPa) independent of the size of glass beads. After the matric suction of about 100kPa, negligible water content change was observed in the sample in the drying path. Image taken of the sample at 100kPa under drying path (Fig. 2c) was similar in terms of appearance to that of the dry sample (Fig. 2d) suggesting that within the residual zone the amount of water within the voids is very small. It was noted that when the mould containing the beads was lifted, the beads did not fall apart due to gravitational forces suggesting that the liquid bridge induced adhesive forces were holding the sample together.

When matric suction for the previously dried sample (through increasing the matric suction to ~300kPa) was decreased the sample wetted – primary wetting (Fig. 1). Until about the water-entry value, water content increased at a rate almost

similar to the one for the drying path. Thereafter the change of water content per unit change in suction increased significantly. The resultant wetting path in this funicular regime was different from the drying path, giving rise to a hysteresis that has been observed in previous studies of on both coarse and fine soils (e.g. Leverret, 1940; Yang et al., 2004). The hysteresis is bigger for finer Type 2 beads and at low suctions for both sample types. At matric suctions greater than about 20kPa there is no hysteresis in water retention behaviour of the samples, typical of what is observed in coarse soils (e.g. Yang et al., 2004). In addition, the difference between water content of the sample undergoing drying and that undergoing wetting at extremely low suctions (near saturation) was smaller for finer particles, typical of what is reported in the literature for soils (e.g. Yang et al., 2004).

Table 1 Water retention characteristics of the tested glass beads and the fitting parameters

Glass beads type	***Water retention characteristics***						***Van Genutchen (1980) curve fitting parameters***				
	Ψ_a	Ψ_r	Ψ_w	θ_s	θ_r	θ_w	θ_r	Drying		Wetting	
								α	n	α	n
	(kPa)			%			(%)	-			
1	1.5	7.3	5.3	22	1.1	1.0	0.7	0.277	3.744	1.132	2.615
2	4.2	12	2.9	22	1.4	1.3	1.0	0.139	4.124	0.750	2.342

After first drying and wetting cycle, Type 2 beads were subjected to second drying path to explore the effect of further cycles of drying and wetting on the water retention behaviour (Fig.1). It is interesting to note that the second drying path quickly joined the primary drying path suggesting that at relatively high suctions the observed drying path may be a characteristic path of the material. This is in contrast with soils where subsequent drying path are often distinctly different from the first drying path (e.g. Ng and Pang. 2000).

The van Genuchten (1980) empirical model (Eq. 1) was found to provide a satisfactory fit to the hysteretic drying-wetting experimental data, as shown in Fig. 1. The least squares curve fitting parameters are shown in Table 1 with m = 1-1/n.

$$\theta = \theta_r + (\theta_s - \theta_r)\left\{1 + (\alpha\psi)^n\right\}^{-m} \quad (1)$$

where θ is the volumetric water content at a given matric suction, ψ and θ_r and θ_s are the residual and saturated volumetric water contents. In this study however, water content is presented as gravimetric water content.

5 Conclusions

The water retention curves for 0.09-0.15mm and 0.25-0.50mm particle size ranges of similar composition glass beads have been presented. Starting from a saturated sample, the hysteretic drying and wetting paths have been carefully measured and

was found to be well described by the van Genutchen (1980) empirical model through least squares curve fitting procedure. The features of WRC observed for soils have been generally well captured with spherical glass beads. The results show that particle-water interaction alone can produce the hysteretic water retention characteristics with the particle size significantly affecting the retention capacity. Reducing the particle size from 0.25-0.50mm to 0.09-0.15mm increased the material air-entry value, residual matric suction and water entry value and also the primary wetting maximum water content. The results further suggest that the increasing hysteretic behaviour observed in soils upon subsequent drying-wetting cycles comes from factors other than the inert water-particle interaction since this is not observed in the present study. Cycles of drying and wetting, on the other hand, was found to have no effect on the water retention behaviour of glass beads except in the saturation capillary regime.

References

Houston, W.N., Dye, H.B., Zapata, C.E., Perera, Y.Y., Harraz, A.: Determination of SWRC using one point measurement and standard curves. In: Proc. 4th Int. Conf. Unsat. Soils, Carefree, Arizona, April 2-6, vol. 2, pp. 1482–1493 (2006)

Kawajiri, S., Shibuya, S., Kato, S.: Effects of matric suction on elastic shear modulus for three unsaturated soils. In: Alonso, Gens (eds.) Unsaturated Soils, vol. 1, pp. 271–275. Taylor and Francis Group, London (2010)

Loverett, M.C.: Capillary behaviour in porous solids. AIME 142(1), 152–169 (1941), doi:10.2118/941152-G

Ng, C.W.W., Pang, Y.W.: Experimental investigations of the soil-water characteristics of a volcanic soil. Can. Geotech. J. 37, 1252–1264 (2000)

van Genutchen, M.T.: A closed-form equation for predicting the hydraulic conductivity of unsaturated soils. Soil Sci. Soc. Am. J. 44, 892–898 (1980)

Yang, H., Rahardjo, H., Leong, C.E., Fredlund, D.G.: Factors affecting drying and wetting soil-water characteristic curves of sandy soils. Can. Geotech. J. 41, 908–920 (2004), doi:10.1139/T04-042

Evaluation of Collapse Potential Investigated from Different Collapsible Soils

Qasim A.J. Al-Obaidi[1], Saad Farhan Ibrahim[2], and Tom Schanz[1]

[1] Soil and Rock Mechanics Department,
Civil and Environmental Engineering Faculty,
Ruhr University Bochum, Germany
eng.qasim79@yahoo.com,
tom.schanz@ruhr-uni-bochum.de
[2] Civil, Environmental and Geodetic Engineering Department,
Ohio State University, Columbus, Ohio, USA
drsaadfarhan@yahoo.com

Abstract. Collapsible soils are considered as one of the problematic soils, and widely distributed in North America, Europe, Russia and Asia. They show low dry density and moisture content in all testing schedule due to presence of cementation bonds or loess structure especially at unsaturated state in arid or semi-arid regions. Moreover large deformation, rapid settlement and high decrease in void ratio of a meta-stable soil structure occurred during wetting and loading. Two types of unsaturated collapsible soils are used in this study from different area in the world. Collapse potential(I_c) and collapse index (I_e) magnitude are determined according ASTM (D5333-03) by using the conventional Oedometer device in a constant temperature and humidity environmental at different stress level. It was noted that the value of collapse potential (I_c) affected by the rate of secondary consolidation (Creep) and time of wetting. It shows high values when flooding the specimens by water during primary consolidation. It is concluded that there is an increases in collapsibility due to removal of bonding between cementing particles upon wetting due to stress release and leaching of soil during water infiltration leading to softening due to rearrangement of soil particles.

1 Introduction

Numerous researches are dealing with the investigation of the main reasons of foundation failure problems and they found that the partially or fully wetting of the moisture-sensitive soils causes either collapse (in gypseous or loess soils) or swell (in some clayey soils such as bentonite or kaolin). Thus, the wetting process of soil in nature causes volume change, reduction in the bearing capacity and shear strength. This leads to a major challenge when designing the foundations and during or after the construction of engineering structures.

L. Laloui and A. Ferrari (Eds.): Multiphysical Testing of Soils and Shales, SSGG, pp. 117–122.
springerlink.com

2 Experimental Work

2.1 Soil Samples

Two types of collapsible soils were used in this work; the first soil is Sandy Gypseous soil (GI) where a disturbed soil sample of a stiff to very stiff light to reddish brown with white blocks and crystal particles of Gypsum were taken from Al-Ramadi city in the west of Iraq. The second soil is Silty clayey Loess soil(LG) where a disturbed soil samples of a medium to stiff dark to reddish brown Silty clayey soil with some black spots were taken from a site near Dresden city in the east of Germany.

2.2 Laboratory Tests

2.2.1 Physical, Classification and Chemical Tests

Physical, chemical and other types of tests were conducted according ASTM methods, while other tests of Soil classification, Relative density and Chemical tests were carried out according DIN 18123, 18126 and 38414-S4 respectively. Summary of physical, classification and chemical tests results are explained in table (1) below.

Table 1 Summary of physical, classification and chemical tests results

Soil properties	(GI) soil	(LG)soil
In place dry density, (gm/cm^3)	1.30	1.60
Natural moisture content, (%)	2	21
Specific Gravity(by Kerosene)	2.35	2.63
Liquid Limit,(%)	NP	28.2
Plastic Limit,(%)	NP	16.8
Plasticity Index,(%)	NP	11.4
Max.dry density,(Proctor) (gm/cm^3)	1.70	1.74
Optimum moisture content,(%)	8.0	16.4
Relative density,(%)	82	-
Initial void ratio, e_o	0.81	0.64
Fines, Passing sieve (0.075mm), (%)	29	98
Soil classification, USCS	SP	CL-ML
Gypsum Content,(%)	70$^{(*)}$	-
Ca,(mg/l)	689	17.2
Sulphate , (mg/l)	1780	5.9
S,(%)	20.3	0.02

$^{(*)}$Gypsum content, $x_{(\%)} = \left[\frac{W_{45°C} - W_{105°C}}{W_{105°C}}\right] \times 4.778 \times 100$ (Al-Mufty2000)

Where: W_{45}°C = weight of dried soil sample at 45°C.
W_{105}°C = weight of dried soil sample at 105°C.

2.2.2 Collapse Tests

2.2.2.1 Single Oedometer Test (SOT)

Collapse can be defined as a decrease in height of a confined soil following wetting at a constant vertical stress. Single Oedometer test method used to determine the magnitude of potential collapse that may occur for a given vertical (axial) stress and an index for rating the potential for collapse. The collapse potential(I_c) can be determined at any stress level as follows (ASTM D5333-03):

$$I_{c\,(\%)}=\left[\frac{\Delta e}{1+e_o}\right]\times 100$$

Where: Δe: Change in void ratio resulting from Wetting. e_o: Initial void ratio.

Soil samples were statically recompacted in the oedometer ring using distilled water at natural dry density and natural moisture content of (2%) for Gypseous soil (GI) while it was Hydroscopic moisture content of (2.5%) for Loess soil. Figures (1,2 and 3)shows that the collapse potential (I_c) of (GI) and (LG)soils increase linearly with the increase in collapse stress level which can be attributed to the gradual decrease in void ratio, leading to break-down of the interparticle cementing bonds associated with large volume change and with increase in vertical stress. This behavior confirm with results of Barden et.al 1973,Al-Mohammadi et.al1987 and Fattah et.al.2008.It is observed from figures (4 and 5) that about (50%) of final compression of (GI) soil occurred during the first (12 hr) of wetting after that the soil collapsed by constant deformation settlement with time. It was noted that the value of collapse potential (I_c) affected by rate of secondary consolidation (Creep) and time of wetting. It shows high values when flooding the specimens by water during primary consolidation. These results confirm with the results of Al-Mohammadi 1987, Al-Aithawi 1990 and Nashat 1990. Such behavior not observed for Loess soil (LG). (See figure 4, 6 and table 2).

2.2.2.2 Double Oedometer Test (DOT)

Typical results of double Oedometer test (DOT) for both Gypseous and Loess soil are shown in figures (7 and 8) respectively. The value of collapse potential (I_c) obtained by (DOT) of (GI) soil is less than these value obtained from (SOT), while the opposite behavior was observed for Loess soil (LG), see figure (3). These results confirmed by Houston et.al.2001 and Charles et.al.2007.

Table 2 Single (SOT) and Double (DOT) Oedometer tests results

Soil type	Test type	Time (day)	Vertical stress, kPa					
			25	50	100	200	400	800
			Collapse potential(I_c),%					
GI	SOT	1	0.7	1.5	2.9	3.4	4.0	6.2
		3	1.1	2.1	4.0	4.7	4.9	7.9
		7	1.4	2.6	4.8	5.2	5.8	9.4
		15	-	-	-	-	-	10.8
	DOT	1	0.6	1.2	2.0	3.4	4.2	5.9
LG	SOT	1	Swell	Swell	2.0	5.0	6.0	11.0
	DOT	1	1.0	2.2	4.4	7.0	9.6	11.8

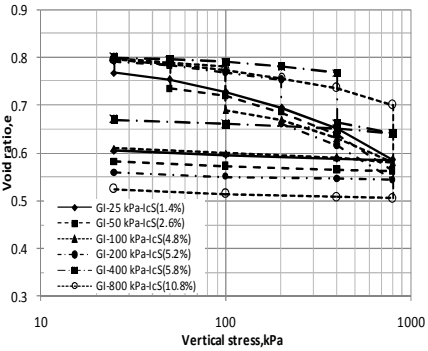

Fig. 1 Single Oedometer collapse test-(GI) soil

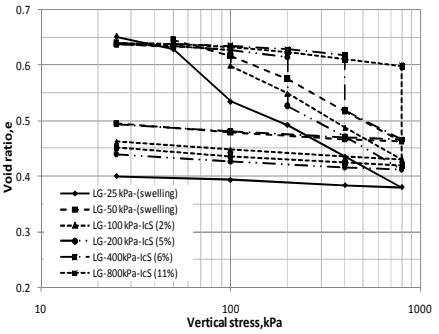

Fig. 2 Single Oedometer collapse test-(LG) soil

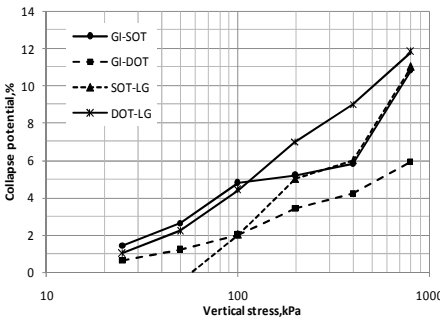

Fig. 3 Collapse potential variation with stress level of (GI, LG) soil

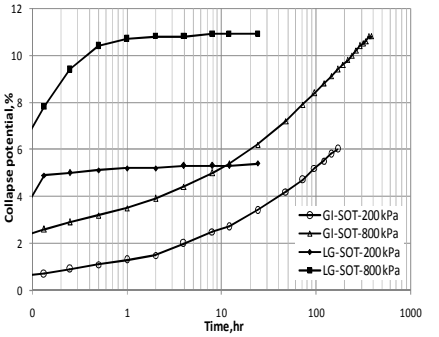

Fig. 4 Collapse potential-Time relationship of (GI,LG) soil

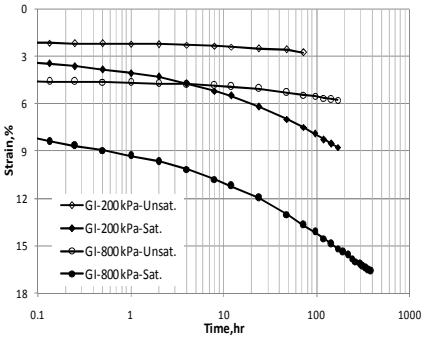

Fig. 5 Strain-Time relationship of soil (GI)

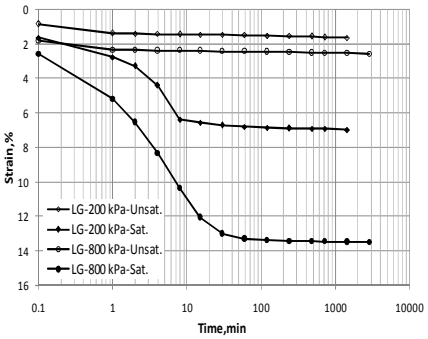

Fig. 6 Strain-Time relationship of soil (LG)

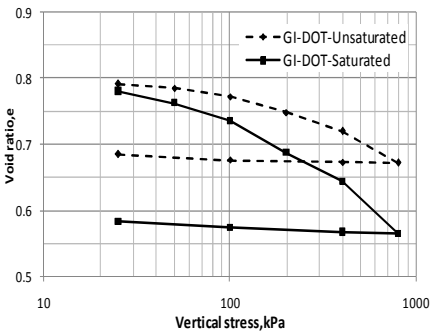

Fig. 7 Double Oedometer test DOT of soil (GI)

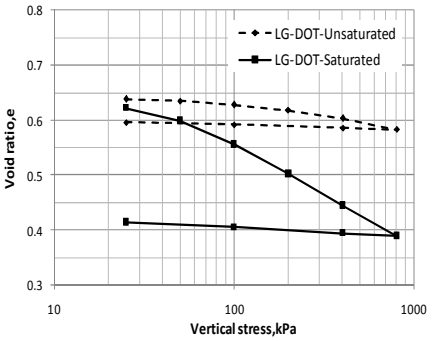

Fig. 8 Double Oedometer test DOT of soil (LG)

3 Conclusions

1. Increase the collapse potential is directly proportional to overburden effective pressure to join the soils containing high levels of gypsum.
2. Secondary consolidation rate (Creep) has major effect on the collapse potential I_c of sandy soil, while such effect not observed for clayey soil.
3. The dry compression strain of Sandy soil is almost because affected by disturbance and/or low value of specific gravity and dry density of gypsum.
4. There was of (GI) soil. The standard consolidation curve is not give clear picture of compressibility characteristics of gypseous soil and due to removal of bonding between cementing particles upon wetting (no definite end point observed during primary consolidation).
5. Single Oedometer Test gave more accurate and higher values of ((I_c) than these value of (I_c) getting from (DOT) due to more losing of cementing agent by dissolving of gypsum and singularity of specimen.

References

Al-Aithawi, A.H.: Time-Dependent Deformation of a Gypseous Silty Soil, MSc.Thesis, Civil Engineering Department, University of Baghdad, Iraq (1990)

Al- Mohmmadi, N.M., Nashat, I.H., Bako, G.Y.: Compressibility and Collapse of Gypseous Soils. In: Proc. 6th Asian Conf. on Soil Mechanics, Tokyo (1987)

Al-Mufty, A.A., Nashat, I.H.: Gypsum Content Determination in Gypseous Soils and Rocks. In: 3rd Int. Jordanian Conference on Mining, pp. 500–506 (2000)

ASTM D5333, Standard Test Method for Measurement of Collapse Potential of Soils (2003)

Barden, L., McGown, A., Collins, K.: The collapse mechanism in partly saturated soil. Eng. Geol. 7, 49–60 (1973)

Ng, C.W.W., Bruce, M.: Advanced Unsaturated Soil Mechanics and Engineering. Taylor and Francis Group, London (2007)

DIN 38414-S4, German standard methods for the examination of water, waste water and sludge; sludge and sediments (group S); determination of leachability by water (S 4) (Publication date: October 1984)

Fattah, M.Y., Al-Shakarchi, Y.J., Al-Numani, H.N.: Long–Term Deformation of Some Gypseous Soils. Engineering and Technology Journal 26(12) (2008)

Houston, S.L., Houston, W.N., Zapata, C.E., Lawrence, C.: Geotechnical and Geological Engineering 19, 333–355 (2001)

Jennings, J.E., Knight, K.: A Guide to Construction on or with Materials Exhibiting Additional settlement Due to Collapse of Grain structure. In: Proceeding of 6th Regional Conference for Africa on Soil Mechanics and Foundation Engineering, Durban, South Africa, pp. 99–105 (1975)

Nashat, I.H.: Engineering Characteristics of some Gypseous Soils in Iraq. PhD Thesis, Civil Eng. Dep., University of Baghdad (1990)

Testing in Non-isothermal Conditions

Thermo-Hydro Mechanical Column Experiment to Study Expansive Soil Behaviour

Tom Schanz[1], Long Nguyen-Tuan[1], and Maria Datcheva[2]

[1] Chair for Foundation Engineering,
Soil and Rock Mechanics,
Ruhr-Universität Bochum, Germany
{tom.schanz, long.nguyentuan}@rub.de

[2] Institute of Mechanics - Bulgarian Academy of Sciences Acad. G. Bontchev,
block 4, 1113 Sofia Bulgaria
datcheva@imbm.bas.bg

Abstract. Understanding the heat transfer, water flow, and swelling pressure development in engineered clay barrier and the evaluation of the influence of these phenomena on the barrier performance are important issues in constructing nuclear waste repositories. The thermal, hydraulic and mechanical processes that take place within the clay barrier during its functioning lifetime are strongly coupled and therefore difficult for experimental and numerical modelling. In order to collect valuable experimental data for predicting the long term barrier functionality it is necessary to carry out tests with known and controlled initial and boundary conditions as well as to measure temperature, water content and mechanical stress along the specimen in a reliable and robust way. For this reason a new apparatus has been developed for laboratory testing of coupled thermo-hydro-mechanical behaviour of clay-buffer material under conditions close to the situation in the field. The main objectives of this paper are: (1) to describe the experimental device; (2) to introduce the sensors implemented and their calibration, and (3) to present the first experimental results obtained with the new equipment.

1 Introduction

Coupled thermo-hydro-mechanical (THM) soil behaviour is of importance in a variety of practical problems such as geothermal energy production from deep sedimentary reservoirs, waste storage facilities, oil and gas production. However, coupled THM aspect is recently gaining more interest from researchers and engineers involved in the conceptual design of engineered barriers for storage of spent nuclear fuel and nuclear waste. The coupled THM behaviour of the material is of paramount consideration in constructing the buffer for the nuclear waste containers.

The clay used as buffer material, initially unsaturated, is subjected to a heat emitted by the radioactive waste, hydraulic gradient induced by water intruding from the host rock, and swelling and shrinkage phenomena due to the variation of water content and temperature. The concept of the THM column test is to simulate the real scenario in the repository of wetting of the buffer material from the host rock and

L. Laloui and A. Ferrari (Eds.): Multiphysical Testing of Soils and Shales, SSGG, pp. 125–130.
springerlink.com

heating due to the decay of nuclear waste. Therefore the column test represents the processes, e.g. distribution with time of temperature (T), pore water pressure (P_l) and displacements (u) within a thin slice along the buffer radius. Column type apparatuses had been used already for studying buffer behaviour and results are reported in e.g. Mohamed et al. (1992); Gatabin and Billaud (2005); Villar et al. (2006). In this paper we present a column test equipment that is a further improvement of the device reported in Manju et al. (2008). The main features of the new device are: 1. measurement of the swelling pressure at both sides of the sample; 2. application of gradients of suction and temperature; 3. measurement in three sections along the sample of water content, suction and temperature without significant disturbance of the sample. In addition it is presented a new solution for measuring relative humidity (RH) providing temperature controlled environment for the RH sensors ensuring equal temperature in the RH sensor's chamber and at the same height level in the sample avoiding this way vapour condensation.

2 Description of the THM-Column Testing Device

The general layout of the THM-testing cell is presented in Fig. 1. The cell is built up of three parts: a bottom plug, cylindrical cell and a top plug. The housing of each part is made of 316L stainless steel. The three parts are fitted together and with the base plate by six 12 mm diameter screws per joint. The device is placed on a shelf that can be inclined in order to place in or out the parts of the specimen. The water tightness of the cell is guaranteed by means of O-rings capable of withstanding temperature of up to 100°C.

Bottom and top plugs have similar arrangement. They consist of load cell, electrical heating, water cooler and water supply system. The bottom plug includes a base supporting the cell body on its external collar. In order to ensure homogeneous water supply a 3 mm thick porous stainless steel disk is placed in contact with the sample. The top plug is covered with stainless steel plate to keep the load cell fixed.

Cell body comprises of PTFE and metal cases. The PTFE case is placed to limit the heat dissipation. It is 17 mm thick with internal diameter of 150 mm, height of 410 mm and thermal conductivity of 0.23 W/m.K. The metal case is made of stainless steel to ensure the rigidity of the cell as well as to provide mechanical support for the PTFE case. The thickness of the metal case is 25 mm, its internal diameter is 167 mm and the height is 410 mm. The cell housing has preliminary calibrated holes for sensor installation.

The hydration system supplies de-aired and de-ionized water on both top and bottom of the specimen. The water is injected to the cell by means of burette placed over a precision scale, and nozzle fitted with a valve through the upper hydration line.

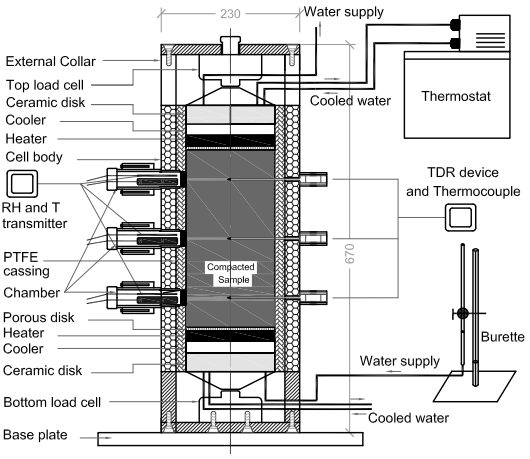

Fig. 1 Layout of the new column device for testing the thermo-hydro-mechanical behaviour of expansive soils.

Water content sensors: Water content is measured by means of MiniTrase (6050X3K1) of Soilmoisture Equipment Corp. employing Time Domain Reflectometry (TDR) method. Three Mini Buriable Waveguide probes specially designed for column studies are placed along the sample in beforehand drilled holes of the same diameter as the waveguides. The small size of the waveguides reduces the disturbance of the sample.

RH–sensors: *Humidity and Temperature transmitters (VAISALA HMT337)* are used for monitoring the relative humidity profile at three positions along the surface of the sample. The device includes a humidity sensor that changes its dielectric characteristics with small variations in humidity and temperature elements (Pt100). The accuracy of the humidity sensors including non-linearity, hysteresis and repeatability is $\pm 1.0\%$ over the range of 0-90 % RH and ± 1.7 % over the range of 90-100 % RH. A *temperature controlled chambers (RH-chamber)* were specially designed for placing the RH–sensors and to avoid water condensation. The temperature in the RH-chamber is kept the same as the temperature inside the soil specimen measured by the buried temperature sensor at the same level as the level of the RH-chamber. There are temperature sensors and heaters inside the RH-chamber to maintain the target temperature. The chamber is screwed to the metal cell and the hole in the cell case is made watertight by means of O-ring. The porous stone installed next to the sample allows the exchange of vapour between the soil sample and the RH-chamber as well as prevents material extrusion due to soil swelling.

Temperature sensors: Thermocouple devices are used to measure temperature at three levels along the sample.

Load cells: The top and the bottom of the THM-cell are equipped with load cells in order to measure the mechanical pressure due to soil swelling and shrinkage. Ceramic disks is mounted next to the load cells in order to prevent overheating.

Electrical Heaters and Water Cooler System: Each electrical heater includes 4 heater sources embedded in a metal plate and one thermocouple to control the temperature. The water cooler plate is located next to electrical heater and the thermostat can control the water temperature in the range from -50 to 150°C with accuracy of ±0.02°C.

3 Sensor Calibration Tests

Calibration of the RH sensors: The relative humidity sensors were calibrated against data obtained applying chilled-mirror method as it is proved to provide higher accuracy, Agus and Schanz (2005). Six different solutions were used for this calibration: NaCl 38 g/l, NaCl 63g/l, NaCl 125 g/l, KCl saturated, $NaCO_3$ saturated, LiCl saturated. The solutions were placed in six desiccators together with the RH and temperature sensors until reaching steady state. The measured RH data are compared with the corresponding readings of the chilled mirror hygrometer and this way the calibration curves for each of the RH sensors were obtained.

Calibration of the TDR sensors: The water content sensors (TDR probe) are calibrated against temperature variation for the material used in this study (sand-bentonite mixture) and for the relevant range of temperature. The results are reported in Schanz et al. (2011) where by means of an originally designed device experimental data are collected for obtaining the relation between water content, dielectric constant, and temperature.

For the rest of the utilised sensors the manufacturer calibration data were used.

4 First Experimental Results

The mixture of sand (50%) and Calcigel bentonite (50%) is selected as a material for the first tests. The ingredients were mixed, wetted and kept at air-tight container for more that 2 weeks for achieving equilibrium and compacted to a targeted density of 1.4 (g/cm^3).

HM-Test – Hydration under Constant Room Temperature. The first test with sand-bentonite mixture was carried out at room temperature (20.5±0.5°C in average). The soil specimen is hydrated with de-aired and de-ionised water from the bottom applying appr. 15 kPa water pressure. Fig. 2 presents the measured with time and along the specimen water content and suction and the readings of the top and bottom load cells converted to stress.

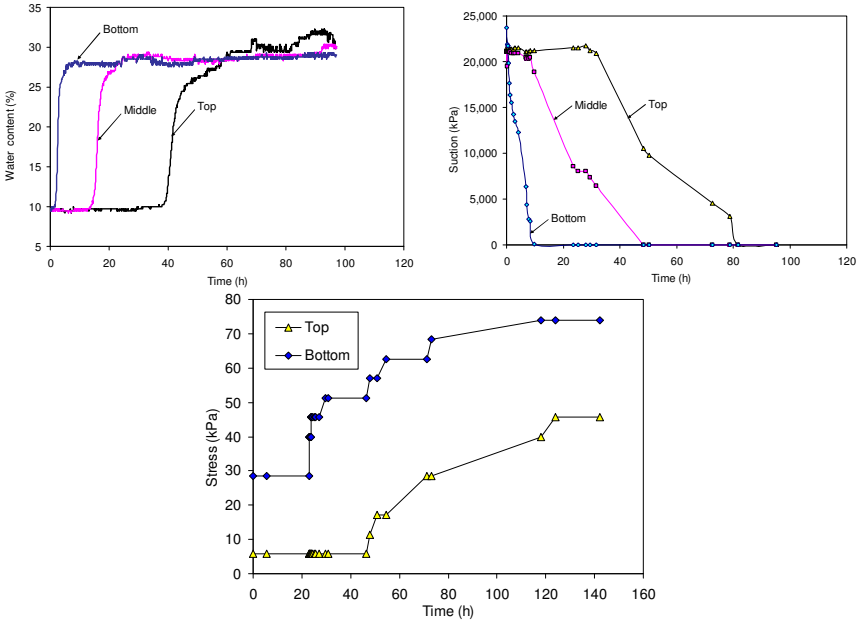

Fig. 2 HM–test at room temperature: evolution of water content, suction and vertical stress.

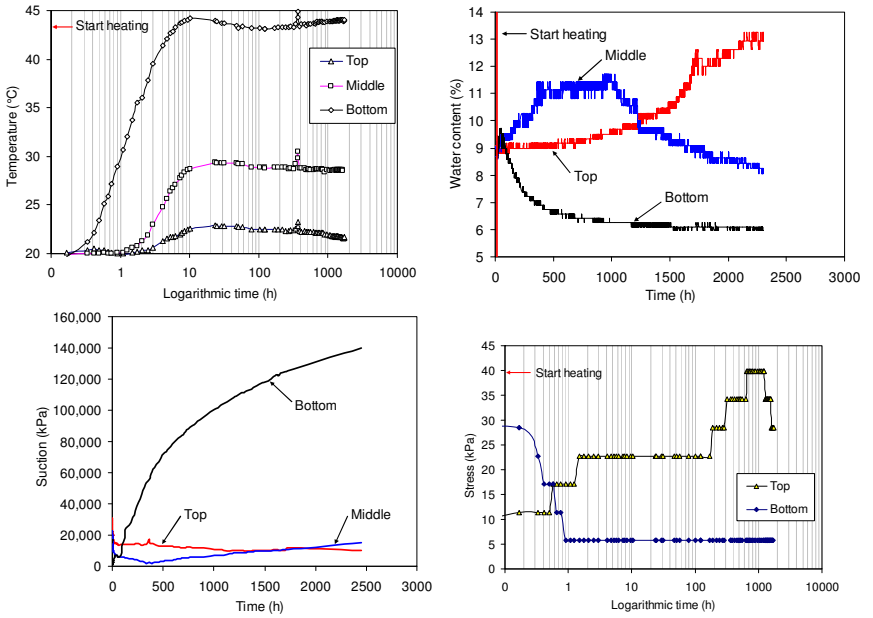

Fig. 3 THM–test: evolution of temperature, water content, suction and vertical stress

THM-Test – Application of Temperature Gradients. During this test the heater at the bottom was heating the sample to 80°C whereas at the top of the specimen the temperature was controlled to be 20°C by means of the heater and the water cooler. It is foreseen to supply water from the top during the application of the temperature gradient and the test is running but not completed. The evolution of the temperature, water content, suction and swelling pressure with time and along the specimen is shown in Fig. 3

5 Conclusion

A new column test device for laboratory investigation of coupled thermo-hydro-mechanical behaviour of expansive soils has been constructed and shown to give reasonable results for sand-bentonite mixture in conditions close to those for the nuclear waste buffer. The column device is designed to apply temperature and hydraulic loading from top and bottom of the sample and thus allowing exerting thermal and suction gradients. The device is equipped with water content, temperature and relative humidity sensors at three different heights along the specimen. The water content and temperature sensors are specially fitted in their size to minimise sample disturbance. Special attention is paid to calibrate the sensors taking into account the influence of high temperature. The advantage of measuring swelling pressure simultaneously at the top and the bottom of the sample is evident. The first tests also demonstrate the ability of the THM-testing device to provide rich data for understanding the processes during heating/cooling and wetting of expansive soils. It can be concluded that the new column testing device is a promising tool for laboratory investigation of coupled thermo-hydro-mechanical behaviour of soils.

References

Agus, S.S., Schanz, T.: Comparison of four methods for measuring total suction. Vadose Zone Journal 4(4), 1087–1095 (2005)

Gatabin, C., Billaud, P.: Bentonite THM mock-up experiments: Sensors data report, Technical report, CEA, Rapport NT-DPC/SCCME 05-300-A. CEA, Paris

Manju, M., Schanz, T., Tripathy, S.: A column device to study THM behaviour of expansive soils. In: The 12th International Conference of International Association for Computer Methods and Advances in Geomechanics (IACMAG), Goa, India (October 2008)

Mohamed, A., Yong, R., Kjartanson, B.: Temperature and moisture distributions in a clay buffer material due to thermal gradients. In: MRS Proceedings, vol. 294, pp. 417–425 (1992), doi:10.1557/PROC-294-417

Schanz, T., Baille, W., Nguyen-Tuan, L.: Effects of temperature on measurements of soil water content with time domain reflectometry. ASTM - Geotechnical Testing Journal 34(1), 1–8 (2011)

Villar, M., Gomez-Espina, R., Martin, P.: Behaviour of mx-80 bentonite at unsaturated conditions and under thermo-hydraulic gradient, Band 1081, Informes técnicos Ciemat (2006)

Shear Strength of Clay during Thaw

Anders Beijer Lundberg

University of Technology Delft
A.BeijerLundberg@tudelft.nl

Abstract. Increased vertical depths of non-frozen soil in permafrost profiles have been observed in field measurements, but material behaviour during this thaw process has not been investigated thoroughly. An experimental analysis of the undrained shear strength of clay soil during thaw has therefore been carried out. The reduction of undrained shear strength during the phase change from frozen to residual thawed soil was simulated in a climate controlled room. A clay sample was frozen in -18 °C and then slowly thawed at constant temperature, after which series of vane shear tests were performed. The results show a temperature-dependant reduction in the undrained shear strength of the material. The low soil temperatures in the thawed permafrost layer seen in field tests indicate that this mechanism could have practical significance for the safety of structures located in permafrost areas.

1 Introduction

Permafrost soils consist of the active layer and the permafrost layer, Fig. 1. The active layer periodically thaws during the warm season (Jorgenson et al, 2006). Recently increased temperatures in the arctic regions, as well as increased depth of the active layer have been observed (Duarte et al, 2012). It is believed that global climate change is the cause of this alteration in ground conditions (Osterkamp et al, 1999).

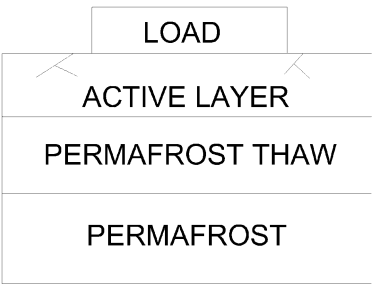

Fig. 1 Permafrost profile

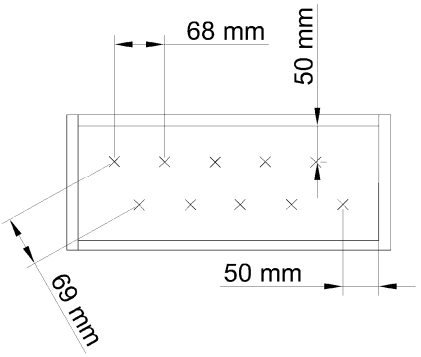

Fig. 2 Sample container

L. Laloui and A. Ferrari (Eds.): Multiphysical Testing of Soils and Shales, SSGG, pp. 131–136.
springerlink.com

Extensive infrastructure developments such as pipelines and port facilities are located in the permafrost-dominated arctic zones. Most structures were designed for constant depth of the active layer and constant minimum soil strength during the warm period. Increased temperatures and permafrost thaw, which can be defined as increased depth of the active layer, may result in large soil deformations in these regions (Williams, 1995).

Since laboratory heat transfer properties and field measurements of surface temperatures are available, accurate simulations of soil temperatures have been performed (Nicolsky et al, 2009). Also, thermo-hydro-mechanical coupled numerical methods for soils are in use (Chijimutsu et al, 2000). An uncoupled model of permafrost thaw - pipeline interaction in clay and sand is displayed in Xu et al, 2009. Numerical models could therefore be used to simulate both the permafrost thaw and the mechanical behaviour over several decades, if assumptions regarding surface temperature levels are made. This would simplify practical design of large-scale structures in the arctic permafrost areas.

For simulations of practical interest, numerical models require accurate input parameters. The mechanical behaviour of both the frozen and the thawed soil must be included. Frozen soil has been investigated by various researchers and the shear strength appears to be dominated by the ice crystals. The soil shear strength can therefore be correctly modelled with a Mohr-Coulomb yield condition (Watson et al, 1973, Andersland & Al-Nouri, 1970).

The strength of the thawed soil is of much interest because of the reduction in shear strength after thaw. Correct modelling of soil post-thaw is therefore of some importance. The largest reduction in shear strength is seen in clay soils (Xu et al, 2009). Instantaneous material degradation after thaw has previously been assumed, which will lead to large deformations directly after the onset of thaw (Watson et al, 1973). This modelling assumption has large consequences for the soil bearing capacity, since ground temperatures in the lower active soil layer frequently are 1 – 5 ºC (Osterkamp et al, 1999). However, there could also be gradual material change in the soil fabric, which has not previously been explored in detail. The interface between the permafrost and the active layers is also not generally clearly defined because of material variability, and can consist of frozen and non-frozen patchy zones which are intertwined (Jorgenson et al, 2006).

A simple hypothesis about the shear strength of soil pre- and post-thaw is therefore tentatively stated: the frozen soil is dominated by the structure of the ice crystals, leading to frictional material behaviour which conveniently is described with the Mohr-Coulomb yield criteria. The thawed soil will have the residual drained or undrained shear strength of the soil. During thaw, when the ice content of the soil is not fully carrying the load, the shear strength decreases from the frozen strength to the residual strength. Fine-grained material such as clay transforms from a material dominated by frozen frictional shear strength to a residual thawed state, depending on the temperature of the clay soil. This is expressed in Eq. 1.

$$\tau_{thaw} = C_{res} + (C_{fr} - C_{res}) \exp(-aT) \tag{1}$$

where τ_{thaw} is the undrained shear strength of the thawed clay, C_{fr} and C_{res} are the frozen and residual shear strength, and a is an experimentally determined constant,

controlling the decay of undrained shear strength. If the transitional strength during thaw is found, a complete description of the clay can be given.

An investigation of the undrained shear strength of the frozen clay during slow thaw has therefore been performed. The period in which the active layer reaches the permafrost can be assumed to occur over a short period of time during the warm season (Osterkamp et al, 2006), which points to undrained soil conditions. The drainage conditions of the soil will also be influenced by the existence of ice crystals in the soil, which will reduce the permeability, leading to undrained or partially drained conditions. To reduce the problem of permafrost bearing capacity during thaw to a condition of plastic yield at undrained conditions is thereby a reasonable modelling approach. Tests were consequently carried out to investigate the undrained shear strength of soil during thaw, as well as exploring possibilities of general tests on frozen soil.

2 Test Procedure

To investigate the undrained shear strength of clay, a complete climate-controlled testing procedure was designed. The very complex natural consolidation, soil freeze and thaw processes were simplified to one freeze-thaw cycle, which was reasonable since an estimation of the initial strength reduction of the soil was the aim of the test. Because several tests were needed for an approximation of the strength-temperature curve (Eq. 1), a simple and relatively rapid test method was required. The variability expected from different samples was deemed to be large and a single sample was consequently preferred. Because of these difficulties, climate-controlled triaxial tests were not used. Instead the vane-shear test (ASTM D4648M) was chosen. The main advantages were the fast test procedure, the ability to open the clay material for internal temperature measurements and repeatability. Also, the vane shear test was used by Watson et al, 1973.

The testing procedure consisted of sample preparation and test execution during thaw. Kaolin clay slurry was mixed and consolidated in a small preparation centrifuge. After consolidation an initial vane shear test was carried out to assure sufficient undrained shear strength before freezing. The sample was subsequently frozen in a commercial Bosch GSL11425GB freezer at -18 ° C for 24 hours. After freezing the sample was placed in a climate controlled room for the thaw procedure. After a predetermined thawing period to assure a sufficient level of soil thaw, the test execution commenced. Vane shear tests were carried out at specified spots in the soil sample, Fig. 2. These were located at opposite corners. Following the vane shear test a thermometer was inserted into the cavity created by the vane, and the internal soil temperature was measured. The surface temperature in the middle of the sample, room temperature and relative humidity of the room were measured after each vane test. After test execution the sample remained in the climate controlled room until the following day, when a further test was carried out to estimate the residual undrained shear strength at full thaw.

Two tests were performed. In the first test the sample container was isolated in order to thaw mainly through one-dimensional diffusion. The sample was

removed from the freezer at 6:30 in the morning. Due to the limited thaw time and the isolation, the sample remained too hard to test that day. The following day the sample had reached residual strength and no thermal degradation could be observed. Another sample was prepared, and removed from the freezer the night before testing. No isolation was used. This time the sample was soft enough for vane shear testing. Table 1 shows test conditions and test duration. Table 2 shows Atterberg limits and undrained shear before the test, and at residual state.

During the test execution, nine vane shear tests were performed. As a result of the slow shear strength degradation of the first sample, an initial test interval of 2 hours was chosen. However, the second vane test showed a large reduction in undrained shear strength. A new test interval of one hour was therefore adopted. After the final test, the clay sample remained in the climate room for 9 hours, after which an additional vane shear test was completed.

Table 1 Test data

Freezing temperature	Thawing temperature	Relative humidity during thaw	Thaw time before test start	Test duration	Time before residual test
-18 ° C	24.5 ° C	33%	9 h.	9 h	33 h

Table 2 Soil properties

Liquid limit	Plastic limit	Plasticity index	Strength before freezing	residual shear strength
35	68	33	18.5 kPa	17.6 kPa

3 Results

Fig. 3a shows the undrained shear strength plotted against the length of the thaw (in hours) at the time of the vane test. The residual undrained shear strength is reached relatively quickly. In Fig. 3b the undrained shear strength is plotted against the internal temperature in the soil at the location of the test (the thermometer had been inserted into the cavity created by the vane). A large reduction in undrained shear strength is seen until an internal temperature of approximately 18° C, where an asymptotical residual strength is observed. The test of residual properties, carried out 15 hours after end of the previous test, suggests that residual strength is reached relatively quickly after thaw has commenced. A reduction in strength is seen after 16h in Fig. 3b where the measured value is lower than the residual shear strength. The reason might be the influence of nearby sample disturbances, given that the sample location was in the center of the container.

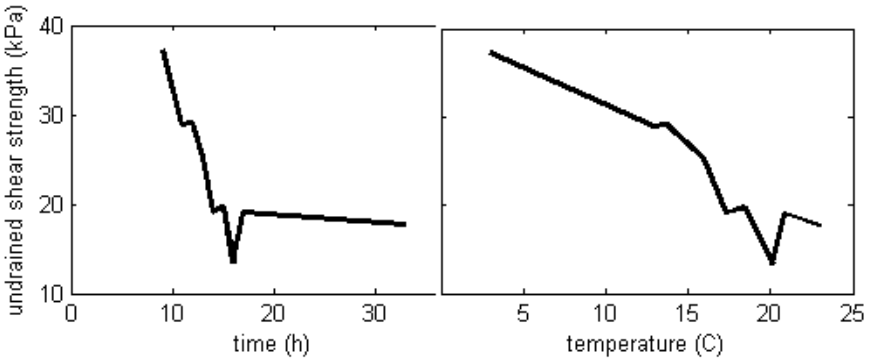

Fig. 3a Strength decay against time **Fig. 3b** Strength decay against temperature

4 Discussion and Conclusions

The results indicate that the assumption about thermal reduction of undrained shear strength during thaw of frozen soil was correct. The hypothesis about exponential decay could not be corroborated because of the non-continuous decay of the undrained shear strength with temperature. The results indicate a quadratic or linear rate of decay. A larger number of tests are needed to clearly distinguish the rate of strength reduction throughout the thaw process, especially after large strength reduction is observed. Also, isolation of the sample during the test execution phase will improve test quality. The reduction in undrained shear strength could moreover be the results of disturbances in the soil after the first test, after which a large strength reduction was observed. The fast thaw process could also have influenced the strength degradation.

Nonetheless, the large difficulties in performing a large number of tests at different temperatures imply that adequate simplification must be made to capture the main features of the strength reduction. The demonstrated test method is an addition to the rather limited number of current procedures to test these soils. For practical applications a sample from the field must be efficiently tested during thawing to estimate the reduction of strength. This strength can then be compared to a thermal profile to estimate the bearing capacity of the soil. Sample properties, test, and sampling variability must be taken into account to give information about the strength of the soil during permafrost thaw.

To conclude, vane shear tests were made to explore the change in undrained shear strength for a thawing clay soil after freezing. The result shows a temperature-dependant large reduction in undrained shear strength, which reaches a residual value as the temperature increases. These mechanisms must be taken into account for accurate description of permafrost thaw, especially when the temperature of the active soil layer is relatively low.

References

Andersland, O.B., Al Nouri, I.: Time-Dependent Strength Behaviour of Frozen soils. Journal of Soil Mechanics – ASCE Division 96(4), 1249–1265 (1970)

Chijimatsu, M., Fujita, T., Kobayashi, A., Nakano, M.: Experiment and validation of numerical simulation of coupled thermal, hydraulic and mechanical behaviour in the engineered buffer material. International Journal for Numerical and Analytical Methods in Geomechanics 24(4), 401–424 (2000)

Duarte, C.M., Lenton, T.M., Wadhams, P., Wassmann, P.: Abrupt climate change in the Arctic. Nature Climate Change 2, 60–62 (2012)

Jorgenson, M.T., Shur, Y.L., Pullman, E.R.: Abrupt increase in permafrost degradation in Arctic Alaska. Geophysical Research Letters 33, 45–49 (2006)

Nicolsky, D.J., Romanovsky, V.E., Panteleev, G.G.: Estimation of soil thermal properties using in-situ temperature measurements in the active layer and permafrost. Cold Regions Science and Technology 55(1), 118–129 (2009)

Osterkamp, T.E., Romanovsky, V.E.: Evidence for warming and thawing of discontinuous permafrost in Alaska. Permafrost and periglacial Processes 12(2), 154–162 (1999)

Watson, G.H., Slusarchuk, W.A., Rowley, R.K.: Determination of some frozen and thawed properties of permafrost soils. Canadian Geotechnical Journal 10(4), 592–606 (1973)

Williams, P.J.: Permafrost and climate change: geotechnical implications. Phil. Trans. Royal Soc. A 352, 347–358 (1995)

Xu, J., Abdalla, B., Eltaher, A., Jukes, P.: Permafrost thawing-pipeline interaction advanced finite element model. In: OMEA 2009, Honolulu, Hawaii (2009)

Tests in Thermo-Hydraulic Cells to Simulate the Behavior of Engineered Barriers

M.V. Villar, R. Gómez-Espina, P.L. Martín, and J.M. Barcala

CIEMAT, Avd. Complutense 40, 28040
Madrid, Spain
mv.villar@ciemat.es

Abstract. Laboratory tests in thermo-hydraulic cells that simulate the conditions of the sealing material in a radioactive waste repository are very useful to identify and quantify processes taking place in the engineered barrier. This kind of tests have gone on at CIEMAT for the last 20 years, evolving from simple designs in which just temperatures inside the material were measured, to the current designs that involve the measurement of temperature and relative humidity, total pressure and water intake. Tests kept running for different periods of time (up to several years) and the analysis of the material upon dismantling included mineralogical, geochemical, microstructural, hydro-mechanical and chemical studies, what allowed gaining insight into the time evolution of the properties of the barrier.

1 Introduction

The design of radioactive waste repositories in deep geological media includes the construction of a barrier around the waste containers constituted by a sealing material, usually bentonite-based. The behaviour of a repository is determined to a large extent by the changes that may occur in the properties of the engineered barrier as a result of the combined effects of the heat generated by the radioactive decay and of the water and solutes supplied by the surrounding rock. Since the performance of large-scale tests is complicated and time-consuming and the boundary conditions in them are not always well controlled and known, laboratory tests in thermo-hydraulic (TH) cells that simulate the conditions of the sealing material during operation are a valuable alternative to identify and quantify processes. Tests of these kinds were carried out at CIEMAT laboratories for the last 20 years, involving different materials, dimensions, instrumentation and operation times.

2 Cells Design

In the TH cells the sealing material can be subjected simultaneously to heating and hydration (Fig. 1). They are cylindrical and designed to be hermetic and non-deformable. The heat generated by the radioactive decay of the wastes in the containers is simulated by an electric heater and the simulated groundwater is injected

L. Laloui and A. Ferrari (Eds.): Multiphysical Testing of Soils and Shales, SSGG, pp. 137–142.
springerlink.com

(usually at pressures around 1 MPa, although this factor was seen not to affect greatly the hydration rate) through a porous stone or a stainless steel sinter that assures a uniform distribution of water over the sample surface.

The first TH cells used at CIEMAT (CT cells) were manufactured in stainless steel to avoid the deformation by the high swelling pressures expected to be developed by the bentonite on saturation (Villar et al. 2005). The bentonite was compacted directly inside the cell, the resulting block having approximately 15 cm in diameter and 13-15 cm in length. Hydration took place through the bottom of the cell and the heater was placed in the upper part of the cell. Three heater configurations were used: a plane heater of the same diameter as the bentonite block, an axial heater of 10 cm length, and a small heater placed in the middle of the upper surface of the block. The bentonite was instrumented with thermocouples and the water intake was measured with an electronic volume change apparatus.

In order to reach higher degrees of saturation in a shorter time, a small, cylindrical, hermetic cell was designed, the CA cell (Villar 1995). The compacted sample (7.6 cm length, 3.8 cm diameter) was placed inside the cell, which was designed to provide facing hydraulic and thermal gradients and isotherms parallel to the sample ends. The cell had an external body made of stainless steel and an internal 5-mm thick Teflon jacket whose role was to avoid as much as possible the heat transmission along the cell walls. The cell was closed by a stainless steel lid on top perforated in the middle to allow the injection of water through it. The base of the cell was made of stainless steel and it was placed directly on a heating plate. No parameters were measured online, and the water intake was estimated from the difference between the final and the initial weight of bentonite.

To simulate the whole thickness of the barrier in the Spanish reference concept, cells of inner length 60 cm and internal diameter 7 cm were manufactured in Teflon (cells CG-60) (Villar et al. 2008). To avoid the deformation of the cell by bentonite swelling, they were externally covered with steel semi-cylindrical pieces. Several blocks of compacted bentonite were stacked inside these cells, in this way, some information about the effect of joints in the barrier could be gathered. The bottom part of the cells was a flat stainless steel heater (set usually at temperatures between 100 and 140°C) and over the upper lid of the cell there was a deposit in which water circulated at a controlled, lower temperature, so that to generate a constant thermal gradient. Hydration took place through the upper surface. The kind of water used could be deionised or simulate the groundwater in the host rock where the repository is excavated. The water intake was measured as a function of time in some of the tests with an electronic volume change equipment. The first version of these cells was instrumented with thermocouples inserted in the bentonite at different levels along the column, whereas newer ones were instrumented with capacitive sensors measuring relative humidity and temperature. It was possible to change their modular configuration so that to have columns of 20, 40 or 50 cm length (cells CG-20, CG-40, CG-50). The most recent version of these CG cells included the insertion of a load cell on top, to measure the pressure exerted by the material on saturation, the measurement of the heater power, an extra

external isolation around the cell body (necessary when working with materials of very low thermal conductivity, such as materials with low initial degrees of saturation), and a change of the water intake measuring system. The new method consisted of a low pressure bladder accumulator filled with the hydration water and connected to the hydration line, whose weight is continuously measured by means of a load cell. The duration of the tests in this kind of cells spanned from 0.5 to more than 9 years (still running).

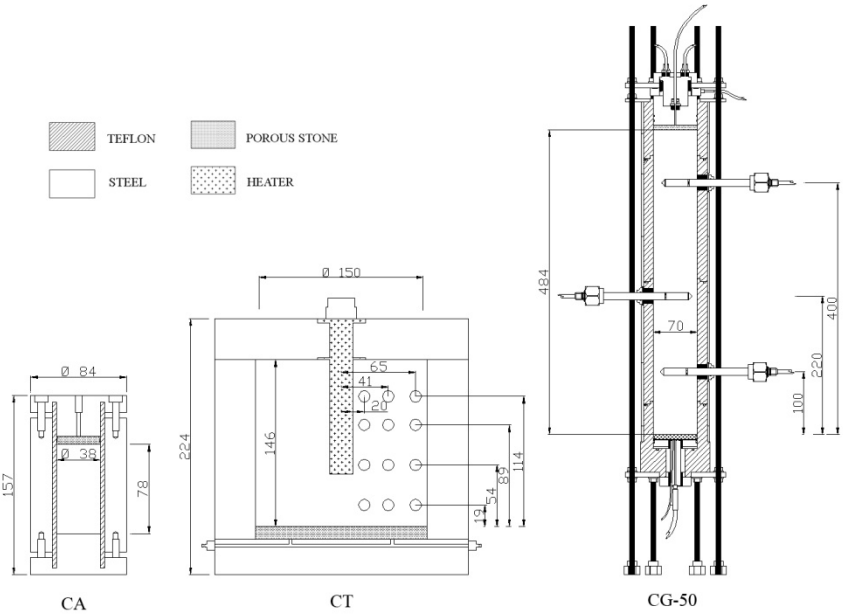

Fig. 1 Schematic representation of thermo-hydraulic cells CA, CT and CG-50

3 Overview of Results Obtained

Among the online information provided by the tests in cells, temperature was the most reliable. It was mainly affected by the boundary conditions, particularly by the heater temperature and geometry, the geometry of the cell and the materials it was made of, the external isolation and, to a lesser extent, by the thermal conductivity of the material tested. For example, in the CT cells the high thermal conductivity of the steel cell walls greatly affected the shape of the thermal field inside the bentonite (Fig. 2). The steady state was quickly reached for all the configurations (less than 48 h) and the subsequent changes of water content, usually slow, gave place to slight changes in the temperature field.

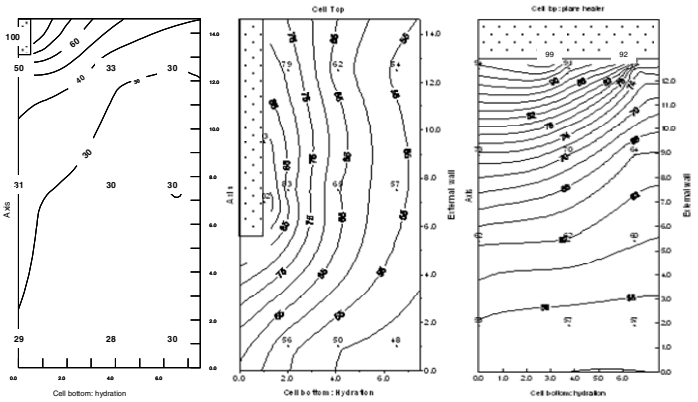

Fig. 2 Isotherms in tests performed with compacted bentonite in stainless steel CT cells with different heater configurations set at 100°C (half section of the cells)

Relative humidity (RH) is another parameter of great interest that could be followed online. The accuracy of the measurements depends on the range of RH, and the sensors are usually sensitive to high temperatures and salinities. The RH of the material was greatly affected by thermal gradient and depended on the proximity to the heater or the hydration surface. Thus, heating imposed a movement of water vapour from the hot areas to cooler ones, what was reflected by a sharp increase in relative humidity in the sensors closest to the heater, followed by a gradual decrease that was recovered in the long term. Fig. 3 shows the different evolution of RH inside a 40-cm long bentonite column hydrated under thermal gradient (left) and at isothermal conditions (right) in cells CG-40.

Postmortem analyses were performed in samples taken along the columns and at different radius. In cells CA and CG the geometry could be considered uniaxial. The thermal and hydraulic gradients during operation gave place to water content gradients that tended to homogenise over time. This could be clearly observed in tests performed under the same conditions for different periods of time (Fig. 4, left). Since the tested materials were expansive, particularly the bentonite-based ones, the water content increase implied swelling and dry density decrease. The cells being confined volumes, the swelled bentonite pushed neighbouring areas of lower water content, causing their compression and consequent dry density increase, which was enhanced by the shrinkage due to drying (Fig. 4, right).

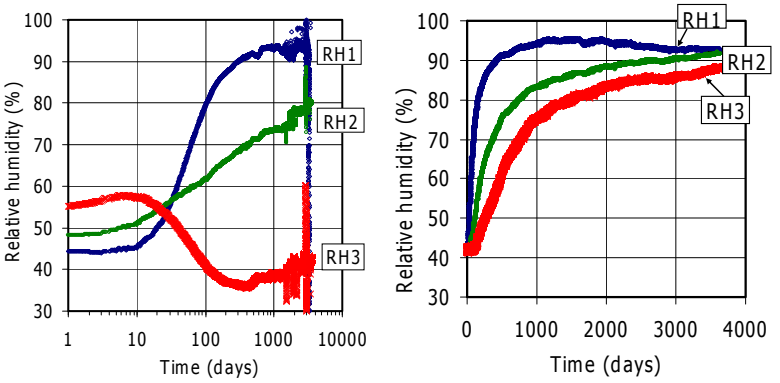

Fig. 3 Evolution of relative humidity inside FEBEX bentonite columns in cells CG-40 heated at 100°C (left) and isothermal (right). Sensor RH1 at 30 cm from the heater, RH2 at 20 cm and RH1 at 10 cm

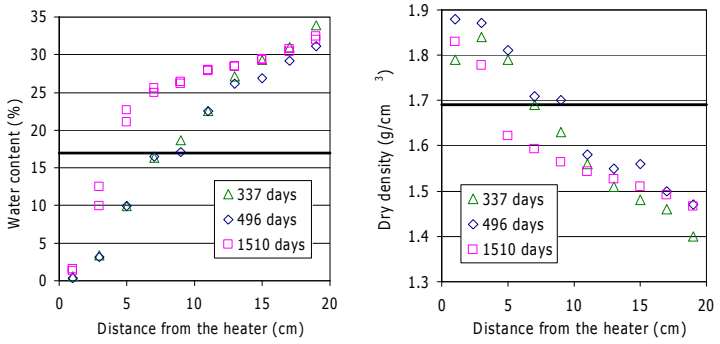

Fig. 4 Final dry density in 20-cm long MX-80 bentonite columns after different periods of TH treatment in CG-20 cells. The horizontal lines indicate the initial value (Gómez-Espina & Villar 2010)

The chemical analyses of the samples upon dismantling allowed the verification of the movement of soluble species by advection and diffusion. A way to determine changes in the chemical composition of the pore water is the performance of aqueous extracts in which the concentration of ions was measured. Clear changes in the composition of the cation exchange complex were also observed. Pore size distribution by mercury intrusion porosimetry and specific surface area were also usually measured. In some tests permeability, swelling pressure and swelling capacity were determined in intact or remoulded samples, since these properties are key to evaluate the actual performance of the barrier. All these properties were related to dry density.

4 Concluding Remarks

The tests in thermo-hydraulic cells are an effective and simple way to reproduce the state of the sealing material in a repository under controlled boundary conditions. One of the problems found is the reproduction of the actual temperatures and thermal gradient, what is due to the differences in geometry and size. The thermal distribution is affected by the geometry of the assembly (the component's areas, the properties and thicknesses of the materials and interfaces), so the best parameters to reflect the ability of the material to transfer heat would be thermal resistance or thermal impedance, which should be determined individually for each test configuration. Thus, even within the same cell configuration, the change of the tested material can induce drastic changes in the temperature distribution. Usually the temperatures reached in a laboratory test, for a given heater/container temperature, are lower than the real ones. This difference can be reduced by improving the external isolation of the cell. Another problematic issue is the sealing of the cells, *i.e*. the assurance of their air-tightness, which can be jeopardised by the deterioration of o-rings and the defective sealing of the sensors' ports.

With respect to the variables measured online, the water intake has demonstrated to be the most problematic in long-term tests, due to the drift over time of the measuring devices (balances, water volume change apparatus). This has been overcome by using deposits continuously weighted by load cells. Finally, the harsh conditions inside the material (high temperature and salinity) can be challenging for the long-term performance of the sensors, although the capacitive sensors with connections appropriately modified have proven to be robust enough.

Acknowledgments. The research leading to these results has received funding from the European Atomic Energy Community's Seventh Framework Programme (FP7/2007-2011) under Grant Agreement n°249681, the PEBS project.

References

Gómez-Espina, R., Villar, M.V.: Geochemical and mineralogical changes in compacted MX-80 bentonite submitted to heat and water gradients. Applied Clay Science 47, 400–408 (2010)

Villar, M.V.: Thermo-Hydro-Mechanical characterization of the Spanish reference clay material for engineered barrier for granite and clay HLW repository: Laboratory and small mock-up testing. Publicación Técnica ENRESA03/95. Madrid, p. 251 (1995)

Villar, M.V., Martín, P.L., Barcala, J.M.: Modification of physical, mechanical and hydraulic properties of bentonite by thermo-hydraulic gradients. Eng. Geol. 81, 284–297 (2005)

Villar, M.V., Fernández, A.M., Martín, P.L., Barcala, J.M., Gómez-Espina, R., Rivas, P.: Effect of heating/hydration on compacted bentonite: tests in 60-cm long cells. Colección Documentos CIEMAT, Madrid, p. 72 (2008)

Influence of Freeze-Thaw Action on Hydro-mechanical Behavior of Unsaturated Crushable Volcanic Soils

Tatsuya Ishikawa[1] and Tetsuya Tokoro[2]

[1] Faculty of Engineering, Hokkaido University
t-ishika@eng.hokudai.ac.jp
[2] Tomakomai National College of Technology
t-tokoro@civil.tomakomai-ct.ac.jp

Abstract. The objective of this study is to evaluate the effect of freeze-thaw action on the strength and water retention-permeability characteristics of crushable volcanic coarse-grained soils in unsaturated conditions. A series of triaxial compression tests, water retention tests and permeability tests were performed for volcanic coarse-grained soils under different freeze-thaw histories. Test results showed that the particle breakage caused by the freeze-thaw action made the shear strength in unsaturated conditions decrease and the water retentivity increase, while not affecting the permeability. These indicate that the freeze-thaw action has strong influences on the hydro-mechanical characteristics of a crushable volcanic coarse-grained soil in unsaturated conditions even if the soil lacks in frost-susceptibility.

1 Introduction

In Hokkaido, a cold and snowy island in northern Japan, a natural disaster such as slope failure at cut slope is often occurred in snow-melting season. Figure 1 shows a type of slope failure mechanism for frost-heaving and thawing surface layer observed in the snowy cold regions. For example, in the slope failure of plastic-flow type, the surface failure regarding a boundary surface between loose thawing soil and hard frozen soil as a slip surface occurs by the water infiltration due to rainfall and snowmelt. The natural disaster in cold regions is deemed to be caused by both the increase in degree of saturation arising from snow-melting and thaw of ice lens within soils and the change in deformation-strength characteristics of soils resulting from freeze-thaw action. Much of Japan is covered by volcanic soils, which have been produced since the quaternary period due to volcanic activity. Even in Hokkaido, volcanic soils are widely distributed over 40% of the total area. As volcanic coarse-grained soils generally show non-frost-susceptibility, so far little attention has been paid to the volcanic coarse-grained soils, wherein significant particle breakage occurs even under relatively low stress levels, i.e., the subsurface layer subjected to freeze-thaw action with snowfall.

L. Laloui and A. Ferrari (Eds.): Multiphysical Testing of Soils and Shales, SSGG, pp. 143–148.
springerlink.com

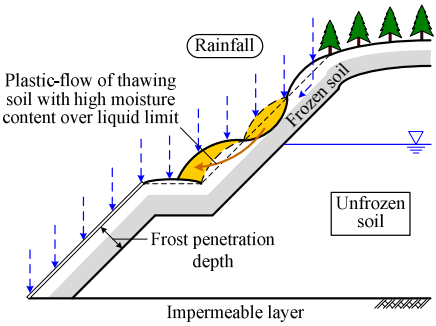

Fig. 1 Slope failure mechanism for frost-heaving surface layer in snow-melting season

This study evaluates the effect of freeze-thaw action on the strength characteristics and water retention-permeability characteristics of crushable volcanic coarse-grained soils in unsaturated conditions. A series of triaxial compression tests and water retention tests and permeability tests were performed for volcanic coarse-grained soils under different freeze-thaw histories.

2 Methodology

2.1 Test Apparatus and Test Materials

Ishikawa et al. [1] developed a freeze-thawing triaxial apparatus for unsaturated soils and a freeze-thawing permeability apparatus for unsaturated soils that could be used to reproduce a freeze-thaw sequence to a cylindrical specimen, as experienced by in-situ soils in cold regions. Details of the test apparatuses and measurements of the various state quantities are provided in previous work [1].

Two different volcanic coarse-grained soils, namely Kashiwabara volcanic soil and Touhoro volcanic soil, were employed as a test material. Details of the test materials are provided in previous works [2][3]. According to a past study [4], these volcanic soils have exhibited extremely low maximum and minimum densities because they are particularly porous constituent particles with a large number of intra-particle voids. In addition, it has been shown that these volcanic soils are non-frost susceptible geomaterials though the densification of particle structure occurs by particle breakage due to freeze-thawing [2].

Cylindrical specimens of volcanic soils for triaxial compression tests and permeability tests were prepared by the air pluviation (AP) method [5], a procedure that adjusts the falling height of test samples so that the density after consolidation (ρ_{dc}) equals the in-situ density. To ensure an experimental accuracy from the ratio of the maximum particle size versus the specimen size, the large soil particles above certain specified grain sizes were screened out from the original sample while preparing the test specimens. Details of the methods for the preparation of test specimens used in this study are provided in previous work [2][3].

2.2 Test Program

In this study, triaxial compression tests, water retention tests and permeability tests were performed on unsaturated volcanic coarse-grained soils before and after freeze-thaw. According to "Test method for frost susceptibility of soils (JGS 0172-2003)", freeze-thaw of the quasi-saturated specimen was one-dimensionally conducted with open-system freezing which allows water inflow/outflow from the specimen during freeze-thawing. On the back of the freeze-thaw process, two kinds of laboratory element tests were performed as explained below. Monotonic loading triaxial compression tests on a specimen with various degrees of saturation were performed in fully drained condition (CD test) under a prescribed constant net normal stress (σ_{net}) of 49 kPa. In addition, a particle size analysis was conducted before and after each test to assess the degree of particle breakage that transpired throughout the test. On the other hand, constant head permeability tests for unsaturated soils were carried out by steady-state method under a prescribed constant σ_{net} of 49 kPa. In the permeability test, the measurement of the coefficient of permeability corresponding to a given matric suction or water content was repeated by increasing the matric suction in steps. The axis-translation technique was adopted to set an intended matric suction, which was achieved by decreasing pore water pressure while keeping confining pressure and pore air pressure constant. Moreover, the volume of water inflow and outflow during each increment of matric suction was measured, and was used in calculating the water content of the specimen, thereby yielding the soil-water characteristic curve during the drying process and the coefficients of permeability from a single test specimen. For detail information about testing methods, former studies [1][2] is to be referred.

3 Results and Discussions

3.1 Influences on Strength Characteristics

Figure 2a shows the relationships between the peak shear strength (q_f) and the matric suction (s) obtained from the test results on both volcanic soils undergoing different freeze-thaw histories. Here, N_f=0 shows the results of non freeze-thawed specimen, and N_f=1 shows those of freeze-thawed specimens. For plots with the same matric suction, the peak shear strength of a freeze-thawed specimen drops as compared with that of the non freeze-thawed specimen irrespective of matric suction or degree of saturation despite the fact that the small increase in the density was caused by freeze-thaw. Meanwhile, regardless of the freeze-thaw history, the peak shear strength decreases with decreasing matric suction as expected. However, the influence of the water content on the peak shear strength of crushable volcanic coarse-grained soils is insignificant in comparison with the influence of the freeze-thaw action.

The degradation in the deformation-strength characteristics of saturated volcanic coarse-grained soils has to do with the increase in the fine content arising from freeze-thaw action [3]. Figure 2b shows the relationships of freeze-thawed and

non freeze-thawed specimens between the increment of fine content (ΔF_c) through a test and the matric suction (s). It illustrates that particle breakage of both volcanic soils becomes more pronounced by the freeze-thaw action. The graph also shows a consistent increasing tendency of particle breakage with decreasing matric suction, which indicates that specimens with high water content are crushed to a greater extent than dry specimens. The tendency similar to the above-mentioned results can be observed in the relationships of peak shear strength to matric suction as shown in Figure 2a. Accordingly, the particle breakage, mainly the particle breakage caused by freeze-thaw, is closely related to the decrease in peak shear strength of crushable volcanic soils, under unsaturated conditions too.

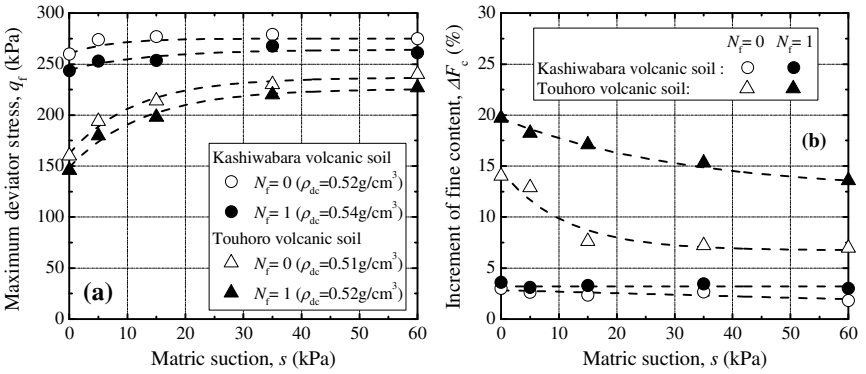

Fig. 2 Influences of freeze-thaw on (a) peak strength and (b) particle crushability

3.2 Influences on Water Retention-Permeability Characteristics

Figure 3a shows soil-water characteristic curves (SWCCs) along a drying process obtained from the test results on both volcanic soils undergoing different freeze-thaw histories. Figure 3b compares the relationships of the coefficient of permeability (k_w) to the matric suction (s), obtained from the same tests as Figure 3a. For the plots with the same degree of saturation (S_r) in Figure 3a, the matric suction of a freeze-thawed specimen, namely the water retentivity, rises as compared with that of the non freeze-thawed one, though the shape of the SWCCs with unclear air-entry values are almost unchanged. The reason seems to be due to the grain refining of crushable volcanic soils mainly caused by freeze-thaw, which ultimately results in a gradual increase in the water retentivity of the soil. This tendency agrees well with a past research which reports the variation of the SWCC arising from the change in grain size distribution [6].

On the other hand, the coefficient of permeability decreases inversely with the increase in the matric suction as expected. However, the freeze-thaw history has little influence on the decreasing tendency of k_w with matric suction as contrasted with the effect of the SWCC, and for every volcanic soil the relationship seems to be approximated as a curve with a slight dispersion regardless of the presence or

absence of freeze-thaw process, as shown in Figure 3b. These results indicate a possibility that under the real in-situ condition where the constant pore water pressure due to the specified groundwater level is applied at the atmospheric pressure, namely under the constant matric suction, the freeze-thaw action induces the increase in the fine content due to particle breakage at the fragmental volcanic soil ground, and thereby leads to the rise in the water retentivity while keeping the hydraulic conductivity constant. However, there is room for further investigation as to a validity of the above-mentioned tendencies in higher suction range.

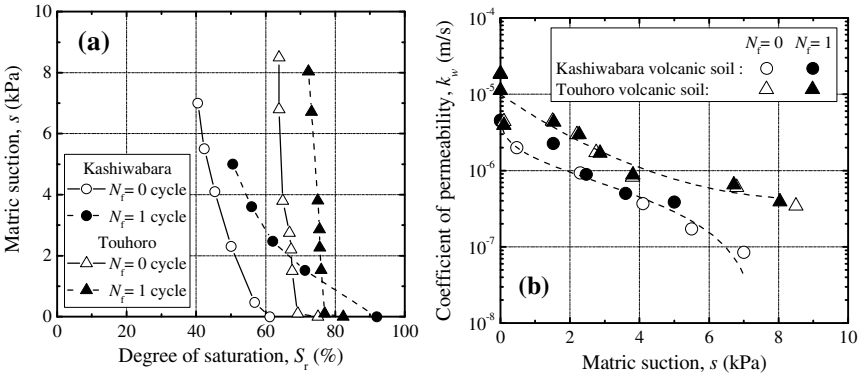

Fig. 3 Influence of freeze-thaw on (a) water retentivity and (b) permeability

4 Conclusions

From the findings in this study, it seems reasonable to conclude that a freeze-thaw action has strong influences on the hydro-mechanical behavior of a crushable volcanic coarse-grained soil in unsaturated conditions even if the soil is a non-frost susceptible geomaterial. Figure 4 summarizes the influences of freeze-thaw action on the hydro-mechanical characteristics of unsaturated volcanic coarse-grained soils, which have been revealed from this study. In general, the slope failure due to rainfall in warm regions is mainly caused by a) the increase in weight of soil mass, b) the decrease in suction of unsaturated soil with the increase in water content and c) the increase in pore water pressure with the rise in groundwater level and seepage pressure [7]. With consideration given to Figure 4, at the fragmental volcanic soil ground in cold regions, the increase in the unit weight of the soil and the degradation in the strength property with particle breakage owing to freeze-thawing may lead to a surface slope failure at thawing seasons. Accordingly, even if replacing frost susceptible geomaterials with non-frost susceptible volcanic coarse-grained soils for the construction of new roads and railroad, sufficient attention should be given to the influence of the freeze-thaw action on the stability of the embankment and/or the cut slope in terms of design and maintenance, in addition to the exogenous factors of slope failure in warm regions.

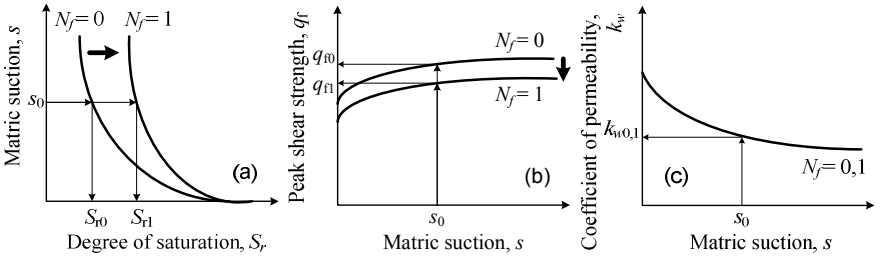

Fig. 4 Conceptional effects of freeze-thaw on (a) SWCC, (b) strength and (c) permeability

References

Ishikawa, T., Tokoro, T., Ito, K., Miura, S.: Testing methods for hydro-mechanical characteristics of unsaturated soils subjected to one-dimensional freeze-thaw action. Soils and Foundations 50(3), 431–440 (2010)

Ishikawa, T., Miura, S., Tokoro, T.: Effect evaluation of freeze-thaw action on hydro-mechanical behavior of unsaturated granular materials. In: 17th International Conference on Soil Mechanics and Geotechnical Engineering, Alexandria, October 5-9, vol. 1, pp. 833–836 (2009)

Ishikawa, T., Miura, S.: Influence of freeze-thaw action on deformation-strength characteristics and particle crushability of volcanic coarse-grained soils. Soils and Foundations 51(5), 785–799 (2011)

Miura, S., Yagi, K. (2003) Mechanical behaviour and particle crushing of volcanic coarse-grained soils in Japan. In: Characterisation and Engineering Properties of Natural Soils Singapore, pp. 1169–1203, December 2–4 (2002)

Miura, S., Toki, S.: A sample preparation method and its effect on static and cyclic deformation-strength properties of sand. Soils and Foundations 22(1), 61–77 (1982)

Fredlund, M.D., Fredlund, D.G., Wilson, G.W.: Prediction of the soil-water characteristic curve from grain-size distribution and volume-mass properties. In: Proceedings of 3rd Brazilian symposium on Unsaturated Soils, Rio de Janeiro, April 22-25, pp. 1–12 (1997)

Kitamura, R., Sako, T.: Contribution of “Soils and Foundations” to studies on rainfall-induced slope failure. Soils and Foundations 50(6), 955–964 (2010)

Plane-Symmetrical Simulation of Flow and Heat Transport in Fractured Geological Media: A Discrete Fracture Model with Comsol

Biguang Chen, Erxiang Song, and Xiaohui Cheng

Department of Civil Engineering, Tsinghua University, Beijing, China

Abstract. Fractured geological formations are ubiquitous in geothermal reservoir and enhanced geothermal system. Because of the fast path formed by fractures and the multirate exchange between fracture and matrix, the system cannot be well modeled by single or multi-continuum models. Discrete fracture and matrix model can explicitly accounting for the geometry of fractrues and the contribution of each individualfracture to fluid flow and heat transport, and the exchange between fracture and matrix.In this paper a discrete fracture model is established and implemented in the commercial FEM software Comsol. The model is validated and then used to simulate a randomly generated fracture network to study the characteristic of flow and heat transport in fractured porous media.

1 Introduction

Hydrothermal systems such as deep geothermal reservoir and enhanced geothermal systems are charaterised by complex interactions between heat transfer, fluid flow, deformation, species transport and chemical reactions. For the lifetime and economy reason, the most important and concerned process is fluid flow and heat transport. The geological formations in the deep geothermal system are usually fractured rock which is extremly heterogenous. Conventional continuum method such as dual-porosity concepts captures the feature that fracture is the main flow pathway and matrix is the main energy storage, but it may not applicable to represent real fracture networks at the comtinuum scale, and it cannot simulate the exchange term between fracture and matrix accurately. Many discrete fracture network(DFN) model only consider the fluid flow in fracture, whichis reasonable when the permeability of rock matrix is very low. But in the heat transport problem, heat extraction from the high tempreture rock matrix is animportant process, which means that the heat transport in matrix and interaction of fracture and rock matrix must be calculated accurately. Discrete fracture and matrix(DFM) model is an useful tool to capture this through embeding the fractures as lower-dimensional element in the matrix, and matrix is also taken into account in the numerical model. But one should be aware that DFM model is computationally expensive because the entire fracture network and matrix need to be computed. It may be powerful in studying the characteristic of

L. Laloui and A. Ferrari (Eds.): Multiphysical Testing of Soils and Shales, SSGG, pp. 149–154.
springerlink.com

fractured porous media in a small scale but it is hard to be used in a site scale simulation.

In this paper a DFM model will be suggested and implemented in Comsol.The model is validated by comparing with analytical solution. Then the model is applied to simulate a randomly generated fracture network.

2 Governing Equations

Here we consider single phase flow and heat transport in the fractured porous media, the permeability of matrix maybe rather low like the granite, and can also be relative high like sandstone and limestone so that the fluid flow in matrix plays a significant role in the transport process. And we assume that the mechanical process is ignorable so that the permeability of fracture and matrix do not change in the simulation.

According to the general theory of transport in porous media, the mass conservation equation and energy conservation equation of matrix are:

$$S\frac{\partial P}{\partial t}+\nabla(-\frac{\kappa}{\eta}\nabla P)=0 \tag{1}$$

$$C\frac{dT}{dt}+\nabla(-\lambda_{eq}\nabla T)+C_w(-\frac{\kappa}{\eta}\nabla P)\cdot\nabla T=0 \tag{2}$$

where S is the storage coefficient, κ is the intrinsic permeability of matrix, η is dynamic viscosity of water(here we assume the work fluid is water), C is volumetric heat capacity of the mixture, which is usually averaged on thevolume, λ_{eq} is effective heat conduction coefficient which is also averaged on thevolume, C_w is volumetric heat capacity of water. In the 3D model equation(1) should also take gravity into account. In the equstion(2) we employ the instant local thermal equilibrium assumption, because the flow velocity in the matrix is very small, the assumption is appropriate. And darcy's law is emploied in both equation (1) and (2).

In the fractures, the governing equations are:

$$d_f S_f\frac{\partial P}{\partial t}+\nabla_T(-\frac{\kappa_f}{\eta}d_f\nabla_T P)=f_{up}{}^f+f_{bottom}{}^f \tag{3}$$

$$d_f C_f\frac{\partial T}{\partial t}+d_f\rho_w c_w\vec{u}_w\cdot\nabla_T T-d_f\nabla_T(\lambda_f\nabla_T T)=f_{up}{}^e+f_{bottom}{}^e \tag{4}$$

where d_f is the aperture of the fracture, S_f is fracutre storage and κ_f is intrinsic permeability of fracture. Actually the fractures are rough and have varying aperture along the length, but in the numerical models the assumption of smooth parallel plates model and cubic law are usually emploied for convenience.

Here we simply assume that $\kappa_f = d_f^2/12$. Similarly, C_f is the volumetric heat capacity of fractures, $\vec{u}_w = \frac{\kappa_f}{\eta}\nabla_T P$ is the darcy velocity of water in fracture. ∇_T means tangential derivatives of P and T. Here another important assumption is that pressure and temperature distribution along fracture cross section is uniform, more complicate situation and theory foundation can refer to the literature(Martin et al., 2005).With this assumption the dimensionality of fracture can be reduced from d to d-1, that is the fractures are lines in two dimensional models or two-dimensional surfaces in three dimensional models. And because the aperture of fracture is usually very small, this assumption is also reasonable.

In the right side of equation (3) and (4), f_i^j is the exchange term between fracture and matrix. Up and bottom stand for matrix from different sides of the fracture. The superscript'f' means fluid flux and 'e' means energy flux. They can be caculated by equations (5):

$$f_{up}{}^{f} = -\frac{\kappa}{\eta}\frac{\partial P_{up}}{\partial n_{up}} \qquad (5a)$$

$$f_{bottom}{}^{f} = -\frac{\kappa}{\eta}\frac{\partial P_{bottom}}{\partial n_{bottom}}$$

$$f_{up}{}^{e} = \rho_w c_w \cdot (-\frac{\kappa}{\eta}\frac{\partial P_{up}}{\partial n_{up}}) \cdot T - \lambda_{eq}\frac{\partial T_{up}}{\partial n_{up}} \qquad (5b)$$

$$f_{bottom}{}^{e} = \rho_w c_w \cdot (-\frac{\kappa}{\eta}\frac{\partial P_{bottom}}{\partial n_{bottom}}) \cdot T - \lambda_{eq}\frac{\partial T_{bottom}}{\partial n_{bottom}}$$

where n_{up} and n_{bottom} are the outward normal directionof the matrix when treating fractures as the boundary of rock matrix. And the form of equation (5) consists with the form of the conservation equations of the matrix, which make sure the accurate calculation of exchange term and conservation of mass and energy in the whole system.

3 The Finite Element Equations

The governing equations can be spatially discretized by the standard GalerkinFEM method. As mentioned above, the dimensionality of fractures is lower than the matrix. In fracture surface the fracture elements have the same node with matrix, which means the nodal variables of fracture elements and matrix elementsare the same in the fracture surface. By substitute the exchange term into the discrete equation (1)-(4), and add the equations of matrix and fracture, we can avoid to explicitly calculate the exchange term in equation (5). The final discretized equations can be expressed by:

$$M_f \frac{\partial P}{\partial t} + K_f P = F_f$$
$$M_e \frac{\partial T}{\partial t} + K_e T = F_e \tag{6}$$

In the equation(6):

$$M_f = \int_\Omega N^T S N d\Omega + \int_\gamma N^T d_f S_f N d\gamma$$

$$K_f = \int_\Omega \frac{\kappa}{\eta} \nabla N^T \nabla N d\Omega + \int_\gamma \frac{\kappa_f}{\eta} d_f \nabla_T N^T \nabla_T N d\gamma$$

$$F_f = \int_{\Gamma_1} N^T \overline{q_f} d\Gamma_1 + \int_{\partial\gamma_1} N^T \overline{Q_f} d\partial\gamma_1$$

$$M_e = \int_\Omega N^T C N d\Omega + \int_\gamma N^T d_f C_f N d\gamma$$

$$K_e = \int_\Omega \lambda_{eq} \nabla N^T \nabla N d\Omega + \int_\gamma \lambda_f d_f \nabla_T N^T \nabla_T N d\gamma + \int_\Omega C_w N^T \left(-\frac{\kappa}{\eta} \nabla P \right) \nabla N d\Omega$$

$$+ \int_\gamma C_w d_f N^T \left(-\frac{\kappa}{\eta} \nabla_T P \right) \nabla_T N d\gamma$$

$$F_e = \int_{\Gamma_1} N^T \overline{q_e} d\Gamma_1 + \int_{\partial\gamma_1} N^T \overline{Q_e} d\partial\gamma_1$$

where Ω is the matrix domain, γ is the fracture domain, Γ_1 and $\partial\gamma_1$ is Dirichlet boundary, N is the shape function, P and T are the nodal pressure and nodal temperature, $\overline{q_f}$ and $\overline{Q_f}$ are the outflow flux of matrix boundary and fracture boundary, $\overline{q_e}$ and $\overline{Q_e}$ are the energy flux of matrix boundary and fracture boundary.

This formulation is implemented in the commercial FEM software Comsol, the stiffness matrix of fracture can be added by modifying the weak terms of the so called interior boundaries which represent the fractures.

4 Validation

In order to demonstrate the accuracy and stability of the DFM model, numerical solution is compared to an analytical solution. Following the concept of Lauwerier, the plane-symmetric solution (Barends, 2010) can consider conduction and convection in the reservoir and thermal bleeding in the overburden. It has the same assumption with the numerical model that the temperature in the cross section of reservoir is the same; the temperature of reservoir and overburden at the interface is the same too. Similar to fracture, this DFM model can also be used to calculate the analytical model of reservoir. Figure 1 shows that numerical solution agrees well with the analytical solution.

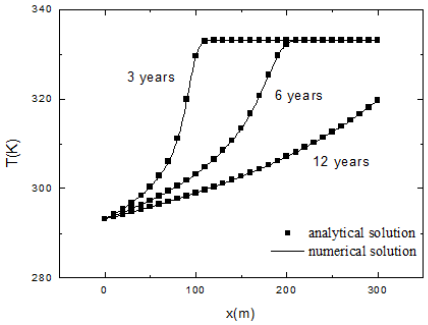

Fig. 1 Temperature along the reservoir in different time

5 Simulations of Fractured Network

The suggested approach is applied to simulate a randomly generated fracture network (see Figure 2). The size of the domain is 20m*20m. Cold water flows into the domain through left boundary and is heated by the hot rock, then flow out through the right boundary. The up and bottom boundary is isolated. The difference pressure of left and right boundary is 100kPa.

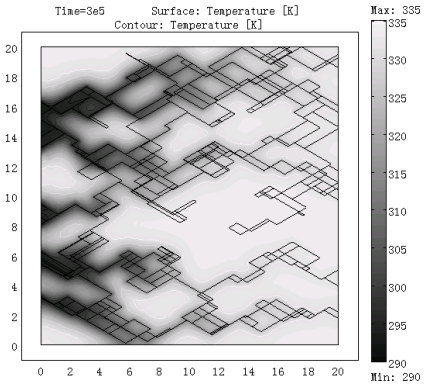

Fig. 2 Temperature distribution in rock matrix and fractures

Some other parameters of the model are in the table 1. It should be mentioned that the fracture network is randomly generated from the statistical data and poor connective fractures are deleted for the computational reason. The aperture and permeability of the fractures can be assigned different but in this model all the fractures are the same.

Table 1 Parameters in numerical model

Initial temperature (K)	Inflow temperature (K)	Fracture permeability (m^2)	Matrix permeability (m^2)
333.15	293.15	1e-8	1e-14

The temperature distribution in rock matrix and fractures after 2.3 days is showed in the figure 2. It shows that fluid follows the preference path and extracts energy from the matrix.

Figure 3 is the breakthrough curves at the right boundary in different matrix permeability. It shows that when matrix permeability is very small the outflow temperature is controlled by fractures and early breakthrough is expected. When matrix permeability is relatively high its influence in flow and heat transport should not be ignored.

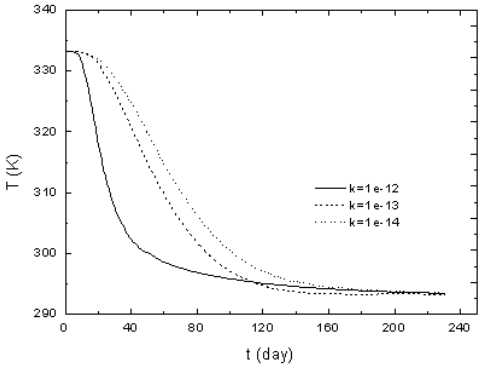

Fig. 3 Temperature distribution in rock matrix and fractures

6 Conclusions

A discrete fracture model has been developed which is used to solve the single phase flow and heat transport problem in fractured geological media. It can accurately calculate the interaction of fracture and rock matrix. The model is implemented in the Comsol software and applied to simulate a fracutre network.

References

Barends, F.B.J.: Complete Solution for Transient Heat Transport in Porous Media, followingLauwerier's concept. In: SPE Annual Technical Conference and Exhibition, Florence (2010)

Martin, V., Jaffré, J., Roberts, J.: Modeling fractures and barriers as interfaces forflow in porous media. SIAM 26, 1667–1691 (2005)

Formulation of Tsinghua-Thermosoil Model: A Fully Coupled THM Model Based on Non-equilibrium Thermodynamic Approach

Zhichao Zhang and Xiaohui Cheng

Department of Civil Engineering,
Tsinghua University,
Beijing, China

Abstract. A fully coupled THM model for saturated soil based on non-equilibrium thermodynamic approach is developed. In the model, THM coupling processes are described by a set of migration coefficient model and energy functions from which constitutive relations of all fields are deduced theoretically. Granular entropy is introduced to describe the interparticle movement and respective non-elastic dissipation, and a mechanical constitutive model without yield surface is established. Conversion from bound pore water to free pore water induced by temperature elevating is considered in the model to simulate thermal-induced consolidation.

1 Introduction

Since the 80s of last century, the THM coupling problem has become an important scientific research focus in many engineering areas such as geothermal resources development, oil exploration and nuclear waste storage. To establish a reasonable THM model is one of the key approaches to assess the impacts of THM coupling process in these fields, and many THM models had been proposed by researchers[1~4]. Irreversibility is one of the most important features of THM coupling processes in soils, e.g., irreversible thermal contraction of saturated clay[5,6], so it cannot be described by simple elastic theory. Therefore, many THM models introduce classical elasto-plastic constitutive model considering the influence of temperature, e.g., the thermal Cam-clay model[7,8]. Another useful approach for THM problem in soils may be the non-equilibrium thermodynamic approach. Based on this approach, Yiming Jiang[9] proposes a new elasto-plastic constitutive model without giving the yield surface, flow rules and hardening or softening rule in advance. In this paper, such an approach is extended to THM problem and a fully coupled THM model is developed for saturated soil.

L. Laloui and A. Ferrari (Eds.): Multiphysical Testing of Soils and Shales, SSGG, pp. 155–161.
springerlink.com

2 Basic Equations of the Model

2.1 General Assumptions

(1) Assumed that the soil material can be divided into solid phase and liquid phase. The liquid phase is composed of free pore water and bound pore water. Bound water can be converted to free water by temperature elevating, but there is no mass exchange between solid phase and liquid phase.
(2) Assumed that every phase is continuous in space, and the overall conservation and entropy equations can be expressed into the superposition of the corresponding equations of every phase.
(3) Assumed that all phases have the same temperature. Assumed that there is no solidification and vaporization for liquid phase in the temperature range considered in this paper, and the soil always maintain saturation state.

2.2 Mass Conservation Equation

The mass conservation equations of solid phase, free water and bound water are

$$d_t[\rho_s(1-\phi_1-\phi_2)] = \rho_s(1-\phi_1-\phi_2)d_t\varepsilon_{kk} \tag{1a}$$

$$d_t(\rho_{fw}\phi_1) = -\rho_{fw}[\phi_1(V_k - v_k)]_{,k} - \phi_1(V_k - v_k)\nabla_k\rho_{fw} + \rho_{fw}\phi_1 d_t\varepsilon_{kk} + Q \tag{1b}$$

$$d_t(\rho_{bw}\phi_2) = \rho_{bw}\phi_2 d_t\varepsilon_{kk} - Q \tag{1c}$$

where, d_t is material derivative of solid phase, and it has a relation $d_t = \partial_t + v_k\nabla_k$ with spatial derivative ∂_t; ρ_s, ρ_{fw} and ρ_{bw} are the densities of solid phase, free water and bound water respectively; $d_t\varepsilon_{kk}$ is the volumetric strain rate of solid skeleton (the strain and stress are all taken compression as positive in this paper); V_k and v_k are the velocities of solid phase and free water respectively; ϕ_1 and ϕ_2 are porosity of free water and bound water respectively; $\phi_1(V_k - v_k)$ is the flow velocity of free water; Q is the conversion rate from bound water to free water induced by temperature elevating and can be $Q = \rho_{bw}\alpha_{bf}\phi_2 d_t T$, where α_{bf} is a conversion rate parameter and T is the temperature. The flow velocity is

$$\phi_1(V_i - v_i) = -\frac{K}{\mu}\nabla_j p + \frac{K}{\mu}\rho_{fw}g_k - \frac{K}{\mu}\theta_{ij}\nabla_j T \tag{2}$$

where, p is pore pressure; K is the intrinsic permeability; μ is kinematic viscosity of water; g is the gravity acceleration; The three terms in the right of eq.(2) represent Darcy flow, density flow and flow directly induced by temperature gradient, respectively; θ_{ij} is a thermal coupling coefficient.

2.3 Momentum Conservation Equations

Provided that the stress of solid phase, free water and bound water are σ_{ij}^{s}, σ_{ij}^{fw} and σ_{ij}^{bw}, the overall momentum conservation can be described as the eq.(3).

$$\begin{aligned}&\rho_s(1-\phi)d_t v_i+\rho_{bw}\phi_2 d_t v_i+\rho_{fw}\phi_1 d_t V_i+(V_j-v_j)\rho_{fw}\phi\nabla_j V_i\\&+\nabla_j(\sigma_{ij}^{s}+\sigma_{ij}^{fw}+\sigma_{ij}^{bw})=g_i[\rho_s(1-\phi)+\rho_{fw}\phi_1+\rho_{bw}\phi_2]\end{aligned}\tag{3}$$

The firth and fifth terms of the left of eq.(3) represent the momentum changes per time induced by convection and the stress on element boundary, respectively.

2.4 Entropy Equation

According to the second law of thermodynamics, any irreversible processes must cause the increase of entropy. Thus, the entropy equation is

$$\rho_s(1-\phi)d_t\upsilon_s+\rho_{fw}\phi_1 d_t\upsilon_{fw}+\rho_{bw}\phi_2 d_t\upsilon_{bw}=\frac{R}{T}+\nabla_k f_k-(V_k-v_k)\rho_{fw}\phi_1\nabla_k\upsilon_{fw}\tag{4}$$

where, υ_s, υ_{fw} and υ_{bw} are the entropy per mass of solid phase, free water and bound water respectively; R/T represents the total entropy production rate induced by all irreversible processes; $\nabla_k f_k$ and $(V_k-v_k)\rho_{fw}\phi_1\nabla_k\upsilon_{fw}$ represent the entropy changes induced by thermal conduction and convection respectively.

3 Constitutive Relations: Thermodynamic Approach

3.1 Granular Entropy Equation[9]

For granular materials like sand and clay, there is another important energy dissipation mechanism compared to common solid materials; that is the mesoscopic interactions between particles such as friction, slide, breaking and collision which are important sources of non-elasticity of materials. Here, a new independent state variable *granular entropy* s_2 is introduced to describe these interparticle interactions and it can be linked to non-elasticity by thermodynamic method. The granular entropy equation has a similar form with eq.(4):

$$\rho_s(1-\phi)d_t\upsilon_2=R_2/T_2-I\tag{5}$$

Where, υ_2 is granular entropy per mass of solid phase; ϕ is total porosity of fluid phase, i.e., $\phi=\phi_1+\phi_2$; T_2 and R_2/T_2 are called granular temperature and granular entropy production rate respectively. I represents the conversion form granular entropy to macroscopic entropy increase in the form of heat generation.

3.2 Quantification of Entropy Production R

In non-equilibrium thermodynamic theory[10], variables promoting a thermodynamic system to deviate thermodynamic equilibrium state are called dissipation forces, and entropy production produced by per unit dissipative force is called dissipation flow. According to this theory, entropy production R in the system of saturated soil can be written as:

$$R = \frac{q_k}{T}\nabla_k T + \sigma_{ij}^{(1s)} d_t \varepsilon_{ij} + \sigma_{ij}^{(1f)} V_{ij} + Y_{ij}\pi_{ij} + I_2 T_2 + \chi_i (V_i - v_i) \tag{6}$$

where, $\nabla_k T$, $d_t \varepsilon_{ij}$, V_{ij} ($V_{ij} = (V_{i,j} + V_{j,i})/2$), π_{ij} (called non-viscous granular contact stress), T_2 and $V_i - v_i$ are dissipation forces; the variables in front of them are respective dissipation flows. q_k is flux of thermal conduction; $\sigma_{ij}^{(1s)}$ and $\sigma_{ij}^{(1f)}$ are viscous stress of solid phase and free water; Y_{ij} , I_2 and χ_i are the dissipations flows induced by π_{ij} , granular temperature and convection, respectively.

Then, dissipation flows in eq.(6) can be further modeled by migration coefficient model in non-equilibrium thermodynamics[10]. The followings are simple mathematical forms of three most important dissipation flows.

$$q_i = \kappa_{ij}\nabla_j T + \theta_{ij}(V_j - v_j)\,,\ \kappa_{ij} = \kappa_s (1-\phi)\delta_{ij} + \kappa_f \phi \delta_{ij} \tag{7a, b}$$

$$Y_{ij} = \lambda_s (T_2)^a e_{ij}^e + \lambda_v (T_2)^a \varepsilon_{kk}^e \delta_{ij}\,,\ I_2 = \gamma T_2 \tag{7c, d}$$

where, κ_s and κ_f are thermal conductivity of solid phase and fluid phase; λ_s and λ_v are migration coefficients related to non-viscous dissipation flow Y_{ij} ; a is a constant material parameter; θ_{ij} is coupling coefficient tensor between dissipations generated by convection and heat conduction. C_f is heat capacity of fluid phase. $e_{ij}^e = \varepsilon_{ij}^e - \varepsilon_{ij}^e \delta_{ij}/3$ is the deviator elastic strain.

Similarly, granular entropy production R_2 can be written as:

$$R_2 = \sigma_{ij}^{(2)} d_t \varepsilon_{ij} + M d_t T\ ,\ \ \sigma_{ij}^{(2)} = \eta_2 T_2 d_t \varepsilon_{ij}^* + \zeta_2 T_2 d_t \varepsilon_{kk} \delta_{ij}\ ,\ \ M = \frac{\pi_{kk}\alpha_{bf}\phi_2}{3(1-\phi)} \tag{8a, b, c}$$

where, $\sigma_{ij}^{(2)} d_t \varepsilon_{ij}$ and $M d_t T$ represent granular entropy production activated by macroscopic deformation and conversion from bound water to free water through temperature elevating, respectively. M is a migration coefficient that can describe thermal contraction of saturated soils. η_2 and ζ_2 are migration coefficients related to deviator strain rate ($\varepsilon_{ij}^* = \varepsilon_{ij} - \varepsilon_{kk}\delta_{ij}/3$) and volumetric strain rate, respectively.

3.3 Non-elastic Strain Dissipation

We note the total strain and non-elastic strain as ε_{ij} and ε_{ij}^{D}, respectively, thus the relation between elastic strain, total strain and non-elastic strain can be:

$$d_t\varepsilon_{ij}^{e} = d_t\varepsilon_{ij} - d_t\varepsilon_{ij}^{D} \tag{9}$$

As mentioned in section 3.1, the nonelastic dissipation is activated by granular entropy movement, and nonelastic flow $d_t\varepsilon_{ij}^{D}$ can be deduced theoretically.

$$d_t\varepsilon_{ij}^{D} = Y_{ij} - Y_{ij}^{h}T_2 \tag{10}$$

where, Y_{ij}^{h} is a state variable related to unloading and reloading. Obviously, eq.(10) is also a kind of flow rule but decided by an absolutely different approach compared to classical mechanical constitutive model.

3.4 Stress-Strain Constitutive Relations

The stress of every phase of saturated soil can be theoretically deduced as eq.(6), where ω_e is elastic energy density function, $\sigma_{ij}^{(1s)}$ and $\sigma_{ij}^{(1f)}$ are viscous stress of solid skeleton and free water phase, α is Biot consolidation coefficient.

$$\sigma_{ij}^{s} = \pi_{ij} - \sigma_{ij}^{(1s)} + \alpha p(1-\phi)\delta_{ij},\ \ \pi_{ij} = \partial\omega_e \big/ \partial\varepsilon_{ij}^{e} \tag{11a, b}$$

$$\sigma_{ij}^{fw} = \alpha p\phi_1\delta_{ij} - \sigma_{ij}^{(1f)},\ \ \sigma_{ij}^{bw} = \alpha p\phi_2\delta_{ij} + \phi_2\pi_{kk}\delta_{ij}/[3(1-\phi)] \tag{11c, d}$$

The elastic energy density function is described using elastic strain (see eq.(12)). B is a parameter that has the same dimension with stress and is the function of packing density of granular particles. c is a material parameter represents the bonding effect between particles. K_b and β_T are the bulk volumetric modulus and the elastic expansion coefficient of the granular skeleton respectively; T_0 is called reference absolute temperature; ξ and ς are two dimensionless parameters.

$$\omega_e = B(\varepsilon_{ve}^{e} + c)^{1.5}\left[\frac{2}{5}\varepsilon_{ve}^{2} + \xi\varepsilon_{se}^{2} + \varsigma\frac{(\varepsilon_{III}^{3})^{5/3}}{(\varepsilon_{se}^{2})^{3/2}}\right] + 3K_b\beta_T(T-T_0)\varepsilon_{ve}^{e} \tag{12a}$$

$$\varepsilon_{ve} = \varepsilon_{kk}^{e},\quad \varepsilon_{se} = \sqrt{e_{ij}^{e}e_{ij}^{e}},\quad \varepsilon_{III} = \sqrt[3]{e_{ij}^{e}e_{jk}^{e}e_{ki}^{e}} \tag{12b}$$

Eq.(11b) and eq.(12) provide a bounding surface in e-p'-q space (see figure.1) which is reached when $\det[\partial^2\omega_e \big/ (\partial\varepsilon_{ij}^{e}\partial\varepsilon_{kl}^{e})] = 0$ ($\partial^2\omega_e \big/ (\partial\varepsilon_{ij}^{e}\partial\varepsilon_{kl}^{e})$ is the Hessian matrix of ω_e), and the state beyond this surface cannot be reached any time.

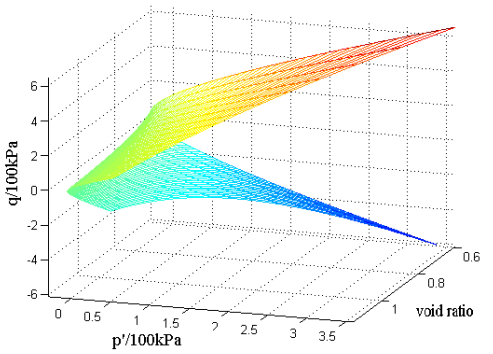

Fig.1 Bounding surface in e-p'-q space （e: void ratio; p': effective mean stress; q: deviator stress）

When the bound water content is relatively small and the viscous stress can be ignored, the total stress can be written as the following:

$$\sigma_{ij} = \sigma_{ij}^{s} + \sigma_{ij}^{fw} + \sigma_{ij}^{bw} = \pi_{ij} + \alpha p \delta_{ij} \tag{13}$$

Obviously, eq.(13) is the effective stress principle in classical soil mechanics, and π_{ij} becomes the effective stress of the granular skeleton.

4 Summary and Conclusion

In this paper, a fully coupled THM model based on non-equilibrium thermodynamic approach is developed. The model includes: ①basic equations eq.(1)~(4); ②constitutive relations eq.(5),(9)~(11),(15); ③migration coefficient model eq.(6)~(8). In the model, energy dissipations in THM coupling processes are described by a set of migration coefficient model and energy functions from which constitutive relations of every field can be deduced. For the hydrological field, the conversion from bound pore water to free pore water induced by temperature elevating and the subsequently thermal-induced particle reorganization are described. For the mechanical field, a constitutive model quite different from classical ones is established without the need of define yield surface and various flow and hardening or softening rules. Using this model, we will make some simulation of non-isothermal consolidation and shearing for saturated soil in our next step research work.

References

Von Terzaghi, K.: Die berechnug der Durchlassigkeitsziffer desTones aus dem Verlauf der hydrodynamischen Spannungserscheinungen. Sitzungsber Akad Wiss Math-Naturwiss Section Iia 132(3/4), 125–138 (1923)

Biot, M.: General theory of three-dimensional consolidation. J. Appl. Phys. 12, 155–164 (1941)

Freeman, T.T., Chalaturnyk, R.J., et al.: Fully Coupled Thermo-Hydro- Mechanical modeling by COMSOL Multiphysics, with applications in reservoir geomechanical characterization. In: The Proceedings of the COMSOL Conference, Boston (2008)

Tong, F., Jing, L., Zimmerman, R.W.: A fully coupled thermo- hydro-mechanical model for simulating multiphase flow, deformation and heat transfer in buffer material and rock masses. International Journal of Rock Mechanics & Mining Sciences 47, 205–217 (2010)

Baldi, G., Hueckel, T., et al.: Pellegrini R. Developments in modelling of thermo-hydro-geomechanical behaviour of Boom clay and clay-based buffer materials. Report: 13365/2 EN. Commission of the European Communities (1991)

Cekerevac, C., Laloui, L.: Experimental study of thermal effects on the mechanical behaviour of a clay. Int. J. Numer. Anal. Meth. Geomech. 28, 209–228 (2004)

Hueckel, T., Borsetto, M.: Thermo-plasticity of saturated soils and shales: constitutive equations. J. Geotech. Eng. ASCE 116(12), 1765–1777 (1990)

Laloui, L., Cekerevac, C.: Thermo-plasticity of clays: An isotropic yield mechanism. Computers and Geotechnics 30, 649–660 (2003)

Jiang, Y., Liu, M.: Granular solid hydrodynamics. Granular Matter 11, 139–156 (2009)

De Groot, S.R., Mazur, P.: Non-Equilibrium thermodynamics. North-Holland Pub. Co., Amsterdam (1962)

Thermo-Hydraulic Behaviour of Boom Clay Using a Heating Cell: An Experimental Study

Lima A.[1], Romero E.[1,*], Gens A.[1], Li X.L.[2], and Vaunat J.[1]

[1] Department of Geotechnical Engineering and Geosciences,
Universitat Politècnica de Catalunya,
c/ Jordi Girona 1-3, Campus Nord,
Building D2, 08034 Barcelona, Spain
Enrique.romero-morales@upc.edu
[2] EURIDICE / SCK.CEN,
Boeretang 200, 2400 Mol, Belgium

Abstract. Boom clay formation is a potential host rock for geological disposal of high-level nuclear waste in Belgium. Heating pulse tests with controlled power supply and controlled hydraulic boundary conditions were performed under constant volume conditions to study the hydraulic impact of thermal loading on the clay. Selected test results of intact borehole samples retrieved in horizontal direction are presented and discussed. The study focuses on the time evolution of temperature and pore water pressure changes along heating and cooling paths, i.e. pore pressure build-up during quasi-undrained heating and later dissipation at constant temperature towards the applied hydraulic boundary condition.

1 Introduction

Belgian Boom clay is the subject of extensive research dealing with all phenomena that may possibly affect its performance as potential geological host formation for high-level nuclear waste. Specifically, thermal phenomena may play an important role in this low permeability clay. To this end, the paper explores the consequences of thermal impact by presenting selected results of a comprehensive test program using an axi-symmetric heating cell with temperature and pore pressure sensors. Heating pulse tests at different temperatures (the maximum temperature was limited to 85 °C) and under constant volume conditions were performed at controlled hydraulic boundary conditions, i.e. constant water pressure at the bottom boundary and upper boundary with no flow condition. Test results are presented and interpreted in terms of the time evolution of temperature increase / decrease, water pressure increase / decrease, and the evolution of the quasi-undrained pressurisation coefficient along the heating and cooling paths.

* Corresponding author.

L. Laloui and A. Ferrari (Eds.): Multiphysical Testing of Soils and Shales, SSGG, pp. 163–168.
springerlink.com

2 Tested Material and Experimental Programme

Table 1 summarises the main volumetric and gravimetric properties of Boom clay (Mol, Belgium), slightly overconsolidated Tertiary clay that contains kaolinite (20%–30%), illite (20%–30%) and smectite (10%) (Lima, 2011). A specimen was trimmed from a borehole sample retrieved in horizontal direction with dimensions of 75 mm in diameter and 100 mm in height (bedding planes are parallel to the direction of axial symmetry).

Table 1 Main properties of Boom clay (Lima, 2011)

Property	Value
Density (Mg/m^3)	around 2.05
Dry density (Mg/m^3)	1.65 to 1.67
Gravimetric water content (%)	around 25
Density of soil solids (Mg/m^3)	2.67
Void ratio	0.60 to 0.62
Degree of saturation (%)	around 100
Liquid limit (%)	56
Plastic limit (%)	29
Vertical water permeability (m/s) flow orthogonal to bedding	2.4×10^{-12}
Horizontal water permeability (m/s) flow parallel to bedding	4.3×10^{-12}

The experimental programme was carried out on a fully-instrumented cell (75- mm diameter and 100 mm high) with a controlled-power heater (H) housed inside the cell, as shown in Figure 1 (Lima, 2011; Muñoz *et al.*, 2009). Two miniature pore water pressure transducers (Pw_1 and Pw_2) located at different heights of the lateral wall of the cell and three thermocouples (T_1, T_2 and T_3) were used to monitor the sample response. A fourth thermocouple (T_4) was installed inside of the water bath. The cell has top (u_u) and bottom (u_b) valves to control the hydraulic conditions. The protocol of the tests included three main phases: hydration, heating and cooling. During the hydration phase, the backpressure (u_b in Fig. 1) was increased in steps. The upper valve was maintained open under atmospheric conditions during this initial phase. Throughout the course of the heating phase, the bottom drainage was maintained open at a water backpressure of 1 MPa using an automatic pressure/volume controller, while the upper valve was kept closed. This backpressure is important since it allows measuring the pore pressure drop during the cooling phase without invading the negative range (below atmospheric conditions). The initial and external temperatures were always regulated by submerging the cell inside a temperature controlled water bath at 19 ºC.

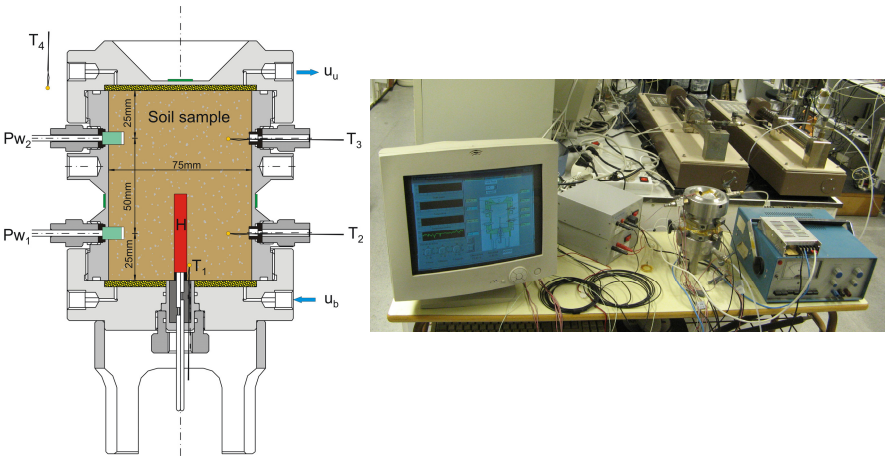

Fig. 1 Scheme and general view of the heating cell with all its components

3 Experimental Results

3.1 Hydration Phase

Water permeability was measured under steady-state conditions during the hydration phase (5.7×10^{-12} m/s) and was in agreement with the horizontal permeability reported in Table 1 (flow parallel to bedding planes). Figure 2(a) shows the time evolution of water volume outflow measured under steady-state conditions at a backpressure of 1 MPa (upper valve was maintained open). Figure 2(b) presents the pore water pressure distribution under steady-state conditions at different elevations on the sample. The results confirm the linear relationship of the pressure distribution in this homogeneous soil prior to the thermal phase.

3.2 Heating and Cooling Phases

Figure 3 shows the results obtained along the thermal phase, in which a power input of 19.15 W was applied to the heater. Particularly, Figure 3a presents the time evolution of temperature changes at different positions. Figure 3b complements the time evolution picture by presenting the corresponding water pressure changes. The maximum temperature in the heater reached 85ºC during this thermal phase (Fig.3(a)), which was accompanied with a maximum pressure build-up during the quasi-undrained heating of Pw_2=1.83 MPa and Pw_1=1.69 MPa. During the heating stage, the pore water pressure increased due to its larger thermal expansion coefficient. The changing magnitude of pore water pressure depends on the rate and range of temperature increase/decrease (quasi-undrained heating), soil

compressibility (dependent on the stress state), thermal expansion coefficient, water permeability, porosity, as well as the applied hydraulic boundary conditions. The change in pore water pressure under thermal loading and saturated conditions have been analysed assuming volumetric compatibility between soil matrix and their constituents (liquid and solid) using compressibility and thermal expansion coefficients (Agar *et al.,* 1986; Vaziri *et al.,* 1990).

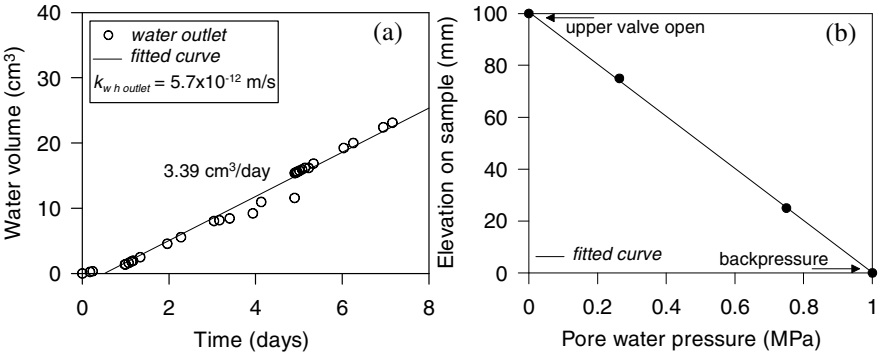

Fig. 2 Hydration phase. (a) Time evolution of water outflow volume under steady-state condition. (b) Pore water pressures at different elevations and under steady-state condition

Along the thermal phase, a higher pressure build-up is detected at Pw_2 because the measuring point is located at a larger distance from the draining boundary. After the heating path, pore water pressure dissipates at constant temperature towards the value applied at the bottom boundary. Pore water pressure Pw_2 dissipates more slowly due to its larger distance to this draining boundary. These pressure responses were successfully reproduced by Lima (2011) when simulating the test results with the finite element program CODE_BRIGHT (Olivella *et al.*, 1996).

Figure 4 presents a zoom of part of the time evolution of pore water pressure (Pw_1) and temperature (T_2) changes during the heating and cooling phases. These sensors are located close to the draining boundary and at the same height (Fig. 1). Pressure changes develop at a faster rate during temperature changes. In fact, pressures start to dissipate before the temperature reaches its maximum or minimum value in the heating or cooling phases. The same process has been observed by Gens *et al.* (2007) coming to the conclusion that the dissipation by liquid flow overcomes the thermal effect, explaining the fact that the pore pressure evolution does not exactly match the variation of temperature. Figure 5 shows the time evolution of the quasi-undrained pressurisation coefficient during heating and cooling phases. The maximum values reached were $\Delta u/\Delta T$=0.192MPa$^{\circ}$C^{-1} and 0.109 MPa$^{\circ}$C^{-1} for the heating and cooling phases, respectively.

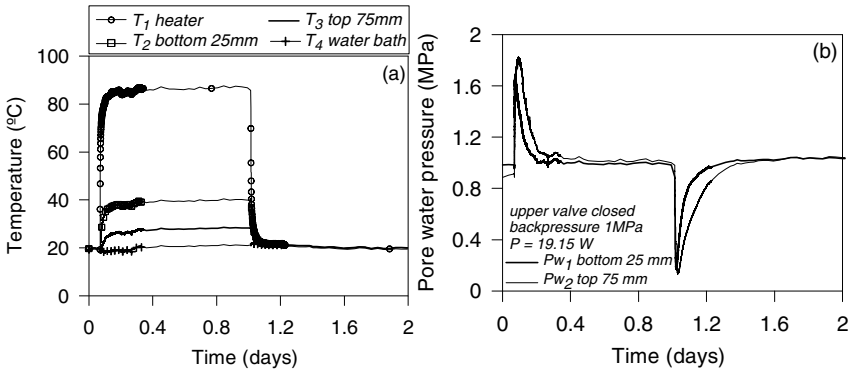

Fig. 3 Thermal phase: (a) Time evolution of temperatures and (b) pore water pressures

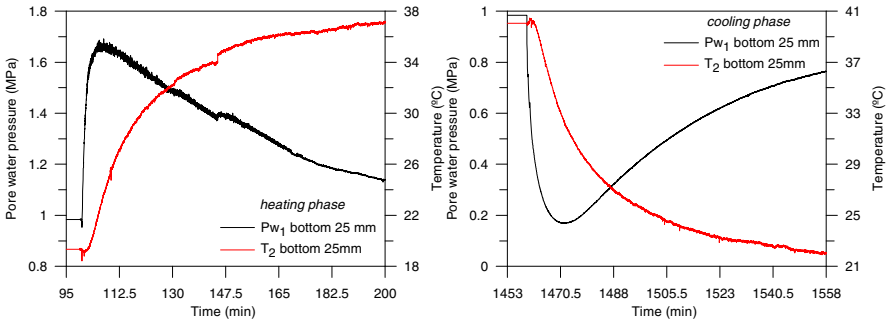

Fig. 4 Zoom of time evolution of pore water pressure (Pw_1) and temperature (T_2) changes during heating/cooling paths

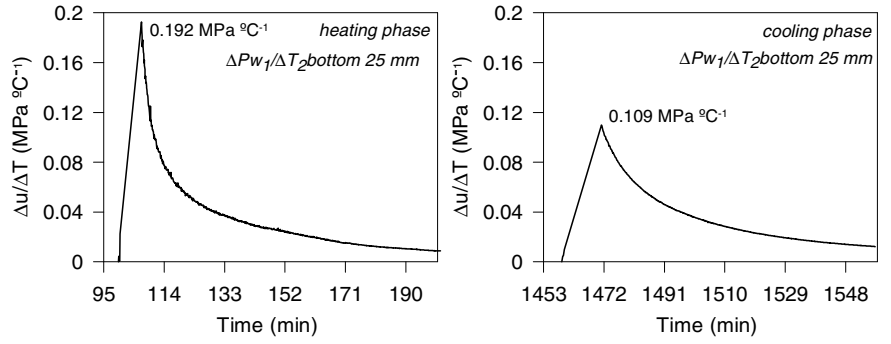

Fig. 5 Zoom of time evolution of quasi-undrained pressurisation coefficient during heating/cooling paths

4 Summary and Conclusions

Thermal impact may play an important role on the hydro-mechanical behaviour of low-permeability clayey formations. In this context, a series of tests along heating and cooling paths were performed on Boom clay to study the hydraulic impact and consequences of thermal loading on this deep clay formation. Heating tests under constant volume conditions and different target temperatures (maximum 85°C) were performed under controlled hydraulic boundary conditions. Attention is focused on the time evolution of temperature and pore water pressure changes during heating and cooling paths–i.e., pore pressure build-up during quasi-undrained heating and later dissipation to the applied hydraulic boundary conditions–. Pore water pressures started to increase or dissipate towards the hydraulic boundary condition applied before the temperature reached its maximum or minimum value in the heating or cooling phases, i.e. pore pressure evolution did not match the temperature one. A value of the quasi-undrained pressurisation coefficient, defined as the pore pressure increase due to unit temperature increase, around 0.192 $MPa^{o}C^{-1}$ and 0.109 $MPa^{o}C^{-1}$, was obtained for heating and cooling phases, respectively. The extensive data collected has been used by Lima (2011) to calibrate thermal and hydraulic properties by back-analysing joint thermal and hydraulic results using a fully coupled thermo-hydro-mechanical code (CODE_BRIGHT, Olivella *et al*., 1996).

Acknowledgements. The authors acknowledge the financial support provided by EIG EURIDICE/SCK•CEN (Belgium) through a PhD collaboration project with International Centre for Numerical Methods in Engineering (CIMNE, Spain).

References

Agar, J.G., Morgenstern, N.R., Scott, J.D.: Thermal expansion and pore pressure generation in oil sands. Canadian Geotechnical Journal 23(3), 327–333 (1986)

Gens, A., Vaunat, J., Garitte, B., Wileveau, Y.: In situ behaviour of a stiff layered clay subject to thermal loading: observations and interpretation. Géotechnique 57(2), 207–228 (2007)

Lima, A.: Thermo-hydro-mechanical behaviour of two deep Belgium clay formations: Boom and Ypresian clays. PhD Thesis. Universitat Politècnica de Catalunya, Spain (2011)

Muñoz, J.J., Alonso, E.E., Lloret, A.: Thermo-hydraulic characterisation of soft rock by means of heating pulse tests. Geotechnique 59(4), 293–306 (2009)

Olivella, S., Gens, A., Carrera, J., Alonso, E.E.: Numerical formulation for a simulator (CODE_BRIGHT) for the coupled analysis of saline media. International Journal for Computer-Aided Engineering and Software 13(7), 87–112 (1996)

Vaziri, H.H., Byrne, P.M.: Numerical analysis of soil sand under nonisothermal conditions. Canadian Geotechnical Journal 27(6), 802–812 (1990)

Micro-scale Investigations and Image Analysis Techniques

Pore Size Distribution and Soil Water Suction Curve from Micro-tomography Measurements and Real 3-D Digital Microstructure of a Compacted Granular Media by Using Direct Numerical Simulation Technique

Felix H. Kim[1], Dayakar Penumadu[1], Volker P. Schulz[2], and Andreas Wiegmann[3]

[1] Civil and Environmental Engineering, University of Tennessee, Knoxville, TN, USA
fkim@utk.edu
[2] Baden-Wuerttemberg Cooperative State University Mannheim, Germany
[3] Fraunhofer ITWM Kaiserslautern, Germany

Abstract. Predictive measurement of capillary pressure – saturation relationship of a porous media is obtained based on the actual microstructure obtained from high resolution tomography data. X-ray micro-tomography provided a high contrast for silica phase, and actual geometry of sand particles and void distribution. The morphological opening (erosion + dilation) is used to get a pore size distribution using the concept of granulometry. Full-morphology approach is used to model the quasi-static wetting and non-wetting phase distribution of a primary drainage process. Predicted soil water suction curves for a compacted silica sand sample is presented along with the effects of assumed contact angle between water and silica surface.

1 Introduction

The deformation and fluid flow behavior of partially saturated granular medium (soil) is a complex and important problem. The complexity arises from the particulate nature of soil which is composed of three phases (solid, gas, and liquid). The true nature of deformation and fluid flow can be revealed more accurately when the particulate material is studied at the grain/pore scale. The small size (< 1 mm) of individual particle and the large number of particles involved has prohibited researchers from studying soil at grain/pore level with traditional experimental and numerical techniques. Recently, imaging technique such as X-ray tomography technique has been used popularly to study the soil and porous rock geometry [1, 2]. The fluid phase of porous media has also been visualized with X-ray by using contrast agents [3, 4]. Neutron imaging technique has also been used to study mainly the fluid phase without using a contrast agent [5-7]. The authors have recently performed an experimental approach to utilize the dual modality contrast of neutron and X-ray tomography images to study three phases of partially saturated sand [8].

L. Laloui and A. Ferrari (Eds.): Multiphysical Testing of Soils and Shales, SSGG, pp. 171–176.
springerlink.com

Traditionally, numerical simulations have been performed at the macroscopic level with continuum assumption. Discrete element method (DEM) has been developed and applied to study the particulate nature of granular materials focusing on the solid phase [e.g. 9, 10, 11]. The complex nature of pore geometry makes it difficult to simulate the fluid flow. Several research projects have been performed to simulate the fluid flow behavior at a pore level from realistic microstructure of various porous media generated either from X-ray tomography or by stochastic methods [12-14]. Macroscopic properties such as permeability, thermal conductivity, diffusion and capillary pressure–saturation curves of porous media have been obtained from microstructure of various porous media [15-17].

In this research, predictive measurements of transport property are computed from a realistic microstructure of sand column obtained from X-ray microtomography. Phase distribution for different saturation according to change in capillary pressure is computed and visualized, and capillary pressure – saturation curves (soil water suction curves) were generated.

2 X-ray Tomography

The three dimensional (3D) realistic microstructure of dry Ottawa sand (20/40 Oil Frac) column is obtained from microfocus X-ray tomography at Helmholtz-Zentrum-Berlin (HZB). The dry Ottawa sand is placed in a custom developed thin walled aluminum compaction mold as shown in Fig. 1a. The inner dimension is about 10 mm dia. × 23 mm height. The average Ottawa sand grain diameter is around 700 µm. The system consists of micro focus X-ray source and a flat panel detector. The detector has 50 µm pixel sizes, and the specimen was magnified about 4.46 times resulting in the effective image voxel size of 11.2 µm. The image data was smoothened with 3D median filter and thresholded to binary data. Parts of the volume comprising about 1000^3 voxels (11.2^3 mm^3/voxel) as shown in Fig. 1b are used for the analysis. An example tomography slice is shown in Fig. 1c, and good contrast between sand phase and air phase is presented. The 3D view of the thresholded sand phase is shown in Fig. 1d. Porosity was measured from the segmented image data as approximately 0.353 for the given volume.

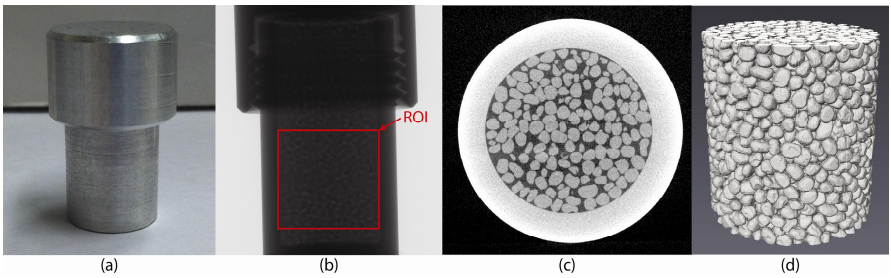

Fig. 1 Picture of the aluminum compaction mold (a), X-ray radiography of dry Ottawa sand specimen (b), reconstructed slice (c), and 3D volume rendering of the dry Ottawa sand specimen segmented from X-ray tomography (d)

3 Full-Morphology Model and Result

In [13], Schulz et al. employed a so-called full-morphology model for the quasi-static drainage simulation of liquid water in a porous media. In this model which is based on the work by Hilpert et al. [18], the stationary distribution of wetting phase (WP) and non-wetting phase (NWP) for an arbitrary capillary pressure (p_c) can be determined. The simulations presented here run the full morphology method as implemented in the GeoDict code (www.geodict.com). The pore size is the main factor determining the drainage at a given capillary pressure. Morphological opening is used to determine the pore size distribution as shown in Eq. (1) where X represents the pore space and B is the structuring element. O_B is the pore space that the structuring element fits in determined from morphological opening process.

$$O_B(X) = \bigcup \{B \mid B \subseteq X\} \tag{1}$$

A spherical structuring element with radius r is used, and the method assumes a spherical interface between WP and NWP. The geometric pore size distribution is obtained with this method for the given data set as shown in Fig. 2.

The radius r is the constant curvature radius of the WP and NWP interface, and it is also related to capillary pressure determined with Young – Laplace equation shown in Eq. (2). Capillary pressure (p_c) is related to surface tension (γ) between WP and NWP and contact angle (θ) between WP and solid phase.

$$p_c = \frac{2\gamma \cos\theta}{r} \tag{2}$$

A simulation of drainage condition can be performed by applying morphological opening operations with a test for connectivity to NWP reservoir. It is assumed that the volume is connected to NWP reservoir in one end and WP reservoir on the other end. The porous medium is assumed to be fully saturated with the WP initially, and NWP replaces the WP to simulate drainage process. In this case, the pore radius (r) was varied from 11.2 µm to 313.6 µm in 28 equal steps. The capillary pressure was varied from 12.991 kPa to 0.467 kPa according to Eq. (2) for contact angle of 0°. The surface tension (γ) was assumed to be 72.75 mN/m. The pore space is eroded by spheres with increasing radius r starting with the smallest radius corresponding to the largest capillary pressure. The pores can be filled with NWP if the erosion of the pore space has a continuous connection to the NWP reservoir. The eroded pore phase is dilated with the same structuring element to complete the opening process. The saturation of the WP is basically the volume fraction of WP compared to the total volume of pores. The whole process is repeated for the next structuring element with a larger radius. Based on the results of capillary pressure and WP saturation, a capillary pressure – saturation curve is generated.

Three different contact angles of water (0°, 27°and 60°) were used, and capillary pressure – saturation curves for primary drainage and arbitrarily mobile fluids are shown in Fig. 3. The advancing and receding contact angle of water on silica is

found to be near 60° and 27° respectively [19]. It shows that the difference with contact angle affected the capillary pressure –saturation relationship significantly. An example stationary WP and NWP distributions for different capillary pressures are presented in Fig. 4 for the case of 0° contact angle.

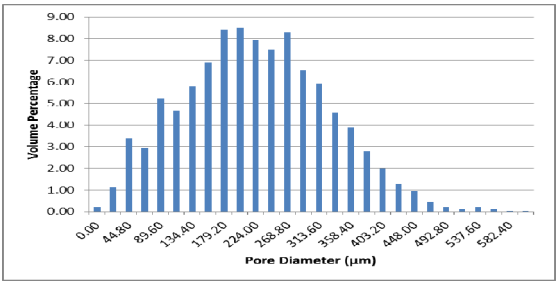

Fig. 2 Pore size distribution obtained from morphological opening process

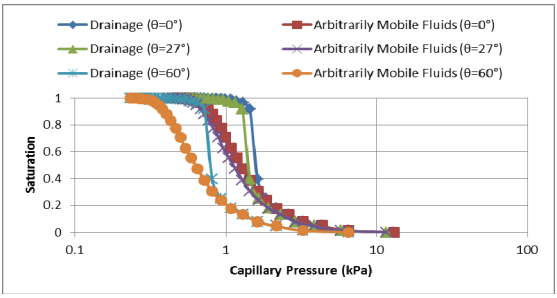

Fig. 3 Predictions of saturation versus capillary pressure (suction) for different contact angles

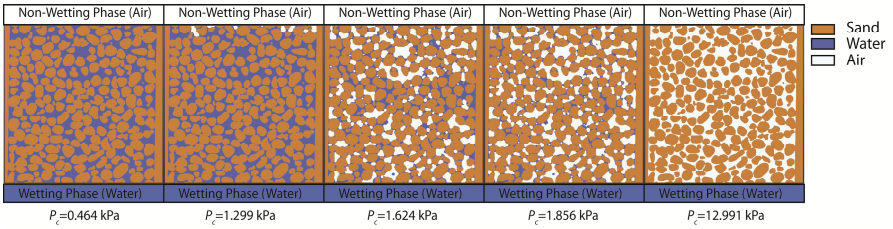

Fig. 4 Phase predictions at different capillary pressures for contact angle of 0°

4 Conclusion

A direct numerical simulation approach was applied to predict capillary pressure – saturation curve based on a realistic microstructure of dry Ottawa sand obtained with X-ray micro-tomography. General description of the full morphology method

was explained. Capillary pressure – saturation curves for appropriate contact angles were simulated, and the effect of contact angle with predictive measurement was demonstrated. The predictions of suction versus saturation for Ottawa sand generally agree with published literature. The direct numerical simulation technique not only provides simulation results based on actual geometry of porous media, but it also provides opportunity to compare simulation results directly with image data of physical experiment results. Other transport properties such as permeability, thermal conductivity and diffusion can be obtained from a realistic geometry, and the results will be presented in the future publications.

References

Desrues, J., Chambon, R., Mokni, M., Mazerolle, F.: Void ratio evolution inside shear bands in triaxial sand specimens studied by computed tomography. Geotechnique 46(3), 529–546 (1996)

Alshibli, K.A., Sture, S., Costes, N.C., Frank, M.L., Lankton, M.R., Batiste, S.N., Swanson, R.A.: Assessment of Localized Deformations in Sand Using X-Ray Computed Tomography. Geotecnical Testing Journal 23(3), 274–299 (2000)

Al-Raoush, R.I., Willson, C.S.: A pore-scale investigation of a multiphase porous media system. Journal of Contaminant Hydrology 77(1-2), 67–89 (2005)

Schnaar, G., Brusseau, M.L.: Pore-Scale Characterization of Organic Immiscible-Liquid Morphology in Natural Porous Media Using Synchrotron X-ray Microtomography. Environmental Science & Technology 39(21), 8403–8410 (2005)

de Beer, F.C., Middleton, M.F.: Neutron Radiography Imaging, Porosity and Permeability in Porous Rocks. South African Journal of Geology 109(4), 541–550 (2006)

Hassanein, R., Meyer, H.O., Carminati, A., Estermann, M., Lehmann, E., Vontobel, P.: Investigation of Water Imbibition in Porous Stone by Thermal Neutron Radiography. Journal of Physics D: Applied Physics 39(19), 4284–4291 (2006)

Kim, F., Penumadu, D., Hussey, D.S.: Water Distribution Variation in Partially Saturated Granular Materials Using Neutron Imaging. Journal of Geotechnical and Geoenvironmental Engineering, American Society of Civil Engineers (ASCE) 138(2), 147–154 (2012)

Kim, F.H., Penumadu, D., Gregor, J., Kardjilov, N., Manke, I.: High resolution neutron and X-ray imaging of granular materials, Under Review. Journal of Geotechnical and Geoenvironmental Engineering (2012)

Iwashita, K., Oda, M.: Rolling Resistance at Contacts in Simulation of Shear Band Development by DEM. Journal of Engineering Mechanics 124(3), 285–292 (1998)

Yimsiri, S., Soga, K.: DEM analysis of soil fabric effects on behaviour of sand. Geotechnique 60(6), 483–495 (2010)

Cundall, P.A., Strack, O.D.L.: A discrete numerical model for granular assemblies. Geotechnique 29(1), 47–65 (1979)

Spanne, P., Thovert, J.F., Jacquin, C.J., Lindquist, W.B., Jones, K.W., Adler, P.M.: Synchrotron Computed Microtomography of Porous Media: Topology and Transports. Physical Review Letters 73(14), 2001–2004 (1994)

Schulz, V.P., Becker, J., Wiegmann, A., Mukherjee, P.P., Wang, C.-Y.: Modeling of Two-Phase Behavior in the Gas Diffusion Medium of PEFCs via Full Morphology Approach. Journal of The Electrochemical Society 154(4), B419–B426 (2007)

Hazlett, R.D.: Simulation of capillary-dominated displacements in microtomographic images of reservoir rocks. Transport in Porous Media 20(1), 21–35 (1995)

Ferréol, B., Rothman, D.H.: Lattice-Boltzmann simulations of flow through Fontainebleau sandstone. Transport in Porous Media 20(1), 3–20 (1995)

Becker, J., Schulz, V., Wiegmann, A.: Numerical Determination of Two-Phase Material Parameters of a Gas Diffusion Layer Using Tomography Images. Journal of Fuel Cell Science and Technology 5(2), 21006–21009 (2008)

Vogel, H.-J., Tölke, J., Schulz, V.P., Krafczyk, M., Roth, K.: Comparison of a Lattice-Boltzmann Model, a Full-Morphology Model, and a Pore Network Model for Determining Capillary Pressure–Saturation Relationships. Vadose Zone J. 4(2), 380–388 (2005)

Hilpert, M., Miller, C.T.: Pore-morphology-based simulation of drainage in totally wetting porous media. Advances in Water Resources 24(3-4), 243–255 (2001)

Ishakoglu, A., Baytas, A.F.: The influence of contact angle on capillary pressure-saturation relations in a porous medium including various liquids. International Journal of Engineering Science 43(8-9), 744–755 (2005)

Porosity and Pore-Size Distribution of Geomaterials from X-ray CT Scans

H.S. Shin[1, *], K.Y. Kim[1], and G.N. Pande[2]

[1] Geotechnical Eng. Research Dept., Korea Institute of Const. Tech. (KICT), Republic of Korea
hyushin@kict.re.kr
[2] Centre for Civil & Computational Engineering, Swansea University, UK and President, International Centre for Computational Engineering, Rhodes, Greece

Abstract. Determination of transport properties of geomaterials is an important issue in many fields of engineering analysis and design. For example, in petroleum engineering, permeability of an oil reservoir may be crucial in establishing its viability for exploitation whilst prevention of leakage from underground storage facilities for oils and gas, nuclear waste as well as CO2 crucially depends on its long term values. Permeability is an illusive parameter which is difficult to obtain not only in field situations but also in controlled laboratory environment. Its determination is further complicated by the fact that values are needed for low permeability porous media such as clays/rocks at various degrees of saturation and at elevated temperatures which makes physical experiments not only expensive but also difficult and time-consuming. Permeability is indirectly related to the porosity, pore-size distribution and pore-architecture. A well-known way to obtain this information is through mercury porosimetery but this procedure has safety issues associated with it. Moreover, it is not an easy experiment to conduct. In this paper, we demonstrate the use of micro X-ray CT scanning technique to obtain porosity and its variation in clays. Since the resolution of micro CT equipment is not high enough to be able to observe specific pores in clays, an experimental programme to correlate porosity with data from scanning was undertaken. It consisted of consolidating specimens made from a mixture of kaolinite and bentonite in an oedometer, unloading them and obtaining 32mm samples from various locations, scanning them as well as determining void ratio of these specimens using standard laboratory procedures. It is observed that the Average CT Number (ACTN) for the specimens correlated well with the porosity (void ratio) whilst spatial variation of CT numbers seems to indicate the capability of scanners to capture pore size distribution. This indicates the possibility of computing permeability of low porosity media through CT imaging.

[*] Currently Distinguished Visitor, International Centre for Computational Engineering, Rhodes, Greece.

L. Laloui and A. Ferrari (Eds.): Multiphysical Testing of Soils and Shales, SSGG, pp. 177–186.
springerlink.com

1 Introduction

In recent years, geotechnical engineering has benefited from advances in various high-technology fields such as computing, instrumentation, electronics and information systems. However, investigation of hydro-mechanical characteristics of the geomaterials has still many limitations. In particular, a reliable estimation of permeability is a matter of the utmost importance in many fields where reliable barriers are required to prevent flow of radioactive contaminants, oil and gas from underground storages.

In this respect, engineers dealing with very fine soil materials like clay have been searching for more advanced techniques for determining porosity, pore-size distribution and permeability[1] under various field conditions. Visualizing and quantifying micro-scale internal structures and physical composition of a material in an undisturbed state is now feasible using 3-dimensional images by X-ray CT (Computed Tomography) methodology.

The advantage of X-ray CT is that it helps engineers to obtain reliable information of the pore and grain structure rapidly in clean and less hazardous environments. They also have a further advantage in that the same specimen can be scanned several times in a variety of mechanical and environmental conditions and interaction between different phases such as solid, water and air can be investigated at any location within the specimen.

In this paper, research on the measurement of porosity[2] (or void ratio), one of the important geotechnical design parameters for fine grained soils, utilizing the micro CT X-ray scanning technique, is presented. In engineering practice indirect methods are used to obtain porosity and permeability. Unlike the case of sandy soils, these parameters are crucial for clays in geotechnical design since they play a key role in deciding consolidation settlement and time (Fox and Berles, 1997). They are also prone to large measurement errors when conventional methods are used. For example the discrepancy between measured and in-situ values of permeability can be of several orders of magnitude. Micro X-ray CT technology seems to be a step forward towards solving this problem.

In the past, Micro X-ray CT research tool has been adopted by Peyton et al. (1992) who tried imaging minute pores of undisturbed sand specimens in the early stages and Zeng et al. (1996) measured the density of specimens based on precision image processing analysis of CT data. Hereafter, the research on the changes of pore-structure was conducted by Wong (2000), Alshibli et al. (2003), and Riyadh et al. (2006). However, all studies have hitherto been restricted to sandy soils. In this paper, we explore if CT technology can be applied to fine cohesive soils whose particles are much smaller than the minimum pixel size of micro X-ray CT. Here we study porosity and pore size characteristics of

[1] This generic term is used to denote inter related terms such as ‘absolute’ and ‘relative’ permeability as well.

[2] In this paper, the terms ‘porosity’ and ‘void ratio’ have been used inter changeably due to their popularity in petroleum and geotechnical engineering fields respectively.

laboratory prepared artificial clay specimens after subjecting them to various consolidation pressures. Section 2 gives an overview of CT scanning methodology and the facilities available at the Korean Institute of Construction Technology (KICT). Section 3 describes procedure adopted for preparation and testing of clay samples using standard laboratory methods whilst section 4 describes techniques used for calibration and standardization of imaging data. Scanning results are presented and discussed in Section 5 and finally conclusions and recommended guide lines for future research are given in Section 6.

2 Overview of Micro X-ray CT

Devised and commercialized by Hounsfield in 1971, CT (Computed Tomography) is the technology which embodies the analysis of three-dimensional images obtained by seeing through objects using X-rays from various angles, to obtain sectional diagrams of various objects. X-ray CT techniques have been commonly used in the past in the fields of medicine and manufacturing for the detection of fractures and defects in a variety of manufactured consumer goods. In recent years, it is being increasing used in the fields of biotechnology, forensic archaeology and other related areas. Its utilisation in the study of mechanics of geomaterials is, however, recent but growing.

A CT scanner consists of three components viz. a source to generate X-rays, a detector to measure their penetration in the object being scanned and a manipulator to locate and rotate the object through 360°. Fig. 1 shows the equipment used in this study at KICT .

The micro X-ray source in the CT scanner is of the 'sealed-type' with radiation power of up to 90kV. Its resolution is 250μA, and the minimum focal spot size is 5 microns (0.005 mm). The scanning chamber can accommodate objects of size up to 300 mm in diameter and 500 mm high.

In general, the factor which governs the capacity of X-ray equipment is the source, but the factor which constraines the use of CT scanner methodology is its resolution. The detector captures the attenuated X-rays passing through the scanned object. It is made by Rad-icon, is 50 mm × 50 mm in size and has a pixel pitch of 48μm, and its limiting resolution is 10Lp/mm (line pair per millimeter).

The manipulator used in the CT scanner at the KICT is of 'low noise' type and is used for locating and holding specimen tight for minimizing 'trembling' which invariably takes place during rotation of the object. Moreover, there is a discrepancy due to rotating axis not being absolutely vertical which leads to 'noise' in CT data. This noise in the KICT scanner used for this study is less than 0.01mm, which, however, has been corrected by a 'reconstruction' software.

Fig. 1 Micro X-ray CT equipment of KICT (a) view of micro CT scanner (left), (b) arrangement of three major parts (source, manipulator and detector from right hand side, respectively in upper right figure), (c) zoomed manipulator & detector (lower right)

3 Experimental Programme on Artificial Clay

The aim here is to obtain specimens of clay of controlled porosity for scanning and correlating image analysis data with the experiments. With this in view, it was decided to make two sets of samples: one from kaolinite (100 %) and the other from a mixture of kaolinite (90%) and bentonite (10%). It is well known that kaolinite has low volume ion exchange capacity, whilst bentonite has high positive ion exchange capacity. It was therefore expected that pore characteristics of the two sets may be different. In this study, moisture content was set to twice the 'liquid limit' for preparing the clay specimens, A solidifying agent was also added in each case and the resulting slurry was sieved through a No 10 sieve to remove any foreign matter. About 20 specimens of two different compositions were then consolidated in K_0 conditions to a vertical pressure ranging from 150 kPa to 400 kPa. After unloading and removing the samples from the mould, they were horizontally cut into three parts identified as 'upper', 'middle' and 'lower' part. Three cylindrical samples, 32 mm in diameter and 20 mm thick were carefully scooped from each of these parts for scanning using an acrylic sampling ring (see Fig. 2).

Fig. 2 Sampling process: (a) cutting (b) sampling (c) ready for CT scanning

A number of samples got disturbed and these were not scanned. Porosity was subsequently determined for these specimens using conventional methods. The results are presented in Table 1 together with results of CT scanning, which are discussed below.

Table 1 Results of void ratio measurement and the modified CT numbers for certain areas of each specimen (see Fig. 5 for definition of the area)

Vol. fraction (Kaolinite : Bentonite)	Pre-consolidation pressure	Cutting location	Void ratio (e)	Modified CT number (MCT) (-CT no*10)				Average MCT
				Area 1	Area 2	Area 3	Area 4	
9:1	400kPa	Upper Part	1.46	1752	1735	1722	1741	1741
			1.46	1635	1670	1660	1654	1654
			1.46	1584	1584	1621	1655	1611
	350kPa	Upper Part	1.47	1692	1757	1625	1697	1693
			1.47	1653	1720	1668	1635	1669
			1.46	1640	1589	1612	1607	1612
		Middle part	1.63	1960	1947	1898	1951	1939
			1.58	1850	1798	1718	1866	1808
	200kPa	Upper Part	1.59	1882	1911	1783	1911	1872
			1.56	1706	1778	1739	1771	1749
			1.57	1799	1818	1753	1850	1805
		Middle part	1.57	1842	1733	1733	1691	1750
			1.59	1923	1842	1873	1831	1867
			1.48	1692	1724	1682	1696	1699
10:0	350kPa	Upper Part	1.56	1811	1813	1911	1896	1858
			1.55	1849	1794	1778	1846	1817
			1.57	1724	1691	1735	1725	1729
	300kPa	Upper Part	1.69	2208	2095	2106	2170	2145
			1.64	2174	2135	2104	2109	2131
			1.68	2157	2110	2123	2144	2134
		Middle part	1.69	2203	2145	2148	2192	2172
			1.65	2103	2151	2277	2043	2144
	250kPa	Upper Part	1.79	2306	2298	2280	2232	2279
			1.88	2468	2389	2481	2515	2463
			1.82	2258	2393	2334	2305	2323
		Middle part	1.82	2309	2293	2244	2272	2280
			1.82	2258	2226	2179	2185	2212
			1.81	2121	2148	2177	2132	2145
	150kPa	Upper Part	1.61	1924	1895	1850	2001	1918
			1.61	1884	1903	1852	1976	1904
			1.61	1807	1973	1889	1993	1916

4 CT Number: Standardization and Calibration

4.1 Grayscale and CT Number

X-ray CT scan results display grayscale images signifying the intensity of attenuated X-rays represented as contrast ratio ranging from completely white to absolutely black. The corresponding numerical range is $0 \sim 2^{15}$ in 16 bit system. However, the values are dependent on experimental parameters (X-ray machine, distance to the specimen etc.) as well as environment conditions such as room temperature, humidity etc.. In this respect a correction to obtain standard consistent values is required. Unlike the field of medical sciences where a qualitative comparative image is adequate, for engineering analysis the grayscales are converted into a 'CT number' as follows:

$$I = I_0 e^{-\mu x} \tag{1}$$

where I_o is the intensity of the un-attenuated X-ray beam, I is the beam's intensity after it traverses a thickness of x in the material and μ is the linear 'attenuation coefficient' which has a unique value for any material depending on the power of X ray beam and atomic number of constituents of the material being scanned. For improvements in quality of images, some corrections known as 'gain' (normalization) and 'offset' (subtraction) are made as follows.

$$\mu_{corr} = A[\frac{\mu_{org} - \mu_{air}}{\mu_{ref} - \mu_{air}}] - B\mu_{dark} \tag{2}$$

where μ_{mat}, μ_{air} and μ_{ej} are linear attenuation coefficients of the scanned material, air and a very homogeneous reference material, respectively. μ_{dark} is of a dark image taken without X-ray. A and B are constants called 'gain' and 'offset' coefficient, respectively. The reference material chosen in this study is 'water' as it is one of the constituents of our clay samples. Gain and Offset do not affect the final results, but are used to produce a contrast in the images. Then standard CT numbers are determined by:

$$CT = K\left(\frac{\mu_{corr} - \mu_{water}}{\mu_{water}}\right) \tag{3}$$

Where μ_{water} is linear attenuation coefficient of water. K is a constant adopted as '1000' as a standard. Therefore, CT number of water and air always become '0' and '-1000' respectively as μ_{air} =0 in standard ideal conditions. CT numbers for other materials fall between -1000 and 1000 and reflect CT values of constituents like soil, water and air content in them. However, these CT Numbers have to be determined on the particular equipment being used as well as for the environmental conditions prevailing at the time of scanning as described in Section 4.2 below.

4.2 Gain and Offset Correction for CT Number Standardization

The standardization of CT number is an essential task for quantitative evaluation of porosity and pore characterization from CT images. In this study, the apparatus for the 'gain' and 'offset' correction assembled at the KICT is shown in Fig. 3 and used to obtain CT values independent of X-ray CT scanning equipment and environmental factors. It is a generic setup and is planned to be used for CT scanning studies of other materials such as stones, rocks, ceramics and machine components and manufactured through powder technology.

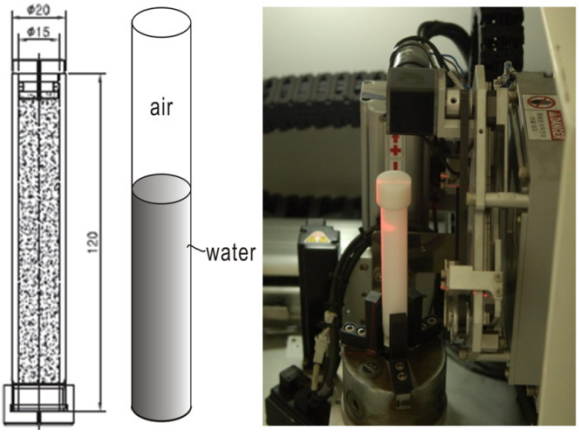

Fig. 3 The apparatus for Gain-Offset correction

After a number of studies, the values of Gain and Offset were selected as 0.2 and 0.1, respectively and were applied to raw data to obtain CT values for all clay specimens and are given in Table 1 above.

5 Porosity and Pore Size Distribution

In general, platelets of clay are smaller than 5 μm in the Unified Soil Classification System. It would, therefore, appear that micro X-ray CT equipment with a resolution of 25 μm would be inadequate to physically view the pores and connecting channels. It is indeed true but our aim here is to assess if the variations in porosity can be picked by the CT scanner as this would lead to a rapid tool to obtain porosity and pore-size distribution which in turn can be adopted to compute permeability. For this reason, even though a number of platelets as well as connecting channels will co-exist in one pixel as shown in Fig. 4, CT numbers will reflect this situation. In general, as the number of platelets (solids) increases in a pixel, CT number should change at the same time (Richard et al., 2001). In the following we will deal with the issue of determination of porosity first, followed by an attempt to identify if the CT scans are capable of detecting possible non-uniformity within the samples.

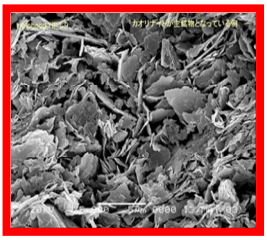

Fig. 4 Clay platelets within a pixel

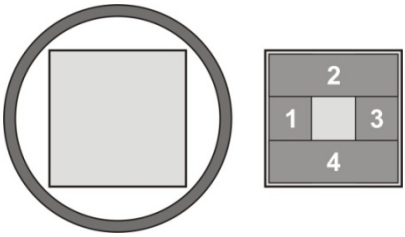

Fig. 5 Areas on which CT values are collected by avoiding the area disturbed by sampling tool

5.1 Estimation of Porosity or Void Ratio

CT numbers for all specimens from four different areas of the specimens (Fig. 5) are shown in Table 1. For estimation of porosity we need an average value of CT numbers for the specimens, which is in the last column of the table 1. Fig. 6 shows a plot of void ratio against average CT number for all cases. A linear relationship is noted. A regression analysis between the average CT number and void ratio leads to Equation (4) below.

$$e = (-0.005) \times (CT\ Number) + 0.6581 \tag{4}$$

The correlation coefficient (R^2) and standard deviation (SD) between the void ratio and CT number is 0.91 and 0.38 respectively, which shows high correlation. In particular, it seems that the linear correlation is stronger in the range of smaller void ratios, compared with the range of higher void ratios.

We now focus our attention at the spatial variation of CT numbers at various locations from where the samples for scanning have been extracted. Here we use a Modified CT number (MCT) for the sake of clarity and convenience. It is simply = - CT x 10. Fig. 7 shows the variation of MCT as well as void ratios within the specimens. It is seen that void ratio at the top part of the specimen is higher than the middle part. It is consistent with the loading history in which compression is followed by swelling due to release of stress. It is further noted that the higher void ratio is reflected in the MCT numbers. In this figure, on the left hand side, computed values of void ratio from Equation (4) are also plotted. A close matching is noted indicating that a relationship between CT numbers and porosity may be unique for a clay like material.

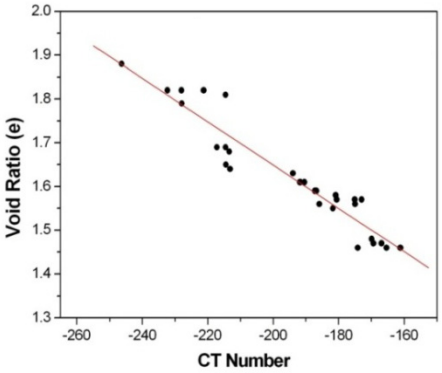

Fig. 6 Relation between void ratio and CT Number

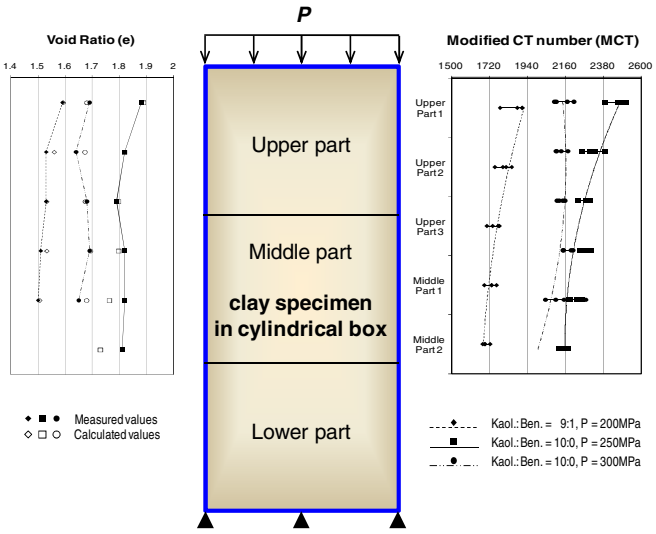

Fig. 7 Distribution of void ratios and MCT values along the thickness of clay specimens

6 Conclusions

In this study CT imaging technique from X ray machines having a resolution of 25 microns has been used to estimate pore characteristics of fine grained soils like clay. The following specific conclusions can be drawn:

(1) For a quantitative analysis of scanning results from micro X-ray CT images, estimation of 'gain' and 'offset' parameters specific to an equipment and environment are required to be determined to obtain accurate CT numbers. This was carefully carried out and seems to have produced consistent set of results.

(2) Although in all specimens more than a one water saturated pores co-exist within a pixel, it is possible to visualize the distribution of pores and pore-structure from the CT numbers. Thus, the concept of estimating porosity from scans for fine grained soils was established.
(3) From the CT numbers of specimens composed of kaolinite and bentonite pre-consolidated to pressures ranging from 150 – 350 kPa inducing different porosities, a correlation between CT number and the porosity was established. The correlation coefficient (R^2) was found as 0.91, indicating a strong linear relationship between the two variables.
(4) CT values in consolidated specimens indicate that there is a clear spatial variation of average values within the specimens which indicates that this methodology can be used not only for rapid determination of porosity but also for pore-size distribution. This will prove to be a major breakthrough as the alternative techniques are expensive, time consuming and have safety issues associated with them.

References

Alshibli, K.A., Batiste, S., Sture, S.: Strain Localization in Sand: Plane Strain versus Triaxial Compression. Journal of Geotechnical and Geoenvironmental Engineering 129(6), 483–494 (2003)

Fox, P.J., Berles, J.D.: CS2: A piecewise-linear model for large strain consolidation. International Journal for Numerical and Analytical Methods in Geomechanics 21, 453–475 (1997)

Peyton, R.L., Haeffner, B.A., Anderson, S.H., Ganzer, C.J.: Applying X-ray CT to measure micropore diameters in undisturbed soil cores. Geoderma 53, 329–340 (1992)

Ketcham, R.A., Carlson, W.D.: Acquisition, optimization and interpretation of X-ray computed tomographic imagery: applications to the geosciences. Computers & Geosciences 27, 381–400 (2001)

Riyadh, A.R., Khalid, A.A.: Distribution of local void ratio in porous media systems from 3D X-ray micro tomography images. Physica A 361, 441–456 (2005)

Tollner, E.W., Melear, N.D., Rodriguez, L.A., Wright, M.E.: Soil Aggregate Size Distributions Using X-Ray Images. Transactions of the American Society of Agricultural Engineers 41(4), 1207–1215 (1998)

Wong, R.C.K.: Shear Deformation of locked Sand in Triaxial Compression. Geotechnical Testing Journal 23(2), 158–170 (2000)

Volumetric Strain Mechanisms and Induced Anisotropy Analyses in Clayey Materials

Mahdia Hattab[1] and Jean-Marie Fleureau[2]

[1] Laboratoire d'Étude des Microstructures et Mécanique des Matériaux (LEM3), UMR CNRS 7239, Université de Lorraine, Ile du Saulcy, 57045 Metz Cedex1, France
mahdia.hattab@univ-metz.fr
[2] Laboratoire de Mécanique des Sols Structures et Matériaux (MSSMat), UMR CNRS 8579, Ecole Centrale Paris, Grande voie des vignes, 92295 Châtenay-Malabry Cedex

Abstract. The study deals with an experimental analysis of the coupling between the macroscopic scale behavior and the local deformation properties of clayey materials, with a special focus on the induced anisotropy phenomenon. The analysis was first conducted on a remolded saturated synthetic clay called kaolin P300, then on deepwater marine clayey sediments from the Gulf of Guinea where the influence of the structure (cementation and fabric) was examined.

1 Introduction

In remolded saturated reconstituted clay, macroscopic strain mechanisms are directly related to the applied stress tensor. At the microscopic scale, it is well known that structural anisotropy progressively develops itself with the loading, as shown for instance by the structural changes during oedometric loading (Delage and Lefebvre, 1984, and others) or axisymmetric triaxial loading (Hattab and Fleureau, 2010). However, few data exist linking micro and macro mechanisms. Experimental investigations are often conducted separately at the two scales of observation. In the case of intact sediments, where the strain mechanisms are more complex because of the structure effect (including fabric and bonding), the macroscopic behavior can be approximated by comparing the different responses of the natural structured sediment and the remolded one under similar loadings (Leroueil et al. 1979, and others). The aim of the present paper is 1) to attempt to explore, in remolded clays, the induced structural anisotropy which occurs at the microstructural level, and then to try to relate it to the strain mechanisms at the macroscopic scale and 2) to examine the effect of bonding and fabric on the local mechanisms with a special focus on cementation damage. Analyses were first carried out on saturated synthetic clay samples (Kaolin P300), and secondly on natural and remolded deepwater marine sediments. Investigations were made on isotropic path, and on triaxial constant lateral effective stress path. Microstructure variations were then examined from two complementary techniques, the scanning electron microscopy (SEM) for the fabric evolution, and mercury intrusion porosimetry (MIP) for pore space variation.

L. Laloui and A. Ferrari (Eds.): Multiphysical Testing of Soils and Shales, SSGG, pp. 187–193.
springerlink.com

2 Materials and Methods

Two types of soils were used in this study: a yellow kaolinite marketed under the name of Kaolin P300, provided as dry powder, and a natural deepwater sediment in the Gulf of Guinea called GoG clay (see Fig. 1 where a SEM image of intact sediment is represented). Geotechnical characteristics and mechanical tests conducted on these sediments can be found in different studies, for instance in De Gennaro et al. (2005) and Hattab and Favre (2010).

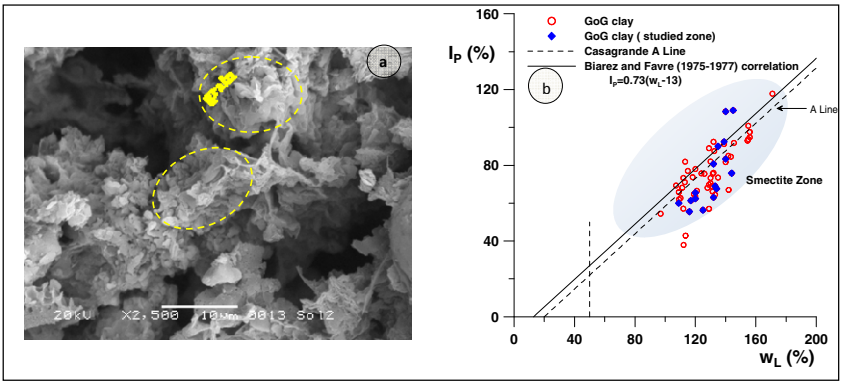

Fig. 1 Geotechnical characteristics and SEM image of natural GoG clay

For the Kaolin P300, all the clay specimens (h_0 = 35 mm and d_0 = 35 mm) were initially prepared in a mold and consolidated under an effective vertical stress σ'_v=120 kPa (after sedimentation of the slurry). The applied triaxial loading path was as follows: an isotropic loading up to the isotropic stress $p'_{c,0}$ = 1400 kPa, an isotropic unloading down to an OCR of 1.4 ($p'_{c,1}$ = 1000 kPa), then a classical drained triaxial path under σ'_3 = 1000 kPa.

For the marine sediment three drained triaxial tests at constant σ_3 were performed on specimens of remolded and intact sediments (h_0 = 53 mm and d_0 = 35 mm) as follows: For the remolded sediment, σ'_3 = 100 kPa, σ'_3 = 200 kPa and σ'_3 = 600 kPa. For natural sediment, σ'_3 = 40 kPa, σ'_3 = 200 kPa and σ'_3 = 600 kPa.

3 Results and Discussions

Previous studies on kaolin P300, detailed in Hattab and Hicher (2004), showed that two strain mechanisms simultaneously occur during the triaxial loading: an isotropic-type mechanism which is due to the isotropic part of the stress tensor (p'), and a deviatoric-type mechanism due to the deviatoric part of the stress tensor (q). In these studies a domain has been identified in the (p'-q) plane in which only the isotropic mechanism is activated whatever the stress path. Fig. 2a presents in this context the macroscopic behavior in the (p'-q) plane, where the strain vector variation along purely deviatoric triaxial paths is also presented.

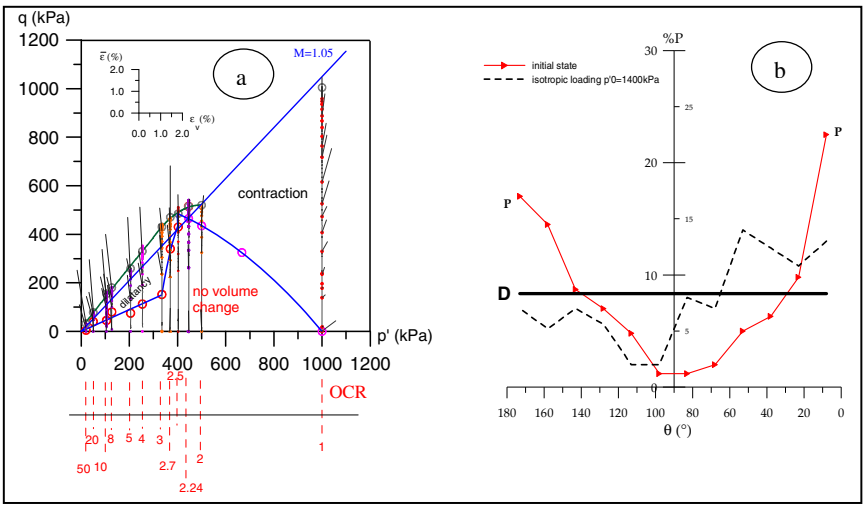

Fig. 2 Macroscopique strain mechanisms during triaxial loading and particles orientation changes between initial one-dimensional consolidation and isotropic loading

From the microstructural point of view, Fig 2b, which translates in the (θ-%P) plane the percentage of oriented particles as a function of their orientation, shows a clear *U*-shape in the initial state of the material (one-dimentional consolidation). A structural anisotropy of the soil thus exists with a *principal mode of orientation* towards the plane normal to the axial stress direction (horizontal plane). After isotropic loading, a broken line appears closer to the **D** line (which represents the structural isotropy of a fictional material). An activation of the depolarization mechanism is here clearly highlighted. Analyses performed along the triaxial paths (Fig. 3) show that the *depolarization* tendency persists at 5% of axial strain (which is a point very close to the isotropic mechanism domain discussed above). The *U*-shape reappears at ε_1 = 15%, with *principal orientation modes* towards the horizontal (0° and 180°), and also towards 20° and 40° with respect to the horizontal. At the end of the triaxial loading (ε_1 = 25%), the orientation curve no longer has the *U*-shape, but a strong anisotropy is observed, with a *principal orientation mode* between 40 and 20°, but also toward the horizontal plane. A more detailed analysis focused on microstructural organization at 25% of axial strain, with various overconsolidation ratios, was published in Hattab (2011) which confirms these results for all the values of the consolidation stress.

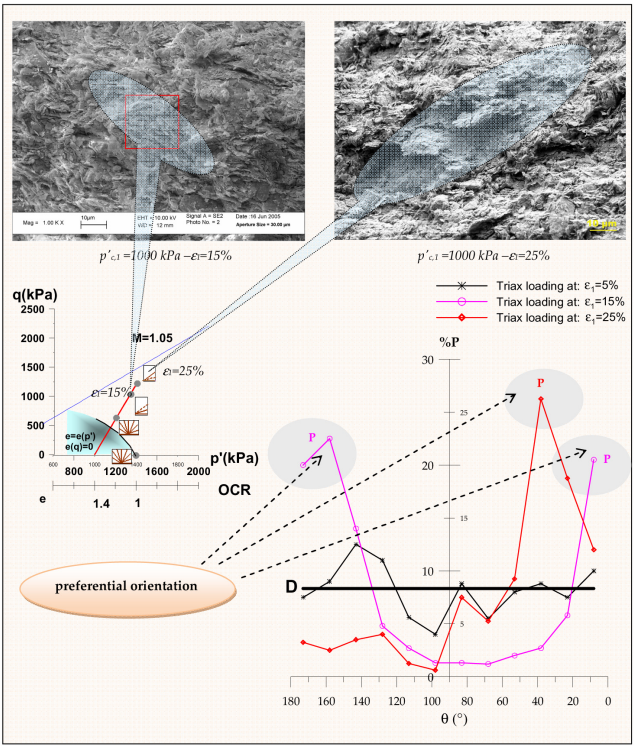

Fig. 3 Microstructural variation along triaxial path

Triaxial axisymmetric tests results are presented in the (logp'-e) plane in Fig. 4a. Readers can find a more extensive study in Hattab et al. (2012) where it appears that the behavior of the natural specimens converges towards that of the remolded specimens without however reaching it, even at the end of the loading. The micro-structural analysis in the initial state (Fig. 4b) shows a complex porosity in the case of the intact material and a bimodal porosity in the remolded sediment. In both cases, one can identify an inter-aggregate type of pores, and an intra-aggregate type. Volume changes obtained at the macroscopic scale appear to be the result of a decrease in the inter-aggregate pore volume in both remolded and intact specimens (Fig. 5 and Fig. 6). SEM photos show successive bands of oriented particles which are clearly visible in the remolded material (Fig. 5). An oriented structure is much less visible in the natural sediment (Fig. 6); it is nevertheless apparent in some parts of the material, and seems to be more frequent as the material becomes closer to the remoulded one under higher stresses.

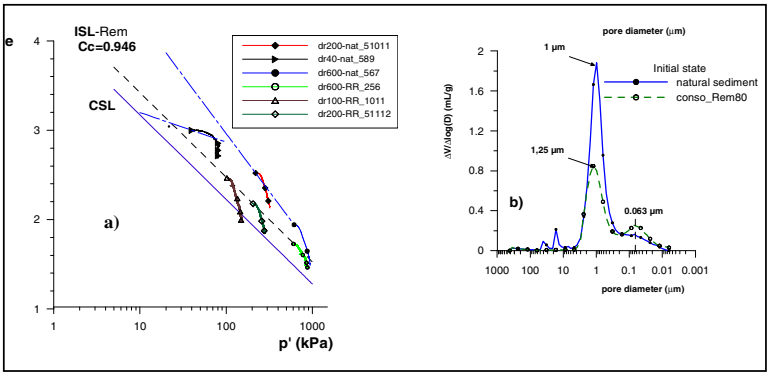

Fig. 4 Remolded and natural GoG sediments behavior

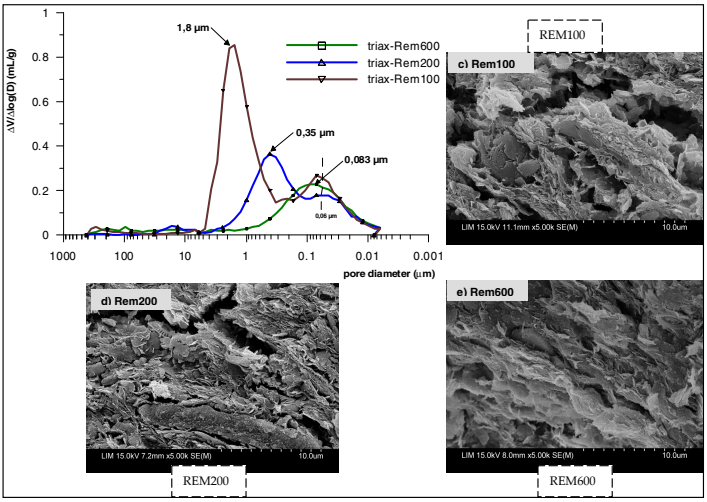

Fig. 5 Microstructural variation in the case of remolded GoG sediments

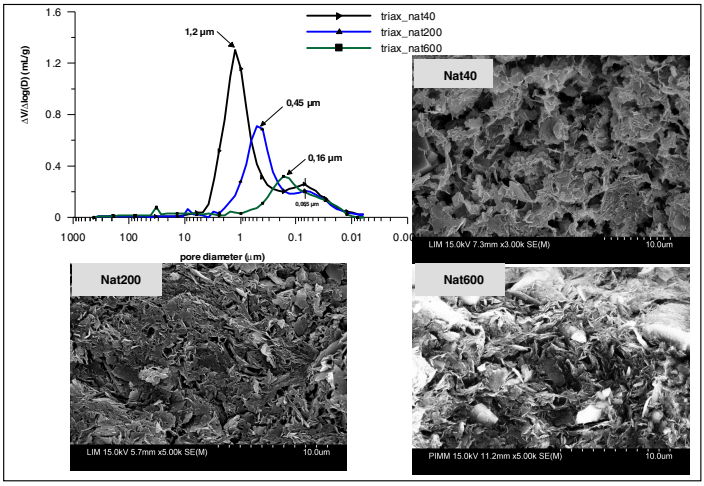

Fig. 6 Microstructural variation in the case of natural GoG sediments

4 Summary and Conclusion

One of the major conclusions that can be drawn from this study is that the mechanisms of volumetric deformation are mainly due to aggregate sliding. In all the studied loading cases, the inter-aggregate pore volume decreases (whereas the intra-aggregate pore volume remains fairly constant). This change is directly linked to the amplitude of the applied stress tensor in the remolded material, whereas it is necessary to add the effect of cementation damage in the case of the intact sediment. SEM images suggest that preferential directions of particle groups are formed in the remolded GoG sediment, and parallel cracks develop between these groups. The bonding between aggregates seems to delay greatly the reorientation mechanism which becomes possible only when the progressive degradation of the bonds provides more freedom to the aggregates to slide against and rotate around each other.

References

De Gennaro, V., Puech, A., Delage, P.: On the compressibility of deep water sediments of the Gulf of Guinea. In: Proc. Int. Symp. on Frontiers in Offshore Geotechnics, Perth, Australia, pp. 1063–1069 (2005)

Delage, P., Lefebvre, G.: Study of the structure of a sensitive Champlain clay and of its evolution during consolidation. Canadian Geotechnical Journal 21, 21–35 (1984)

Hattab, M.: Critical state notion and microstructural considerations in clays. C. R. Mécanique 339, 719–726 (2011)

Hattab, M., Hicher, P.Y.: Dilating behaviour of overconsolidated clay. Soils and Foundations 44(4), 27–40 (2004)

Hattab, M., Favre, J.-L.: Analysis of the experimental compressibility of deep water marine sediments from the Gulf of Guinea. Marine and Petroleum Geology 27, 486–499 (2010)

Hattab, M., Fleureau, J.-M.: Experimental analysis of kaolinite particle orientation during triaxial path. International Journal for Numerical and Analytical Methods in Geomechanics 35(5), 947–968 (2011)

Hattab, M., Hammad, T., Fleureau, J.-M., Hicher, P.-Y.: Behaviour of a sensitive marine sediment – Microstructural investigation. Paper submitted to Geotechnique (2012)

Leroueil, S., Tavenas, F., Brucy, F., La Rochelle, P., Roy, M.: Behaviour of de-structuted natural clays. Proc. Am. Soc. Civ. Engrs. 105, GT6, 759–778 (1979)

Application of X-ray Tomography to the Characterisation of Grain-Scale Mechanisms in Sand

G. Kaddhour[1], E. Ando[1], S. Salager[1], P. Bésuelle[1], C. Viggiani[1], S. Hall[2], and J. Desrues[1]

[1] Grenoble-INP , UJF-Grenoble 1 , CNRS UMR 5521, Laboratoire 3SR, Grenoble F-38041, France
simon.salager@hmg.inpg.fr
[2] Lund University, Division of Solid Mechanics, Lund, Sweden

Abstract. X-ray micro-tomography allows 3D imaging at sufficiently high spatial resolution to distinguish all the individual sand grains in a small sample (10mm diameter), as well as the distribution of air and/or water at this scale. Since this imaging technique is completely non-destructive, an imaged sample can be made to evolve by controlling some relevant variable (*e.g.*, imposed deformation, suction), and can subsequently be re-imaged. This allows processes to be followed in 4 dimensions (3D + relevant variable). This paper shows the application of this technique and philosophy to the study of two different phenomena: localised deformation resulting from imposed triaxial compression, and the water retention behaviour of sand. The experimental techniques and setups for these two studies are detailed, and the fundamental steps of image treatment are outlined. Some key results are given to demonstrate the power of this "full-field" characterisation approach, such as rotations and displacements for each of the 50,000 grains of a sample in which a shear band occurs as well as the evolution of local measurements of porosity and degree of saturation in a sand where suction is being varied.

1 Introduction

Recent developments in the application of x-ray micro-tomography in laboratory geomechanics have allowed all the different phases of sand in a test sample to be seen and identified in 3D. Combining such imaging capabilities with experiments carried out "in situ" within an imaging set-up had led to the possibility of directly observing the grain-scale mechanisms as they happen: grain displacements and breakage, the evolution of water repartition, etc. This paper aims to illustrate these kind of techniques through two experimental studies, one focusing on water retention behaviour (e.g. [3]), and the other on localised deformation in sand (e.g. [1]). The manuscript starts with a brief description of the devices used and the methods associated: the Laboratory 3SR x-ray scanner and the testing devices (a pressure plate apparatus and a triaxial cell, both adapted to x-ray scanning). The methods of image treatment and analysis are then presented. In order to illustrate these

L. Laloui and A. Ferrari (Eds.): Multiphysical Testing of Soils and Shales, SSGG, pp. 195–200.
springerlink.com

experimental methods, 3D measurements are finally described, map of porosity and degree of saturation all along a drying path and particles displacement during triaxial shearing.

2 Experimental Methods

X-ray Tomography: The x-ray scanner used in this study is a specialised lab scanner in Laboratory 3SR, Grenoble (Fig. 1b). It includes a Hamamatsu micro-focus x-ray source emitting a cone beam and a 1920 by 1536 pixel x-ray flat panel detector (measuring 195 by 244 mm). The sample to be scanned is placed between the source and the detector, on a translation and rotation stage, the latter being necessary for the specimen to be imaged at different angular positions. The range of x-ray energy of the source is 40 to 150 kev, allowing a range of different sample sizes and densities to be imaged. The spatial resolution (expressed in terms of voxel size) depends on the "zoom" level (i.e., the distance between the sample and the source); it cannot be smaller than the smallest spot size (5µm in low-power mode) and is limited upward by the physical size of the detector.

In the case of water retention analysis, scans are performed close to the highest zoom level for this apparatus. In order to perform successful scans, the spot size must be carefully controlled, which means putting a limit on the total x-ray power (and therefore the flux); this implies a relatively long scanning time of several hours for a single tomography. Such long scans are vulnerable to differential displacements (due to temperature change in the cabin) in the acquisition system, requiring corrections to the acquired images. A set of 1200 images acquired in a given state of suction are reconstructed into a 3D volume measuring 1500 vx where each voxel (a pixel in 3D) measures 7.5 μm^3 and contains a value of x-ray attenuation.

In the case of triaxial shearing, the voxel size of the 3D tomographic images is in the order of 15 μm^3 which allows individual grains to be clearly identified. A set of 1024 images acquired are reconstructed into a 3D volume measuring 1000x1000x1800 px.

Material: The two studies presented are carried out on Hostun HN31 sand, angular quartz sand, with D50 between 200 and 400µm, successor to the RF and S28 varieties that have been extensively studied in Grenoble in [2].

Pressure Plate: A "micro" pressure plate apparatus for investigating water retention has been specially developed allowing suction to be controlled by tensiometry (Fig. 1b). The sand sample is located between a ceramic disk in the bottom (air entry value of 5 bar) and a porous stone in the top, where water continuity from the bottom and air continuity from the top are guaranteed. A water tank that can move vertically over a scaled rule is connected to the water reservoir in the bottom of the cell. Moving the tank down creates difference in hydraulic head and since there is continuity in the liquid phase, suction is thus applied in the sample. To ensure full saturation, all phases of sample preparation are carried out completely under water.

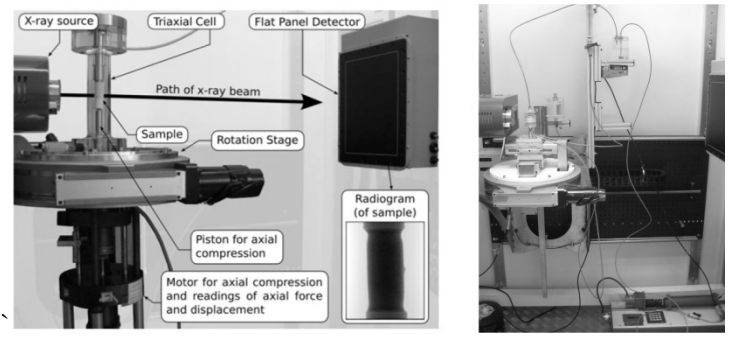

Fig. 1 a) Laboratoire 3SR Triaxial set-up ; b) photograph in place of pressure plate.

Triaxial cell: a separate, triaxial compression apparatus, has also been developed (Fig. 1a). It is practically the same as a conventional system, except the much smaller sample size (22x11mm) and the shape of the confining cell (which is made from Plexiglas - very transparent to x-rays). Note that the tensile reaction force is carried by the cell walls and not by tie bars (which avoids having any obstacles to the x-ray beam). The axial load and hence the deviator stress are applied using a motor-driven screw actuator, which also does not interfere with the x-rays (See [4] for full details). The samples are prepared by pluviation into a membrane stretched in a mould.

3 Data Analysis

The reconstruction is performed on high-speed GPU software (Digisens' DigiCT 2.4.2) using a standard Feldkamp back-projection algorithm – reconstructions are processed for beam hardening. The reconstructed 3D image allows examination of the entire sample domain. Fig. 2 presents a reconstructed image of the pressure plate apparatus for a suction of 1.2 kPa showing a vertical slice containing the sample's axis. Since the reconstructed x-ray attenuation coefficient depends mainly on the mass density, the three phases in the specimen can be distinguished in terms of their grey level (which corresponds to an x-ray attenuation coefficient). Grains are the most attenuating phase and appear lighter, air is the least attenuating and appears dark and water (where present) corresponds to an intermediate grey level. The repartition of the water menisci and air bubbles are clearly seen, together with the shape of grains.

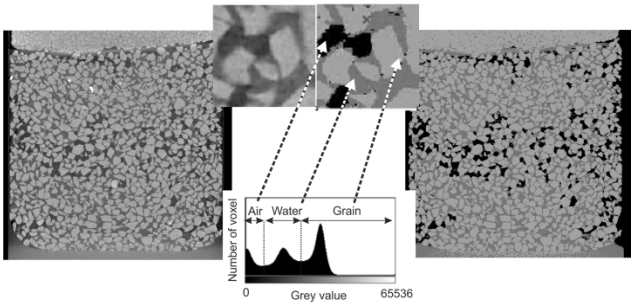

Fig. 2 Vertical slice of pressure plate apparatus, for a suction of 1.4 kPa. The image to the left is the "raw" reconstructed image, the one to the right is the trinarised image.

Fig. 2 shows the volume grey level distribution in the whole specimen. The distribution shows three peaks corresponding to the three phases; as before, the most attenuating phase (sand) has the highest value. The three peaks visible in the histogram show quite a wide distribution of grey values (*i.e.*, they are not Dirac functions). This spread for air and water cannot be explained by a dispersion of the x-ray absorption because the properties in these phases are expected to be homogeneous (albeit a small heterogeneity is possible inside grains). This spreading is due to i) image noise due to acquisition and reconstruction, ii) partial volume effect when several phases "share" the space inside one voxel, this causes the grey level of this voxel to be a result of the volume average of phase attenuation values and so is an intermediate value between peaks.

Image Analysis for Pressure Plate Experiment: The volume has been "trinarised" (each voxel is the image is assigned either to grain, water, or air phase) using two thresholds, one between air and water peaks and the second one between water and grain peaks. This last one is chosen in such a way that volume of voxels identified as grain phase correspond to volume of grains that has been estimated from the weight of the sample (in a dry state). The threshold between air and water is chosen to correspond to the local minimum in the grey level distribution. Fig. 2 shows a vertical and a horizontal slice from a trinarised image of the sample at 1.4 kPa suction.

Image Analysis for Triaxial Experiments: In order to be able to measure individual grain kinematics, grains must be identified in all of the reconstructed 3D image of the sample. This is achieved by binarising the images, designating all voxels above a certain threshold as grain, and those below as pore. The threshold value is chosen so that the grain volume selected equals the measured volume of the grains in the sample. These binarised images (containing a single, interconnected grain mass) are separated into individual grains using a watershed algorithm - at which point grains can be labelled. ID-Track [1] can then be used to follow grains from one image to another, recognising them locally, based on invariant grain features, such as volume.

4 Key Results

Water Retention Behaviour: as a result of the full field measurements previously done, values of porosity and degree of saturation are obtained in 3D throughout the volume for each applied level of suction. These fields can be analysed and relations between them studied. The results presented in Fig. 3 shows vertical slices through the field of porosity, degree of saturation, and the relation between the two, for a suction value of 2 kPa. It appears that the high porosity region is linked with the low degree of saturation region. Similarly, the high degree of saturation zones are linked to low porosity ones. The map of porosity and degree of saturation retrieve properly the variables for the entire sample field.

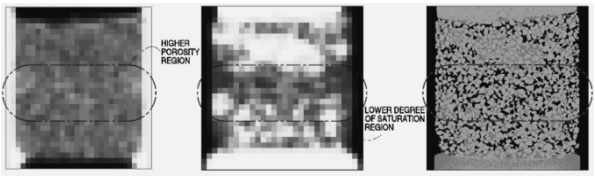

Fig. 3. Porosity map (left) degree of saturation map (centre) and trinarised image (right).

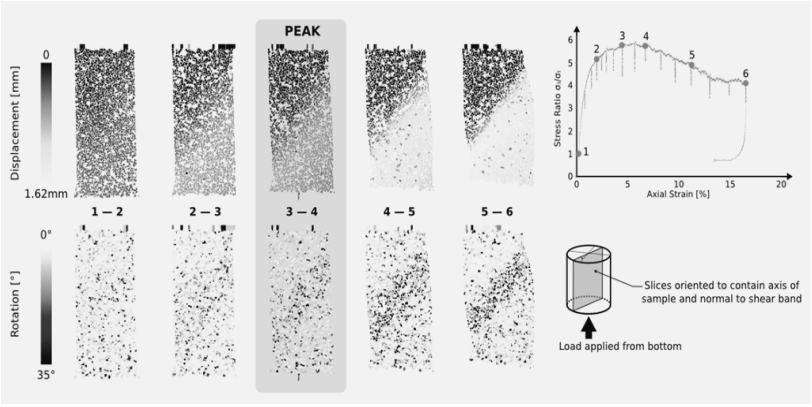

Fig. 4 Results of ID-Track on 5 strain increments for a triaxial compression test on Hostun Sand.

Localised Deformation in Sand: Fig. 4 shows displacements and rotations for all grains measured with ID-Track over the five increments of loading shown. This rich micromechanical information allows localised phenomena like shear banding to be studied at the grain scale. One key result is that the shear band is visible earlier in the test from the displacement maps (some indications of the position of the shear band in the increment before the peak) than in the rotation maps (rotations

concentrate after the peak). In the residual stress state, the width of the shear band, as measured by from the displacement maps is 7-8 grains wide, whereas is it is wider when looking at the rotations of grains.

5 Conclusion

X-ray tomography allows us to go beyond boundary measurements and understand what is happening inside materials. This paper shows how for two different investigations on sand it is possible to image a process in 3D. Using a pressure plate apparatus different hydraulic equilibrium states are imposed on a Hostun sand sample from which trinarised images of the entire sand volume are obtained. This allows a 3D quantitative analysis of the specimen's characteristics. Consequently, not only the global water retention curve is obtainable through image processing, but also a local relation between suction, porosity and degree of saturation can be computed for each point in the sample. For the data coming from triaxial compression tests, individual grain kinematics are measured. This allows phenomena such as strain localisation to be analysed at the grain scale. These examples of the application of x-ray micro-tomography in laboratory geomechanics show the power of this non-destructive method, allowing us to go beyond measurements at the boundaries and allowing the characterisation of different processes in 3D.

References

Andò, E., Hall, S., Viggiani, G., Desrues, J., Besuelle, P.: Grain-scale experimental investigation of localised deformation in sand: a discrete tracking approach. Acta Geotechnica 7(1), 1–13 (2012)

Flavigny, E., Desrues, J., Palayer, B.: Le sable d'Hostun RF. Revue Francaise de Geotechnique 53, 67–69 (1990)

Riedel, I., Andò, E., Salager, S., Bésuelle, P., Viggiani, G.: Water retention behaviour explored by X-ray CT analysis. In: Proceedings of E-UNSAT 2012, Napoli (2012)

Viggiani, G., Lenoir, N., Bésuelle, P., Di Michiel, M., Marello, S., Desrues, J., Kretzschmer, M.: X-ray micro tomography for studying localised deformation in fine-grained geomaterials under triaxial compression. C. R. Mécanique 332(10), 819–826 (2004)

Observation of Shear Banding Characteristics of Sand in Torsional Shear Test Using Image Analysis Technique

Seto Wahyudi, Yukika Miyashita, and Junichi Koseki

Dept. of Civil Engineering, Institute of Industrial Science (IIS), The University of Tokyo
Ce-202, 4-6-1 Komaba, Meguro-ku, Tokyo, 153-8505, Japan
seto-w@iis.u-tokyo.ac.jp, ymiya@iis.u-tokyo.ac.jp,
koseki@iis.u-tokyo.ac.jp

Abstract. Accurate measurement in shear banding and strain localization studies is critical in characterizing the microstructural behavior within failure area. This research is aimed to investigate the effects of initial relative density on the shear banding behavior of sand. A series of tests on Toyoura sand with different initial relative densities were conducted using a hollow cylinderical torsional shear apparatus under drained condition. Unlike the tests conducted on prismatic specimens on plane strain condition, the tests conducted on hollow cylinderical specimens require more complex data analysis due to the curvature of their outer side surface. The test results both dilatancy rate and shear band expansion magnitude are found to have unique relationships with the specimen initial relative density.

1 Introduction

One of the important phenomenons associated with the microstuctural behavior within failure area in geomechanics is so called shear banding. Shear banding process is initiated at the state when the mobilized strength of geomaterial reaches its peak and develops as shear deformation continues. Researchers have found that shear banding and strain localization behaviors were affected by various parameters such as particle mean diameter, confining stress among others.

Recent studies on shear banding and strain localization were mostly conducted in plane strain compression test. However, in this paper, shear banding observations were conducted by using hollow cylinder torsional shear apparatus. Unlike plane strain compression test, torsional shear apparatus is capable of simulating the rotation of major principal stress direction during loading process. However, shear banding observation in torsional shear test may complicate the analysis process due to the cylindrical specimen surface. Moreover, limited numbers of researches that are related with shear banding studies have been conducted by using torsional shear apparatus. Therefore, this paper is aimed to investigate the effects of relative density on shear banding of sand while at the same time providing special image analysis method that can be used in torsional shear test.

L. Laloui and A. Ferrari (Eds.): Multiphysical Testing of Soils and Shales, SSGG, pp. 201–206.
springerlink.com

2 Experimental Program

Toyoura sand was used as the test material. Its particles have an angular or sub-angular shape with the following physical properties: specific gravity, G_s=2.656; mean diameter, D_{50}=0.162mm; fines content, F_c=0.1%; max. void ratio, e_{max}=0.992; min. void ratio, e_{min}=0.632. Tests were conducted on hollow cylindrical specimen having the height of 30cm, the inner and outer diameters of 12cm and 20cm, respectively.

A series of test were conducted under different values of initial relative density at Dr_0= 53.9% (e_0=0.779), Dr_0= 73.2% (e_0=0.710) and Dr_0= 81.7% (e_0=0.680), which correspond to loose, medium dense and dense packing. Specimens were prepared by pluviation of air-dried sand particles into a mold through air. Their falling height was kept constant throughout the pluviation process in order to obtain specimens with highly uniform density. To satisfy fully saturated condition (B-value $\geq$ 0.96), double vacuuming was used during the saturation process, considering the large size of the specimen.

A drained shear loading with constant shear strain rate of 0.15%/min. was applied while maintaining other stresses at $\sigma_z'=\sigma_r'=\sigma_\theta'$= 100 kPa throughout the loading process up to 20% global shear strain deformation.

For the image analysis purpose, black dots of about 1.0 mm in diameter were pasted at a constant spacing of 5mm x 5mm on the front face of outer membrane covering the specimen. A digital camera with the resolution of 3456 x 2304 pixels was employed to take a series of digital photos. The photo-taking timer was regulated by the control system connected via D/A board to the computer. During torsional shear loading, each photo was taken at a constant interval time of 1 minute, which corresponds to 0.15% in terms of global shear strain increment ($d\gamma$). In addition, to enhance the contrast between the black-colored target dots and bright color of membrane, two sets of light sources were prepared on each side of torsional shear apparatus.

3 Data Analysis Procedures

The digital camera transforms three-dimensional object into two-dimensional image as projected on the image plane. As a result, cylindrical surface of the specimen in hollow cylinder apparatus would create so called warping distortion on the image plane as shown in Fig. 1(a). In addition, the refraction of water inside the cell chamber and the possibility of unsymmetrical initial setting of the camera would enhance the distortion.

In analyzing the image, the apparent orthogonal coordinates (x,y) from the target dots were tracked by an image tracking software (Move-tr/2D Ver. 7.21) with the accuracy of about 0.1mm. Then, correction is applied to convert the apparent coordinates into the real ones (x',y') as shown in Figs. 1(a) to 1(b). In this study, the correction functions were formulated using polynomial function as shown below:

$$x' = f_1(x, y) \text{ and } y' = f_2(x, y)$$

$$x'_{(m)} = a_{0(m)} + a_{1(m)}x_{(m)} + a_{2(m)}y_{(m)} + a_{3(m)}x^2_{(m)} + a_{4(m)}xy_{(m)} + a_{5(m)}y^2_{(m}$$

$$y'_{(n)} = b_{0(n)} + b_{1(n)}x_{(n)} + b_{2(n)}y_{(n)} + b_{3(n)}x^2_{(n)} + b_{4(n)}xy_{(n)} + b_{5(n)}y^2_{(n)}$$

where, *x'* and *y'* are the real/corrected coordinates in horizontal and vertical directions, respectively. *x* and *y* are the apparent coordinates in horizontal and vertical directions, respectively. The coefficients a_0 through a_5 and b_0 through b_5 are assigned based on calibration results by means of least square error method. *m* and *n* are the number of column and row, respectively.

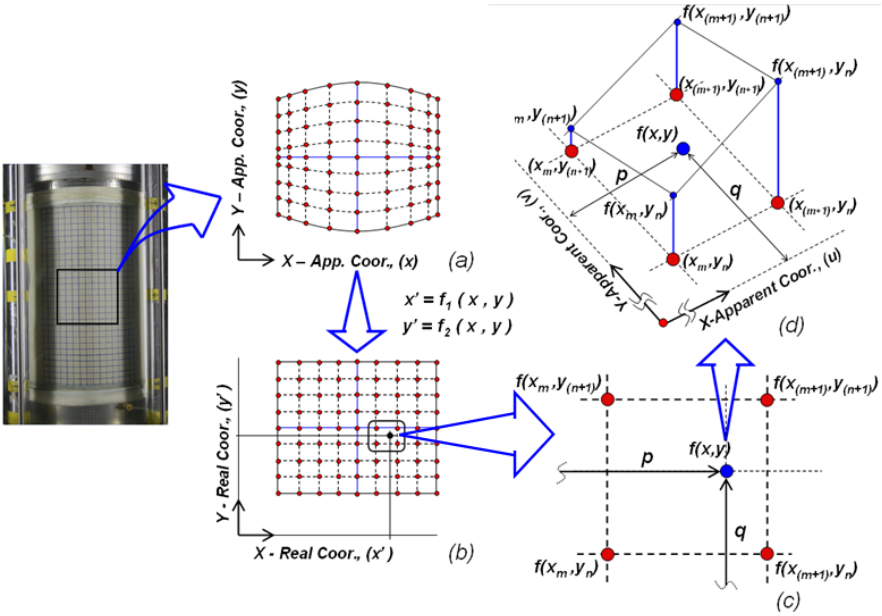

Fig. 1 Image analysis procedure

In addition to the correction given above, the unknown real coordinate located in between other known coordinates is evaluated by using bilinear-interpolation method as shown in Figs. 1(c) and 1(d). This method works by weighting the unknown value relative to their four known nearest-neighborhood values. The formulation of bilinear-interpolation method is given in equation below:

$$(x', y') = f(x, y)$$

$$= \frac{1}{(x_{m+1} - x_m)(y_{n+1} - y_n)} \begin{bmatrix} f(x_m, y_n).\{(x_{m+1} - p).(y_{n+1} - q)\} + \\ f(x_{m+1}, y_n).\{-(x_m - p).(y_{n+1} - q)\} + \\ f(x_m, y_{n+1}).\{(x_{m+1} - p).-(y_n - q)\} + \\ f(x_{m+1}, y_{n+1}).\{-(x_m - p).-(y_n - q)\} \end{bmatrix}$$

where, p and q are the apparent coordinates of random target point in horizontal and vertical directions, respectively.

In this study, shear banding characteristics is presented in the form of relationship between shear displacement across the shear band (Us) and the change of shear band expansion (Un). Therefore, the evaluation of shear displacement (Us) and shear band expansion (Un) as well as the angle of shear band (θ) will be discussed as follows.

Evaluation of shear band angle (θ): In torsional shear test, shear band is formed in a spiral shape with a certain inclination angle. Shear band angle was evaluated by measuring both vertical and horizontal distances between two observation points (H and L) located across the shear band as shown in Fig. 2(b).

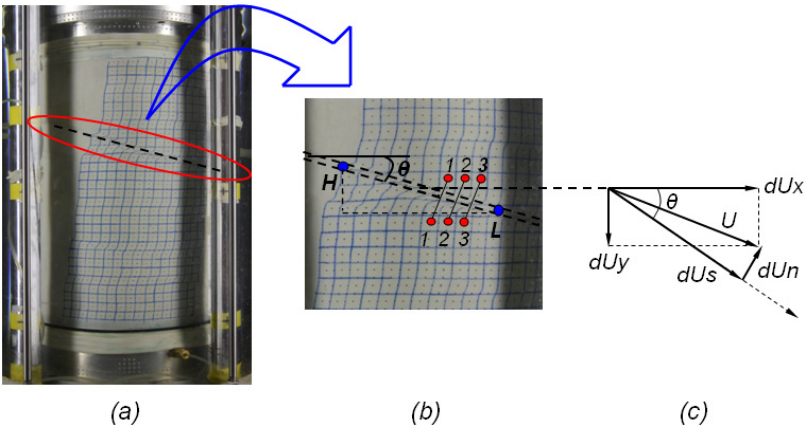

Fig. 2 Shear band expansion (Un) and shear displacement (Us) evaluation procedures

Evaluation of shear displacement (Us) and shear band expansion (Un): Three pairs of target points located just outside of shear band were selected as shown in Fig. 2(b). Then, their relative displacements in parallel and perpendicular with the shear band (dUs and dUn, respectively) were evaluated as shown in Fig. 2(c). Finally, shear displacement (Us) and shear band expansion (Un) were obtained by integrating these increments. The accuracy of evaluation was confirmed by comparing the respective results from the three pairs of observation.

4 Test Results and Discussion

Global shear stress ratio-shear strain relationship and global volumetric strain-shear strain relationship are shown in Fig.3. Both figures clearly show that denser specimens consistently achieve higher peak of shear stress ratio $(\tau/p')_{peak}$ and higher positive dilatancy. It can be seen in the global volumetric strain-shear strain relationship, that the dilatancy rate remains positive during the post peak strain-softening region and even at the residual stress states; however, this dilatancy behavior is different from the local behavior within the shear band as discussed later.

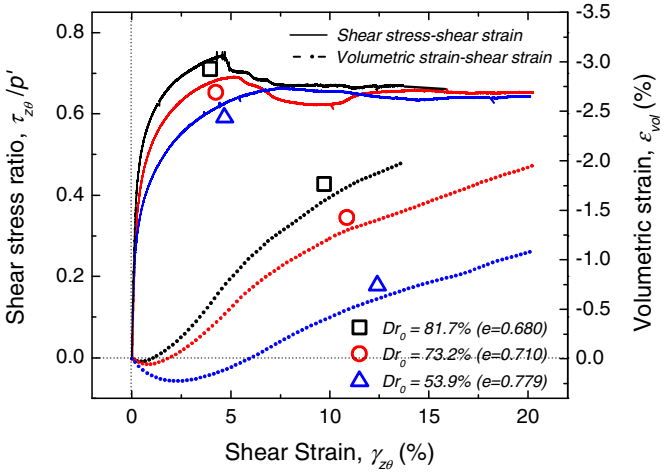

Fig. 3 Stress-strain and volumetric strain-shear strain relationships

Yoshida et al. (1994) [1] revealed the shear banding process is initiated near the peak stress state and develops through the residual stress states. Therefore, shear displacement and shear band expansion in the post-peak stress state region are evaluated as $(Us\text{-}Us_{peak})$ and $(Un\text{-}Un_{peak})$, respectively, where Us_{peak} and Un_{peak} are the values of Us and Un at the peak stress state.

Shear displacement and shear band expansion relationship is plotted in Fig. 4. This figure shows shortly after the onset of shear band formation around the peak stress state, the shear band expanded rapidly and then at some point the expansion rate $(=dUn/dUs)$ was decreased towards zero. The latter local behavior in shear band was found to be different from their global behavior as previously discussed. It was also observed that the shear band subsequently exhibited slight contraction.

Figure 4 also suggests that initial relative density of specimen affects the behavior of shear band. First, denser specimens initially exhibited higher expansion rate (positive dilatancy). Second, denser specimen reached larger amount of shear band expansion. In the current tests, the dense and medium dense specimens reached expansion of approximately 0.9 mm and 0.8 mm, respectively, while the

loose specimen reached expansion of approximately 0.5 mm. Similar findings have been reported by Yoshida et al. (1994) [1], where the final value of shear band expansion (*Un*) is found to depend on the initial relative density.

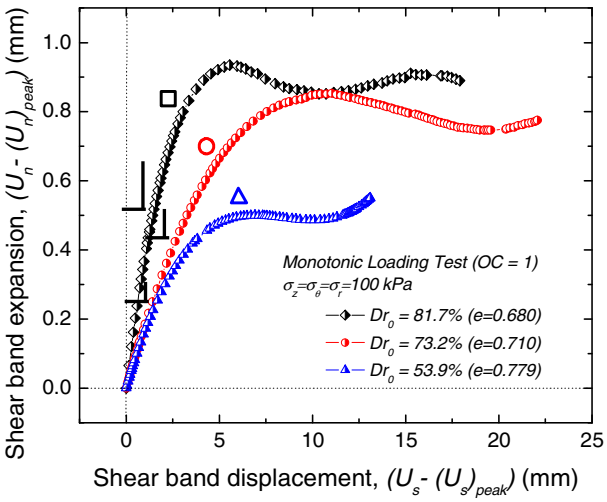

Fig. 4 Shear band expansion-shear displacement relationship

5 Conclusions

The investigation of local behavior within the shear band and the global behavior of sand in torsional shear test revealed several observations, as summarized below:

1. The expansion rate (*dUn/dUs*) within the shear band is affected by the specimen initial relative density. Specimen with higher initial relative density shows higher rate.
2. The final value of shear band expansion (*Un*) depends on the specimen initial relative density, where denser specimen shows higher expansion.
3. The global behavior of specimen is slightly different from their local behavior within shear band. During the post-peak strain softening and residual stress states region, the global behavior shows continuously positive dilatancy rate, while the local behavior shows decrease in the expansion rate of shear band that is followed by slight contraction.

Reference

Yoshida, T., Tatsuoka, F., Siddiquee, M.S.A., Kamegai, Y., Park, C.S.: Shear banding in sands observed in plane strain compression. In: Chambon, R., Desrues, J., Vardoulakis, I. (eds.) Localization and Bifurcation Theory for Soils and Rocks, pp. 165–179. Rotterdam, Balkema (1994)

Experimental and Quantitative Study on Micro-structure of Soft Soil in Suzhou

Xiaozhao Li, Liang Cao*, Zhiyong Xiong, Rong Yang, and Juan Ma

NJU-ECE Institute for Underground Space and Geo-environment, School of Earth Sciences and Engineering, Nanjing University, 210093 Nanjing, P.R. China
bingshimoya@126.com

Abstract. Based on division of the engineering geological strata groups of Eastern Plain area in Suzhou City of China, we identify two soft soil strata among them, which will bring negative impacts on local underground construction. In order to obtain digital micro-structure images of undisturbed soft soil by SEM, free piston thin wall sampler and frozen drying-paste method are used for preparation of the specimens. By utilizing the micro-image processing software of Mifas, we can get the quantitative indicators of the SEM images, such as the index of directionality and eccentricity of particles. It is found that the microscopic structure analysis of two soft soils could appropriately explain their macro-mechanical differences.

1 Introduction

With high water content, strong compressibility, low strength, low permeability, significant rheological behavior, poor engineering properties and low foundation bearing capacity of soft soil, it will bring about bad impact on local underground construction on some occasions. Suzhou is situated on the lower reaches of the Yangtze River and on the shores of Taihu Lake and is a part of the Yangtze River Delta region. In recent years, with rapid growth of urban economy and concentration of population, there are urgent needs to construct urban tunnels and underground infrastructures in Suzhou where quaternary system deposits of soft soil are widely distributed. Therefore, it is important to reveal the local intrinsic reasons regarding its micro-structure variations of soft soil, which could be bound up with its macro engineering properties and environment of sedimentation (Zhou et al., 2011).

Over the last decades, the microscopic research of soft soil mainly refers to following parameter: such as total acreage of particles, statistical perimeter, average pore diameter, shape factor, roundness, anisotropy rate, cementation of clay mineral, inter contacting relationship and so on (Chen, 2011; Li and Hua, 2006). And related testing techniques also appear to develop significantly, such as X-ray diffraction, Scanning Electron Microscope (SEM), X-Ray, CT, digital image measurement, photoelastic experiment, and TDR technology. In this study,

* Corresponding author.

L. Laloui and A. Ferrari (Eds.): Multiphysical Testing of Soils and Shales, SSGG, pp. 207–212.
springerlink.com

we used SEM technology to obtain digital micro-structure images of undisturbed specimens of two soft soil strata, and related quantitative indicators of their SEM images, such as the directionality and eccentricity index of particles were accordingly analyzed. Such a work is useful for better understanding the basic engineering properties and sedimentary environment of soft soil strata in Suzhou, as well as providing important experimental data to establish the relationship between soil micro-structure and macro- mechanical characteristics.

2 Experimental Methods

2.1 Sampling Location

According to the basic topography and landform conditions, urban planning area in Suzhou can be divided into two main geomorphic units: the Western Denudation Hilly Area and the Eastern Sedimentary Plain Area. The Eastern Sedimentary Plain Area could also be divided into High Alluvial-lacustrine Plain Area and Low-lying Lacustrine Paludal Plain Area (Cao et al. 2012). Two soft soil strata (3) and (7) are respectively obtained in two boreholes of SZZT16# at Chefang Town and SZZT33# at Zhouzhuang Town (Fig.1). Then free piston thin wall samplers are utilized to get undisturbed soil specimens in the Low-lying Lacustrine Paludal Plain Area. According to the laboratory testing results of soft soil specimens of these two strata, mean value of their physical and mechanical indicators are listed in Table 1. Strata (3) and (7) might function in effect as the first and second soft soil stratum in Suzhou, which are mostly composed of muddy silty clay with high water content, high void ratio, high compressibility, poor permeability, low strength, and strong heterogeneity. These two weak-sensitive strata should be paid more attention to non-homogeneous settlement during the design of shallow foundation structures and underground subway foundations. Due to low shear strength and obvious rheological characteristics of soft soil stratum (3), it is hard for foundation pit to be self-supported during excavation. As for stratum (7), silty clay with fine sand interbed is usually a sediment deposited alternately by silty clay and fine sand, appearing to be a "thousand layers cake".

Table 1 Physical and mechanical indicators of soft soil in Suzhou

Stratum	Borehole	Average depth (m)	Void ratio (/)	Water content (%)	Dry density (g/cm^3)	Plasticity index (/)	Liquidity index (/)
(3)	SZZT16	5.3~5.8	1.34	49.9	1.16	14	2.22
(7)	SZZT33	26.9~27.2	1.02	37.1	1.34	10	1.32

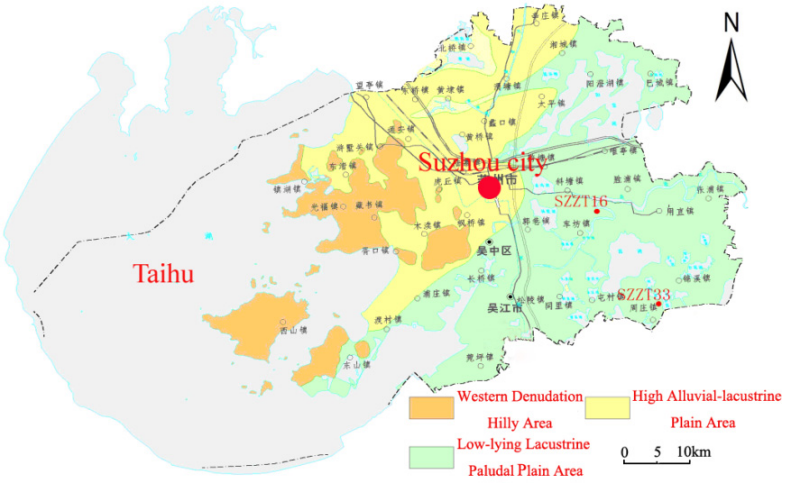

Fig. 1 Geomorphic units division and sampling locations in Suzhou urban planning area

2.2 Preparation for the Microscopic Structure Analysis

Frozen-drying method is utilized to eliminate the pore water in soil, in order to avoid volume expansion during the transformation from water to crystal ice. After that, several soil strips are manually made by slightly breaking the soil specimen off, instead of directly cutting with mechanical cutting tools. The size of each soil strip is approximately 15 mm (length) ×10 mm (width) ×10 mm (height). Finally, we use a wide adhesive tape to pick off the floating particles on the surface of soil specimen carefully. So a smooth, clean and fresh working surface for microscope observation is finally obtained.

It is pointed out that a high magnification factor (>3000X) by SEM would give rise to "image geometric distortion" of soil microscopic image (Tang et al. 2008). Taking the microscopicspecimen of stratum (7) for example: firstly, we analyze the total structural features by using a relatively low magnification factor (500X), and select a representative observation area avoiding oversized pores or particles (Fig.2a). Then the magnification factor is raised up to 2000X in order to study the pore and particle characteristic at a reasonablemagnification level (Fig.2b). Finally, soil microscopic images and related quantitative parameters are analyzed by the software of MiFas (Cao et al. 2010). Pores in black and particles in light gray could be automatically identified by setting contrast threshold value in this software (Fig.2c). If the threshold value is set very high, more pixel points will be mistakenly classified as the pores instead of particles, which will result in the increase of pores quantity and overall porosity ratio.

Therefore, with the experimental referential data of stratum (3) and (7), which is obtained from the measurement of porosity ratio (42.7% and 49.5%) in laboratory tests, we set 75 as a referring threshold value in Mifas and get their approximate two-dimensional porosity ratio of 40.8% and 47.6% of micro-structure images after binary conversion and noise reduction process.

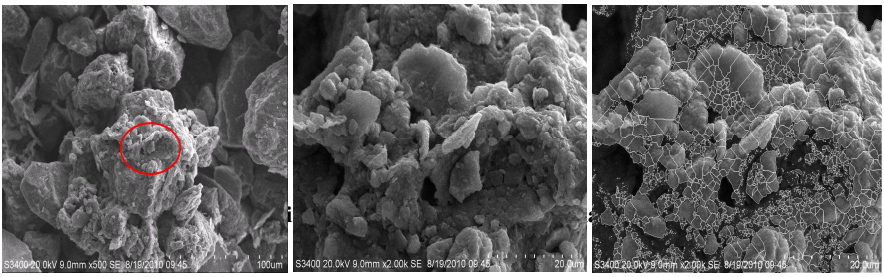

(a) 500X (b) 2000X (c) 2000X

Fig. 2. Experimental images by SEM and analysis process

3 Results and Discussion

3.1 The Directionality of Particles

The directional angle is defined as the angle between particle's long axis and horizontal direction. Due to the symmetry of directional range 0~180° with 180°~360°, the rose diagram of 0 ~ 180 ° is accordingly drawn to represent the directional angle and the particles' distribution probability in Fig.3. The particle amount and corresponding distribution probability of six main distribution ranges are also statistically listed in Table 2.

It is found that the particles distribution regularity for stratum (3) and (7) has followed some certain similarities, both of their directional angleare mostly distributed in the range of (0, 15°) and (90, 105°), which could indicate that anisotropy of soft soil in Suzhou is relatively high and weak-structured.Thereby the macro-sensitivityis relatively low, which is consistent with our indoor sensitivity testing results: the soil sensitivity of stratum (3) is between 3 and 4, and it is between 2 and 3 for stratum (7).

As for the two dominant distribution range of (0, 15°) and (90,105°), corresponding distribution probability is 23.48% and 21.15% for stratum (3) shown in Fig.3a, whereas 28.52% and 16.16% for stratum (7) shown in Fig.3b. Therefore, the distribution probability of stratum (3) in the range (0, 15°) is lower than stratum (7), but the distribution probability in the range (90,105°) is relatively high due to lower vertical gravity stress. Because particle's long axis is approximately the same direction with gravity stress in the range of (90,105°), the contact area is relatively small and a stable microscopic structure is likely to develop under vertical loads in the process of soil consolidation, so the angle between long axis and the horizontal direction will gradually decrease, and the directional angle of (0, 15°) could be supposed to be a more stable load-bearing form than that of (90,105°) for soil particles. This could be one kind of microscopic mechanism leading to explain the difference of macro engineering properties that compression coefficient of stratum (3) is smaller than (7) from the analysis of our micro-scale experiments.

Table 2 Amount in each direction angle interval and distribution probability

Stratum	Particle amount in each directional angle range / Distribution probability					
	(0, 15°)	(45, 60°)	(60, 75°)	(90, 105°)	(135, 150°)	(165, 180°)
(3)	668/ 23.48	224/ 7.88	398/ 13.98	602/ 21.15	179/ 6.28	288/ 10.13
(7)	743/ 28.52	205/ 7.87	153/ 5.87	421/ 16.16	210/ 3.01	236/ 9.05

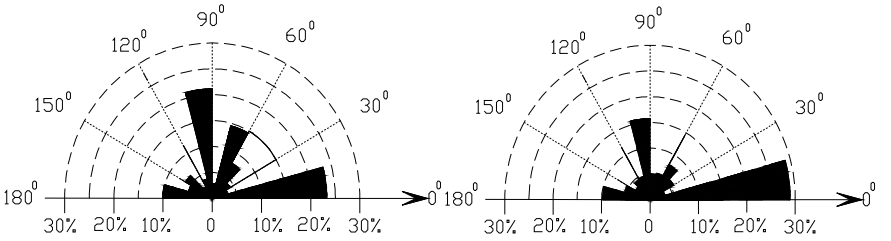

(a) stratum(3) (b) stratum(7)

Fig. 3 Rose diagram of directional angle for stratum (3) and (7)

3.2 Eccentricity of Particles

The eccentricity of particle is defined as the length ratio of short axis and long axis, which ranges from 0 to 1. Generally, an aspheric and narrow particle has a lower value of eccentricity. We can learn from Fig. 4 that the eccentricity value of soft soil stratum (3) and (7) is mainly concentrated in the range of (0.4, 0.5) and (0.9, 1.0). However, the total distribution probability of stratum (7) in the distribution range (0.6, 1.0) is 62.09%, which is nearly twice the value of stratum (3). It is indicated that larger burial depth along with higher consolidation pressure will give rise to the increase of elliptic or round particles and decrease of aspheric and narrow ones for stratum (7). Besides, stratum (3) is recently-deposited lacustrine soft soil rarely affected by fluctuation flow in the Holocene alluvium, whereas the stratum (7) is coastal-shallow marine deposited during the upper Pleistocene period. At last, Gehu transgression also gives an important impact on the formation of stratum (7), this transgression since Pleistocene was controlled by area tectonism and closely interrelated to fluctuation of sea level. So due to the hydrodynamic depositional environment and historical transgressive effects, the particles of stratum (7) are well-sorted and with a better psephicity from the microscopic analysis of particles' eccentricity.

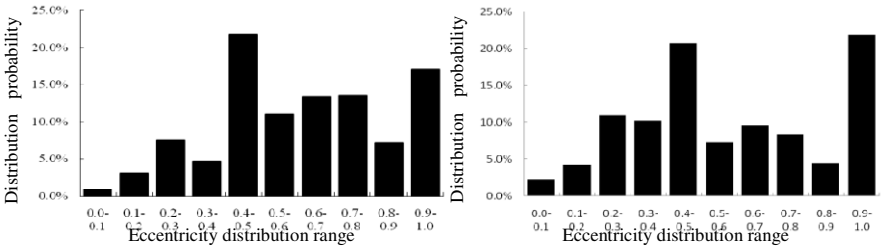

(a) stratum(3) (b) stratum(7)

Fig. 4 Distribution probability of particles' eccentricity for stratum (3) and (7)

4 Conclusions

It is found that both of the specimen directional angle of two soft soil strata are mainly distributed in the range (0, 15°) and (90, 105°). And corresponding distribution probability is 23.48% and 21.15% for stratum (3), whereas 28.52% and 16.16% for stratum (7). It is illustrated that the anisotropy of soft soil in Suzhou is relatively high and weak-structured. In addition, specimen from stratum (3) has a relatively higher distribution probability of eccentricity in the distributionrange (0.6, 1.0), due to its coastal-shallow marine depositional environment and historical transgressive hydrodynamic effects.

Acknowledgements. This study was financially supported by the Sino-Swiss Science and Technology Cooperation Program (2009DFA22680) and Graduate Student Innovation Project of Jiangsu Province (CX10B_019Z).

References

Cao, L., Liu, W.B., Li, X.Z., Zhao, X.B., Zhang, H.: Micro Mechanics Study of Granular Soil Based on the Confined Compression Tests. In: Proceedings of the International Symposium on Geomechanics and Geotechnics: From Micro to Macr., vol. 1, pp. 421–425 (2010)

Cao, L., Li, X.Z., Tacher, L., Yang, R.: Three-Dimensional Geological Modeling Based on Division of Engineering Geological Strata Units. Adv. Sci. Lett. 5(2), 510–514 (2012)

Chen, W.L.: Quantifying soil micro-structure using fractals under dynamic replacement with rip rapping and removing silt, pp. 427–432. Crc Press-Taylor & Francis Group, Boca Raton (2011)

Li, X.Z., Hua, A.Z.: Prediction and prevention of sandstone-gas outbursts in coal mines. Int. J. Rock Mech. Min. 43(1), 2–18 (2006)

Tang, C.S., Shi, B., Wang, B.J.: Factors affecting analysis of soil microstructure using SEM. Chinese J. Geot. Eng. 30(4), 560–565 (2008)

Zhou, H., Fang, Y.G., Gu, R.G., Zeng, C.: Microscopic analysis of saturated soft clay in Pearl River Delta. J. Cent. South Univ. T 18(2), 504–510 (2011)

Development of a New Experimental Device in Order to Improve Swelling-Shrinkage Analysis of Clayey Soils

Tatiana Maison[1], Jean-Bernard Kazmierczak[2], Farid Laouafa[2], and Patrice Delalain[2]

[1] LaSalle Beauvais Polytechnic Institute - 19, rue Pierre Waguet - B.P. 30313 - 60026 Beauvais Cedex - France
Tatiana.maison@lasalle-beauvais.fr
[2] INERIS - Parc Technologique Alata - B.P. 2 - 60550 Verneuil-en-Halatte - France
Jean-Bernard.KAZMIERCZAK@ineris.fr, Farid.laouafa@ineris.fr, Patrice.delalain@ineris.fr

Abstract. The swelling-shrinkage of natural clayey soils was analyzed at the microscopic level, in an Environmental Scanning Electron Microscope (ESEM). They were subjected to several wetting-drying cycles with a new experimental device (patent n° 10-54771). It allows measuring simultaneously the surface strain evolution and the water content according to the relative humidity. The relation between these two parameters was established. These results can be correlated to water content evolution profiles function with the depth performed in situ (Maison, 2010).

1 Introduction

The swelling-shrinkage of clayey soils requires, for its estimation on a given area, parameters obtained by laboratory tests, leading on samples with a volume of several cubic centimetres. The low kinetic of clayey soils involves time tests until three months for triaxial tests or retention curves.

Nowadays, this drawback can be overcome with the use of the Environmental Scanning Electron Microscope (ESEM). The control of the hygrometric conditions in the ESEM chamber allows the analysis of the specimen under *in situ* hygrometric conditions (Romero and Simms 2008). The samples can be study in powder form, which decrease a time test to 24 hours for clays.

In order to study the swelling/shrinkage behaviour in clayey soils, ESEM observations were carried out on natural clays (taken in situ). Two clays are presented as example: an homogeneous natural clay (Greek montmorillonite) (Fleureau et al. 1993, Souli et al. 2008) and an heterogeneous natural clay (Romainville clay) (Audiguier et al. 2007).

The purpose of this paper is to suggest the observation and analyse of the swelling-shrinkage evolution of the two natural clays according to the water content. For this purpose, an experimental device was developed in order to weight the

L. Laloui and A. Ferrari (Eds.): Multiphysical Testing of Soils and Shales, SSGG, pp. 213–218.
springerlink.com

sample in powder form simultaneously with the observation of clay particles. With the weight evolution measurement and the intial water content, the water content evolution can be obtained and linked with the surface strain evolution of clay particles.

From these results, some applications can be imagine like the linking with in situ water content evolution measurements according to the depth. The extrapolation from the microscopic scale of the ESEM to the macroscopic scale of structures should be established for the estimation of swelling-shrinkage on a given area for example.

2 Macroscopic Clay Features

The Greek montmorillonite comes from Milos Island, in the Cyclades archipelago, and has a sedimentary origin. As its name indicates, it is composed mainly of smectite, an expansive clay species. The main features of this clay are shown in Table 1. For this clay, about 90 % of free swelling were measured on sample with classical geotechnical tests (Fleureau et al. 1993).

Romainville clay comes from the East of Paris (France), and has also a sedimentary origin. The clay species present in the specimen are kaolinite, illite and illite/smectite interlayers and it also contains carbonate, quartz and feldspar. This material was characterized by Audiguier et al. (2007) (Table 1). The swelling intensity for remoulded Romainville clay averages 25 %.

Table 1 Geotechnical characterisation of Greek montmorillonite (Fleureau et al. 1993, Christidis et al. 1997) and Romainville clay (Audiguier et al. 2007)

	Liquid limit, wL, %	Plastic limit, wP, %	Plasticity index, Ip	Specific surface, m²/g	CEC, meq/100 g
Greek montmorillonite	170	60	110	61.76	104.4
Romainville clay	75	40	35	195	39.5

3 Experimental Procedure

3.1 Environmental Scanning Electron Microscopy (ESEM): Advantages and Drawbacks

The ESEM is an electronic microscope device which allows observations of samples (soil for instance) under controlled environmental conditions (sample temperature, water vapour pressure, thus hygrometry).

Among all the qualities of the ESEM apparatus, a very important one is to maintain the sample unremoulded without any preparation (freezing, lyophilisation and coating as in classical mode). The sample's structure and natural water content are then unperturbated. On the other hand, its main drawback is linked to

the image quality (contrast and brightness) which strongly depends on the chamber humidity. When dealing with long time wetting-drying cycles, the difficulty is to maintain a constant time step in order to reach a high image definition.

The experimental procedure consists in applying regular time steps (varying from 30 minutes to one hour according to the type of clay), in order to let sufficient time for the hydration and dehydration processes to reach stationary state. The rate of wetting is also smoother than the *in situ* condition and closer to it. With such a process, a good accuracy in hydration of clay particles and in swelling measurements at high relative humidities can be reached.

With this experimental procedure, we measure the surface strain evolution according to the relative humidity and it appears to be interesting to get the water content of the sample simultaneously.

3.2 Clay Powder

The Greek montmorillonite and Romainville clay are analysed in powder form and subjected to one wetting/drying cycle. To get ESEM observations, the powder is put on a double sided carbon tape, to avoid particle displacement during wetting. The temperature is kept constant equal to 18°C inside the seclusion finger and the pressure is controlled in order to obtain the imposed hygrometry. The initial hygrometry in the ESEM chamber depends on the environmental conditions in laboratory.

The clay powder is wetted up to 100 % with steady steps of different duration according to the type of clay (from 30 minutes to one hour). The times to reach steady states are determined for a regular relative humidity rise and fall. At high relative humidities, where the maximum of deformation is reached, the steps are closer. The volume or surface changes are real time followed. The surface deformation induced by swelling and shrinkage is calculated by analyzing ESEM images on particles of 50 µm size in average.

The term “surface strain” is used to define the relative surface change of the particles at time t_i:

$$\varepsilon_s = \frac{S_i - S_0}{S_0} = \frac{\Delta S}{S_0} \tag{1}$$

where S_i = surface strain at time t_i; S_0 = initial surface of the grain.

Under isotropic assumption, the volumetric strain ε_v is equal to:

$$\varepsilon_v = \alpha \varepsilon_s \tag{2}$$

Where $\alpha \in \Re$.

3.3 Experimental Device

In order to measure the water content of the sample simultaneously, a new experimental device was developed within the ESEM, which were patented (patent n° 10-54771). The principle is to weight the sample and obtain an accurate water content intensity and evolution according to the relative humidity. For this purpose, the experimental device consists of a strength sensor coupled to a lever arm for the amplification of the weight evolution. The lever arm is such long for a sufficient amplification and is made with aluminium in order to improve the electric conductivity. Its extremity contains a cup with a hollow where the microsample of soil (in powder form) of very small volume (some cubic millimetres) is putting down and a tray for the observation area. In order to concentrate the relative humidity on the sample, the extremity of the lever arm is surrounded with a copper seclusion finger which is linked with the Peltier stage of the ESEM. In order to maintain the entire device in the ESEM chamber with the experimental conditions (pressure and temperature), a cover is setting up. A data acquisition board allows following simultaneously some parameters in the ESEM chamber as the temperature inside the seclusion finger (PT100 sensor), the pressure inside the ESEM chamber (pressure gauge) and the weight evolution of the sample (strength sensor).

4 Experimental Analysis

These experiments allow determining two types of results. The measurements on the observation area allow obtaining the evolution of surface strain according to the relative humidity. For the same size of clay particles (50 µm), the time needed to reach steady states (30 minutes for the Greek montmorillonite, 1 hour for the Romainville clay) and the swelling intensity (60 % for the Greek montmorillonite, 27 % for the Romainville clay) are different. Let us recall that the first one is composed mainly of smectite, and the second one of various components (kaolinite, illite, illite/smectite interlayers, carbonates, quartz, feldspar). Swelling can develop freely in Greek montmorillonite thanks to smectite. Otherwise, swelling can be prevented in Romainville clay due to two parameters: (i) the presence of kaolinite and illite, which are clay species with hard bounds; (ii) carbonates known for constituting cementation (Maison et al. 2009). However, the general look of the curve is similar, showing that the most part of surface strains occurs at high relative humidities (superior to 75 % of relative humidity). It can be underlined that the swelling intensity measured for Romainville clay in ESEM observations is similar to the swelling value measured with classical oedometric free swelling tests (Maison et al. 2010).

The measurements of weight evolution with the experimental device allow obtaining the water content evolution according to the relative humidity. The quality of this curve depends strongly of the quantity of soil, the time of steady steps and the stability of environmental conditions during the experiment.

These two curves can be linked in order to obtain the surface strain evolution according to the water content (Fig. 1). We find again the difference between the

two types of clays with the water content range (until 28 % for Greek montmorillonite; until 12 % for Romainville clay) due to the presence of smectite which allows an evolution of water content more important.

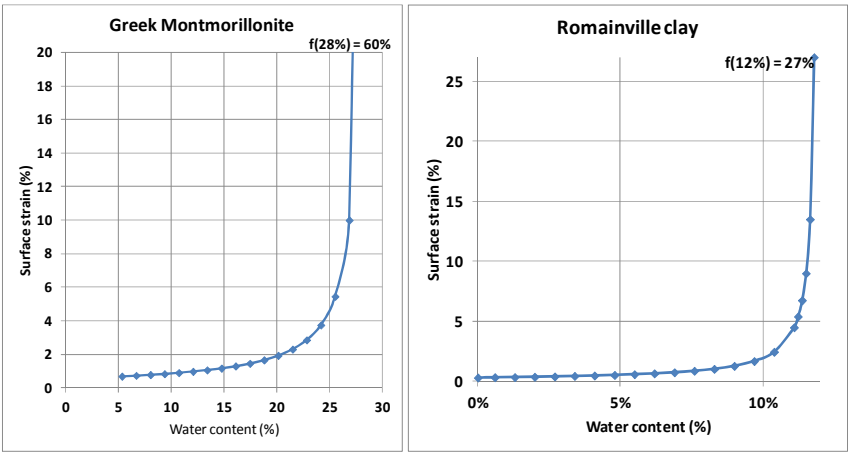

Fig. 1 Curve linking the surface strain evolution to the water content for Greek montmorillonite and Romainville clay.

5 Conclusion and Perspectives

The study of the swelling-shrinkage of clayey soils nowadays mainly constitutes of laboratory tests which require several weeks for obtaining results. We propose a different approach which consists of study clayey soils with an ESEM with small quantities of sample. The time experiment is also dramatically decrease (until 24 hours). The tests consist of measure the surface strain evolution according to the water content thanks to a new experimental device. The results obtained on Romainville clay are coherent with those obtained at mesoscopic scale (laboratory tests).

From these results, we can imagine some applications with simple approaches in order to extrapolate to the macroscopic scale of structures. An analytical approach, based on in situ measurements of water content evolution according to the depth, should allow the fast estimation of differential compaction on a structure. It should be used by laboratory or engineering consulting firm as a fast approach which can stand on data easily accessible. A numerical approach, based on the analogy with the thermomechanical behaviour, should allow leading numerical simulations on several structures submitted on swelling or shrinkage.

References

Audiguier, M., Geremew, Z., Laribi, S., Cojean, R.: Caractérisation au laboratoire de la sensibilité au retrait-gonflement des sols argileux. Rev. franç. Géotec. 120-121, 67–82 (2007)

Christidis, G.E., Scott, P.W., Dunham, A.C.: Acid activation and bleaching capacity of bentonites from the islands of Milos and Chios, Aegean, Greece. Appl. Clay Sci. 12, 329–347 (1997)

Fleureau, J.M., Kheirbek-Saoud, S., Soemitro, R., Taibi, S.: Behavior of clayey soils on drying-wetting paths. Can. Geotech. J. 30, 287–296 (1993)

Kazmierczak, J.B., Maison, T., Delalain, P., Laouafa, F.: Device and method for characterising a material. Patent 10-54771, June 14 (2011)

Maison, T., Laouafa, F., Fleureau, J.M.: Volume changes of swelling clayey soils at microscopic scale level. UNSAT 2010, Barcelona, Spain, September 6-8 (2010)

Maison, T., Laouafa, F., Fleureau, J.M., Delalain, P.: Analyse à l'échelle microscopique des mécanismes de dessiccation et de gonflement des sols argileux. In: Hamza, M., Shahien, M., El-Mossallamy, Y. (eds.) Comptes Rendus du 17e Congrès International de mécanique des sols et d'ingénierie géotechnique, ICSMGE 2009, Octobre 5-9, pp. 660–663. IOS Press BV, Alexandrie (2009)

Romero, E., Simms, P.H.: Microstructure Investigation in Unsaturated Soils: A Review with Special Attention to Contribution of Mercury Intrusion Porosimetry and Environmental Scanning Electron Microscopy. Geotech. Geol. Eng. 26, 705–727 (2008)

Souli, H., Fleureau, J.M., Trabelsi Ayadi, M., Besnard, M.: Physicochemical analysis of permeability changes in the presence of zinc. Geoderma 145, 1–7 (2008)

Localisation Processes and Size Effects for Fissured Clay Specimens

Claudia Vitone[1], Federica Cotecchia[1], and Cino Viggiani[2]

[1] Technical University of Bari, Italy
[2] UJF-Grenoble 1, Grenoble-INP, CNRS UMR 5521, Laboratoire 3SR, Grenoble F-38041, France
c.vitone@poliba.it

Abstract. The paper presents the results of Digital Image Correlation (DIC) method applied to plane strain tests carried out on specimens of fissured clays from the south of Italy. Information about physical properties and Fissuring IDentity of the clays are reported together with an outline of the global behaviourial framework of the fissured clay Represententative Element Volume (REV). DIC has been used to explain some discrepancies found in the global shearing behaviour of some specimens which did not fit the framework. DIC revealed the sources of such discrepancies, which made these specimens much smaller than the REV.

1 Introduction

Soil geological history can generate significant lack in homogeneity and continuity of the soil meso-structure. Discontinuities make represent element volumes of clays behave rather differently from intact natural soils. In particular, fissuring is known to be generally responsible for a huge decay of the clay strength, even by comparison with that of the same soil when reconstituted in the laboratory (Vitone and Cotecchia, 2011). The authors have shown that the interpretation of the fissured clay behaviour can be still developed within the framework of critical state soil mechanics (Schofield & Wroth, 1968) by following the same strategy as that used to interpret the mechanical behaviour of unfissured structured clays (e.g. Burland, 1990; Cotecchia & Chandler, 2000). Research results have allowed for the definition of a behavioural framework of fissured clays applying to materials of different fissuring features. However, behavioural discrepancies with respect to the framework may be recorded when testing clay specimens of low to medium fissuring intensity which are likely to be smaller that the clay REV. This paper aims at focusing on the causes of these discrepancies by analysing the results of the application of the Digital Image Correlation (DIC hereafter) method to plane strain compression test data for fissured clay specimens from the south of Italy.

L. Laloui and A. Ferrari (Eds.): Multiphysical Testing of Soils and Shales, SSGG, pp. 219–225.
springerlink.com

2 Physical Properties, Fissuring Identity and Macro-behaviour

Fissured clays from highly tectonized deposits of marine origin, outcropping either in the inner (Senerchia, SE in the following) or the outer portions (Santa Croce di Magliano, SCM, and San Giuliano di Puglia, SGP) of the Apennines in the South of Italy have been largely investigated. The most intensely fissured clays are both the SCM and SE scaly clays (Figures 1a and 1b respectively). Less fissured are the SCM bentonite clays (Figure 1c) SCM and the SGP Toppo Capuana marly clays (Figure 1d). The clay fraction of the four clays ranges from 47% to 91% and the clays are all highly plastic; activity varies from high, for SCM bentonite, to medium-high for the other clays. Mineralogical analyses showed that all the clays have high content of swelling minerals (see Vitone & Cotecchia, 2011, and Vitone et al., 2009 for further details). The fissuring features of the four clays have been analysed in order to determine their Fissuring IDentity (F-ID). In Figure 1 specific keys distinguish the F-IDs of the four clays within the general characterization chart of fissuring proposed by Vitone & Cotecchia (2011). The orientation and intensity of fissuring (i.e. categories F and I in Figure 1, respectively) are found to have crucial impact on the clay mechanical behaviour. For three of the clays here of reference, fissure orientation is random, F3; only the SCM scaly clay has single fissure orientation, F1. The intensity of fissuring is *very high*, I6, for both SE and SCM scaly clay, where the intense network of fissures defines lens-shaped fragments (i.e the *scales*) of millimetre size. Bentonite clay and SGP clay have lower fissuring intensity (i.e. *high*, I5, to *medium*, I4) Given the approach to fissuring as a feature of the clay structure, the effects of fissuring on the clay mechanics have been interpreted by comparing the fissured clay behaviour with that of the same clay when reconstituted in the laboratory (Burland, 1990; Cotecchia and Chandler, 2000). In particular, this comparison has been reported for the four clays here of reference based upon both triaxial and oedometer test results (e.g. Cotecchia & Vitone, 2011). Here-forth the authors have derived the applicability to fissured clays of the sensitivity framework. Figures 2a and 2b report the sketches of the behavioural trends recognized in compression and shear for I6 to I4 clays, together with the corresponding trends for unfissured clays. For unfissured clays, either sensitive or reconstituted, Cotecchia and Chandler (2000) introduced the parameter stress sensitivity ratio, $S_\sigma = p'_y / p^*_e$, to quantify the influence on the clay bounding surface of the microstructure, meant to be a clay internal state variable. $S_\sigma \geq 1$ for unfissured clays. The framework in Figure 2a shows that fissuring may be considered as part of the structure internal state variable and as such it influences S_σ. For I4 to I6 clays, the compression gross yield states are found to lie to the left of the intrinsic compression line (Burland, 1990), and are characterized by $S_\sigma < 1$. Post-gross yield compression causes strengthening of the fissured clay structure, which is reflected by an increase of S_σ and $\lambda < \lambda^*$ (Figure 2a). Moreover, Vitone & Cotecchia (2011) showed that the whole state boundary surface of the clay (SBS) is even smaller than that of the reconstituted (SBS^*; see Figure 2b).

Fissuring generates effects on the shearing behaviour that are opposite to those induced by sensitive unfissured microstructures, i.e. a reduction in strength with respect to the reconstituted clay and a gradual gain of strength with post-gross yield compression.

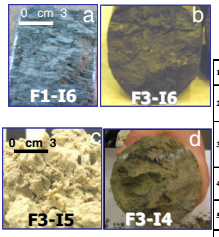

	INTACT SOIL		DISCONTINUITY NATURE			DISCONTINUITY ORIENTATION[1]	DISCONTINUITY GEOMETRY		
	Main sediment A	*Undrained strength*[2] B	*Type* C	*Roughness*[3] D	*State* E	F	*Shape*[4] G	*Continuity*[4] H	*Intensity*[5] I
1	Clay °/*/**	Mudstone	Depositional	Very rough	**Fresh** °/*/**	Single*	**Planar** °/*/**	Continuous	**Rare:** **<3m²/m³->1m³**
2	Silt	**Stiff clay**°/*	**Stress relief** **	Rough	**Slightly weathered** °/*/**	Few	Curved °/*	Many intersections°/*/**	**Very low:** **3÷10 m²/m³ - 0.027÷1 m³**
3	Silty clay °	Firm clay*	**Shear induced** °/*/**	Slightly rough	Highly weathered °/*	**Random** °/**	Hinged °/*	**Some intersections**	**Low:** **10÷30 m²/m³- 0.001÷0.027 m³**
4	**Clayey silt**	Soft clay**		**Smooth** °/*/**	Iron stained surfaces °		Folded °/*/**	**Very few intersections**	**Medium:** **30÷100 m²/m³-27÷1000 cm³**
5	**Marly clay**			Very smooth °/*	**Coated**		**Conchoidal**		High **: 100÷300 m²/m³- 1÷27 cm³
6				Slickensided °/*					Very high°/*: >300m²/m³-<1cm³

Fig. 1 Characterisation chart of fissured clays and F-IDs of the clays. Key: Bold: SGP marly clay; °: SE scaly clay; *: SCM scaly clay; **: bentonite clay.

However, in some cases fissured clays show behavioural trends which do not fit this framework. For example, Vitone et al. (2012) showed that during undrained triaxial shearing of dilative highly overconsolidated specimens (see *path I* in Figure 2c) premature failure may occur due to the onset of sliding, following a path similar to *path II* in Figure 2c, that is characterised by a maximum friction angle about residual. For a given specimen size, the recurrence of this type of behaviour has been found to increase with decreasing fissuring intensity. In the following, the DIC method (e.g. Viggiani & Hall, 2008) is shown to shed light on the sources of the premature sliding and on how these are connected to strain localization processes.

3 DIC Analysis of Local Patterns of Behaviour

The results presented in the following are part of a large testing programme which consisted of plane strain tests carried out at Laboratoire 3SR in Grenoble with zero confining pressure (i.e. σ_3 kept zero throughout the test) on either SCM scaly clay or bentonite clay specimens. Specimens of two sizes were tested, the smaller size being about 40 mm in width, 80 mm high and 35 mm thick and the other one about twice the smaller one. The digital images (pixel size from 27 µm to 40 µm) were analyzed using the DIC software 7D (Vacher et al., 1999) with a grid step and a pattern size equal to 10 pixel (Vitone et al., 2012). Figure 3 shows the results of only two tests, carried out on large specimens; the coloured maps report the magnitude of the shear strains, ε_s (upper row), and of the volumetric strains, ε_v (bottom row; red symbols refer to dilation, the blue ones to contraction).

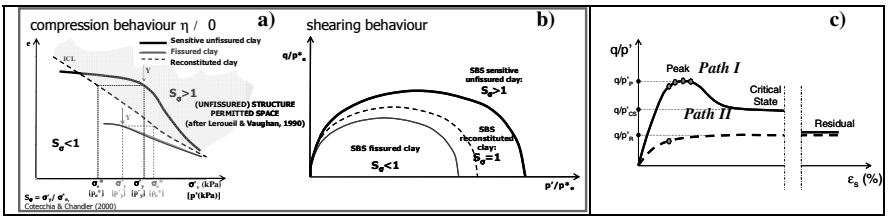

Fig. 2 a-b) Behavioural trends in compression and shear; c) stress ratio – strain paths.

3.1 Large Specimen of SCM Scaly Clay (F1-I6)

Figure 3a shows the results of DIC for the test SCALYA, containing sub-horizontal fissure orientation (i.e. F1/0°). During increment 0-2, a few sub-horizontal regions in the upper portion of the specimen exhibit volumetric contraction and higher shear strains than the rest of the specimen, which corresponds to sealing and relative adjustment and sliding of sub-horizontal fissures. Only later in the test (increment 23-24), shortly before the load peak, several other sub-vertical regions of strain localization occur, which still exhibit a dilative attitude. Several different strain localization regions are active just before peak (increment 26-27), that appear converging to define a large shear band crossing the specimen. It seems that peak is the outcome of a competition between different localization processes, up to the arrangement of a shear band that develops through the connection of solely part of the active strain localization regions. The other regions will become not active post-peak, where instead the shear band will become thinner and come to separate the specimen into two sliding portions. Evidently, apart from the initial test stage, in the rest of the test it has been the pervasive very high intensity fissuring of the clay (I6) to control the overall soil response as for REV condition.

3.2 Large Specimen of SCM Bentonite Clay (F3-I5)

During the first stage of the test BB (increments 5-7 and 11-13 in Figure 3b) on the SCM high intensity fissuring bentonite, DIC revealed the pre-existence of fissures that will be referred to as *second level* fissures, because more extended, H1, and of lower intensity (i.e. probably I3). It follows that DIC is revealing that the F-ID of the clay coming from the visual inspection of the clay mesostructure, should be modified to take into account also this *second level* that superimposes on the most pervasive I5 network (*first level* fissuring). In particular, at increment 11-13 a distinct horizontal large fissure, which crosses almost entirely the lower part of the specimen, is observed to contract. In the following part of the test, in this case there occurs further development of strain localization about the second level fissures, that act as catalysts of strain localization, leaving the other parts of the specimen almost undeformed. Since increment 29-31, i.e. far before peak, a well defined pattern of strain localization regions is already established. This controls the specimen response till the end of the test.

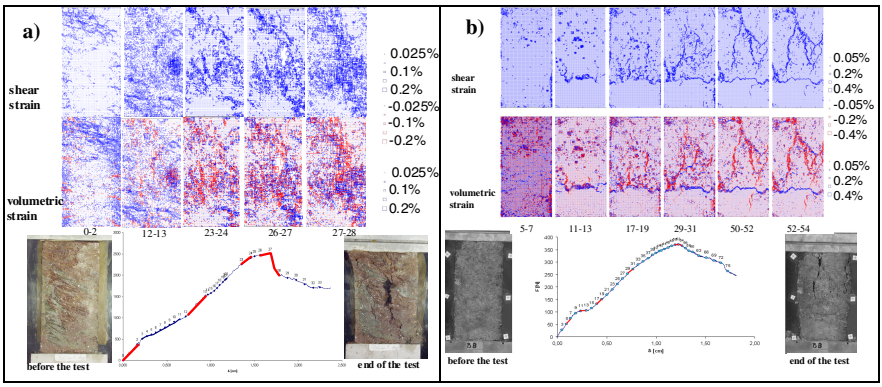

Fig. 3 a) Test SCALYA and b) Test BB. Load-displacement curve and DIC-derived shear and volumetric strain fields for selected load increments (in red along the curves).

4 Discussion of the Results and Research Perspectives

The strain field analyses by means of DIC have provided an insight into the different localisation processes occurring in fissured clay specimens either about (test SCALYA) or significantly smaller than REV (test BB). As commonly observed for REV of both sand and clay specimens (e.g. Desrues & Viggiani, 2004; Rechenmacher, 2006), also for fissured clay REV it is only after one of the strain localisation regions 'wins the competition' and dominates the material response, that significant softening ensues (in terms of global response) and a complete shear band develops. As sketched in Figure 4, *path a*, four stages can be recognised during test SCALYA (REV-type behaviour): stage I, where first and second level fissures are closing, stage II, which is characterised by pervasive contractive volumetric strains across the entire specimen; stage III, either at or slightly before peak, when distinguished localized regions become well defined; stage IV: only few stain localization regions keep being active; stage V, when the narrowing of the strain localization regions brings about the nearly rigid body sliding of portions of the specimen. Conversely, DIC has shown that when the specimen is much smaller than REV, strain localisation is limited solely to few regions since early stages of loading. These regions act as *catalysts* of further strain localization and control the specimen response up to large strains, bringing about a loss of strength, resulting in the erasure of peak strength and a very limited positive hardening (*path b* in Figure 4). Further studies are ongoing to apply DIC to triaxial compression tests on specimens of fissured clays under X-ray tomographic monitoring. Figure 5 shows a first example of the application of this technique to a scaly clay specimen of 20 mm in diameter (a voxel size of 14 µm was achieved). Just scanning the specimen, from the two cross-sectional tomographic slices (figure 5b-c) it is evident that this technique could allow for detecting the extension of fissuring, its width and its evolution (also inside the specimen) troughout a triaxial test.

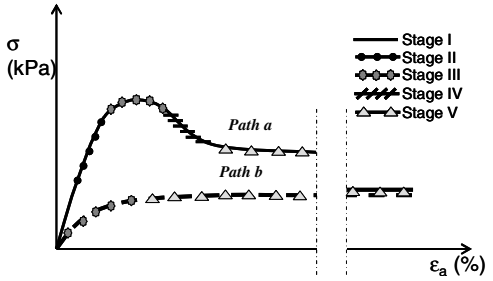

Fig. 4 Sketch of global stress-strain behaviour and stages of local patterns.

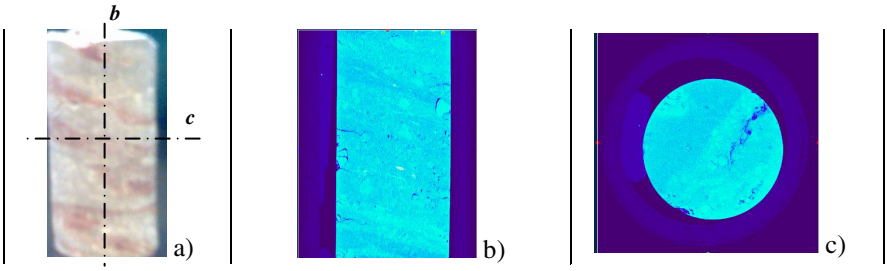

Fig. 5 Photograph a), vertical b) horizontal c) tomographic slices of a triaxial specimen of scaly clay.

References

Burland, J.B.: On the compressibility and the shear strength of natural clays. Géotechnique 40(3), 329–378 (1990)

Cotecchia, F., Chandler, R.J.: A general framework for the mechanical behaviour of clays. Géotechnique 50(4), 431–447 (2000)

Cotecchia, F., Vitone, C.: On the model requirements to predict the behaviour of fissured clays. XV ECSMGE, Athens, Greece, pp. 525–530 (2011)

Desrues, J., Viggiani, G.: Strain localization in sand: an overview of the experimental results obtained in Grenoble using stereophotogrammetry. Int. J. Num. Anal. Meth. Geom. 28, 279–321 (2004)

Rechenmacher, A.L.: Grain-scale processes governing shear band initiation and evolution in sands. Journal of the Mechanics and Physics of Solids 54, 22–45 (2006)

Schofield, A.N., Wroth, C.P.: Critical state soil mechanics. McGraw-Hill, London (1968)

Vacher, P., Dumoulin, S., Morestin, F., Mguil-Touchai, S.: Bidimensional strain measurement using digital images. Proceedings Institution of Mechanical Engrs. 213, Part C, 811–817 (1999)

Viggiani, G., Hall, S.A.: Full-field measurements, a new tool for laboratory experimental-geomechanics. In: Fourth Symp. Deformation Characteristics of Geomaterials, Atlanta, pp. 3–26 (2008)

Vitone, C., Cotecchia, F.: The influence of intense fissuring on the mechanical behaviour of clays. Géotechnique 61(12), 1003–1018 (2011)

Vitone, C., Cotecchia, F., Desrues, J., Viggiani, G.: An approach to the interpretation of the mechanical behaviour of intensely fissured clays. Soils & Foundation Journal 49(3), 355–368 (2009)

Vitone, C., Cotecchia, F., Viggiani, G., Hall, S.H.: Strain fields and mechanical response of a high to medium fissured bentonite clay. Int. J Numer. Anal. Meth. Geomech., paper accepted (2012)

Experimental Study of the Deformation Pattern around a Penetrating Coned Tip

P. Paniagua, A.S. Gylland, and S. Nordal

Norwegian University of Science and Technology (NTNU),
Trondheim, Norway
priscilla.paniagua@ntnu.no

Abstract. Improved knowledge on the deformation pattern around the tip during cone penetration tests is needed. In the present experimental work, the observations and measurements of real soil behavior around a penetrating tip in laboratory tests are presented. Two experimental setups are described: one involving freezing the sample after penetration to preserve deformation patterns and failure features, and one involving computerized tomography. Similar failure patterns were observed in both tests regarding compression directly under the tip and shear structures along the shaft that might be related to a process of accumulation and release of friction during penetration.

1 The Cone Penetration Test in Silty Soils

The cone penetration test (CPT or CPTU) involves pushing a cylindrical probe with a conical tip into the ground at a constant speed, normally 2 cm/s. The resistance during penetration, sleeve friction and pore-water pressure are measured to interpret soil material layering and geotechnical parameters (Lunne et al., 1997).

The CPTU application in intermediate soil (silty soils) faces undrained to partially/fully drained penetration conditions. Standard correlations for clean sands or clay may not be applicable (Poulsen et al., 2011) and new correlations are needed for appropriate interpretation. Improved understanding of the failure mechanism involved during penetration is here important to help in CPTU results interpretation. Previous simplified theories are used for this purpose: bearing capacity; cavity expansion; steady state deformation and incremental finite-element analysis. Unfortunately most theories assume a penetration mechanism that either does not capture the trends observed in the field or imply assumptions that contradict the actual failure mechanism (White & Bolton, 2004). The tests presented in this paper are part of an extensive research in which a procedure to interpret CPTU data for silty soils is being developed. The research focuses in physical penetration and physical pore pressures build up and dissipation during CPTU.

The objective of this paper is to visualize and characterize the deformation patterns that develop around the penetrating conical tip during CPTU in silty soil. Experimental studies, one involving freezing the sample after penetration and one involving computerized tomography, were performed. The first allows for direct

L. Laloui and A. Ferrari (Eds.): Multiphysical Testing of Soils and Shales, SSGG, pp. 227–232.
springerlink.com

high resoultion observation of the mechanisms at hand while the latter allows for 3D imaging following the evolution of the penetration process in time and space. Their results are presented as observations, descriptions and measurements of the real laboratory soil behavior around the penetrating tip.

2 Properties of the Silt Tested

The soil is a non-plastic uniform silt from Vassfjellet, Klæbu, Norway. 94% of the material is lower than 0,074 mm grain size and 2,5% is lower than 0,002 mm. The maximum void ratio (e_{max}) is 1,462; the minimum void ratio (e_{min}) is 0,565 and the optimum water content is about 20%. e_{max} was obtained by allowing a slurry to settle out in a graduated cylinder (method by Bradshaw & Baxter, 2007) and e_{min} by using a modified compaction method for fine grained soils (Sridharan & Sivapullaiah, 2005). Isotropic consolidated drained triaxial tests on rebuilt silt samples show a friction angle φ of 40°, a cohesion value of 6,3 kPa and an $E'_{50}{}^{ref}$-modulus of 14000 kPa.

3 Freezing after Penetration

3.1 Test Procedure

A soil sample (18 cm diameter and 25 cm length) was built into a 25 cm diameter and 35 cm length plexiglass cylinder internally padded by three layers of a compressible material with 940 kPa elasticity modulus (Fig. 1a). The sample preparation followed the under compaction method (Ladd, 1978) and the modified moist tamping (Bradshaw & Baxter, 2007). The sample was saturated from the bottom to limit air bubbles formation. Ten layers of colored silt (0,25 cm thick) were built into the soil sample separated by 1 cm thick layers of uncolored silt. The layers were inserted with the purpose of tracking soil deformation due to penetration. The sample had a dry density (ρ_d) of 1,369 g/cm³; 60,5% relative density (D_r); 1,157 void ratio (e) for full saturation and 47,2% water content. The expected penetration force was around 30kg for the sample without confining pressure and 100kg for the samples with a 40kPa vertical confining pressure.

An aluminum cone of 3,57 cm diameter, 25 cm length and 60° apex angle was penetrated into the sample down to 15 cm using a conventional loading apparatus (Fig. 1a). Two tests were performed without confined pressure (Test 1 and Test 2) and one test with a confining pressure of 40 kPa (Test 3). The test without confined pressure was consolidated 12 hours with a dead load of 1,70 kPa that was removed during penetration. In this paper, only the results of Test 1 and Test 2 are presented.

After penetration, the sample was frozen (Fig. 1b) which allows removing the molding forms and cone (by heating the steel cone), and cutting the sample through its center.

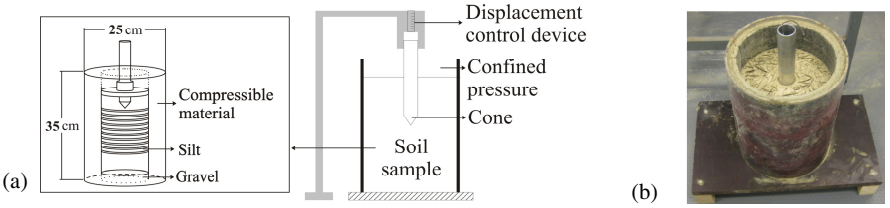

Fig. 1 (a) Model test for freezing after penetration and (b) Picture of frozen sample.

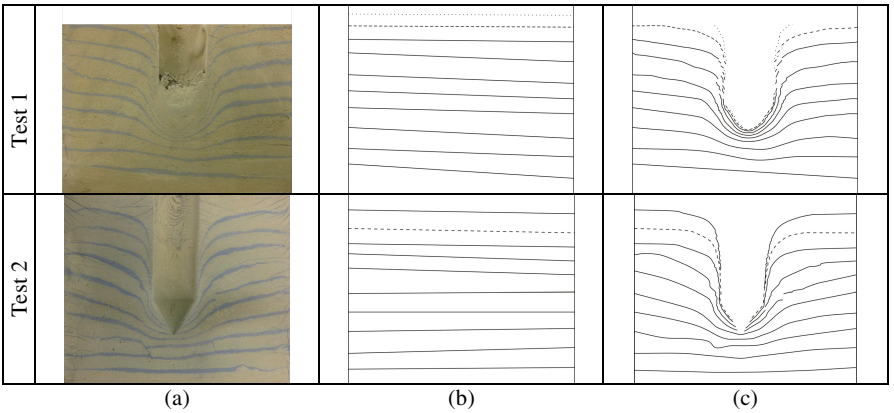

Fig. 2 (a) Deformation pattern after penetration, (b) reconstruction of the layering prior-penetration, (c) reconstruction of the layering post-penetration.

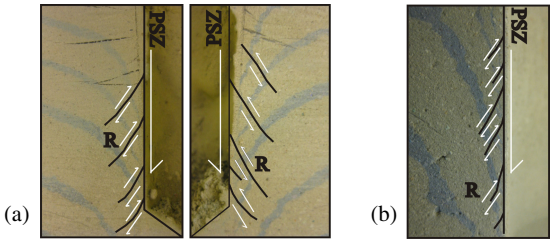

Fig. 3 Reconstruction of the shaft failure features: (a) Test 1 and (b) Test 2.

3.2 Test Results and Discussion

In Fig. 2 is shown the deformation pattern after penetration for Test 1 and Test 2. The failure mechanism follows what has been observed before in sand (for example Robinsky & Morrison, 1964) where the layers are compressed following penetration direction. The influence volume extends to 1,5 cone diameter (D) to the sides from the centerline and 1D to the bottom from the bottom tip. A feature

to our knowledge not reported by others are distinct cracks (shaft failure features = Riedel shears, Fig. 3) along the cone shaft, where the layers are evenly intersected by them. The cracks are believed to be enhanced by the low stress level and we now focus on new tests with higher stress level to see if cracks still develop. Preliminary results indicate that they do but they appear to be less distinct.

The Riedel shears are shear structures which description follows microstructure terminology detailed by e.g. Morgenstern & Tchalenko (1967) and Ahlgren (2001). These geometric structures are part of a kinematic deformation process where displacement discontinuities (observed as the breakdown of the dark grayish layers in Fig. 3) are caused by cone penetration as pure slip. Taking the cone-soil interface as the principal shear zone (PSZ), *en échelon* (arrays) of Riedel shears (R-shears) is observed at each shaft side. The R-shears are oriented around 25° respect to PSZ, which partly coincides with the expected orientation angle of R-shears (45-φ/2). R-shears are part of the early shearing process, there is not visible evidence of further minor shears like R'-shears or P-shears, however, they may be present in a micro-scale of observation which is out of scope here.

4 Computerized Tomography (CT)

4.1 Test Procedure

A plexiglass cylinder (50 cm length) with 25 cm diameter was used to build a dry soil sample (by the under compaction method of Ladd, 1978) wrapped in compressible padding against the plexiglass wall (Fig. 4). Fourteen layers (0,25 cm thick) of silicon powder (Elkem AS) with a grain size between 20-70 µm are located inside the sample for higher contrasts in the images. Each silicon powder layer is intercalated by a 2,25 cm thick silt layer. The sample had ρ_d = 1,240 g/cm³ and D_r = 30%. The expected penetration force is between 30-35 kg.

The CT-apparatus is a Siemens AR-HP fourth generation scanner, from the Department of Petroleum Engineering & Applied Geophysics at NTNU. The sample was scanned after 10 cm, 20 cm and 30 cm penetration. The scanned volume has 5 cm radius (measures from the cone tip centre) and 15 cm length. The scans were obtained for energy of 130 kV, 3 sec of exposure and 300 mAmp.

4.2 Test Results and Discussion

In Fig. 5 is shown the deformation pattern after 10 cm, 20 cm and 30 cm penetration, where the compression of the layers immediately below the tip and the presence of shaft failure features are observed. Supported by an additional study about the density changes between pre- and post-penetration, the strongest influenced volume reaches 1,5D to the sides from the centerline and 1D to the bottom from the tip. For 10 cm and 20 cm penetration, the mechanisms observed are valid only for the low stress level; however, for 30 cm penetration the failure mechanism appears to go deeper with a cone shaped volume failing under the tip.

Following the microstructure description previously mentioned the shear structures are more difficult to observe in this case due to the resolution of the images. However, as observed in the previous case and according to Fig. 3, at PSZ, *en échelon* of R-shears is observed at each side of the shaft (Fig. 5).

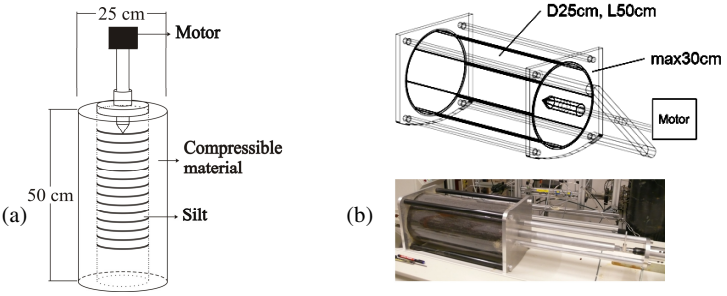

Fig. 4 (a) Sample set-up and (b) Model test apparatus for computerized tomography.

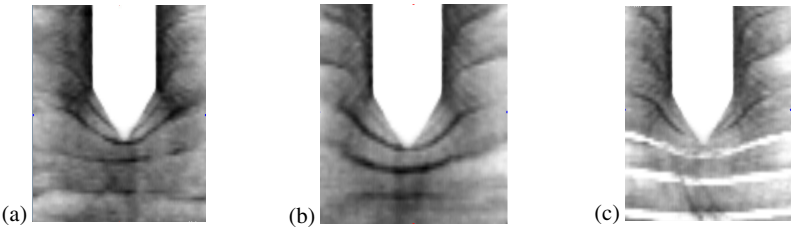

Fig. 5 Deformation pattern after (a) 10 cm, (b) 20 cm and (c) 30 cm penetration.

5 Comparison with Previous Publications

The soil displacement and failure patterns have been studied before by different techniques in plane strain (Muromachi, 1974; White et al., 2004), semi-cylindrical (Roy et al., 1974; Liu, 2010) and axisymmetrical conditions (Robinsky & Morrison, 1964; Yasafuku & Hyde, 1995; Kobayashi & Fukagawa, 2003; van Nes, 2004; Morita et al., 2007). From axisymmetrical studies, only Kobayashi & Fukagawa (2003) and van Nes (2003) studied the penetration in sand of a 60° apex angle cone with smaller diameters than the one used in this study. A general compression failure mode for shallow penetration was observed in contrast to a more radial failure pattern for deep penetration. This compares reasonably well with the results obtained in this study where a spherical cavity expansion around the tip roughly describes the failure pattern. In the vertical direction, some contraction below the tip and expansion near the shoulder may be seen; and radial, there may be contraction around the shoulder and expansion below the tip, as pointed out by Kobayashi & Fukagawa (2003). However, there is no previous evidence of the shear structures (R-shears) like the ones observed in this study.

6 Conclusions

Two different experimental studies regarding a conical tip penetration in silty soil were carried out to observe and describe deformation patterns developed. The initial results show vertical compression below the tip and volumetric expansion behind the shoulder. Distinct shear structures appear along the shaft that could originate from a process of friction accumulation-release that might cause the erratic data signal when CPTU is done on silts on the field, therefore, further research is currently carried out in this direction.

References

Ahlgren, S.G.: The nucleation and evolution of Riedel shear zones as deformation bands in porous sandstone. J. Struct. Geol. 23, 1203–1214 (2001), doi:10.1016/S0191-8141(00)00183-8

Bradshaw, A.S., Baxter, C.D.P.: Sample preparation of silts for liquefaction testing. Geotech. Test J. 30, 324–332 (2007), doi:10.1520/GTJ100206

Kobayashi, T., Fukagawa, R.: Charact of deform process of CPT using X-ray TV imaging tech. In: Di Benedetto, H., et al. (eds.) Deform Charact of Geomater. Taylor & Francis, Lyon (2003)

Ladd, R.S.: Preparing test specimens using undercompaction. Geotech. Test J. 1, 16–23 (1978), doi:10.1520/GTJ10364J

Liu, W.: Axisym centrif model of deep penetr in sand. Dissertation, Univ of Nottingham (2011)

Lunne, T., Robertson, P., Powell, J.: CPT in geotechnical practice. Blackie Academic, NY (1997)

Morgenstern, N.R., Tchalenko, J.S.: Microscopic structures in kaolin subjected to direct shear. Géotechnique 17, 309–328 (1967), doi:10.1680/geot.1967.17.4.309

Morita, K., Otani, J., et al.: Eval. of vert and lateral bearing capacity mech of pile found using X-ray CT. In: Kikuchi, Y. (ed.) Advances in Deep Foundations, Taylor & Francis, London (2007)

Muromachi, T.: Experimental study on application of static cone penetrometer to subsurface investigation of weak cohesive soils. ESOPT 2, 192–285 (1974)

Poulsen, R., et al.: Effect of drainage conditions on CPT in silty soils. PCSMGE, Toronto (2011)

Robinsky, E.I., Morrison, C.F.: Sand displacement and compaction around model friction piles. Can Geotech. J. 1, 81–93 (1964), doi:10.1139/t64-002

Roy, M., Michaud, D., Tavenas, F., Leroueil, S., Rochelle, P.L.: The interpretation of static cone penetration test in sensitive clay. ESOPT 2, 323–330 (1974)

Sridharan, A., Sivapullaiah, P.V.: Mini compaction test apparatus for fine grained soils. J. Test Eval. 28, 240–246 (2005), doi:10.1520/GTJ12542

van Nes, J.: Application of computerized tomography to investigate strain fields caused by cone penetr in sand. Dissertation, Delft University (2004)

White, D.J., Bolton, M.D.: Displacement and strain paths during plane-strain model pile installation in sand. Géotechnique 54, 375–397 (2004), doi:10.1680/geot.2004.54.6.375

Yasafuku, N., Hyde, A.F.L.: Pile end-bearing capacity in crushable sands. Géotechnique 45, 663–676 (1995), doi:10.1680/geot.1995.45.4.663

Micro-scale Testing of Capillary Bridge Evolution due to Evaporation

Boleslaw Mielniczuk[1,2], Tomasz Hueckel[3], and Moulay Said El Youssoufi[1,2]

[1] Laboratoire de Mécanique et Génie Civil UMR UM2-CNRS 5508,
Université Montpellier 2, 34095, Montpellier Cedex 5, France
boleslaw.mielniczuk@univ-montp2.fr
[2] Laboratoire de Micromécanique et d'Intégrité des Structures,
MIST Laboratory, IRSN, CNRS UMR 5508, Université Montpellier 2
hueckel@duke.edu
[3] Duke University, Durham, NC 27708, USA

Abstract. Capillary bridge evolution between two fixed glass spheres during its natural convective evaporation is examined experimentally. For comparison extension tests were also carried out. The calibrated balance recording and digital image processing allow monitoring of a number of key variables of the process: the resultant capillary force, the water mass loss, radii of the bridge curvature. On that basis evaporating surface area, suction and surface tension force, interparticle force, axial stress vs (relative) volumetric mass loss are calculated. Testing shows a gradual decrease of suction within bridges down to zero and into a positive pressure range before a two step failure including a formation of a water thread according to a traditional Rayleigh instability pattern followed by a simultaneous rupture at two points of the lowest (negative) total (Gauss) curvatures of the bridge surface.

1 Introduction

The liquid loss from a porous (granular) material *(i.e.* soil) during evaporation plays a key role in the onset of drying cracks. Studies of desiccation shrinkage undertaken *i.e.* by Hu et al. [1], Kowalski and Mielniczuk [2], Peron at al. [3] revealed that the shrinkage in drying soil develops when soil is still saturated, while cracks appear shortly after the air entry, and formation and rupture of liquid bridges. On the other hand, the apparent cohesion of unsaturated soils is attributed to the generation of suction and capillary forces. Suction hardening and softening (wetting collapse) of granular materials are related to understanding of the evolution and rupture of liquid bridges.

To identify the mechanisms and critical variables that control evolution of the water body (liquid bonds) during evaporation we focus on the evolution and rupture of elementary liquid bridges between two, three and more particles. The important step of these studies is the analysis of the changes of the liquid bridge

L. Laloui and A. Ferrari (Eds.): Multiphysical Testing of Soils and Shales, SSGG, pp. 233–238.
springerlink.com

geometry and interparticle (capillary) forces during desiccation of the smallest clusters of grains at the local scale. In this paper, capillary bridges are addressed between two grains only. Such systems are not only the most elementary ones, but also, it has been seen that more articulated systems break down eventually to a number of two-grain arrangements.

Most of the past studies were conducted in static conditions or during extension of the bridge with a fixed liquid volume [4-8]. Instead, in the present experiments, the driving force of the investigated reponse is evaporation in a constant relative humidity environment, and at a constant predetermined separation of grains.

2 Materials and Methods

Liquid bridge is produced by placing a 4 µl of distilled water between two glass spheres (radius R=4mm, grade 25), with the use of microsyringe. Next, the liquid bridges are exposed to evaporation at constant ambient conditions, at constant sphere separations D from 0.1 to 2.0 mm, or are stretched at a constant speed of 16 µm/s, at several constant water volumes, from 0.2 to 10 µl. The lower sphere is placed on a precision balance (with precision of 10^{-4} g). The upper sphere, attached to the micrometer, is suspended from the support, without any contact with the balance (Fig. 1a).

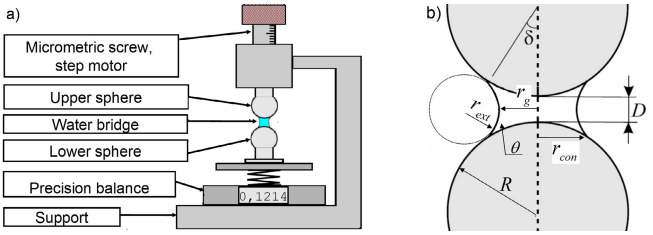

Fig. 1 a) Apparatus configuration to measure capillary force, b) Capillary bridge parameters

The attractive force between spheres is calculated as $F_C=(m_{dry}-m_{exp})\cdot g$, where m_{dry} is the mass of dry lower sphere, m_{exp} is a mass supported by the balance including the lower sphere and the liquid bridge during drying, g is the gravity. The evaporating mass of water is obtained in the same conditions, but also with the upper sphere supported by the balance. The changes in the bridge geometry were recorded by a photo camera with macro lens. The moment of the bridge rupture was recorded with a high-speed digital camera, with 27000 frames per second. Images were processed with Fiji and Mathlab software, to determine gorge radius r_g and external radius r_{ext} (see Fig. 1b). It was hence possible to calculate via Laplace law suction and surface tension force components of the capillary force, and the average axial stress at the bridge neck.

3 Results

Variations of bridge volume (evaporation) or bridge length (extension) are the main factors affecting the radii of the meniscus surface. During evaporation the profile of drying bridge evolves with the receding lateral meniscus surface of revolution, following the classical sequence of Plateau, from the surface of the negative unduloid, through catenoid to negative nodoid (Fig. 2) [9]. Measured value of r_g decreases smoothly as a convex parabola, and external radius r_{ext} decreases proportionally with the decreasing liquid volume. The r_g for the bridge in extension decreases as a concave parabola with the increasing separation, with almost constant r_{ext} (see [10] for details). The duration of the process till the bridge rupture varies from 9 to 67 min for evaporation and up to 150 seconds for extension.

Most notable is a relatively slow change of the bridge shape from a catenoid into a nodoid, which then developing into a very thin water wire. The wire ruptures simultaneously near both ends within 0.3-0.9 msec and then transitions into a small droplet of water, which next free-falls in the gravity field. Eventually the mass of water is separated into two drops attached to each of the spheres (Fig. 2).

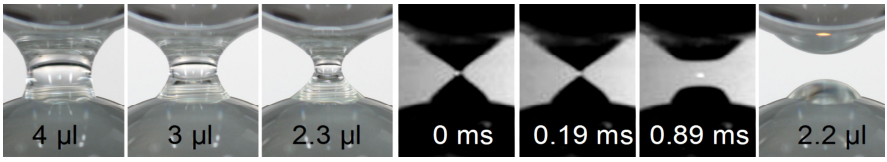

Fig. 2 Evolution of evaporating capillary bridge between two spheres at separation of 1.3mm with the initial total water volume 4 µl, at decreasing water volume (in µl), detail of the rupture process (fast camera, time in milliseconds)

The bridge evolution due to evaporation at D= 1.3 mm is shown in Fig. 2. The bridge ruptures at the water volume V= 2.28 µl., with the water wire 90 µm in diameter, and 130 µm in length (see [11] for details).

Based on the measured evolution of the meniscus radii it is possible to estimate capillary forces, as a sum of a vertical resultant of the surface tension acting at the perimeter of the neck and the Laplace pressure Δp (difference between ambient and internal bridge pressure) expressed as $\Delta p = \gamma(r_g^{-1} - r_{ext}^{-1})$ acting at the cross-section of the neck, $F_C = 2\pi r_g \gamma - \pi r_g^2 \Delta p$ [4, 6, 8], where γ= 0.0496 N/m is the experimentally determined surface tension of the actual water. At our calculations hydrostatic pressure of water bridge acting at the neck level is also considered.

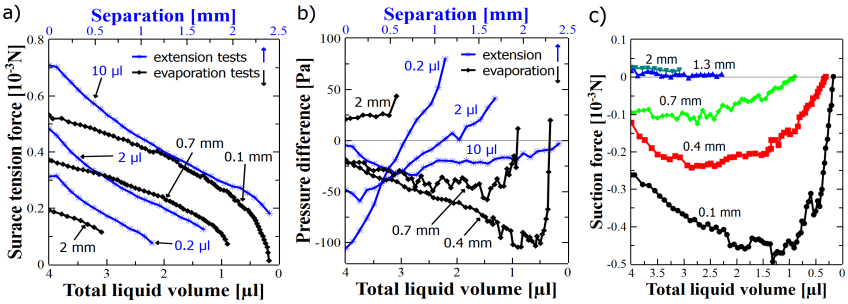

Fig. 3 a) Surface tension force for evaporation and extension tests, b) Laplace pressure changes for both experiments, c) Resultant suction force for evaporation

The surface tension force is positive and decays gradually following the neck perimeter length with volume loss or increasing separation. Its initial value is the highest at small separations and large volumes, as shown on Fig. 3a.

Laplace pressure arises as a consequence of the total bridge curvature, which can be either positive or negative, depending on gorge (neck) and external radii (Fig. 2). It is initially negative (suction) at small separations, but it may be positive at large separations (Fig. 3b). Such cases are described by Kralchevski and Nagayama [12]. Most notable is the evolution of suction during both evaporation and extension showing a consistent decrease until zero, and becoming eventually a positive pressure. Hence, pressure at bridge rupture is positive in all cases (except for the largest volume extension. The resultant suction force however remains attractive (due to surface area factor), for small separations, while reaching negligible positive values (repulsion) near rupture (see Fig. 3c). At large distances the resultant force is consistently repulsive.

The total capillary force (Fig. 4a) decreases consistently in both processes. For evaporation at large separations the force decreases almost linearly with an early sudden jump to zero at the bridge rupture. At separations D smaller than 0.7 mm there is an initial increase of F_C up to a maximum, followed by a decay to zero. At separation D=2 mm the maximum (initial) force value $F_C = 0.14 \cdot 10^{-3}$N (0.14 mN), with force jump of 0.09 mN at 23% of water loss. At D=0.1 mm the maximum force F_C= 0.85 mN at 33% of water loss, and at rupture the force jump is 0.02 mN, at 96% of water loss.

Also during extension the total capillary force F_C decreases to zero, with a slight initial increase at higher volumes.

Based on on the capillary force it was possible to visualize stress evolution for both tests, as presented in Fig. 4b. The values of tensile stress in water in both processes are of the same order of magnitude, with rupture occurring between 200 and 600 Pa, depending on separation D and total liquid volume V.

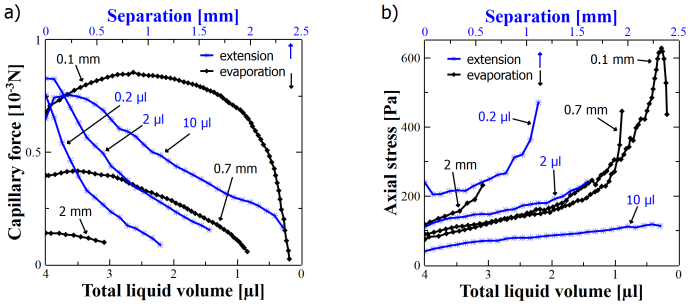

Fig. 4 a) Capillary force evolution during evaporation and extension tests, b) Axial stress vs decreasing volume for evaporation, vs increasing separation for extension tests

The tensile stress at rupture at D= 1.3 mm (V= 2.28 µl) caused by evaporation is 220 Pa. For an ad hoc extension test performed at this particular liquid volume, the bridge ruptures at D= 1.76 mm, with tensile stress of 243 Pa. Notably, the axial stress at rupture is different for every test.

4 Conclusions

The behavior of an evaporating liquid bridge resembles tensile failure of a ductile steel rod, while no external tensile force is applied to the system. The process is controlled by a decreasing volume of the liquid bridge (at constant separation). The moment of rupture is dependent on separation of spheres. For larger separations the bridge rupture alters a smooth desiccation process early, whereas for very small separations, the rupture blends with the vanishing of all the liquid mass.

Notable findings concern the evolution of liquid suction, which monotonically decreases during evaporation (and extension) to zero, and becomes a positive pressure prior to rupture. The total capillary force between the grains remains attractive due to the surface tension effect. However, it also has a decreasing trenda and approaches very small values near rupture.

The intergranular bridge rupture is a two-stage process. The first stage includes a formation of a water thread in the central part of the bridge according to a traditional Plateau-Rayleigh instability pattern, followed by a rupture at simultaneously two points of the lowest (negative) total (Gauss) curvatures of the bridge surface. The later subject is pursued in Mielniczuk et al. [13]. The rupture of the bridge is critically important as it marks the end of suction controlled strengthening of unsaturated granular media. As seen it may occur very early in the process of evaporation in a loose medium with large grain separation. It also determines how much of water is left out after the process of bridge formation and rupture. Notably, the stage where two-grain bridges dry in isolation is the last stage of earlier processes when suction growth plays a crucial role in the removal of water from the porous medium (Hu et al., [1]).

Acknowledgements. The authors acknowledge the partial support of US NSF grant #0700294 of CMMI Division, Geomechanics and Geomaterials and Program (T. Hueckel) and support of CNRS and MIST laboratory (B. Mielniczuk, M.S. El Youssoufi).

References

Hu, L.B., Peron, H., Hueckel, T., Laloui, L.: Desiccation shrinkage of non-clayey soils: multi-physics mechanisms and a microstructural model. Int. J. Numer. Anal. Meth. Geomech. (submitted, 2012)

Kowalski, S.J., Mielniczuk, B.: Analysis of effectiveness and stress development during convective and microwave drying. Drying Tech. 26, 64–77 (2008)

Peron, H., Delenne, J.Y., Laloui, L., El Youssoufi, M.S.: Discrete element modelling of drying shrinkage and cracking of soils. Computers and Geotechnics 36, 61–69 (2009)

Willett, C.D., Adams, M.J., Johnson, S.A., Seville, J.P.K.: Capillary bridges between two spherical bodies. Langmuir 16, 9396–9405 (2000)

Rabinovich, Y.I., Esayanur, M.S., Moudgil, B.M.: Capillary forces between two spheres with a fixed volume liquid bridge: theory and experiment. Langmuir 21, 10992–10997 (2005)

Butt, H.-J., Kappl, M.: Normal capillary forces. Adv. Colloid Interface Sci. 146, 48–60 (2009)

Urso, M.E.D., Lawrence, C.J., Adams, M.J.: Pendular, funicular and capillary bridges: results for two dimensions. J. Colloid Interface Sci. 220, 42–56 (1999)

Soulié, F., Cherblanc, F., El Youssoufi, M.S., Saix, C.: Influence of liquid bridges on the mechanical behaviour of polydisperse granular materials. Int. J. Numer. Anal. Meth. Geomech. 30, 213–228 (2006)

Plateau, J.: The figures of equilibrium of a liquid mass, The Annual Report of the Smithsonian Institution, Washington, DC, pp. 338–369 (1864)

Mielniczuk, B., Hueckel, T., El Youssoufi, M.S.: Evolution of a capillary bridges between two spheres. Part 2. Analysis and Implications (submitted)

Mielniczuk, B., Hueckel, T., El Youssoufi, M.S.: Rupture of a Capillary bridges between two spheres. Experiments, Analysis and Implications (submitted)

Kralchevsky, P.A., Nagayama, K.: Chapter 11 in: Particles at fluid interfaces and membranes, pp. 469–502. Elsevier, Amsterdam (2001)

Mielniczuk, B., Hueckel, T., El Youssoufi, M.S.: Evolution of a Capillary bridges between two spheres. Part 1. Experiments (submitted)

Anisotropy of Mica Probed by Nanoindentation

Rohit Pant[1], Liming Hu[2], and Guoping Zhang[1]

[1] Department of Civil & Environmental Engineering,
Louisiana State University, Baton Rouge, LA 70803, USA
gzhang@lsu.edu
[2] State Key Laboratory of Hydro-Science & Engineering,
Department of Hydraulic Engineering,
Tsinghua University,
Beijing, 100084, China

Abstract. Clay minerals, abundant in soils and shales, are characterized by their distinct, nanoscale layered crystal structure that is known to result in anisotropic responses to loading. Owing to their tiny sizes, it is a significant challenge to determine their anisotropic properties. This paper presents a pioneering nanoindentation study to probe the anisotropy of a muscovite that was subjected to loading at directions both normal and parallel to the basal plane. The hardness, *H*, and indentation modulus, *M*, vary with loading directions. The load-displacement curves indicate remarkable difference during indentation loading and unloading, and the basal plane exhibits a stronger penetration resistance (i.e., *H*) than the edge, while the *M* in the direction perpendicular to the basal plane is smaller than that in the direction parallel to the basal plane. The anisotropic behavior is also interpreted along the mineral's unique layered structure as well as the nanoscale deformation mechanisms.

1 Introduction

Clays and other phyllosilicate minerals consist of fundamental 1:1 layers of 0.7 nm in thickness or 2:1 layers of 1.0 nm thickness with sub-nanometer interlayer spacing usually occupied by hydrated or nonhydrated cations. For these minerals, usually, the interactions between interlayer cations and the fundamental 1:1 or 2:1 layers are much weaker than the atomic bonds between atoms within the layers, and hence play a key role in controlling the elastic and plastic properties (Zhang et al. 2010). Several factors such as the layer charge, *z*, structural and compositional variations, and interlayer spacing are found to influence their elastic modulus. Because of the distinct layered structure, phyllosilicates are expected to exhibit elastic and plastic anisotropy. However, the tiny size of individual clay crystals imposes a significant challenge to the experimental determination of elastic and plastic properties. Past research on mechanical properties of phyllosilicates used techniques such as Brillouin spectroscopy, X-ray or neutron diffraction, ultrasonic measurements, and more recently molecular dynamics simulation.

L. Laloui and A. Ferrari (Eds.): Multiphysical Testing of Soils and Shales, SSGG, pp. 239–245.
springerlink.com

A nanomechanical testing method, nanoindentation, has been utilized to assess elastic and plastic properties of metals, ceramics, thin films and biological specimens. Following the theoretical framework of Vlassak (1993), Vlassak et al. (2003), Swadener and Pharr (2001), Delafargue and Ulm (2004) and others, nanoindentation technique has been further extended to study anisotropy of metals, bones and clay minerals. Similarly, elastic modulus of well-ordered mica and rectorite specimens showed good agreement between experimental and theoretical values for indentation modulus normal to basal plane (Zhang et al. 2009). This paper extends the previous work by performing indentation on mica along loading directions both normal and parallel to the basal plane, thereby examining the anisotropy in these two directions.

2 Experimentation

V1-grade muscovite specimens of 15 x 15 x 0.15-0.3 mm (length x width x thickness) were obtained from Axim Mica, New York, USA. They are clear to translucent with slight brownish hue and show negligible particle or air inclusions. For indentation normal to basal plane, samples were prepared using the procedure described in Zhang et al. (2009). Samples for indentation parallel to basal plane were prepared by mechanically polishing vertical edge of the mica specimen encapsulated in castable resin mix (EpoKwick, Buehler, USA). Indentations were performed by selecting flat surfaces; devoid of any mechanical distress or delamination that may have occurred during polishing. Strict quality control routine were observed which include area function calibration, tip cleaning and indentation on fused silica in between test, as described in the reference. Nanoindentation tests were performed using MTS XP indenter (MTS Nano instruments Inc., Oak Ridge, Tennessee) at ambient condition. An XP indenter equipped with Berkovich tip with a tip radius <20 nm was used to indent under the continuous stiffness measurement (CSM) mode at a constant indentation strain rate ($\dot{h}/h$) of 0.05 s^{-1} where h is indentation depth. CSM mode involved the superimposing of a displacement controlled harmonic loading with frequency of 45 Hz and amplitude of 1 nm.

The harmonic contact stiffness, S, is derived continuously during loading by imposing oscillating displacement and measuring amplitude and phase of the corresponding force (Oliver and Pharr 2004). Indentation modulus, M, (also referred as reduced elastic modulus, E_r) and hardness, H, are obtained as

$$M = \frac{\sqrt{\pi}}{2\beta\sqrt{A_c}} S \qquad H = \frac{F_{max}}{A_c}$$

where β is a dimensionless factor for the indenter tip shape correction and β=1.05 is commonly used for Berkovich indenter (Oliver and Pharr 2004), F_{max} is maximum indentation load at unloading, and A_c is the projected contact area between indenter and sample, which can be obtained solely using indentation parameters (Sneddon 1965; Oliver and Pharr 2004).

3 Analysis of Results

Figure 1 shows the load-displacement curves for both indentation directions. It is evident that the resistance to penetration is remarkably different in the two directions. First, higher resistance to penetration is observed for the loading direction normal to the basal plane than that parallel to it. Second, randomly occurring displacement bursts or pop-ins are more pronounced in the indentations normal to the basal plane. One or more micrometer-sized pop-ins occurred randomly, which are followed by several nanometer-sized pop-ins in between. In contrast, load displacement curves on edge are populated with small displacement bursts ranging a few nanometers. Suppression of large pop-ins on edge surface may insinuate surface deformation at first glance; however, comparable threshold load and pop-in size at small displacements (Fig. 1 inset) imply that insignificant residual stress or deformation is present within the specimen (Wang et al. 2011). It is noteworthy that the cleaving technique used in sample preparation is expected to impart very little surface deformation or additional dislocations (Christoffersen and Kronenberg 1993). Therefore, the load-displacement curves show characteristic indentation features in two mutually perpendicular directions.

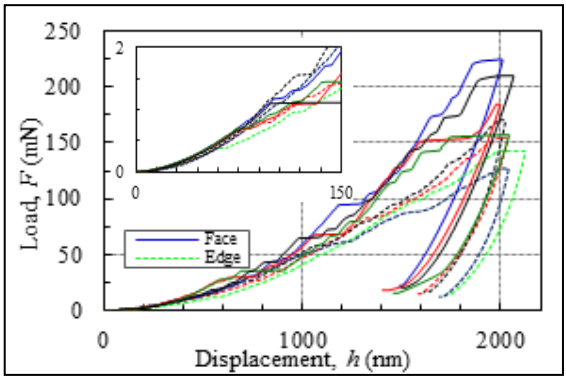

Fig. 1 Indentation load-displacement curves.

Figure 2 show the typical residual imprints for two indentation directions. Indentation imprint on face surface is more symmetrical, while the imprint on edge surface is distinctly elongated. Relics of abrupt cracking, layer delaminations, spallation, and significant surface damage under the indenter are clearly visible, which are also reflected as discontinuities in the load-displacement curves. Also, kink boundaries and material pile-up around the imprint can be noticed. Comparatively, indentation imprint on the edge shows little pile-up, but visible cracks in the direction along the basal place. It may also be possible that some of these cracks may have closed after the load removal. Nevertheless, unlike on the basal plane, indentation impression boundaries on edge are sharply defined.

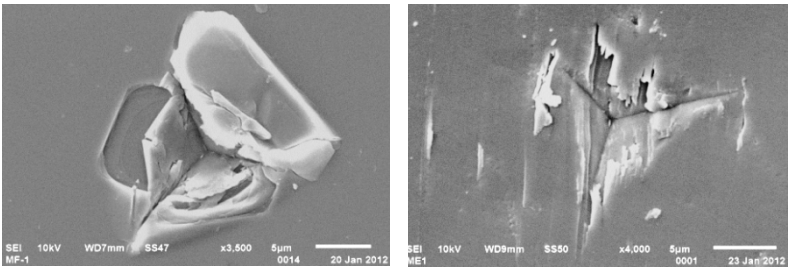

(a) (b)

Fig. 2 SEM images showing the residual indents: (a) face and (b) edge.

Figure 3 shows the indentation moduli and hardness averaged from multiple tests with the error bars representing one standard deviation. In plane indentation moduli (M_E) is higher than out of plane indentation modulus (M_F) while hardness is other way around. Moreover, hardness measured along both directions shows an apparent indentation size effect (ISE); hardness increases with decrease in depth. Hardness curve normal to basal plane exhibits some interesting features. First, hardness decreases rapidly with indentation, after the initial peak, up to the depth of 150-160 nm. However, in between 150- 500 nm average hardness remains constant or rises subtly. Beyond 500 nm to micro range, hardness again decreases with depth. In contrast, hardness measured parallel to basal plane decreases uniformly. It is noteworthy to mention that discontinuity in hardness curve measured normal to basal plane is not an artifact due to area function; indentation were carried simultaneously in all samples with same indenter. Area function was calibrated in the beginning by indenting on standard fused silica and between each set of indentation on mica samples, tip cleaning and indentation on standard fused silica was done to ensure validity of results.

For the sake of simplicity, mica is modeled as transversely isotropic such that axis of symmetry is normal to basal plane. For transversely isotropic solid, indentation modulus in the direction of axis of symmetry (normal to basal plane) is related to elastic constants, C_{ijkl},, (Elliott 1949; Hanson 1992),

$$M_F = 2\sqrt{\frac{C^2_{31} - C^2_{13}}{C_{11}}\left(\frac{1}{C_{44}} + \frac{2}{C_{31} + C_{13}}\right)^{-1}}$$

where C_{mn} are the fourth order elastic stiffness tensors (C_{ijkl}) expressed in reduced notations; $C_{1111}=C_{11}$, $C_{3333}=C_{33}$, $C_{2323}=C_{44}$, $C_{1133}=C_{13}$, $C_{31}=\sqrt{C_{11}C_{33}}$, and $C_{12}=C_{1111}-2C_{1212}$. Similarly, indentation modulus normal to axis of symmetry (parallel to basal plane) can be approximately expressed in terms of elastic constant using an explicit solution (Delafargue and Ulm, 2004),

$$M_E = \sqrt{\frac{C^2_{11} - C^2_{12}}{C_{11}}}\sqrt{\frac{C_{11}}{C_{33}}}M_F$$

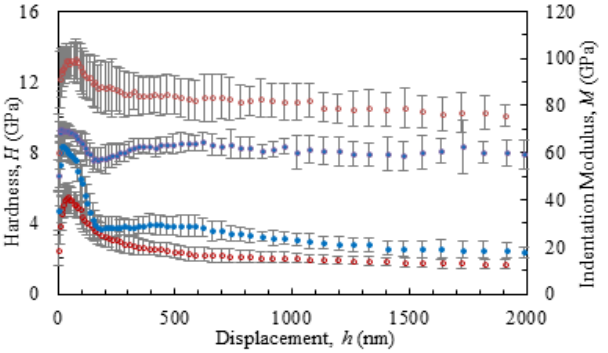

Fig. 3 Relationships between indentation modulus and hardness with depth.

Table 1 summarizes the elastic constants of muscovite cited in the literature and the calculated indentation modulus using above equations. Average experimental indentation moduli at peak value are M_F = 68.5GPa and M_E = 99.0 GPa which gives anisotropy factor M_E/M_F = 1.45. Similarly, average indentation modulus at unloading M_F = 53.5 GPa and M_E = 72.1 GPa gives anisotropy M_E/M_F = 1.35.

Table 1 Calculated indentation moduli and anisotropy.

Elastic Constants (GPa)	(Vaughan and Guggenheim 1986)	(McNeil and Grimsditch 1993)	(Aleksandrov and Ryzhova 1961)
C_{11}	181	176.5	178
C_{33}	58.6	60.9	55
C_{44}	16.5	15	12
C_{13}	25.6	20	15
C_{31}	103	103.7	98.9
C_{12}	48	48	42
M_F	53.7	53.2	46.2
M_E	126.1	121.7	118.14
Anisotropy M_E/M_F	2.35	2.29	2.56

4 Discussion and Conclusions

M_F is 33% higher than the calculated modulus whereas the M_E is about 18% lower than the calculated value (Table 1), resulting in lower anisotropy. However, lower elastic anisotropy was reported in others work (Bobko and Ulm 2008; Ulm and Abousleiman 2006). Cracks, lattice disorientation and phase transformation within the effective volume may influence the measure of mechanical property that is sensed by nanoindentation. Some variation in the result may also be inherent to simplistic transversely isotropic model for triclinic mica structure. Alternatively, indirect methods such as ultrasonic techniques or Brillouin scattering may have some overestimation on their parts.

This study also observed plastic anisotropy as reflected in different hardness value measured for two orthogonal directions. Plastic behavior of well crystallized material is governed by dislocation density, dislocation interaction and active slip systems. In clay minerals such as mica, dislocations are restricted within glide plane i.e. basal plane and no cross slip or dislocation climb has been observed in mica. Therefore, the role of dislocation network, incipient kink band (IKB), and kink band (KB) is significant in affecting the deformation of mica (Barsoum et al. 2004; Zhang et al. 2010). These mechanisms are expected to be highly influenced by the orientation of crystal with respect to the principal deformation stress (Mares and Kronenberg 1993; Christoffersen and Kronenberg 1993), thus resulting in characteristic plastic anisotropy. Therefore, development of dislocation wall in to IKBs and subsequently to KBs result in flow normal to basal plane, manifested as pile-up around the indent. The small pop-ins and serration in the load-displacement curves indicate that small step layer slips or formation of KBs are the main mechanisms of plastic flow. Overall, indentation normal to basal plane manifest a brittle nature, whereas indentation parallel to basal plane exhibit more ductile behavior.

References

Aleksandrov, K.S., Ryzhova, T.V.: Elastic properties of rock-forming minerals II. Bull Acad Scie USSR, Geophys. Ser. English Translation 12, 1165–1168 (1961)

Barsoum, M.W., Murugaiah, A., Kalidindi, S.R., Zhen, T.: Kinking Nonlinear Elastic Solids, Nanoindentations, and Geology. Phys. Rev. Lett. 92(25), 255508 (2004)

Bobko, C., Ulm, F.-J.: The nano-mechanical morphology of shale. Mech. Mater. 40(4-5), 318–337 (2008), doi:10.1016/j.mechmat.2007.09.006

Christoffersen, R., Kronenberg, A.K.: Dislocation interactions in experimentally deformed biotite. J. Struct. Geol. 15(9), 1077–1095 (1993)

Delafargue, A., Ulm, F.J.: Explicit approximations of the indentation modulus of elastically orthotropic solids for conical indenters. Int. J. Solids Struct. 41(26), 7351–7360 (2004), doi:10.1016/j.ijsolstr.2004.06.019

Elliott, H.A.: Axial symmetric stress distribution in aeolotropic hexagonal crystals-the problem of the plane and related problems. Proc. Camb. Phil. Soc. 45(4), 10 (1949)

Hanson, M.T.: The Elastic Field for Conical Indentation Including Sliding Friction for Transverse Isotropy. J. Appl. Mech. 59(2), 123–S130 (1992)

Mares, V., Kronenberg, A.: Experimental deformation of muscovite. J. Struct. Geol. 15(9), 1061–1075 (1993)

McNeil, L.E., Grimsditch, M.: Elastic moduli of muscovite mica. J. Phys. Condens Matter 5(11), 1681 (1993)

Oliver, W.C., Pharr, G.M.: Measurement of hardness and elastic modulus by instrumented indentation: Advances in understanding and refinements to methodology. J. Mater Res. 19(1), 3–20 (2004), doi:10.1557/jmr.2004.19.1.3

Sneddon, I.N.: The relation between load and penetration in the axisymmetric Boussinesq problem for a punch of arbitrary profile. Int. J. Eng. Sci. 3, 10 (1965)

Swadener, J.G., Pharr, G.M.: Indentation of elastically anisotropic half-spaces by cones and parabolae of revolution. Philos. Mag. A 81(2), 447–466 (2001), doi:10.1080/01418610108214314

Ulm, F.-J., Abousleiman, Y.: The nanogranular nature of shale. Act. Geo. 1(2), 77–88 (2006), doi:10.1007/s11440-006-0009-5

Vaughan, M.T., Guggenheim, S.: Elasticity of Muscovite and Its Relationship to Crystal Structure. J. Geophys. Res. 91(B5), 4657–4664 (1986), doi:10.1029/JB091iB05p04657

Vlassak, J.: Indentation modulus of elastically anisotropic half spaces. Philos. Mag. A 67(5), 1045–1056 (1993)

Vlassak, J.J., Ciavarella, M., Barber, J.R., Wang, X.: The indentation modulus of elastically anisotropic materials for indenters of arbitrary shape. J. Mech. Phys. Solids 51(9), 1701–1721 (2003), doi:10.1016/s0022-5096(03)00066-8

Wang, Z., Bei, H., George, E.P., Pharr, G.M.: Influences of surface preparation on nanoindentation pop-in in single-crystal Mo. Scripta Mater 65(6), 469–472 (2011), doi:10.1016/j.scriptamat.2011.05.030

Zhang, G., Wei, Z., Ferrell, R.E.: Elastic modulus and hardness of muscovite and rectorite determined by nanoindentation. Appl. Clay. Sci. 43(2), 271–281 (2009), doi:10.1016/j.clay.2008.08.010

Zhang, G., Wei, Z., Ferrell, R.E., Guggenheim, S., Cygan, R.T., Luo, J.: Evaluation of the elasticity normal to the basal plane of non-expandable 2:1 phyllosilicate minerals by nanoindentation. Am. Mineral 95(5-6), 863–869 (2010), doi:10.2138/am.2010.3398

Compressibility, Strength and Time-Dependent Investigations

Long Term Compression Behaviour of Soft Organic Sediments

Marta Boso and Jürgen Grabe

Institute of Geotechnical Engineering and Construction Management,
Hamburg University of Technology (TUHH), Germany
m.boso@tu-harburg.de

Abstract. Within the coming years a doubling of the container handling in the ports of Hamburg, Germany, is estimated. As a consequence, a significant increase in required space for the new logistic areas is expected. To meet that demand a number of unused canals are backfilled using dredged material from the port or from the Elbe River. The sediments are backfilled in a quasi liquid state, so that they experience one-dimensional consolidation under saturated conditions. In order to study the behaviour of these fills, several laboratory long-term consolidation tests were carried out on soft organic sediments coming from the ports of Hamburg and Bremerhaven. Results show an increase in settlement rate during the secondary compression, the so called tertiary compression. The variation of the tertiary compression coefficient and start-time are investigated in relation to loading, temperature, fibre content, organic content, salinity and gas formation.

1 Introduction

A hundred years old modus operandi to maintain navigable the channels of the Port of Hamburg, i.e. to preserve the water depth, is dredging. In the last century the contaminant load of the dredged sediments built up making the material relocation impracticable because of the contaminant releasing in water. Just in the 80s the political change opened the opportunity for a new strategy against pollution. Nowadays ca. three quarters of the dredge material is relocated in the Elbe River or in the harbour basins within the development plan of the Port of Hamburg, with the aim to generate new areas for storage and handling of containers or other Port activities. In back filling works the deposition of the alluvial mud occurs in a quasi liquid state and it consolidates under saturated conditions, which can be well reproduced in laboratory by means of oedometer tests. Several studies on highly compressible organic soils reveal that the primary consolidation does not represent the most compression and the settlement rate during the secondary compression is not constant as in mineral soils. Therefore neglecting the secondary compression or using a linear prolongation of the curve for the prediction of settlements leads to a significant error. Some authors refer to the increase of strain rate during the secondary compression as tertiary compression. A lot of investigation works demonstrated that increasing fibre and organic contents accelerate and amplify the tertiary compression [1] [2] [3] [4].

L. Laloui and A. Ferrari (Eds.): Multiphysical Testing of Soils and Shales, SSGG, pp. 249–254.
springerlink.com

In this paper the long-term compression behaviour of fluvial organic sediments is presented giving particular attention to the tertiary compression. Sediments coming from different sites of the Port of Hamburg and Bremerhaven are investigated by means of oedometer tests. For all tests the secondary compression index C_α, the tertiary compression index $C_{\alpha t}$, the tertiary compression start-time t_s and, if possible, the tertiary compression end-time t_t were determined from the compression curves e-log t. The effect of loading path, temperature, organic and fibre content, salinity and gassing on the compression behaviour is commented.

2 Soil Description

Sediments have been sampled from Köhlfleethafen and Hamburger Speicherstadt in the Port of Hamburg and from a backfilled zone at the east harbour of Bremerhaven. Table 1 lists the index properties and the grain fractions of the soils. Samples from Köhlfleethafen were taken from a 14 m long drilling core. Up to a depth of 10 m the soil is quite homogeneous and constituted by slightly sandy clayey silt with an increasing organic content with depth. The sediments from this site were tested under both constant and incremental load and the effects of temperature, organic content, fibre content and salinity have been investigated. Sediments from Speicherstadt, classified as sandy silt, were withdrawn at 0,3 m depth. From the homogenized material five identical samples were produced and tested under constant and incremental load. In addition the gassing potential of the soil was estimated. The samples from Bremerhaven were withdrawn from a 20 m long drilling core and the sediments were classified as clayey silt. Five undisturbed samples were withdrawn from the core and tested under constant and incremental load: three at 8 m depth and two at 15 m depth. Details about the fabrication of the samples and the test procedures can be found in [5].

Table 1 Index properties and grain fractions of the investigated soils (mean values).

	w_{nat}	w_L	w_P	O_c	ρ (g/cm^3)	Clay	Silt	Sand
Köhlfleethafen	135,3	113	58,1	10,75	1,23	15÷25	50÷70	0÷5
Speicherstadt	109,3	60,6	33,2	5,1	1,485	5	55	40
Bremerhaven	73,9	104,35	36,5	8,35	1,475	30	65	5

3 Results

In Fig. 1 C_α, $C_{\alpha t}$, t_s and t_t values vs vertical load for remoulded samples from Speicherstadt and undisturbed samples from Bremerhaven are displayed in order to illustrate the differences between constant (CL) and incremental load (IL) tests. The five remoulded samples from Speicherstadt were tested under CL of 15,5 kPa, 28,3 kPa, 53,8 kPa, 104,8 kPa, 206,7 kPa respectively. The sample tested at 15,5 kPa was further incrementally loaded up to the previously listed load levels. Three

samples from Bremerhaven, two from 8 m depth and one from 15 m depth, were tested under CL of 21,9, 79 and 156 kPa respectively. The other two samples were tested under IL.

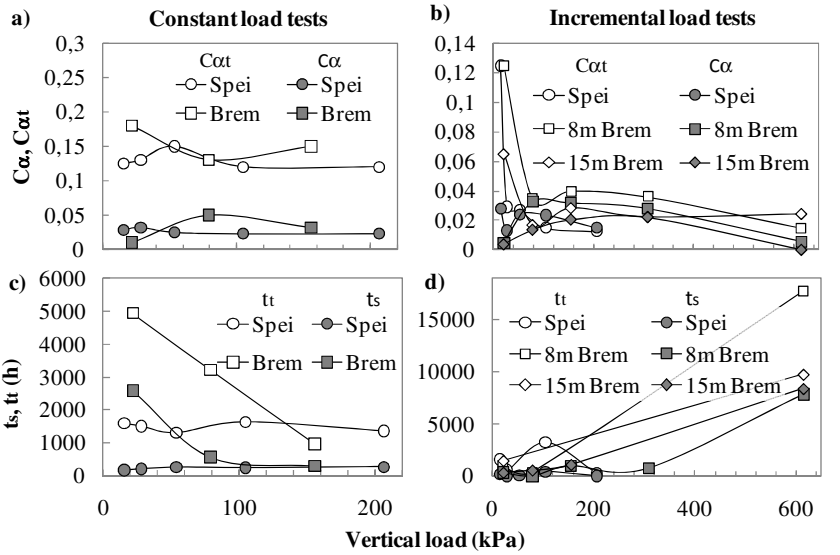

Fig. 1 C_α, $C_{\alpha t}$, t_s and t_t vs vertical load for constant and incremental load tests.

In Fig. 1 a) and b) C_α decreases with increasing load and varies more strongly for samples from Bremerhaven (0,012÷0,05 for CL tests; 0÷0,033 for IL tests) than for samples from Speicherstadt (0,023÷0,032 for CL tests, 0,013÷0,028 for IL tests). This is due to the major homogeneity of the remoulded samples compared to undisturbed samples. For IL tests $C_{\alpha t}$ exhibits a maximum for low vertical loads and then decreases with increasing load. In IL tests $C_{\alpha t}$ approaches C_α while in CL tests $C_{\alpha t}$ decreases slightly but is always greater than C_α. When $C_{\alpha t}$=C_α the tertiary compression is no more detectable. From Fig. 1 c) and d) a common trend for t_s and t_t is not discernable.

Fig. 2 shows C_α, $C_{\alpha t}$, t_s and t_t vs vertical load for three identical samples produced with homogenized material from Köhlfleethafen and tested at three different temperatures under incremental load. C_α is not influenced by the temperature, while the decreasing rate of $C_{\alpha t}$ rises with it. This temperature effect can be explained considering decomposition as one of the causes of the tertiary compression. At high temperature the most part of the organic matter decays during the first loading step emerging in a noticeable tertiary compression. At the last loading step the remaining organic matter protected by the soil fabric is not achievable by bacteria and decay does not take place (C_α=$C_{\alpha t}$). At low temperature the decay is slowed down and organic matter remains longer at disposal for decomposition and

tertiary compression is detectable also at the end of the test ($C_{\alpha t}$>C_α). Fig. 2 b) shows that only t_s is affected by temperature and decreases with increasing temperature reflecting the acceleration of the decomposition at high temperature.

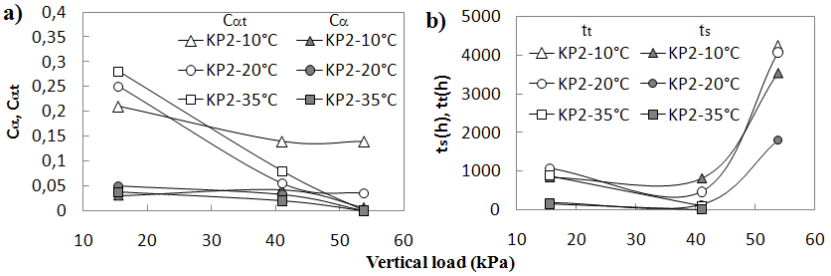

Fig. 2 C_α, $C_{\alpha t}$, t_s and t_t versus vertical load as the temperature changes

Table 2 State variables and C_α, $C_{\alpha t}$, t_s for samples with different organic contents.

	w	e_0	ρ	O_c (%)	C_α	C_{α_t}	t_s (h)	Load (kPa)
Natural organic content	157,1	3,9	1,27	14,1	0,0711	0,41	385	15,5
Reduced organic content	111,8	2,8	1,42	11,7	0,0047	0,16	1318	15,5

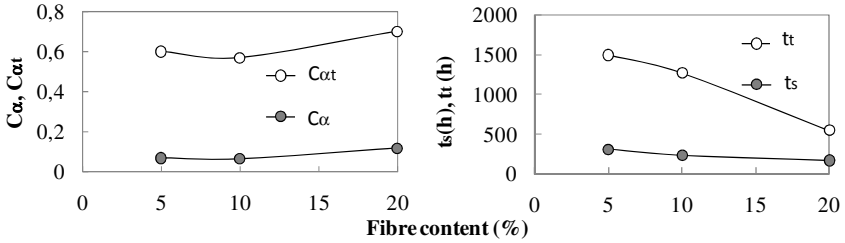

Fig. 3 C_α, $C_{\alpha t}$, t_s and t_t versus fibre content, 15,5 kPa CL tests.

In Table 2 C_α, $C_{\alpha t}$ and t_s for two remoulded samples produced with material from Köhlfleethafen with different organic contents and tested under CL are presented. The O_c of one sample was reduced by means of wet combustion (10% H_2O_2 solution). C_α and $C_{\alpha t}$ decrease with decreasing organic content while the start-time t_s increases. In Fig. 3 results of CL tests on three samples produced with homogenized material from Köhlfleethafen mixed with different cellulose fibre contents are reported. C_α and $C_{\alpha t}$ increase with increasing fibre content, while t_s and the duration of the tertiary compression reduce drastically. These data are the result of the decomposition, so that more available nutrient for the microbial biomass translates in a greater tertiary compression.

In Fig. 4 C_α, $C_{\alpha t}$, t_s and t_t vs salinity and the interaction potential between colloids vs particle distance depending on salinity [6] are reported. Four identical

remoulded samples were produced, flushed with NaCl solutions with different concentrations and tested under constant load of 41,8 kPa. Fig. 4 a) shows that, while C_α is not affected by salinity, $C_{\alpha t}$ decreases with increasing salt concentration. The minimum value of $C_{\alpha t}$ at salinity 0,1% can be explained considering the curve at low salinity of Fig. 4 c), the pick of repulsion forces counteracts the compression resulting in a smaller $C_{\alpha t}$. At higher salinities the attractive forces prevail expecting an increase of compressibility, but in spite of that $C_{\alpha t}$ decreases and the duration of the tertiary compression increases (Fig. 4 b)). A possible explanation can be found in the reduced microbial activity due to the aggressive environment.

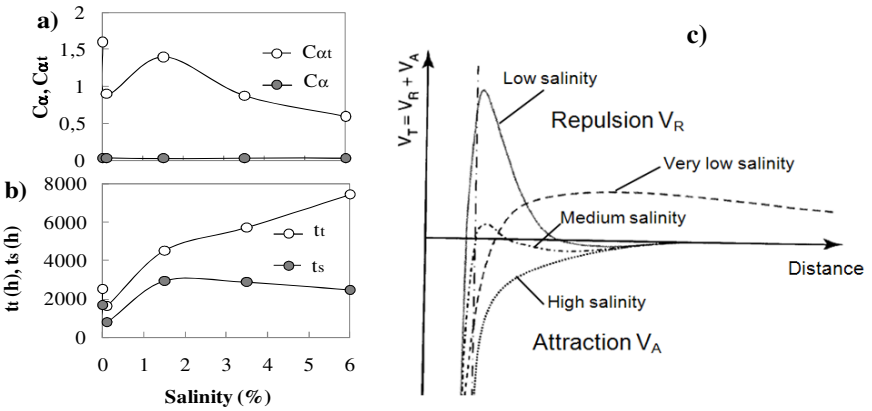

Fig. 4 C_α, $C_{\alpha t}$, t_s and t_t versus salinity [a), b)]. Interaction potential between particles [c)].

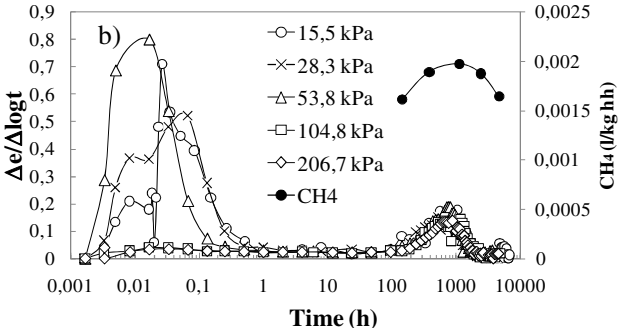

Fig. 5 Deformation rates Δe/Δlogt for samples from Speicherstadt and CH_4 formation rate.

Fig. 5 shows the strain rates of remoulded samples from Speicherstadt tested under constant load (Fig. 1 a)) and the CH_4 formation rate. The gas formation rate has its maximum exactly during the tertiary compression. It is feasible, that small gas bubbles create empty spaces inside the sample and soil particles rearrange filling these spaces and favouring the tertiary compression.

4 Conclusions

For both CL and IL tests C_α and $C_{\alpha t}$ decrease with increasing vertical load. $C_{\alpha t}$ decreasing rate is greater for IL tests than for CL tests as a result of the stored strain and consequent smaller compressibility. With increasing load the tertiary compression dims until it is no more detectable.

Results of temperature controlled IL tests and tests on samples with different organic and fibre contents confirm that decomposition of organic matter is an important factor influencing the tertiary compression. Because of the decay some regions inside the specimen empty and the created voids are occupied by the soil particles causing a volume reduction. The amount of voids and hence the volume reduction is proportional to the amount of decomposed organic matter and microbial activity that in turn depends on the environment. Temperature and salinity act in opposite fashion with respect to the decomposition: temperature favours the bacterial activity, while salinity creates an aggressive environment reducing the bacteria population. As a result $C_{\alpha t}$ increases with increasing temperature and decreases with increasing salinity. Finally gas, product of decomposition, contributes to form voids for the rearrangement of the soil particles and aggregates.

Data of start- and end-time of the tertiary compression are not clear and more investigation and information on the decomposition process and on the organic matter retention are needed for a consistent evaluation.

References

Dhowian, A.W., Edil, T.B.: Consolidation Behavior of Peats. Geotechnical Testing Journal 3(3), 105–114 (1980)

Colleselli, F., Cortellazzo, G., Cola, S.: Laboratory Testing of Italian Peaty Soils. In: Edil, T.B., Fox, P.J. (eds.) Geotechnics of High Water Content Materials ASTM, STP, vol. 1374, pp. 226–240. American Society for Testintg and Materials, West Conshohocken (2000)

Yılmaz, E., Saglamer, A.: Secondary and Tertiary Compression Behavior of Samsun Soft Blue Clay. In: Proc. 15th International Conference on Soil Mechanics and Geotechnical Engineering, Istanbul, August 27-31, vol. 1, pp. 329–332 (2001)

Cevikbilen, G., Saglamer, A.: Effects of organic content on secondary and tertiary compression behavior of clay. In: Proc. of International Conference on Soil Mechanics and Foundation Engineering, vol. 3, pp. 60–64 (2003)

Möller, O.: Zum Langzeit-Kompressionsverhalten weicher organischer Sedimente. PhD Thesis, Institut für Geotechnik und Baubetrieb, TUHH, Hamburg, Germany (2010) (in German)

Jasmund, K., Lagaly, G.: Tonminerale und Tone: Struktur, Eigenschaften, Anwendungen und Einsatz in Industrie und Umwelt. Steinkopf Verlag, Darmstadt (1993)

On Creep Laboratory Tests in Soil Mechanics

Arman Khoshghalb

School of Civil and Environmental Engineering, The University of New South Wales, Sydney 2052, Australia
Arman.khoshghalb@unsw.edu.au

Abstract. Soil exhibits creep behaviour, which is the development of time-dependent shear and/or volumetric strains at a state of constant effective stress. Creep is controlled by the viscous like resistance of soil structure. Creep behaviour influences the long-term settlement of grounds and movement of slopes; therefore it is of significance in geotechnical engineering applications. Creep laboratory tests, mainly one-dimensional and triaxial creep tests, are used to investigate the creep characteristics of soils and to predict the creep behaviour of soil in the long term. Conventional creep tests involve loading a soil sample to a specific effective stress and then allowing the sample to creep under constant effective stress. However, in order to capture the long term creep behaviour of soil, long duration creep tests are required. Therefore, the creep tests are not only laborious and time-consuming which render them impractical in many applications, but also associated with some difficulties and inaccuracies that need to be dealt with. In this study, a review on the conventional laboratory creep tests, the main difficulties associated with them, and the solutions proposed to alleviate these difficulties (if there are any) are presented. The possible sources of inaccuracies in the test results are discussed and practical recommendations are proposed to minimise the inaccuracies in the results.

1 Introduction

Time has a strong effect on the engineering behaviour of both cohesive and granular soils [1]. When soil is subjected to a constant effective stress, it deforms over time, and this is usually called creep [2]. In geotechnical engineering, it is often a challenge to predict the creep behaviour of soil in the long run [2].

In clayey soils, creep is caused by viscous expulsion of double layer water around clay particles and non-recoverable rearrangement and deformation of clay particles [3]. However, in granular soils, the viscous expulsion of absorbed water is insignificant compared to other factors. One argument is that strong force chains are created within particulate assemblies as they are loaded [4]. The most critically loaded columns then starts to buckle and fail resulting in a gradual stabilization process in which the out of balance loads are transferred to more optimally arranged force columns [1]. This process is accompanied by some volume change whose rates decreases continuously and is called creep.

L. Laloui and A. Ferrari (Eds.): Multiphysical Testing of Soils and Shales, SSGG, pp. 255–260.
springerlink.com

2 General Comments on Creep Tests

Conventional creep tests involve loading a soil sample to a specific effective stress and then allowing the sample to creep under constant effective stress. However, long duration creep tests are required in order to capture the long term creep behaviour of soils rendering the creep tests difficult, time-consuming and prone to errors and oversight.

The creep behaviour of soil has been investigated mainly using one-dimensional and triaxial creep tests. These two tests will be discussed separately in the following sections. Like most geotechnical laboratory tests, the results of a creep test are affected by the sample disturbance; therefore care must be exercised in this regard.

Creep tests are often run for a long time, and therefore long-term stability is required. To minimise the potential effect of temperature variations on strain sensors, test should be conducted in a temperature controlled room, however, still some corrections might be needed to account for a small temperature variations during the test because the creep strain rates are usually very low. Hence, temperature must be continuously measured and recorded during the test. One of the corrections proposed in the literature is to assume a sinusoidal pattern for the laboratory temperature variations. Then, based on the transducer characteristics, strain results could be corrected for temperature variations [1]. It is also recommended to take the gauge readings at 12 or 24 hours time intervals when the temperatures reach similar values.

As mentioned above, since the creep strain rates are often small, conventional creep tests are time-consuming. To overcome this difficulty, a methodology has been proposed in the literature to accelerate creep tests [5]. The idea is to accelerate a creep test by overloading the soil to some extent, and then unloading it to the effective stress of interest. The method is based on having the same potential for plastic flow and the creep flow, which is supported by experimental results in the literature [6-7]. Details of this method can be found in [5].

The initial degree of saturation of the soil sample may also alter the creep test results. If the soil sample is dry, the applied total stress is equal to the effective stress, and thus, the soil exhibits the true creep behaviour immediately after the application of the stress. For a saturated or semi-saturated soil sample, however, there might be a primary consolidation phase (depending on the loading rate or straining rate), before soil exhibits its true creep behaviour. In such cases, specifying the time origin for the creep phase is not straightforward. Determining the reference time of creep is important in estimating creep settlements in low permeability soils such as clay. For these cases (when the primary consolidation phase also exists), mainly two approaches have been adopted in the literature to decide when creep deformation starts [8]. The first approach is to take the reference time at the completion of the primary consolidation phase. The time-dependent behaviour after this time is then considered as the true creep behaviour of the soils. The second approach is to take the reference time as an intrinsic parameter for a given soil, which is independent of drainage conditions and soil

thickness. The real soil behaviour might be somewhere in between since the two approaches correspond to two extreme cases [8].

Although creep behaviour of soils can be investigated in both drained and undrained conditions, it is accepted that the drained creep tests represent the true creep behaviour of the soil [8]. Therefore, creep laboratory tests are often performed in the drained conditions. For saturated soil samples, the appropriate loading rate can be found based on the coefficient of consolidation of the soil and the drainage condition of the test so that the full dissipation of excess pore pressure is ensured.

To calculate the creep rate of soil, the increment of creep strain is divided by the period of time in which the increment of strain develops in soil. Theoretically, to have a more accurate creep rate at a specific time, shorter period of time should be selected. However, due to measurement errors in the observations of the deformation of the sample, errors on the measured strain rate tend to increase as the period of time becomes shorter. Therefore, in practice, the choice of the period of time should be determined based on an error analysis. Furthermore, creep strain rates are sometimes very small and very accurate measurements are required for their detection. Therefore, care must be exercised to distinguish between the measuring equipment errors and the creep strain rates. To this end, the error of the transducers must be properly determined and then a detectable creep rate can be defined based on the accuracies of the measuring equipments and the sample dimensions [5]. Strain rates below the detectable strain rate should not be considered as the creep behaviour of soil.

3 One-Dimensional Creep Test

The one-dimensional compression test is used to determine soil parameters associated with laterally confined conditions. The main result of a one-dimensional creep test is a void ratio-log time curve for the saturated sample of the soil at hand at a sustained total stress (A typical graph for a saturated clay sample is shown in Figure 1). Two distinct phases can usually be identified on the plot: primary consolidation and secondary compression. Often, the one-dimensional creep behaviour of soil is characterized by the dimensionless coefficient of secondary compression. This coefficient, shown on Figure 1, is known to be independent of elapsed time, sample thickness and the load Increment.

The one-dimensional creep test is not appropriate for investigating the creep failure. To investigate the creep failure, the triaxial creep tests should be adopted, since in this test, the samples can be allowed to creep at different stress states with reference to the critical state of the soil.

One-dimensional creep tests on granular soils at high stress levels are accompanied with particle crushing. This process depends on the particle size distribution of the soil, particles shapes, relative density of the soil, particles hardness and the saturation ratio of the soil sample [9]. At the moment, the mechanism of soil creep due to particle crushing is not well understood [5]. Particle crushing can be detected by comparing the particle size distribution of the samples before and after the one-dimensional creep test.

Some approaches have been proposed to investigate the effect of particle crushing on the deformation of granular soils and to distinguish between the creep rate and the particle crushing rate in the one-dimensional compression creep test [10-12]. One approach proposed in the literature is to use the law of energy conservation to formulate the process of particle crushing in granular soils. This way, the relation between the void ratio and the amount of particles crushed in one-dimensional compression test can be derived for granular soils. Further description of this approach can be found in [12].

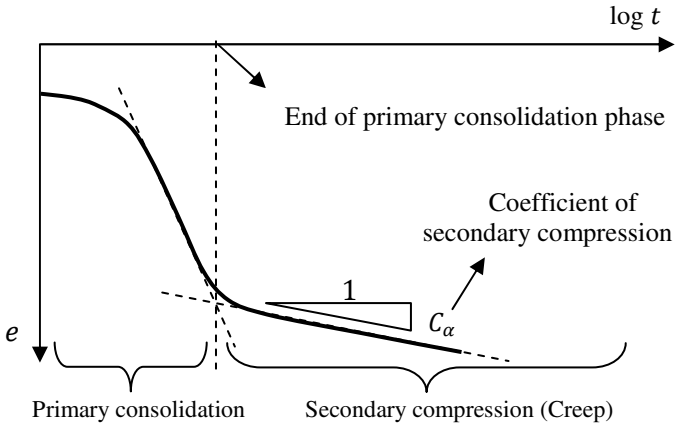

Fig. 1 Typical void ratio versus log time relation of saturated clay sample in one-dimensional compression test.

4 Triaxial Creep Test

In triaxial creep tests, soils samples can be allowed to creep at some certain confining pressures and different deviator stresses. When the results of a creep test performed at a constant stress in a triaxial apparatus is plotted in a strain versus time diagram with arithmetic axes, three parts can often be identified: Primary creep or transient creep, secondary creep or stationary creep and tertiary creep or acceleration creep [8]. The tertiary creep eventually leads to failure of the soil. In a one-dimensional creep test, only primary creep can be seen; secondary and tertiary creep cannot be observed.

In triaxial creep tests, non-uniform end stresses and strains are usually observed due to end restraint. Therefore, end lubrication layers are advised to reduce the end restraint and improve the radial strain uniformity [1]. Usually, top and base platens with the diameter larger than the sample diameter are adopted, so that large radial strains could be accommodated without the sample bulging beyond the pedestal base. Drainage is allowed through a small porous stone located in the centre of the base platen.

Since the creep test takes a long time, penetration of the membrane could also affect the results. In drained tests, it may cause incorrect assessments of volume changes of the sample and in undrained tests, deviation from the ideal constant-volume conditions may be resulted. Few methods have been proposed in the literature to reduce or correct for the membrane penetration. One method is to compare the total volume strain based on the gauge readings with volumetric strains calculated from local sensors, assuming uniform cylindrical deformation of the sample [1]. To correct for the volume change due to membrane penetration, a linear relation between unit membrane penetration (volume change due to membrane compliance per unit surface area of the membrane) and effective confining pressure is assumed [13]. The slope of this line is often called the "normalised membrane penetration" which is independent from the latex modulus, membrane thickness and soil particle size [1].

Another cause of error in the triaxial creep tests is due to end effects, in which axial strains are not uniform over the height of the sample. One solution can be using axial deformation gages which measures the axial strains within the middle halve of the specimen height (from the upper 1/4 to the lower 1/4 of the specimen height) away from the end boundary effects.

As mentioned before, the drainage condition of the soil influences the results of the creep test. However, there are several occasions in the literature where the triaxial creep tests are referred without explaining whether or not the effective stresses were kept constant [8]. Since this has a strong influence on interpretation of the test results, one should always clearly distinguish between creep tests at constant load and creep tests at constant stress.

The load cell compliance can also affect the results of a triaxial creep test. To avoid this effect, some researchers has adopted stress ratio (the effective horizontal stress to the effective vertical stress) equal to 0.95 to represent the “isotropic” stress path tests [1].

The amount of creep strain also depends on the stress rates applied during loading and the length of the creep pauses. Usually, the faster the loading is applied and the longer the pauses are, the more creep strain would be measured. Moreover, if high stresses are achieved in a creep test, strains due to particle crushing should be distinguished from strains due to creep flow.

5 Conclusions

The paper has discussed some issues regarding an experimental study into creep behaviour of soils. The review has mainly focused on investigating the time-dependent behaviour of soil through one-dimensional compression tests and triaxial tests. It was emphasised that to obtain reliable information on soil creep behaviour, precision and long-term stability are required. Several factors, important in either performing the creep tests or interpreting the test results, were then discussed. Despite all the precautions and corrections, errors always take place which affect the test results. However, the errors are far smaller when these corrections and precautions are adopted.

References

Kuwano, R., Jardine, R.J.: On measuring creep behaviour in granular materials through triaxial testing. Canadian Geotechnical Journal 39(5), 1061–1074 (2002)

Mitchell, J.K., Soga, K.: Fundamentals of Soil Behavior, p. 592. Wiley (2005)

Graham, J., Yin, J.-H.: On the time-dependent stress-strain behaviour of soft soils. In: 3rd International Conference on Soft Soil Engineering, Hong Kong (2001)

Jardine, R.J., Kuwano, R., Zdravkovic, L., Thornton, C.: Some fundamental aspects of the pre-failure behaviour of granular soils. In: Proceedings of the Second International Symposium on Pre-failure Deformation Characteristics of Geomaterials, September 28-30. Shers, Italy (1999)

Wang, Z.: Soil Creep Behavior – Laboratory Testing and Numerical Modelling, in Department of Civil Engineering, p. 335. University of Calgary, Alberta (2010)

Lade, P.V., Liu, C.-T.: Experimental Study of Drained Creep Behavior of Sand. Journal of Engineering Mechanics 124(8), 912–920 (1998)

Lade, P.V., Yamamuro, J.A., Bopp, P.A.: Influence of time effects on instability of granular materials. Computers and Geotechnics 20(3-4), 179–193 (1997)

Augustesen, A., Liingaard, M., Lade, P.V.: Evaluation of time-dependent behavior of soils. International Journal of Geomechanics 4(3), 137–156 (2004)

Hardin, B.O.: Crushing of Soil Particles. Journal of Geotechnical Engineering, 1985 111(10), 1177–1192 (1985)

McDowell, G.R., Bolton, M.D.: On the micromechanics of crushable aggregates. Geotechnique 48(5), 667–679 (1998)

Ueng, T.-S., Chen, T.-J.: Energy aspects of particle breakage in drained shear of sands. Geotechnique 50(1), 65–72 (2000)

Wang, Z., Wong, R.C.K.: Effect of grain crushing on 1D compression and 1D creep behavior of sand at high stresses. Geomechanics and Engineering 2(4), 303–319 (2010)

Baldi, G., Nova, R.: Membrane Penetration Effects in Triaxial Testing. Journal of Geotechnical Engineering 110(3), 403–420 (1984)

Variation of Cohesive Sediment Strength with Stress Level

Brendan Casey[1] and John T. Germaine[2]

[1] Dept. of Civil and Environmental Engineering, Massachusetts Institute of Technology, Room 1-339, 77 Massachusetts Ave., Cambridge, MA 02139
bcasey@mit.edu
[2] Dept. of Civil and Environmental Engineering, Massachusetts Institute of Technology, Room 1-353, 77 Massachusetts Ave., Cambridge, MA 02139
jgermain@mit.edu

Abstract. Undrained strengths of a range of natural cohesive soils are investigated over an effective stress range of 0.1 to 10 MPa. The resedimentation technique is effectively used to produce identical samples for K_O-consolidated undrained triaxial compression testing. Normalized shear stress – strain responses and undrained strength ratios are found to vary considerably and consistently when viewed over a significant stress range. The undrained strength ratio of a soil and its variation with stress level can be estimated from liquid limit, an easily measured index property which reflects clay mineralogy and clay fraction of a cohesive soil.

1 Introduction

The shear strength properties of geomaterials are of great importance in geotechnical engineering and geological sciences. Shear strength is an important parameter for the foundation design of buildings, dams, roads and other infrastructure projects, for the determination of submerged and unsubmerged slope stability, and the evaluation wellbore stability in hydrocarbon extraction, to name but a few applications. For cohesive materials (such as clays, clayey silts and mudrocks which are the focus of this paper), short term undrained conditions are typically the critical case for stability analyses. The purpose of this paper is to introduce a method which can readily be used to predict reasonable undrained strengths for a wide variety of normally consolidated (NC) cohesive materials by using an easily measured index property of the material, i.e. the liquid limit.

2 Background

Difficulty in design arises from the fact that undrained strength can vary enormously between different soils. Figure 1 by Ladd (1991) plots values of undrained

L. Laloui and A. Ferrari (Eds.): Multiphysical Testing of Soils and Shales, SSGG, pp. 261–266.
springerlink.com

strength ratio (i.e. undrained strength normalized with respect to the pre-shear vertical consolidation stress, s_u/σ'_{vc}) *measured at various low stresses* versus plasticity index (I_p). The figure includes data on a variety of NC clays and silts in different modes of shear. The undrained strength ratio can be seen to vary from about 0.13 to 0.37 depending on soil type and mode of shear (values as low as 0.07 have been observed for sodium montmorillonite by Mesri and Olson (1970)). The correlation of Ladd (1991) does little but to highlight the difficulty in choosing a reasonable value of undrained strength without resorting to field or laboratory testing.

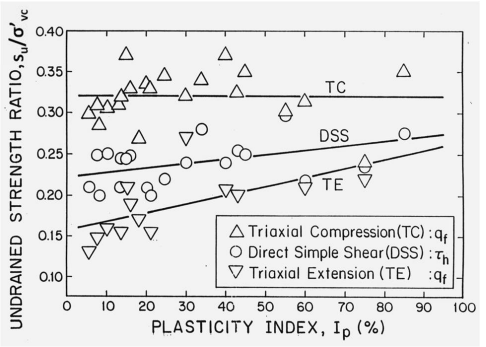

Fig. 1 The undrained strength ratio of various normally consolidated clays and silts plotted against plasticity index (Ladd, 1991)

While it has long been recognized that undrained strength can vary significantly between different soils, a typical assumption made in modeling and design is that individual cohesive soils exhibit *normalized properties*. The normalized soil parameter concept is based on the empirical observation that samples of a particular soil having a similar stress history (i.e. overconsolidation ratio, OCR) but different consolidation stresses, and therefore different preconsolidation pressures (σ'_p), exhibit similar properties (e.g. undrained strength, shear induced pore pressures) when normalized with respect to the consolidation stress. This has led to the SHANSEP (Stress History and Normalized Soil Engineering Properties) design procedure developed by Ladd and Foott (1974). The normalized soil parameter concept is also the basis for other frameworks which describe soil behaviour such as Critical State Soil Mechanics (Schofield and Wroth, 1968), or analytical models such as Modified Cam Clay (Roscoe and Burland, 1968). However, recent research gives strong indication that, when viewed over a significant stress range, very few cohesive soils actually exhibit normalized behaviour. In particular, some soils exhibit considerable variation in normalized undrained strength with effective stress level. This will be developed further in the results section.

The correlations developed in this paper necessitate an introductory description of the Atterberg limits. The Atterberg limits are water contents corresponding to particular index strengths and, in a basic sense, define the transition between

different soil states (Germaine and Germaine, 2009). The limits were adopted in geotechnical engineering as a formal way of classifying clayey and silty soils according to the Unified Soil Classification System. The plastic limit (w_p) is determined by rolling the material into ⅛" threads (ASTM D4318) while the liquid limit (w_L) is determined using either the Casagrande Cup method (ASTM D4318) or the fall cone method (BS 1377). Plasticity index is defined simply as $I_p = w_L - w_p$. A key feature of the Atterberg limits is that they are a function of both the *quantity and type* of clay minerals present in a soil, combining the mechanical effects of these two attributes into a single number. For a given clay fraction, both w_p and w_L will increase with an increasing influence of surface forces in particle interactions. Such surface forces are particularly dominant in smectite-rich materials. In addition, for a given clay mineralogy, both w_p and w_L will increase with increasing clay fraction. The Atterberg limits therefore have strong links to underlying mechanical behaviour. For real soils which typically consist of a complex mixture of clay minerals and larger grains, the limits are a very simple means of providing a first approximation of engineering properties.

3 Test Materials and Methodology

Table 1 lists the soils included in the current study along with their Atterberg limits and clay fraction (< 2 μm). All of the soils have been tested in the M.I.T. geotechnical engineering laboratory within the last 5 years. It can be seen that there is a wide range of soil types included in the study, from a low plasticity silt (Skibbereen Silt) to a medium plasticity glacio-marine clay (Boston Blue Clay) to a high plasticity marine clay (San Francisco Bay Mud).

Apart from the Skibbereen Silt which was prepared using the undercompaction method (Ladd, 1977), the resedimentation technique was used to produce samples of the soils for testing. In addition to the obvious practical problems of sampling disturbance and cost associated with intact samples (particularly for deep or offshore samples), the use of intact samples rather than resedimented ones does not allow for control of the stress history, i.e. σ'_p, of the samples. This makes a systematic investigation of the mechanical behaviour of any soil as a function of both stress level and OCR using intact samples practically impossible. The resedimentation technique also eliminates variability among samples and produces uniform specimens with K_O (i.e. one-dimensional) consolidation histories and complete saturation.

Resedimentation has been progressively developed at M.I.T. since the 1960's. The basic procedure involves incrementally loading a dilute slurry of the homogenized natural material in a tube called a consolidometer. The sample is consolidated to a desired σ'_p before being swelled to OCR~5 prior to extrusion from the consolidometer and mounting in the triaxial device.

Table 1 Summary of soils included in current test program

Soil	Origin	Contributing researchers	Liquid Limit, w_L (%)	Plasticity Index, I_p (%)	Clay fraction (%)
R. Boston Blue Clay	Boston, Massachusetts	author, Abdulhadi (2009)	46.5	22.7	56
R. Ugnu Clay	Alaskan North Slope	author, Jones (2010)	56.5	30.1	44
R. San Francisco Bay Mud	San Francisco, California	author, Kontopoulos (2012)	72.8	43.7	52
R. Gulf of Mexico Clay	Ursa Basin, Gulf of Mexico	author	51.7	28.0	54
R. Presumpscot Clay	Maine	author	33.1	13.7	37
Skibbereen Silt	Skibbereen, Ireland	Grennan (2010)	25.8	7.5	10

Triaxial testing is performed using custom made automated triaxial systems possessing internal load cells for axial load measurement as well as the ability to perform K_O-consolidation. While the use of isotropic consolidation is generally believed to have a small impact on the measured undrained strength of intact overconsolidated specimens, for resedimented specimens or for intact specimens consolidated well into the NC range when the yield surface changes, K_O-consolidation prior to shearing is especially important. The K_O-consolidation algorithm used to control the triaxial testing system ensures zero radial strain of the specimen by continuously adjusting cell pressure to keep volume and axial strains equal. At the end of K_O virgin consolidation specimens are allowed at least 24 hrs of [drained] secondary compression before being sheared undrained over the stress range $\sigma'_{vc} = 0.1 – 10$ MPa in compression mode of shear.

4 Results

For all soils tested, increasing effective stress leads to a more ductile stress - strain response during undrained shear as strain to failure increases and post-peak strain softening is reduced. This is demonstrated in Figure 2 which shows the results of three representative tests performed on NC resedimented Boston Blue Clay (RBBC) at different consolidation stresses (σ'_{vc}) by Abdulhadi (2009). Only axial strains up to 2.5 % are shown in Figure 2 for clarity. Figure 2 also illustrates how the undrained strength ratio (i.e. the peak point of the normalized shear stress – strain curve) decreases with increasing stress level. Figure 3 shows this trend for all tests performed on NC RBBC.

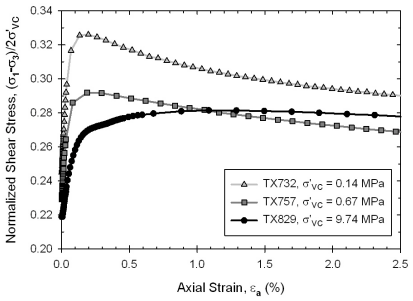

Fig. 2 Normalized stress – strain responses of RBBC measured during undrained shear

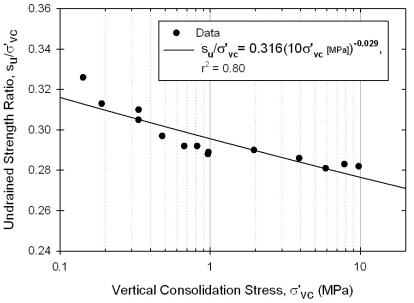

Fig. 3 Variation in undrained strength ratio of RBBC as a function of effective stress

The experimental data shown in Figure 3 is fitted using a power law function of the form: $s_u/\sigma'_{vc} = c(10\sigma'_{vc\ [MPa]})^d$, where c and d are simply fitting parameters equal to 0.316 and -0.029 for RBBC respectively. Consistent variations of s_u/σ'_{vc} with effective stress have been observed for each soil tested. However, the trend is not always for s_u/σ'_{vc} to decrease by the same amount, or even at all. It has been found that the variation in undrained strength with stress level is soil type dependent and can be related to the soil's Atterberg limits. Figures 4a and 4b show the correlations between the parameters c and d with liquid limit respectively. Although there is some scatter in the results, r^2 values of 0.90 and 0.85 indicate that the correlations are certainly significant. Figure 4a illustrates how the parameter c, which is simply the undrained strength ratio at a consolidation stress of 0.1 MPa, increases linearly with w_L. Figure 4b shows how the parameter d, which describes the change in undrained strength ratio with effective stress, decreases logarithmically with w_L. Negative values of d indicate a consistent decrease in s_u/σ'_{vc} with increasing effective stress (e.g. RBBC) while a positive value of d indicates a consistent increase (e.g. Skibbereen Silt).

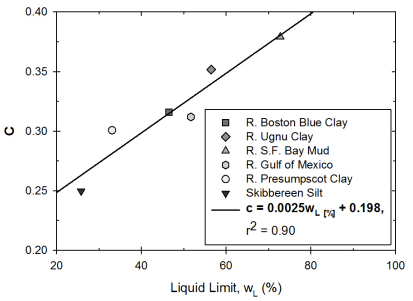

Fig. 4a Correlation between parameter 'c' and liquid limit

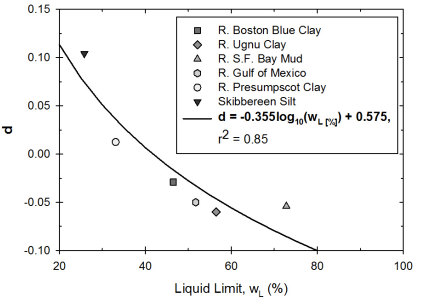

Fig. 4b Correlation between parameter 'd' and liquid limit

5 Conclusions

Series of K_O-consolidated triaxial tests have been performed on a variety of normally consolidated resedimented soils. It has been found that the common assumption of cohesive soils exhibiting normalized properties is valid only if behaviour is viewed over a narrow stress range. Increasing effective stress is found to result in a more ductile stress – strain response during undrained shearing as well as a consistent variation in undrained strength ratio. Undrained strength ratio and its variation with effective stress can be predicted using a power law function containing two soil parameters. These parameters can be estimated from liquid limit, an index property which is related to the quantity and type of clay minerals present in a soil. Previous correlations between undrained strength ratio and the Atterberg limits (e.g. Ladd, 1991) do not consider that the ratio varies with effective stress level and as a result display a great deal more scatter.

Acknowledgments. The work presented in this paper is funded by the UT Geofluids consortium, comprising Anadarko Petroleum, BP, BHP Billiton, Chevron, ConocoPhillips, ExxonMobil, Hess, Schlumberger, Shell, Statoil and Total.

References

Abdulhadi, N.O.: An Experimental Investigation into the Stress-Dependent Mechanical Behavior of Cohesive Soil with Application to Wellbore Stability. Dissertation, Massachusetts Institute of Technology (2009)

Germaine, J.T., Germaine, A.V.: Geotechnical Laboratory Measurements for Engineers. John Wiley and Sons Inc., New Jersey (2009)

Grennan, J.T.: Characterization of a Low Plasticity Silt., Dissertation, Massachusetts Institute of Technology (2010)

Jones, C.A.: Engineering Properties of Resedimented Ugnu Clay from the Alaskan North Slope. Dissertation, Massachusetts Institute of Technology (2010)

Kontopoulos, N.S.: The Effects of Sample Disturbance on Preconsolidation Pressure for Normally Consolidated and Overconsolidated Clays. Dissertation, Massachusetts Institute of Technology (2012)

Ladd, C.C.: Stability Evaluation during staged Construction. 22nd Karl Terzaghi Lecture. Journal of Geotechnical Engineering 117(4), 540–615 (1991)

Ladd, C.C., Foott, R.: New Design Procedure for Stability of Soft Clay. Journal of the Geotechnical Engineering Division, ASCE 100(7), 763–786 (1974)

Ladd, R.S.: Preparing test Specimens Using Undercompaction. Geotechnical Testing Journal 1(1), 16–23 (1978)

Mesri, G., Olson, R.E.: Shear Strength of Montmorillonite. Géotechnique 20(3), 261–270 (1970)

Roscoe, K.H., Burland, J.B.: On the Generalized Stress-Strain Behaviour of 'Wet' Clay. Engineering Plasticity, pp. 535–609. Cambridge University Press (1968)

Schofield, A.N., Wroth, C.P.: Critical State Soil Mechanics. McGraw-Hill (1968)

Meso-scale Oedometer Test System for Volume Change Determination in Problematic Soils

Shahid Azam, Peter Gutiw, and Mavinakere E. Raghunandan

Faculty of Engineering & Applied Science,
University of Regina, Canada
Shahid.Azam@uregina.ca

Abstract. This paper describes the development of a Meso-scale Oedometer Test System (MOTS) for investigating the volume change behavior of problematic soils. The *de novo* test system is designed to measure swelling, collapse, and consolidation properties of 100 times larger than conventional samples. This scale allows for an effective capture of soil structure and for understanding the spatial and temporal variability in volume change. Numerical simulations and load-deformation analyses indicated that the test system can safely be loaded up to 1730 kPa: the deformability of the entire assembly was found to be 4 mm. A preliminary test indicated that the apparatus provides a better estimate of soil volume change.

1 Introduction

The Canadian Prairies offer unique challenges to address complex geotechnical engineering issues. This is particularly for southern Saskatchewan that possesses various types of problematic soils such as expansive clays and erodible sediments. A semi-arid climate prevalent in the region ensures unsaturated conditions in the soils most of the year. The intermittent precipitation events result in swelling (due to hydration of clay minerals), collapse (due to erosion and/or dissolution of materials), and compressibility (due to consolidation and/or particle rearrangement) in the indigenous problematic soils. The presence of desiccation cracks and solution cavities in the soil matrix renders the conventional methods of volume change measurement quite erratic for such soils.

Alternate volume changes in local problematic soils have markedly impaired civil infrastructure such as transportation networks (Imumorin and Azam, 2011), water supply and sewage collection systems (Hu and Hubble 2005), and residential, industrial, and commercial facilities (Ito and Azam 2010). Damages to engineered facilities are clearly manifested in the form of differential heave/settlement in roadways and sidewalks, inclined cracking in slab-on-grade basements and masonry walls, and breakage in underground storage tanks and buried pipelines. Clearly, there is a need to develop a clear understanding of the volume change behavior of local problematic soils.

L. Laloui and A. Ferrari (Eds.): Multiphysical Testing of Soils and Shales, SSGG, pp. 267–271.
springerlink.com

The main objective of this paper is to describe the development of the *de novo* Meso-scale Oedometer Test System (MOTS) for volume change determination in problematic soils. The equipment is housed in the Saskatchewan Advanced Geotechnical Engineering (SAGE) laboratory at the University of Regina, Canada.

2 Design and Fabrication

Figure 1 gives an annotated photographic compilation of the various components of MOTS. Improving the design of a large oedometer for expansive clays (Azam et al., 2000), the new facility eliminates the need for a lever arm by using a pneumatic loading device. The pressure is generated by an air compressor, regulated through a manifold and applied on the sample by a tandem piston actuator. Based on volume, the setup is capable to test samples 100 times larger than conventional size specimens. Ensuring the standard height-to-diameter ratio of 0.27, the meso-scale samples (600 mm diameter and 160 mm height) allow for an effective capture of the spatial variability of matrix discontinuities in problematic soils.

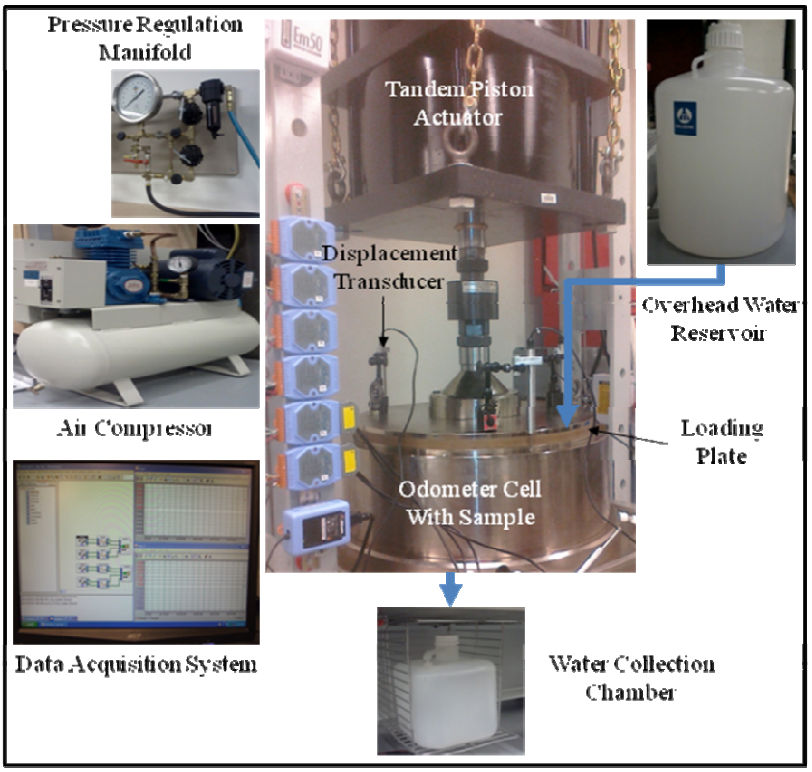

Fig. 1 Meso Scale Oedometer Test System

The initially unsaturated soil sample is flooded with water through a variable height overhead reservoir. A uniform water infiltration is achieved by providing radial and circular grooves in the loading plate. Utilizing a design similar to that of Abduljauwad and Al-Amoudi (1995) for saline soils, drainage is permitted through the bottom plate (with radial and circular grooves). The effluents are collected at regular time intervals to measure the hydraulic conductivity of the specimen during volume changes. This arrangement allows the determination of swelling potential in expansive clays and of collapse potential in erodible soils. Thereafter, the specimen is incrementally loaded to determine the consolidation properties of the soil. The vertical sample deformations are measured at three equidistant locations on the loading plate using linear variable displacement transducers.

3 Calibration and Deformability

MOTS is designed for a loading capacity of 55 tons (49885 kg) that corresponds to a stress of 1730 kPa on the sample. Likewise, the seating stress equates to about 10 kPa, which is the combined weight (275 kg) of the loading plate, alignment coupler, tandem piston, and shaft. To determine apparatus deformability, a schematic model was generated in the computer software SolidEdge ST2. This model was then imported into a finite element program, namely, AutoDesk Algor Simulation Professional 2010. Figure 2 gives the load-deformation analyses by treating the entire assembly as a single solid unit and assuming a linear stress-strain relationship for stainless steel. The maximum deformation of 2 mm was estimated at the edges of the base plate. Likewise, a solid stainless steel block was incrementally loaded in the MOTS. The deformations were around the same locations and were increased to 4 mm due to stress concentrations at the joints.

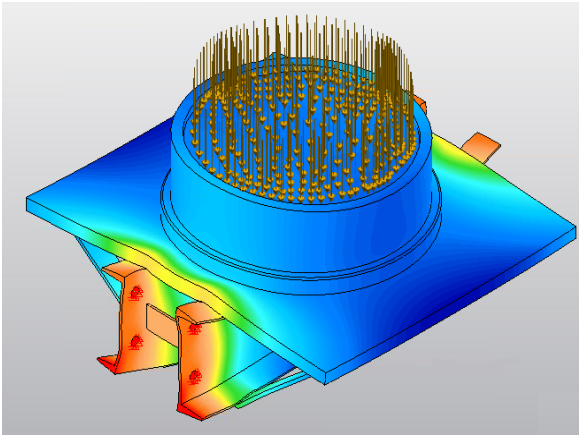

Fig. 2 Load-deformation analyses

4 Testing and Analyses

A consolidation test was conducted in the MOTS on a sandy soil and the data were compared with those from a conventional oedometer. Figure 3 gives the void ratio versus applied stress relationship for the investigated material. The compression index (C_c) in the conventional oedometer was found to 0.09. This value is higher than that typical for such soils, which ranges between 0.05 and 0.06. A lower value of 0.06 was found in the MOTS. This reduction was due to the higher wall contact area of the meso-scale sample compared to the conventional sample. The deforming soil was offered a greater frictional resistance that allowed a smaller change in void ratio under a given load. Despite some experimental error with the initial void ratio, the data clearly indicated that MOTS provides a better estimate of soil volume change.

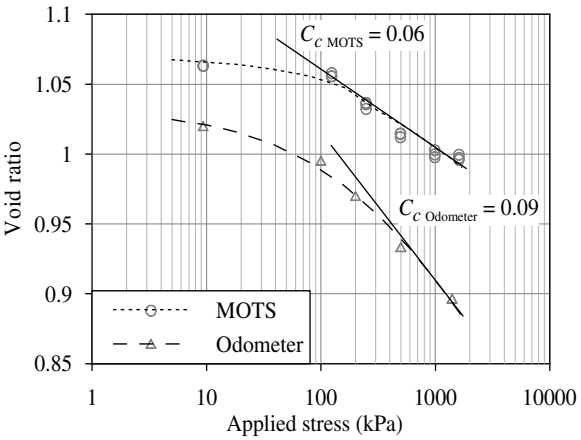

Fig. 3 Void ratio versus applied stress data

5 Modifications and Plans

Thorough instrumentation will be installed (using transducers, sensors, and tensiometers) within the samples to measure, in three dimensions, the changes in loading, deformation, soil pressure, pore pressure, temperature, water content, and matric suction under the applied loading (one-time and cyclic). To simulate seasonal climatic variations, the samples will be tested under room temperature (22 ^{o}C), summer ground temperature (30 ^{o}C), and winter ground temperature (-10 ^{o}C) using ice blocks in an outer Plexiglas tank. All of the information obtained from the tests will be digitally recorded over the entire test duration using an automated data acquisition system.

Chemical analyses on the leachates will be conducted to study the effects of soil-fluid interactions (dissolution, oxidation, hydrolysis, diffusion, and precipitation) on engineering behavior. Several types of liquids are planned to be used such

as water, brines, and miscible and immiscible contaminants. These data will help in correlating the behavior of problematic soils with complex micro-level physico-chemical phenomena at phase boundaries.

It is planned to obtain sub-samples from the meso-scale samples at various test stages for confirmatory tests to determine the following: (a) geotechnical index properties for soil classification; (b) solid composition such as mineralogy by X-Ray Diffraction (XRD) and Differential Thermal Analysis (DTA), cation exchange capacity (CEC), and elemental analyses by Inductively Coupled Plasma (ICP) and mass spectroscopy (MS) methods; (c) pore fluid composition including pH, electrical conductivity (EC), and ions concentration; and (d) morphological characteristics of the resulting fabric using Scanning Electron Microscopy (SEM).

6 Summary and Conclusions

This paper described the development of a Meso-scale Oedometer Test System. The equipment is pivotal in developing a clear understanding of the volume change behavior of problematic soils by incorporating climate impacts (fissures), environmental conditions (fluid flow), and physicochemical interactions (micro-mechanics) in geotechnical engineering. Numerical simulations and load-deformation analyses indicated that the test system can safely be loaded up to 1730 kPa: the deformability of the system was found to be 4 mm. The 100 times larger than conventional sample allows the apparatus to provide a better estimate of soil volume change, as confirmed by a consolidation test on a sandy soil.

References

Abduljauwad, S.N., Al-Amoudi, O.S.B.: Geotechnical behavior of saline sabkha soils. Geotechnique 45, 425–445 (1995), doi:10.1680/geot.1995.45.3.425

Azam, S., Abduljauwad, S.N., Al-Shayea, N.A., Al-Amoudi, O.S.B.: Effects of calcium sulfate on swelling potential of an expansive clay. Geotechnical Testing Journal 23, 389–403 (2000), doi:10.1520/GTJ11060J

Imumorin, P., Azam, S.: Effect of precipitation on geologic development of badlands in arid regions. Bulletin of Engineering Geology and the Environment 70, 223–229 (2011), doi:10.1007/s10064-010-0300-4

Ito, M., Azam, S.: Determination of swelling and shrinkage properties of undisturbed expansive soils. Geotechnical and Geological Engineering 28, 413–422 (2010), doi:10.1007/s10706-010-9301-0

Hu, Y., Hubble, D.W.: Factors contributing to the failure of asbestos cement water mains. Canadian Journal of Civil Engineering 34, 608–621 (2005), doi:10.1139/l06-162

Consolidation of Soft Clays through Radial Flow Using Hydraulically Pressurized Oedometer

Shah M.V. and Shroff A.V.

Applied Mechanics, The Maharaja Sayajirao University of Baroda, Vadodara, India
mvs2212@yahoo.co.in

Abstract. Experimental modelling of prefabricated vertical geodrains namely sand drains, sandwick, coir-jute drain and polypropylene fibre drain of different size (diameter) is carried out using modified hydraulically pressurised Oedometer through inward radial drainage to evaluate various consolidation parameters. Vertical geodrains of 'n' (ratio of sample diameter to drain diameter) values viz. 11.04, 16.93 and 21.71 are simulated in the laboratory to know efficacy of drains under long term static loadings. Object of the present investigation is to modify existing hydraulically pressurized Oedometer for the measurement of pore water pressure at various radial points to obtain experimental isochrones that is sequence of consolidation and at various ratio of radius of drain to radius of influence for corresponding concentric planar location for given height of sample at that time with reference to various factors like type of drain material, various shapes of the drain with minimum and maximum drainage path,'n'value, various volumetric water index, various horizontal permeability to vertical permeability ratio and stress history influencing consolidation characteristics of Kaolinite clay under different loadings. The experimental results were compared with theoretical solutions developed by the authors. The results show a fair agreement between measured and predicted values for all drains of all 'n' values. It is concluded that pore water pressure dissipation process at various time interval can be better graphed and projected by hydraulically pressurised Oedometer.

1 Introduction and Objective of Present Research

The aim of using soft clay like kaolin was to simulate model of large deposits of marine clays encountered along the coastal plains of country like India. The common feature of marine clay is the basic mineral composition having Base Exchange capacity of 37-40 milli equivalents per 100 gms.The properties of marine clays are very much influenced by the salt content and the amount of skeleton of micro structure present. The leaching process creates a metastable structure of marine clay. The rate of consolidation purely depends on the expulsion of pore water. According to Barden, for primarily consolidation the total

L. Laloui and A. Ferrari (Eds.): Multiphysical Testing of Soils and Shales, SSGG, pp. 273–279.
springerlink.com

stress is shared by pressure in the free pore water, plastic resistance in the highly viscous adsorbed double layer, by virtually solid to solid contacts between clay particles. Out of many factors which affect the consolidation process the nature of pore water plays a vital role which is studied in detail by its dissipation characteristics. The experimental model was conceived comprising of central prefabricated vertical geodrains on a cylindrical sample of soft clay. The nature of isochrones at every applied stress was studied in laboratory by modeling various vertical geodrains indigenously developed in the laboratory namely coir-jute drain,sandwick drain and polypropylene fiber drain of different 'n' values(ratio of drain dia to soil sample dia) viz.11.04,16.93 and 21.71 to accelerate the dissipation process. It is interesting to study the rate of development & dissipation nature of pore water using coir fibers, jute fibers, sand, polypropylene fibers as a filler material for better economy. A series of consolidation tests were conducted in 254mm & 152mm diameter hydraulically pressurized oedometer which was specially modified to have continuous measurement of pore water pressure such that complete thickness of soil sample gets covered and simultaneously displacement measurements were also recorded using both electronic and conventional Bishop system. Particularly accelerating rate of soft soil improvement by vertical drains needs technological development in terms of material, installation technique, shape and size of geodrains,easy applicable theoretical solutions and well defined inter-relation between drain and soil for complete dissipation of excess pore water pressure for any loadings. This paper explores the complete experimental model of consolidation through radial flow using large size hydraulically pressurized Oedometer using prefabricated vertical geodrains indigenously developed at the geotechnical engineering laboratory of The Maharaja Sayajirao University of Baroda, India. Paper also discusses the influence of some of the physical and nano mechanics parameters and their vital role in consolidation process using scanning electron microscopy (SEM). Some of the objectives covered in this paper.

- To expedite the in-situ settlement and dissipation of pore water pressures of reinforced soft soil mass under preloading by radial drainage.
- Comparison of average degree of consolidation (U_r) from both settlement and pore pressure measurements for optimum'n' value for various drain models with author's theoretical solution.
- Influence of viscosity of fluid (turbid clay water), clay liquid to gel paste transformation under initial loads, inter capillary capacity of drain material and inter pore discharge capacity of drain cover, velocity of water particle at near soil-drain interface and at greater radius of influence, stress relaxation phenomena due to pore water dissipation and finally load transfer rate mechanism to soil skeleton by keeping same surface area on the consolidation process.
- Comparison of various natural and synthetic drain materials.
- Comparison of pre and post shear strength achieved at the end of consolidation by various drains.

2 Theories of Consolidation

Shroff & Shah (2006,2010) proposed a more generous solution to estimate degree of consolidation considering factors like non-homogeneity of soil, drain material(mechanical & hydraulic properties),drain size and shape, drainage path ratio, ratio of horizontal to vertical permeability and stress history. The above factors are incorporated into a single factor called lumped parameter λ. Considering the ideal circular soil cylinder with central circular drain the following solution is obtained. The assumption of regarding λ as a constant is purely from the considerations of mathematical simplicity but it may prove as well as to be so for most soils.

$$Ur = \frac{e-e_o}{e_1-e_o}$$

$$= \exp\left\{\left(\lambda/2\right)\right\}\left[\frac{Sinh\lambda/2\, R}{Sinh\lambda/2} + 2\pi\sum_{n=1}^{\infty}\frac{(-1)^n .n\, Sin(n\pi R)}{\lambda^2/4+n^2\pi^2}\exp-\left\{\left(\lambda^2/4+n^2\pi^2\right)T\right\}\right] +$$

$$\exp\left\{-\left(\lambda/2\right)\right\}\left[\frac{Sinh\lambda/2\,(1-R)}{Sinh\left(\lambda/2\right)} - 2\pi\sum_{n=1}^{\infty}\frac{n\, Sin(n\pi R)}{\lambda^2/4+n^2\pi^2}\exp\left\{-\left(\lambda^2/4+n^2\pi^2\right)\right\}T\right]$$

Isochrones for various positive and negative values of parameter λ are obtained from which average degree of consolidation is computed using Simpson's rule. Series of curves of average degree of consolidation (U_r) for different values of λ are shown in Fig.1

Table 1 Values of U_R for range of λ

Time factor (Tr)	λ =0.7, U_r(%)	λ =0.5, U_r(%)	λ =0.3, U_r(%)	λ =0.1, U_r(%)
0.02	23.65	25.85	28.86	32.26
0.06	44.89	47.09	49.90	52.91
0.10	59.32	60.92	63.93	67.54
0.14	68.94	70.94	73.95	77.35

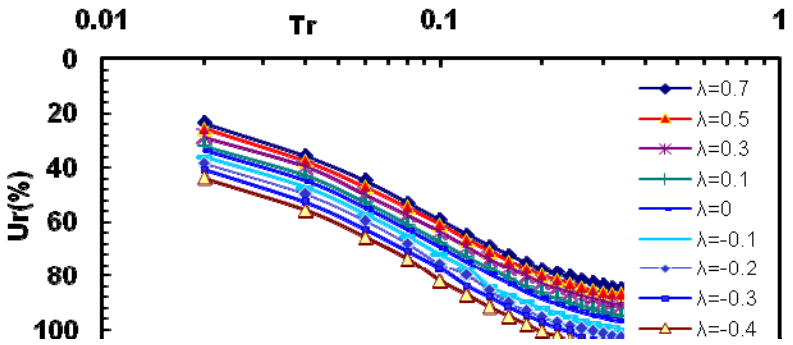

Fig. 1 Average degree of consolidation vs. Time factor for various λ values

3 Experimental Simulations

Hydraulically Pressurized Oedometer: The large size diameter of hydraulic pressurized Oedometer of 254mm were used for testing the remolded samples (see Fig.2).The vertical settlement is measured at the centre of the sample and pore water pressures are measured at the three radial points located at 120 degree each with r/r_e distances as r/4, r/2 and 3r/4 respectively using both conventional dial gauge and bishop system along with displacement transducers & pore pressure transducers connected to data logger system interfaced with PC. For all the tests diameter to height ratio of soil sample was kept constant.

Material Properties, Clay Sample Preparation, Installation of Vertical Drain and Testing Program: Sample is made from soft kaolin clay with G = 2.592, liquid limit (L_L) = 67%, plasticity index (P_I) = 34, belonging to CH (clay of high plasticity) group according to I.S.Classification system. To ensure full maturation of the sample the clay was mixed to form slurry with twice the liquid limit using de-aired distilled water.

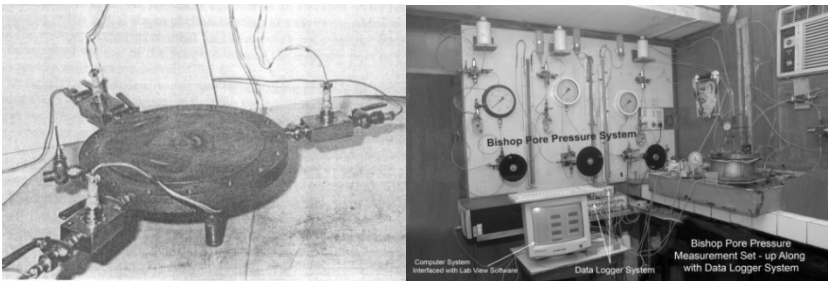

Fig. 2 Arrangement of porous stone at three radial points 120^0 each and complete view of Oedometer set-up with connections

Four types of vertical geodrains were fabricated indigenously viz. sand drain,SD (sand as filler material using mandrel), sandwick,SW (woven polypropylene sheet with sand as filler material), coir-jute drain,CJ (coir-jute fibres of maximum 120mm length placed radially wrapped by filter paper) & polypropylene drain,PF (polypropylene fibre as filler wrapped by filter paper thus prepared in accordance with'n' value equal to 11.04, 16.93 and 21.71 is inserted (placed) in the predrilled hole, formed by thin mandrel at centre of the soil sample in the Oedometer. Shear strength is measured using laboratory vane shear apparatus at the end of consolidation test. Excess pore water pressure of 10kPa is applied by help of screw pump and hydraulic system. Pressures are applied in the range of 20kPa- 320kPa with $\Delta p/p = 1.0$.Each load increment is kept constant for about 120-144 hrs and secondary compression is also recorded.

4 Results and Discussions

From the measurements recorded it was concluded that 'n' equal to 11.04 is the most optimum 'n' value and coir-jute(CJ) drain is the most efficient drain material dissipating fastest excess pore water pressure and thus accelerating greater rate of settlement of clay mass. Faster rate of dissipation was observed in case of CJ in compare to SW, PF, SD for 80kPa, 160kPa & 320kPa pressure while for initial pressures faster rate of dissipation was observed in case of SW for n=11.04. Isochrones for pore pressure at the radial distances for different degree of consolidation for a particular pressure fits satisfactorily with the author's theoretical solution as well as by Barron's equal strain solution. The degree of consolidation obtained both from settlement readings and pore pressure measurements matches very well with theoretical values.

Comparing authors theoretical solution to obtained degree of consolidation with experimental results suggest that λ=-0.2 fits for CJ of n=11.04, λ=-0.1 fits for SW, λ=-0.08 fits for PF, λ=-0.05 fits for of SD for same 'n' value and for same pressure. At every stage of consolidation on each pressure it is observed that though there is uniform stress distribution at every finite distance in saturated clay sample the dissipation of pore water pressure is not passing though equal gradient developed as a whole by each saturated particle though an equal surface area of drain is available. At this junction author proposes three reasons attributing some hindrance in consolidation of soil mass, they are (i) fluid viscosity of turbid clay water creating friction between upper surface of clay particle and water particle itself during its flow from higher pressure gradient to lower. (ii) liquid clay (mineral grain viscosity) transformation to gel and thereafter to semi-solid state under different pressures does not follow exponential nature because mineral grain viscosity decreases as pressure increases and pore water decreases, creating hindrance for pore water to follow steady state condition. (iii) capillary action of drain and inter-capillary action of drain-clay surface decreases at low stress levels but after attaining a certain equilibrium it bounces back and starts increasing at higher stress levels, creating hindrance for pore water particle and inter-water particle force in terms of adhesion/tensile force. It is also observed that creation of pore channels during pore pressure development does not finally contribute during

dissipation stage though pressure is constant, author gives two reasons for this, they are (i) orientation of particle is random at low stresses and also edge to edge and face to face contacts are not well geometrized and due to this same water particle may travel same distance many times and water particle near to drain may escape due to flatter orientation of solid particle. (ii) strain accommodation and particle displacement to a more equilibrium stage takes place only when pore reduction is accompanied by solid rearrangement of particles, but sometimes it is found that velocity of water particle is fast but inter displacement of solid particle is slow because of various physic-chemical forces present on clay surface. Simultaneously it is also seen that displacement of one water particle which is at far distance from the drain pushes the water particle ahead to it but as pore channel gets narrow under higher loads, decrement in dissipation is not observed though rate of compressibility may have reduce to nil. The distinct behavior with respect to the rate of consolidation at any stress is attributed to the low tortousity of horizontal flow in the flocculated soil structure of Kaolinitic clay water system.

Scanning electron microscopy (SEM) results reflects that particle orientation was more towards drain face (Fig.3) and least pores spaces were observed at the centre of the clay-drain specimen at end of consolidation.

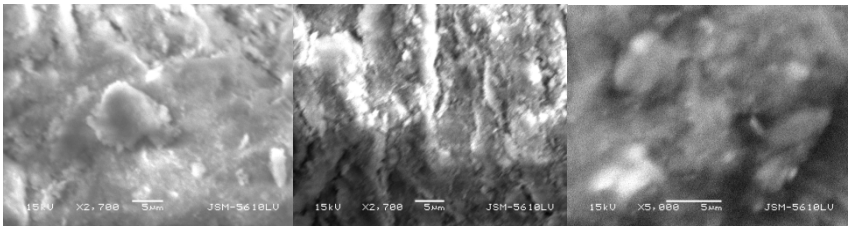

Fig. 3 SEM of CJ- clay sample interface at the end of 320kPa at magnification of X2700 and X5000(at the bottom of sample thickness - near clay-drain face)

SEM analysis further pin points the necessity of role of mechanics in load transfer to soil skeleton considering drain material stiffness along with degree of saturation of drain and soil mass at stages of loading due to continuous suction capacity of clay particle to maintain surface charges and simultaneous effect of temperature in terms of evaporation.

From the above discussion it can be noted that determination of degree of consolidation using various drains through hydraulically pressurized Oedometer, dissipation of pore water considering clay-water as nano particles and treating them as discrete units for further analysis. Generally engineers are interested in a drain material efficient in accelerating rate of settlement of soft mass but if we consider drain as part of elastic material and pour out the effect of physical forces on consolidation through radial flow a better theoretical approach can be put up.

References

Barron, R.: Consolidation of fine grained soils by drain wells. Trans. A.S.C.E. 113, 718–754 (1948)

Hansbo, S.: Consolidation of Fine-grained soils by prefabricated drains. In: Proc. of 10th Int. Conf. on Soil Mechanics and Foundations Engineering, Stockholm, vol. 3, pp. 677–682 (1981)

Rowe, P.W., Barden, L.: A new consolidation cell. Geotechnique 16(2), 162 (1966)

Bishop, A.W.: The influence of an undrained change in stress on the pore pressure in media of low compressibility. Journal of Geotechnique 26(2), 370–375 (1973)

Shah, M.V., Shroff, A.V.: Effect of ratio of influence zone and type of vertical drain on consolidation of soft clay due to radial flow. In: Proc. Fourth International Conference on Soft- Soil Engineering, Canadian Geotechnical Society, University of Alberta, Canada, vol. I, pp. 765–773 (2006)

Shah, M.V., Shroff, A.V.: Experimental Study On Performance Of Sand Drain On Kaolinite With Varying Drain Diameter. In: Proc. of XIII-Danube-European Conf. on Geotechnical Engineering, Danube, vol. I, pp. 349–354 (2006)

Shah, M.V., Shroff, A.V.: Settlement performance of soft clays using prefabricated vertical geodrains with varying diameter. In: Proc. Ninth International Conference on Geosynthetics, International Geosynthetics Society & International Society of Soil Mechanics and Geotechnical Engineering, Brazil, vol. I (2010)

Shah, M.V., Shroff, A.V.: Modeling of Vertical geodrains using modified hydraulically pressurized oedometer. In: Proc. Sixth International congress on Environmental Geotechnics, Indian Geotechnical Society & International Society of Soil Mechanics and Geotechnical Engineering, New Delhi, vol. I (2010)

Shah, M.V., Shroff, A.V.: Non-Linear Theory of Consolidation through Radial Drainage for Soft Soils using Vertical Drains. In: Proc. of XIVth Danube-European Conf. on Geotechnical Engg., Slovakia, vol. I (2010)

Experimental Analyses of Shales Behaviour

Nanochemomechanics of Shale: Coupled WDS-Indentation Analysis

Amer Deirieh[1], J. Alberto Ortega[2], and Franz-Josef Ulm[1]

[1] Department of Civil and Environmental Engineering, MIT, Cambridge, MA 02139, USA
[2] Schlumberger Technology Center, Sugar Land, TX 77478, USA
adirieh@mit.edu, jortega9@slb.com, ulm@mit.edu

Abstract. In this study, a novel methodology is implemented to access the in situ chemomechanics of shale at micrometer length scales. To accommodate the highly heterogeneous microstructure of shale, massive grids of coupled wave dispersive spectroscopy (WDS) and instrumented indentation experiments were performed over representative material surfaces. The extensive datasets of compositional and mechanical properties were analyzed using multi-variate clustering statistics to determine the attributes of active phases present in shale at micro-scales. Our chemomechanical analysis confirmed that the porous clay mechanical phase inferred by statistical indentation corresponds to the clay mineral phase defined strictly on chemical grounds. The statistical indentation and WDS techniques represent a first approach to characterize the chemomechanics of shale at a consistent scale below the macroscopic level. The results represent valuable information for multi-scale modeling of this material, especially for the in situ properties of the porous clay fabric that have been derived thus far only through indirect methods.

1 Introduction

To motivate our experimental investigation in this study, we recall the database compiled by Bobko and Ulm [1] to establish connections between measured nanomechanics and composition of several shale materials. This database covers a broad spectrum of compositional properties for shales. With the focus on elasticity, Figure 1 displays the means and standard deviations of the two measured indentation moduli associated with the porous clay phases of each shale material. The indentation M_1 corresponds to the experiment performed parallel to the natural bedding planes observed in the bulk shale sample, whereas M_3 corresponds to the normal to bedding direction (which is the direction for our experiment reported in this study). These values were obtained from indentation testing based on mechanical understanding, i.e., with no link to chemistry. The indentation data is arranged as a function of the clay packing density η, which neatly synthesizes the composition and porosity information into one parameter (or alternatively, the

L. Laloui and A. Ferrari (Eds.): Multiphysical Testing of Soils and Shales, SSGG, pp. 283–288.
springerlink.com

nanoporosity ϕ=1-η). Each solid data point in Figure 1 corresponds to the mean clay packing density estimated from two different assessments of porosity (directly measured through MIP or inferred from density values) and mean indentation modulus (M_1 or M_3) obtained from indentation experiments. The anisotropic indentation moduli and clay packing density display a remarkable global trend where increasing modulus values correspond to increasing packing densities.

The analysis of the M_i-η relationship and the overall compositional characteristics of each shale material in Figure 1 establishes that the clay packing density controls the mechanics of the porous clay in shale at the microscales. Furthermore, the poor correlations between indentation response and clay mineralogy highlight the secondary role of the latter. The indentation moduli of clay minerals, which were used to derive this model, were obtained from indentation testing with no link to chemistry. In this study, we complement this investigation by coupling the indentation and WDS tests to relate mechanics to chemistry at the micrometer scale. This, in turn, will provide us with means to decide the mechanical properties of shale's constituents at the micrometer scale without having to rely only on mechanical arguments and bulk mineralogy testing.

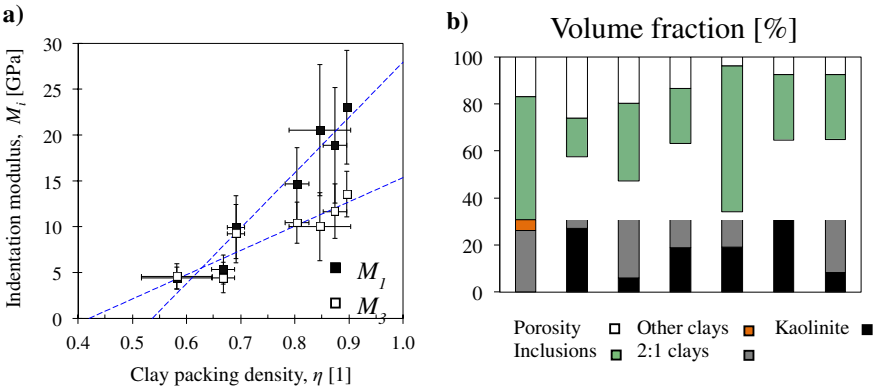

Fig. 1 a) Porous clay stiffness and clay packing density values for shale materials inferred from cluster modeling of grid indentation data. Indentation experiments were performed in the parallel-to-bedding (M_1) and normal-to-bedding (M_3) directions [1]. b) Compositions of the shale materials presented in a and arranged from left to right.

2 Materials and Methods

This study was conducted on one the shale materials presented in Figure 1 as part of the comprehensive study conducted in [1], in particular sample S7. Although information about the geologic origin of the cored samples was not disclosed, these shale materials belong to a comprehensive database of samples from rock formations with little organic content that serve as geological caps to hydrocarbon reservoirs.

This experimental investigation of shale is grounded on the ability to access its in situ chemistry and mechanics at small length scales. Well-established techniques such as wave dispersive spectroscopy (WDS) and state-of-the-art technologies such as instrumented indentation precisely focus on the direct measurements of composition and load-deformation behaviors, respectively, with tunable resolutions reaching micrometer and sub-micrometer dimensions.

To extend the applications of instrumented indentation and WDS to heterogeneous materials, Ulm and coworkers proposed the so-called grid indentation and WDS techniques, which are based on conducting large arrays of individual experiments on the material surface (nanomechanics applications [1] [2], chemistry applications [3]). Provided adequate choices of experimental parameters, each experiment could be regarded as statistically independent, allowing the application of cluster statistics to interpret the indentation and WDS results. Cluster modeling provides a rational means for determining the most likely number of components or clusters associated with the multi-variate data via likelihood criteria. These components can then be given physical meaning based on our mechanical and chemical understanding of shale materials. Finally, the chemo-mechanical investigation in this study involves performing both indentation and WDS tests on the same material surface which will provide us with means to relate mechanics to chemistry at fundamental length scales.

3 Results and Discussion

In this section we present the results of a coupled experiment performed on Sample S7. First, the results from cluster modeling of grid indentation and WDS experiments are discussed separately to determine the types of components that are identified by each methodology. Conclusions then are drawn from the data correlations of the two tests when coupled together.

The results of the statistical indentation assessment of shale S7 is presented in Figure 2b. Via the BIC criterion, four mechanical components were identified from the clustering of indentation modulus and hardness measurements as shown in Figure 2a. The term mechanical component is understood as each of the clusters recognized by the multi-variate statistical approach based on the underlying elasticity and hardness characteristics. On-average modulus and hardness properties display increasing values, ranging between those of cluster 1 (with the lowest values) and cluster 4 (with the highest values). In general, three main types of mechanically active components were established. The first type corresponds consistently to the phase with large M, H values, whose response is expected due to the presence of quartz and feldspar inclusions. In Figure 2b, the so-called inclusion (INC) component type (phase 4) exhibits on-average indentation modulus and hardness values of approximately M ≈140 GPa, H ≈16 GPa. These observations relate in first order to the properties of quartz and feldspar reported elsewhere [4] [5]. The second type of mechanical response corresponds to the components with lower M, H values compared to inclusions and with low volume fractions (phases 2 and 3). Finally, the third type of mechanical component corresponds to the porous clay (PC) phase, identified by the notoriously large volume fraction as

expected from mineralogy tests. The porous clay phase type consistently exhibits the lowest M, H values compared to the inclusion and composite components. This interpretation of cluster modeling of grid indentation experiments is pursued based solely on mechanics arguments with no link to chemistry (see [1]).

The chemical assessment of shale using the statistical WDS technique is detailed hereafter. This grid experiment was performed over the same location used for the indentation experiment discussed above. The implementation of cluster modeling yielded the results that are graphically displayed in Figure 2a. The application of the BIC criterion determined that ten clusters describe the multivariate WDS data. Two types of clusters based on their form are recognized in the projection space shown in Figure 2a: poles and ligands. Pole-type clusters are interpreted as quasi-homogeneous phases that match a particular chemistry known to be present in shale (e.g., components 1 through 8). Components 7 and 8 are located in the region of quartz, with silicon content close to 33.331% [atomic ratio]. Components 1 through 6 are located in the elemental space expected for clay minerals. The chemical data linked to these phases exhibits pronounced spreads in comparison with the quartz pole. This could be explained by the characteristic size of clay minerals being below the scale of the WDS experiment, which hints towards a measurement of on-average composition of the clay minerals contained within the excited microvolume. The second form of clusters determined for this experiment is ligands. A ligand is defined as a cluster associated with the mixture between two chemical phases. These clusters can be identified visually as components that span between poles or known mineral sites in the elemental variable space for shale. The inspection of Figure 2a reveals the presence of two ligands: cluster 9 linking quartz and clay components, and cluster 10 linking the feldspar site and clay component.

Finally, the results of the two tests are brought together to relate mechanics to chemistry at the scale of measurements. The compilations of the WDS and indentation results discussed above are displayed spatially over the actual grids of measurements in Figures 2c and 2d. The chemical components identified through cluster modeling provide remarkable descriptions of the local chemistries in the material surfaces. The sizable grain of quartz (Figure 2c) is well captured through clusters 7 and 8, and the clay matrix and small feldspar grains associated with clusters 1 through 6 and 10, respectively, are also clearly identified. Similarly, the results from cluster modeling of indentation data are also displayed in Figure 2d, showing the spatial arrangements of the grid of indentations. This spatial representation captures the large quartz grains within this shale surface. These results properly establish the mechanical composite components found in grid indentations on shale as tests performed on conglomerates of clay particles near stiffer (harder) inclusions of quartz or feldspar. In contrast, measurements away from boundaries with quartz and feldspar grains provide consistent mechanical measurements that characterize the porous clay phase of shale.

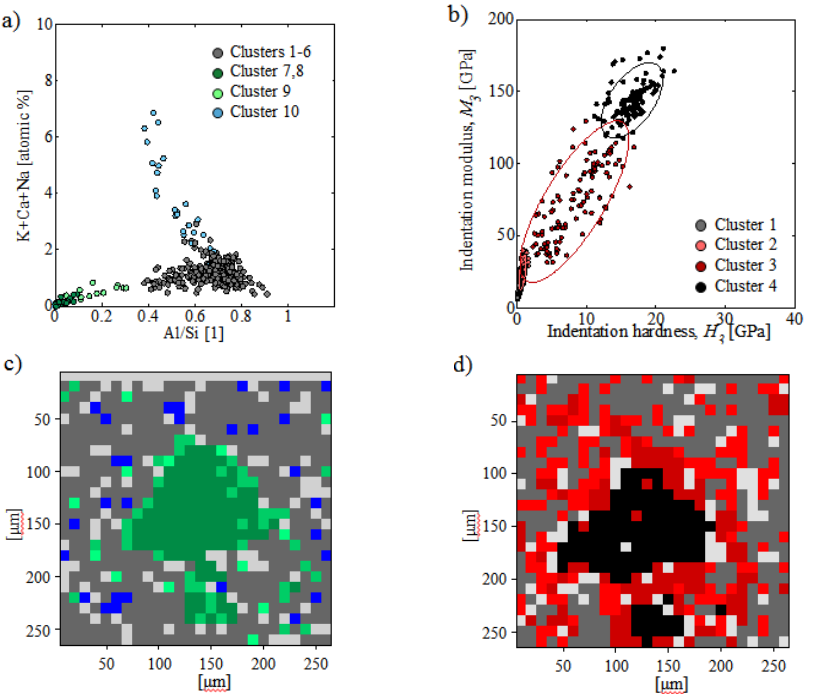

Fig. 2 Cluster modeling of a) grid WDS and b) grid indentation data for the shale material tested in this study. The interpretation of statistical clustering of WDS data recognizes four types of chemical constituents associated with clay (clusters 1-6), quartz (clusters 7,8), quartz-clay mixture (clusters 9), feldspar-clay mixture (cluster 10). The interpretation of statistical clustering of indentation data recognizes the characteristic three types of mechanical responses: porous clay (cluster 1), composites (cluster 2,3), and inclusion (cluster 4). Figures c) and d) display the clustering results of the grid WDS and indentation experiments in their spatial distributions over the probed surface.

4 Conclusions

The coupled chemomechanical analysis of grid indentation and WDS experiments confirmed that the porous clay mechanical phase in shale inferred by the statistical indentation method corresponds to the clay mineral phase defined strictly on chemical grounds. The porous clay characteristic stiffness and hardness behaviors are realized spatially in regions removed from silt inclusions of quartz and feldspar. The higher mechanical properties of the silt inclusions alter the mechanical behavior of the clay matrix near the grain boundaries. This composite behavior sensed by indentation is captured by mechanical components inferred from cluster modeling which display modulus and hardness properties between those of the two bounding solids.

Acknowledgments. We are grateful for the financial support of this study by the MIT-OU GeoGenome Industry Consortium (G2IC) directed by Prof. Younane Abousleiman of the integrated Poromechanics Institute (iPMI) of the University of Oklahoma at Norman, which facilitated the material characterization data (XRD and porosimetry). We are also thankful to Dr. Nilanjan Chatterjee at the Electron Microprobe Facility, Department of Earth, Atmospheric, and Planetary Sciences, MIT for his guidance in performing the WDS experiments.

References

Bobko, C., Ulm, F.J.: The nano-mechanical morphology of shale. Mechanics of Materials 40(4-5), 318–337 (2008)

Constantinides, G., Ravi Chandran, K.S., Ulm, F.J., Van Vliet, K.J.: Grid indentation analysis of composite microstructure and mechanics: principles and validation. Materials Science and Engineering: A 430(1-2), 189–202 (2006)

Deirieh, A., Ortega, J.A., Ulm, F.-J.: Microscale assessment of shale mineralogy: a statistical WDS approach (2012)

Heyliger, P., Ledbetter, H., Kim, S.: Elastic constants of natural quartz. The Journal of the Acoustical Society of America 114, 644 (2003)

Whitney, D.L., Broz, M., Cook, R.F.: Hardness, toughness, and modulus of some com-mon metamorphic minerals. American Mineralogist 92(2-3), 281 (2007)

Shale Swelling/Shrinkage, Suction and Osmosis

Russell T. Ewy

Chevron Energy Technology Co
RussEwy@chevron.com

Abstract. Samples were cut from nine different preserved shales, representing in situ states from 11% to 29% porosity and native water contents from 5% to 15%. In an air environment, each shale shows well-defined relationships among suction, water content, bulk volume and saturation. The native state for some shales corresponds to RH<0.8, even though the samples are fully-saturated. The shales will always shrink if placed into RH lower than native state. In contrast, when placed in direct contact with brines, the shales nearly always swell even when the brine water activity is less than the shale activity. The shales are confirmed to be unable to exclude ions; however, the swelling is correlated with the amount of water gain. Brine contact results in water gain that is difficult to explain through osmotic theory. However, some osmotic-type effects are observed.

1 Scope of Study

In order to better understand shale swelling/shrinkage and its relation to suction, saturation and osmotic forces, a series of laboratory tests was performed on samples obtained from several different preserved shale cores. These shales have the properties listed in Table 1. All the shales contain 60% - 75% clay.

Table 1 Key petrophysical properties of each shale

Shale	Sat. Bulk Dens. (s.g.)	Porosity (%)	Native Activity	CEC (meq/100g)
A	2.17	29	0.96	33
B	2.19	28	0.96	25
C	2.21	26	0.96	21
D	2.32	22	0.92+	25
E	2.34	21	0.88	31
F	2.38	20	0.90	24
G	2.42	18	0.80	32
H	2.54	13	~0.75	35
I	2.51	11.5	0.85 – 0.92	23

L. Laloui and A. Ferrari (Eds.): Multiphysical Testing of Soils and Shales, SSGG, pp. 289–294.
springerlink.com

In one series of tests, the shale samples were subjected to different air humidity environments (varying suction), and changes in water content and sample volume were recorded. In another series of tests, the samples were directly exposed to different brines, which resulted in volume change.

2 Influence of Suction (RH) on Swelling/Shrinkage, Water Content and Saturation

In a vacuum desiccator, a shale sample will come to equilibrium with the suction pressure imposed by the relative humidity (RH). A crossplot of water content (WC) vs. RH is shown in Fig. 1 for the nine different shales. Each data point is a separate sample, which was equilibrated to that particular RH value. In spite of the data scatter, it is seen that a higher RH results in a higher WC. Approximate trend lines have been drawn for a few of the shales. The higher porosity shales undergo much larger changes in WC than the lower porosity shales.

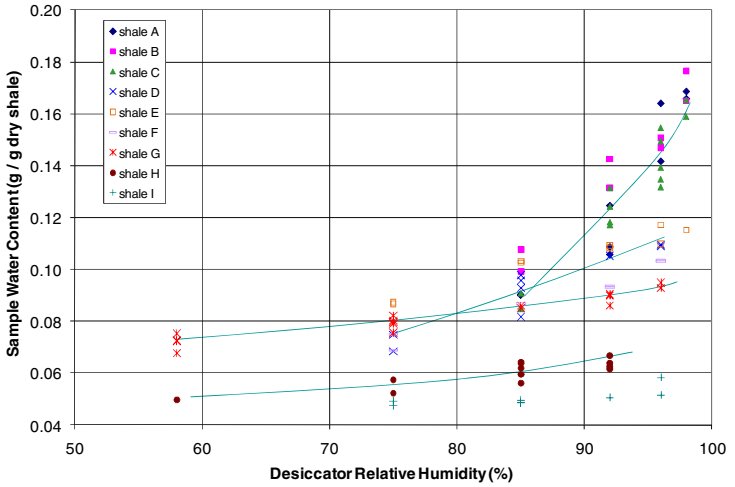

Fig. 1 Equilibrium water content vs. relative humidity. Each point is a separate sample.

Each shale also has a 'native activity' value for which there is no change in WC relative to its initial state. These native activity values are listed in Table 1, and they vary from ~0.75 to ~0.96. If placed into a RH environment of higher activity, the shale will gain water; if placed into a lower RH, it will lose water. In general, the lower porosity shales have lower native activity values.

The native WC for each shale can be determined from Fig. 1 by reading off the value of WC that corresponds to the native activity value for each shale. Native WC values range from ~5% to ~15%. These are fully-saturated states. The existence of low native activity values, with full saturation, suggests that the clays themselves may be contributing to a lowering of the free energy of the pore water.

Fig. 2 shows a crossplot of sample volume (per gram of dry shale) against the sample activity, or relative humidity, at the time of volume measurement. It is seen in this figure that a higher RH corresponds to a larger sample volume.

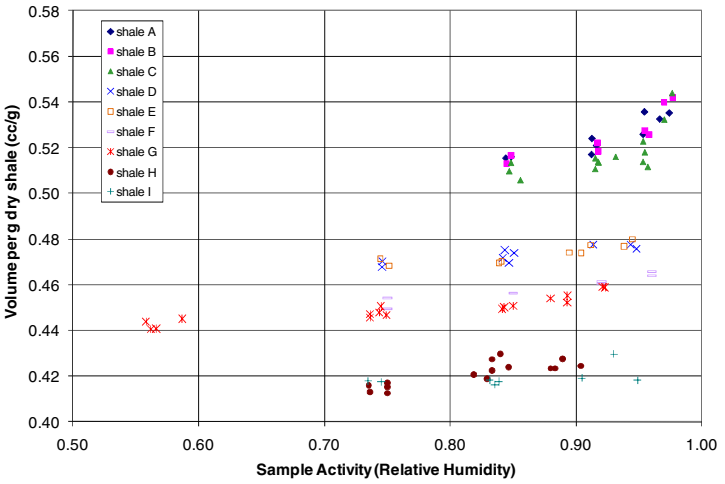

Fig. 2 Sample volume (normalized to dry weight) vs. sample activity.

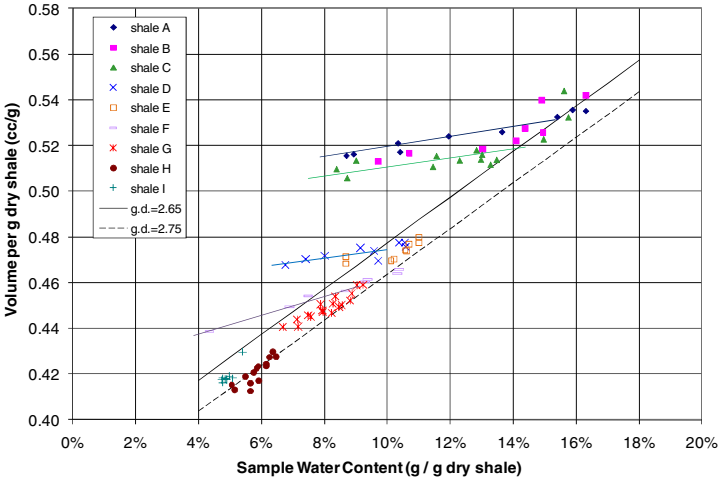

Fig. 3 Sample volume (normalized to dry weight) vs. sample water content. Black lines with unit slope represent fully-saturated conditions (grain densities of 2.65 and 2.75 g/cc)

Sample volume and WC measurements can be combined, as shown in Fig. 3. It is seen in this figure that, above a certain WC value for each shale, the addition or removal of 1 gram of water corresponds to a volume change of 1 cc. This means

that the shale is fully-saturated at all water contents above that critical value. This is confirmed by the theoretical lines of full saturation in the plot.

Below the critical WC value for each shale, the slope of volume (per g) vs. WC is less than 1. In this region, removal of water results in air entering the shale, and the shale is no longer fully-saturated. Even though the shales are not fully-saturated in this region, they still shrink and swell in response to WC changes. Slopes in this region are typically 0.2 to 0.4. Note that the low-porosity shales resist desaturation and remain saturated even at RH as low as 0.75.

3 Swelling/Shrinkage upon Direct Brine Exposure

Swelling/shrinkage due to direct brine exposure, with zero confining stress, was also measured on these shales. Tests were performed using four different brines. Their concentrations were selected to create designated water activity values. The brines used were KCl (0.9 activity), NaCl (0.9 and 0.8), and $CaCl_2$ (0.8).

Fig. 4 compiles the measured swelling for all of the shales, using all four brines. The water activity of each brine is listed along with the salt. Alongside each shale letter code is listed the RH value to which the samples were equilibrated prior to testing. These RH values were set equal to or higher than the shale native activity, in order to ensure full saturation and reduce capillary swelling.

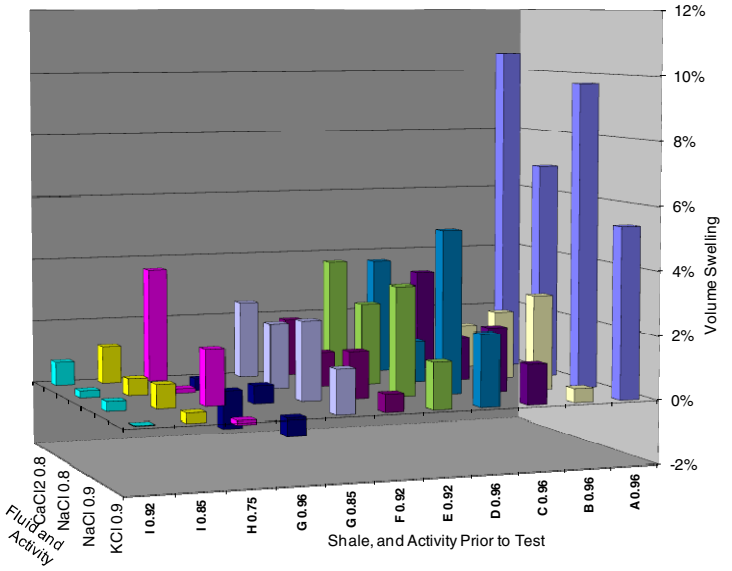

Fig. 4 Swelling (volume change) for shales exposed directly to four different brines.

Using the volume strain, we can plot the beginning and final volume for each sample. This is shown in Fig. 5, vs. sample RH. Each sample set consists of five data points. The circle is the starting state for the set of four samples. The other

data point shapes show the final state. The final activity of each sample is the post-swelling-test measured value, or if the measurement was not performed then the fluid activity is used. This 'sample activity' or 'shale activity' is a measure of the escaping tendency of the H_2O within the shale pore fluid, post-test.

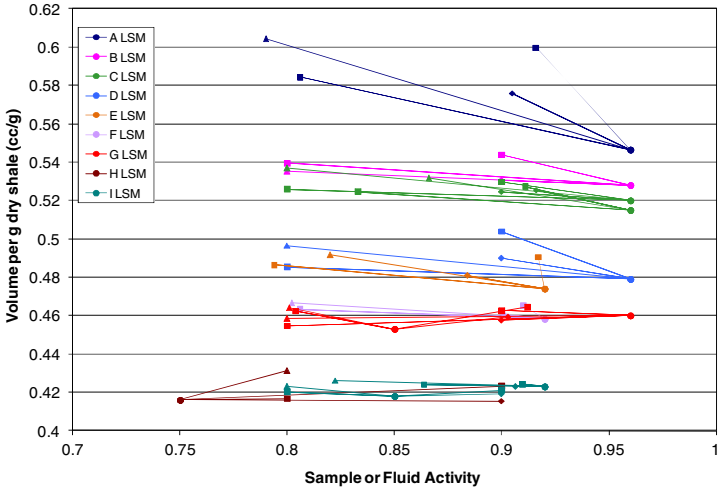

Fig. 5 Beginning (circles) and ending (other symbols) sample volume vs. shale or fluid activity. Squares are NaCl tests, diamonds are KCl tests, and triangles are $CaCl_2$ tests.

There are many observations from these figures. First, it is seen that the results are generally in contrast to the expectations from osmotic theory. Swelling occurs even when the water activity of the brine is less than the shale activity. A lower activity brine should pull water from the shale, resulting in shrinkage.

Shrinkage is observed for a few cases, however. One case is shale G equilibrated to 0.96 RH, which likely 'pre-swelled' this shale. Another case is shale H exposed to KCl brine. In this case the K ion likely exchanged for the Na/Ca ions on the smectite clays, and decreased the average spacing between clay layers.

The second observation relates to the effectiveness of the different salts in reducing swelling. Comparing brines of the same activity, we can conclude that potassium is more effective than sodium at preventing shale swelling, and sodium is more effective than calcium at preventing swelling.

The third observation is that there is at least some influence of osmotic forces in these tests. Swelling with 0.8 activity NaCl is always less than swelling with 0.9 activity NaCl. Lower water activity results in less water moving into the shale and, hence, less swelling. For shales G and I, the samples equilibrated to a higher activity value have less swelling. This too can be explained as an osmotic effect.

The fact that these shales swell even when their activity goes down (Fig. 5) is in direct contrast to the behavior observed when placing shale samples in desiccators of different RH (compare Figs 2 and 5). Immersion in brine causes the

samples to depart from the volume vs. activity relationships observed in Fig. 2. The only exceptions to this behavior are the highly-compacted (low volume) shales.

A small amount of swelling may be due to the release of capillary tension. However, calculations show that this should result in only 0.2% to 0.8% volume swelling. In general this is far less than the actual measured swelling.

Another possible explanation is that the ions themselves are causing the swelling. When a shale is directly exposed to a brine, not only can water move into or out of the shale (as in a desiccator) but cations and anions are also free to diffuse. This is because shales typically have a low osmotic membrane efficiency; they are usually unable to exclude the ions.

However, it does not appear to be the ions that cause the swelling upon brine immersion. The shales are adsorbing much more water than they would if put into a desiccator of the same activity as the brine. For a subset of the samples, careful measurements were performed of the weight gain due to water and the weight gain due to ions. The volume swelling was compared to the water gain, and a strong correlation was found between the water gain and the volume increase. Significant changes in total ion content also confirmed leaky membrane behavior.

4 Conclusions

Preserved shales exposed directly to brines swelled mainly because they adsorbed water. They adsorbed water even though in many cases they were exposed to brines of lower water activity than the starting (native-state) shale activity. The brine cation (Na, K, Ca) indirectly influences swelling by affecting the amount of water adsorption, and the water activity of the brine also has some influence. In air environments of controlled relative humidity each shale exhibits well-defined relationships among suction, bulk volume, water content, and saturation. Shales in natural high-compaction states can remain saturated even under low relative humidity (high suction).

Acknowledgements. The brine-exposure tests were performed by Keith Morton, Rick Chea and Pat Wilder. Jaime Mercado, Mark Shalz and Craig Bovberg assisted with shale sample cutting and preparation, and desiccators. Shale mineralogy and CEC measurements were performed/coordinated by Doug McCarty. Paul Hagin provided many helpful discussions. Chevron management are thanked for their support of this work, through a multi-year Shale Characterization research project.

Polish Experience with Testing of Selected Shales as Material for Road Base Courses

Leszek Rafalski and Jadwiga Wilczek

Road and Bridge Research Institute, 1 Instytutowa str., 03-302 Warsaw, Poland
lrafalski@ibdim.edu.pl

Abstract. Base courses are important layers of road structures and their basic role is to reduce forces produced by service loads. The compaction process as well as climatic conditions influence materials used in base courses. In Poland, laboratory and field experiments were performed with five burnt coal shales as materials for road base courses. The tested shales were originally coarse-grained aggregates susceptible to compaction and frost. The laboratory tests focused on the influence of compaction and frost cycles on shale properties. It was identified that compaction and frost cycles significantly changed shale properties, i.e. grading, sand equivalent, passive capillarity and hydraulic permeability. Crushing of the stone fraction and increase in the silt-and-clay fraction resulted in a tendency to increase passive capillarity as well as reduce the sand equivalent and hydraulic permeability of the tested shales. Long-term field tests were carried out on an experimental road section with a shale base course. After 5 years' operation of the road, the load capacity of the base course did not decrease. It was proved that burnt coal shales may be used in base courses but changes of their properties should be predicted.

1 Introduction

Coal wastes are generated in hard coal mining. One of such wastes is burnt coal shale, which is produced as a result of the alteration of unburnt shale in a colliery tip burning process. The degree of burning determines the properties of shale, and the more burnt the shale, the more resistant it is to water and frost. Processed shale is used in various methods, e.g. [12]. One of the target applications is in road structures. Burnt coal shale is suitable for the construction of road structures. Selected types of burnt shale can be used for base courses. The most common method for making those layers involves the use of compacted aggregate, with shale appropriately crushed and selected in terms of grading [1, 9]. Another solution is to use shale and ash for soil improvement [11]. As shales are coarse-grained materials, appropriate methods are required for testing their properties [2,4,5,6,10]. The applications implemented so far have shown that shale grading can change due to compaction. As upper layers of the road surface may be adversely affected by frost [3,7,8], especially freeze-thaw cycles should be taken into account in base-course technologies and structures. Therefore, research has been carried out into the influence of those factors on shale properties, the results of which are presented in this paper.

L. Laloui and A. Ferrari (Eds.): Multiphysical Testing of Soils and Shales, SSGG, pp. 295–301.
springerlink.com

2 Research Materials and Methods

Tests were carried out on five burnt coal shales from heaps of the Kazimierz Juliusz, Saturn, Powstańców Śląskich, Dębieńsko and Wesoła mines situated in Silesia in the southern part of Poland. Owing to the size of the stockpiles, the statistical homogeneity of shale grading was examined in 53 samples. Laboratory investigations were then carried out to identify changes in the grading of compacted shale when compacted in the Proctor device featuring a cylindrical mould of 25 cm in diameter and holding 10 dm^3 of material, with a 15 kg hammer falling 60 cm. The use of a cylinder with a diameter of 25 cm made it possible to perform tests on samples with actual grading of 0-63 mm without disregarding the stone fraction. The wet sieve analysis was performed. The sample compaction method is presented in Table 1.

Table 1. Sample compaction method

Compaction parameters	Normal method	Modified method	150 % of modified energy	200 % of modified energy
Energy (J/cm^3)	0.59	2.65	3.975	5.30
Number of layers	3	5	5	5
Number of blows per layer	22	59	88	118

The investigation of changes in grading after compaction with variable energy showed a substantial change in burnt coal shale grading after compaction using the modified method. Therefore, changes in other shale properties were examined by testing samples compacted at modified energy. Percentage content of the 0-2 and 0-4 mm fractions was examined, as well as the sand equivalent for the 0-4 mm fraction, passive capillarity of the 0-2 mm fraction and hydraulic permeability at hydraulic gradient i = 0.8. In the final part of the laboratory investigations, changes in the above-mentioned properties were examined of shale compacted using the modified method and additionally subjected to 25 cycles of freezing at –18ºC (4 hours) and thawing at +18ºC (2 hours).

3 Laboratory Investigations Results and Discussion

Shale homogeneity investigations showed that the distribution of results was almost symmetrical and could be approximated by a Gaussian distribution curve. An example histogram of results and a normal distribution curve for the silt-and-clay fraction content is shown in Fig.1.

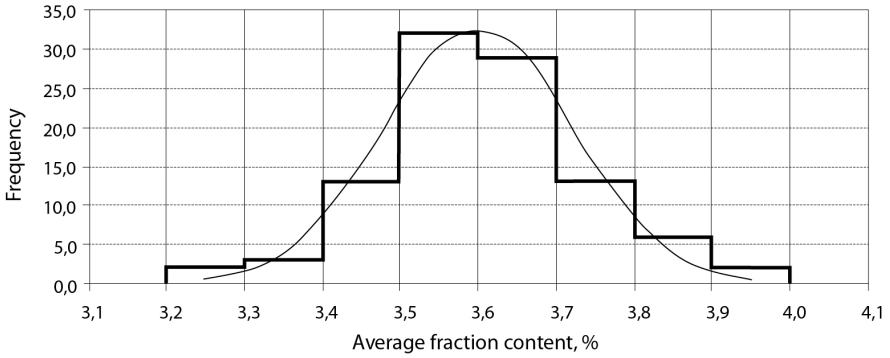

Fig. 1 Histogram and normal distribution curve for the silt-and-clay fraction content

Table 2 shows the results of investigations into grading changes in shales compacted at different energies. The test results represent averages for the five shales under investigation.

Table 2 Changes in the grading of shales compacted at different energy levels

Compaction method and energy	Fraction content (%)			
	silt-and-clay	sand	gravel	stone
Without compaction	3.6	10.5	44.1	41.8
Normal, 0.59 J/cm^3	5.0	15.3	48.7	31.0
Grading change	+1.4	+4.8	+4.6	-10.8
Modified, 2.65 J/cm^3	11.2	21.0	51.5	16.3
Grading change	+6.2	+5.7	+2.8	-14.7
150 % of modified energy, 3.975 J/cm^3	11.3	22.0	52.0	14.7
Grading change	+0.1	+1.0	+0.5	-1.6
200 % of modified energy, 5.30 J/cm^3	11.4	22.4	52.0	14.2
Grading change	+0.1	+0.4	0.0	-0.5
Total grading change	+ 7.8	+ 11.9	+ 7.9	- 27.6

The results presented are indicative of considerable changes in the grading of the tested shales due to compaction. A marked decomposition of the stone fraction can be seen as well as an increase in the content of the gravel, sand and silt-and-clay fractions. This leads to an increase of the shale uniformity coefficient, which has a favourable effect on its compaction. A very large change in grading takes place when modified energy is applied instead of normal energy. A further

increase of energy does not have a significant effect on shale grading (Fig. 2). For this reason, further investigations were carried out with shale compacted at normal energy 0.59 J/cm^3 and at modified energy 2.65 J/cm^3.

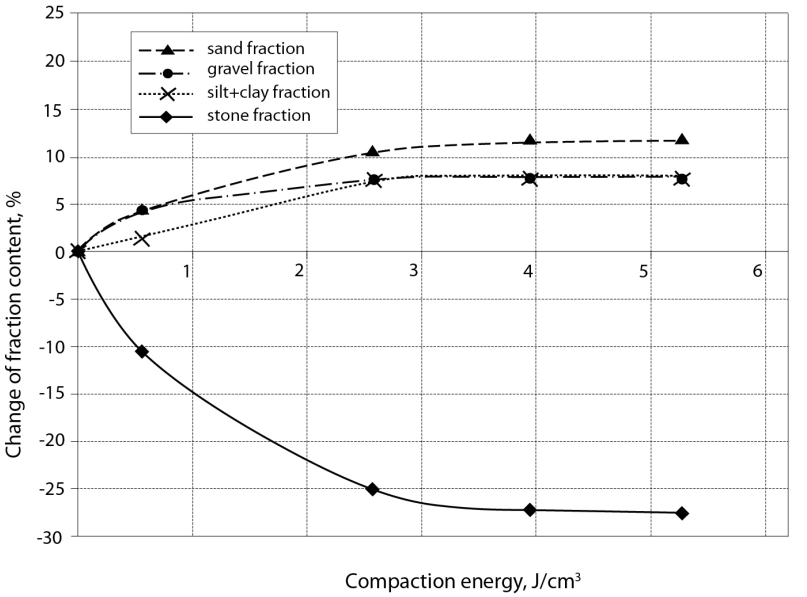

Fig. 2 Grading changes for different shale fractions depending on compaction energy

Table 3 shows the results of tests concerning changes in the content of selected fractions, sand equivalent, passive capillarity and coefficient of permeability of shale due to compaction and frost. Samples for testing permeability in natural condition were prepared in a large Proctor cylinder, shaken on a vibrating table to compaction factor I_s =0.95, avoiding grain crushing.

Table 3 Changes in the content of selected fractions, sand equivalent, passive capillarity and coefficient of permeability of shale due to compaction and frost

Compaction method and energy	0-2 mm fraction content (%)	0-4 mm fraction content (%)	Sand equivalent (-)	Passive capillarity (m)	Coefficient of perme-ability (m/day)
Without compaction	29.7	38.2	70.3	0.08	39.7
Normal, 0.59 J/cm^3	39.3	55.9	50.9	0.48	8.7
Modified, 2.65 J/cm^3	41.0	57.3	47.4	0.55	7.9

Apart from changes in grading, compaction and frost cause changes in the sand equivalent, passive capillarity and water permeability coefficient of shale. Tendencies are observed of a decreasing value of the sand equivalent and increasing passive capillarity. Especially great changes can be noticed in passive capillarity, which increased several times. Despite those changes, shale can still be classified as not frost susceptible material. Compaction and frost also caused the coefficient of permeability of shale to drop several times, but it was not lower than 5 m/day and met the requirements for materials used in filter layers.

4 Field Investigations

The experimental road section with an area of 180 m^2 was constructed on an access road to an aggregate stockpile area in Katowice – Janów. A layer of 50 cm in thickness was made of burnt coal shale from the Kazimierz Juliusz mine and a 25 cm upper layer of concrete aggregate, on which a surface course of bitumen-aggregate mix was laid. The tests showed that as a result of process compaction and after five years' operation of the road with natural freeze-thaw cycles, burnt coal shale changed its properties. Changes in the content of individual fractions ranged from 1.6 to 17.0 %. On the other hand, much smaller changes of grading resulted from traffic loads and from weather conditions during road operation. Changes in the content of the different fractions ranged between 0.3 and 11 % in this case. Immediately after the shale layer was laid, load capacity was tested using the VSS method. The tests were repeated in test pits made in the road surface after 3 and 6 months and after 5 years (Table 4).

Table 4 Results of deformation tests of a burnt coal shale layer

Operation time	Secondary deformation modulus E_2 (MPa)	Deformation index I_o (-)
0	128	2.0
3 months	129	2.0
6 months	136	1.9
5 years	142	2.0

The value of the secondary deformation modulus did not decrease after five years of road operation. A slight increase in the load capacity of the shale layer could result from the binding of fine pozzolan particles contained in shale.

Based on the investigations performed, the test requirements and methods were developed, which should be applied when using coal shale for base courses. It was assumed that geotechnical properties of shale should be evaluated not in natural condition but after compaction at modified energy and freeze-thaw cycles. Requirements were proposed for grading, sand equivalent, bearing ratio, water

permeability coefficient, passive capillarity, abrasion resistance and ignition losses, which are specified in [8].

5 Conclusions

Burnt coal shale in natural condition has the grading suitable for making road base courses. However, it is not resistant to compaction and frost effects. Under laboratory conditions, shale grading changes considerably due to compaction. A distinct difference can be seen in the change of grading of shale compacted with the use of modified energy compared to that compacted at normal energy. An increase of the compaction energy above the modified energy results in small changes in grading. Compaction and water and frost impact cause changes of the sand equivalent, passive capillarity and coefficient of permeability of shale. There are tendencies towards a decrease of the sand equivalent, increase of passive capillarity and decrease of the coefficient of permeability.

In the experimental road section, it was noticed that as a result of compaction and five years' operation of the road, the layer of burnt coal shale changed its properties but the value of the secondary deformation modulus did not decrease.

The results of laboratory and field investigations indicate the need for an in-depth analysis of the properties of shales intended for use in base courses. The application of shale should be preceded by the identification of the changes that may occur when placing the material into the road layer and during road operation. Geotechnical properties of shale should be evaluated not in natural condition but after compaction at modified energy and freeze-thaw cycles.

References

Borchert, C., et al.: Einsatz von Waschbergen im Deichbau. Geotechnik 2, 87–92 (2009)

Khay, M., Nguyen, D., Quibel, A.: Nouvelle technique de repandage et de densification des materiaux granulaires pour couches de chaussees. Bulletin des laboratoires des ponts et chaussees 221, 13–25 (1999)

Kugler, H., Ottner, F., Schwaighofer, B., Strasser, W.: Frost susceptibility of unbound bases. An improved mineralogical assessment. The International Journal of Road Materials and Pavement Design 6(2), 119–134 (2005)

Lecomte, A., Mechling, J.-M.: Compacite des melanges et properties des grains. Bulletin des laboratoires des ponts et chaussees 220, 13–21 (1999)

Ping, W.V., Yang, Z., Ho, R.K.H.: Full-scale laboratory evaluation of moisture effect on resilient moduli of granular pavement subgrade layers. Road Materials and Pavement Design 4(3), 309–330 (2003)

Pisarczyk, S.: The analysis of compaction laboratory tests of soils (in Polish). Maritime Engineering and Geotechnics 6, 400–405 (1996)

Premstaller, M.: Neue kriterien fur die Beurteilung der Frostempfindlichkeit eines nichtbindigen Lockermaterials. Geotechnik 2, 126–128 (1997)

Rafalski, L., Wilczek, J.: Frost-protective layers from weak coarse aggregates in road pavement structures, vol. 57. Road and Bridge Research Institute, Study and Materials, Warsaw (2006) (in Polish)

Skarżyńska, K.M.: The use of unburnt coal shales in road construction (in Polish). Maritime Engineering and Geotechnics 4, 280–286 (1996)

Tong, L., Baus, R.L.: Nonlinear parameters for granular base materials from plate tests. Journal of Geotechnical and Geoenvironmental Engineering, 907–913 (July 2005)

Zeng, Q., Yang, M., Li, J., Luo, F., Liu, J.: An experimental study of alkali soil improvement with coal ash and coal shale. In: 2011 International Conference on Consumer Electronics, Communications and Networks, XianNing, pp. 2915–2918 (2011)

Zhao, M., Xiang, Y.: Natural rubber vulcanizate reinforced by modified coal-shale-based fillers. Journal of Applied Polymer Science 93(3), 1397–1400 (2004)

Experimental Methods for Characterization of Cap Rock Properties for CO_2 Storage

E. Aker, E. Skurtveit, L. Grande, F. Cuisiat, Ø. Johnsen,
M. Soldal, and B. Bohloli

Norwegian Geotechnical Institute, NO-0855, Oslo, Norway
Eyvind.Aker@ngi.no

Abstract. This paper presents laboratory methods utilized at Norwegian Geotechnical Institute for characterizing cap rock for CO_2 storage reservoirs. The focus is on the physico-mechanical characterization of shale using standard rock physical-mechanical testing and some special designed set-ups for advanced experimental conditions. The Brazilian, uniaxial and triaxial tests are explained along with some examples from North Sea, Barents Sea and Svalbard. The CO_2 core flood tests have been designed and carried out in the NGI laboratory for investigating rock-CO_2 interaction. Monitoring techniques such as CT-scanning, acoustic measurement, acoustic emission and resistivity are used and described in the paper. Brief description of development/upgrading of laboratory instruments for conducting more advanced experiments is also included.

1 Introduction

Safe geological sequestration of CO_2 requires comprehensive knowledge of the reservoir, cap rock and surrounding formations. The role of the cap rock is of vital importance because it provides sealing of the reservoir and prevents migration of CO_2 into adjacent aquifers or to the surface. Characterization of shale cap rock is carried out to ensure both short- and long-term integrity of the reservoir and cap rock. The short-term integrity is usually studied through mechanical testing of rock which includes Brazilian, uniaxial and triaxial tests to determine pressurization limit of the reservoir and cap rock. The long term integrity study, however, takes the chemical reactivity of cap rock into consideration. Such tests include CO_2 core flooding tests. A brief description of experimental apparatus and methods are given along with real examples related to the recent studies for characterizing reservoir and cap rock. Methods such as X-ray diffraction, scanning electron microscope and synchrotron radiation are also employed at NGI for microstructure analyses before and after testing, which are not included in this paper (see Voltolini et al., 2009).

L. Laloui and A. Ferrari (Eds.): Multiphysical Testing of Soils and Shales, SSGG, pp. 303–308.
springerlink.com

2 Cap Rock and Reservoir Integrity Tests

In this section the results of mechanical tests and hydro-mechanical experiments on core samples of shale from the North Sea, Barents Sea and the Svalbard are elaborated. The tests include uniaxial and triaxial compression, indirect Brazilian tensile strength and core flooding experiments.

2.1 Uniaxial and Triaxial Compression Tests

The uniaxial compression is a standard rock mechanics test for determining the uniaxial compressive strength (UCS), Young's modulus and Poisson's ratio required for geomechanical analyses and modeling. The test is relatively simple, quick and cheap but the data are not directly applicable to reservoir since, dissimilar to in-situ conditions, there is no confining pressure around the sample during testing.

The triaxial compression test provides the most appropriate values of geomechanical parameters applicable to subsurface conditions. A special triaxial cell has been designed in NGI laboratory which is (see Fig. 1):

- flexible to test cores of different sizes under different drainage conditions,
- able to measure local strains using LVDTs,
- accurate in measuring excess pore pressure,
- capable of testing and determining the coefficient of thermal expansion and stress-strain behavior at high temperature and effective stress (Berre, 2010).

The triaxial apparatus provides effective shear strength parameters; cohesion (c') and internal friction angle (ϕ'), Young's modulus (E) and also Poisson's ratio (ν), shear modulus (G) and unloading-reloading modulus which are the major parameters required for analytical/numerical modeling. The designed apparatus can measure resistivity along with the standard parameters under reservoir conditions.

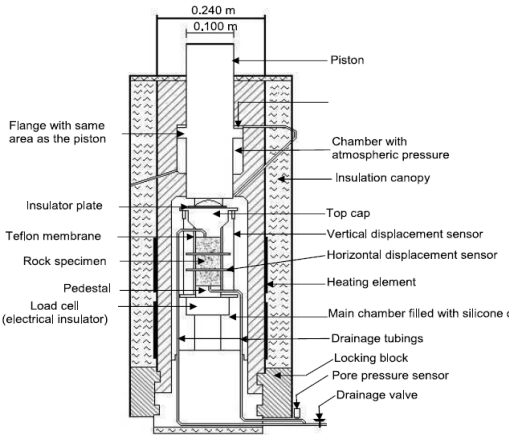

Fig. 1 NGI triaxial apparatus especially designed to accommodate instrumentation close to the sample.

2.2 Brazilian Tensile Test

The standard Brazilian tensile test is conducted on rock samples to obtain indirect tensile strengths. The test is widely used in laboratories because it is simple and cheap. Tensile strength is a major parameter for failure of cap rock and reservoir. In the case of fracture development in cap rock, it will propagate either parallel or perpendicular to shale bedding (see Fig. 2). Accordingly, samples can be loaded parallel and perpendicular to bedding plane in laboratory (as sketched in Fig. 2) to determine fracture pressure and strength anisotropy in the two directions.

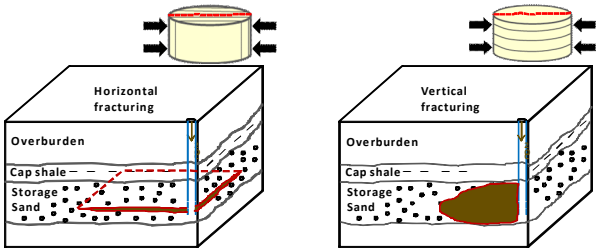

Fig. 2 Schematic illustration of bedding plane and the tested core samples. Left panel: propagation of a horizontal fracture, right panel: propagation of a vertical fracture

The CO_2 storage reservoirs are usually planned at shallow depths where in-situ stresses are relatively low. In some regions like Barents Sea the tensile strength of rock is very high relative to the present day burial depth (as confirmed by the laboratory testing) due to significant uplift. In such cases, the impact of tensile strength on cap rock integrity and fracture pressure would be very important and needs to be considered in assessing cap rock integrity.

2.3 Core Flooding Experiments

The core flooding test was designed to study the mechanisms involved in CO_2 breakthrough process and to determine parameters controlling flow of superctritical CO_2 in low permeable shales. Two shales from the Draupne Formation (porosity ~28% and permeability ~10 nD) in northern North Sea were tested using a high pressure flow cell with the capacity of 30 MPa (Fig. 3). The tests were carried out under isotropic stresses, with axial and radial displacement sensors and measurement of axial P and S wave velocities.

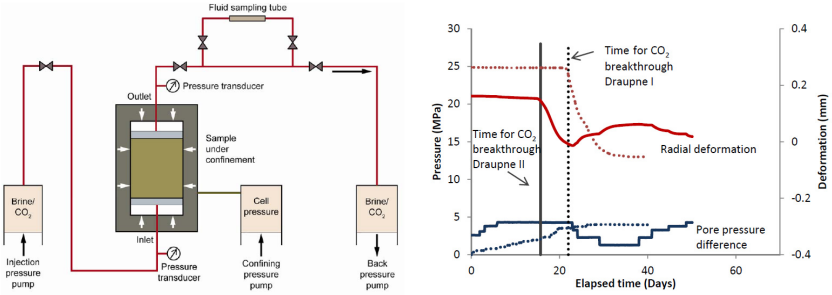

Fig. 3 (left):Schematic drawing of flow cell and (right): deformation and pore pressure difference in a sample during testing (after Skurtveit et al., 2012)

Flooding experiments were carried out in two phases; first a brine saturated test phase and second, a CO_2 injection test with measurements of effective CO_2 permeability for varying pressures. For the Draupne material, CO_2 breakthrough was recognized by an increase in the back pressure pump volume. Radial and axial dilation of the sample was recorded due to CO_2 breakthrough (Fig. 3) accompanied by drop in ultrasonic velocity. The CO_2 breakthrough pressure for Draupne material was dependent on confining pressure and effective stress rather than pore pressure difference across the sample. After breakthrough, the effective CO_2 permeability seemed to follow a simple model for permeability in fractured rock. Thus, it was concluded that the fracture initiation pressure was a critical value in addition to capillary displacement (Skurtveit et al., 2012).

3 Monitoring Techniques

Monitoring the physical properties of material during testing is very important to understand rock behavior in the reservoir. Different methods and instruments used for monitoring of rock properties at NGI are elaborated in this section.

3.1 Combined Resistivity and Acoustic Measurements

NGI uses a modified triaxial cell and a specially designed carbon fibre cell for simultaneous measurement of acoustic velocity and resistivity combined with an X-ray computed tomography (CT) scanner to define rock physical parameters as function of CO_2 saturation. A four-electrode-ring system has been developed, in addition to the top and bottom caps, for more reliable measurements of resistivity and for detecting sample anisotropy and micro-cracking. Thus, radial and axial resistivity can be measured (Wang et al., 2009).

3.2 CT-Scan

Geophysical measurements enable locating compressible fluids like CO_2 in pore spaces. NGI benefits from an advanced CT-Scanner (Nikon Metrology XT H 225 LC) for characterizing samples before testing, monitoring fluid front during tests and identifying post mortem morphology. Fig. 4 shows CT-scan image of CO_2 flow in a sandstone parallel and normal to bedding to display anisotropy effect.

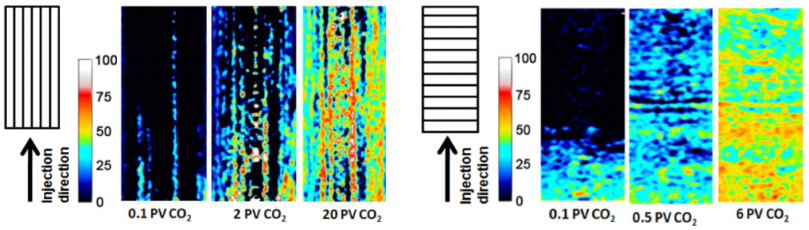

Fig. 4 Distribution of injected CO_2 in a core parallel with (left) and perpendicular to bedding plane (right), (Alemu et al. 2012)

3.3 Acoustic Emission

Acoustic emission (AE) refers to elastic energy being emitted during failure of rock and is an effective method for studying damage initiation and propagation processes in stressed rock. In the triaxial apparatus, the AEs are monitored by 12 piezoelectric transducers (Ergotech Ltd.) that are mounted on the surface of the sample. An event location algorithm is used after testing to compute the source locations in 3D that can be verified by post test CT-imaging (Fig. 5), (Cuisiat et al., 2010). In parallel with the experiments, discrete element modeling is performed to investigate the relationship between grain scale processes and macroscopic response of rock sample during failure.

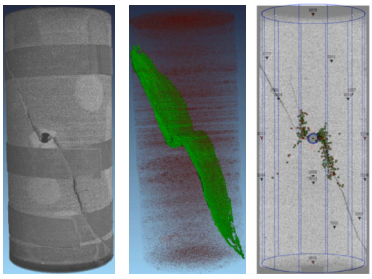

Fig. 5 Monitoring physical properties and acoustic emission of a sandstone. Left: 3D reconstructed image of the core, middle: pores (red) and fracture surface (green), right: acoustic emissions coinciding with fracture plane

4 Future Applications

Several experimental set-ups are under development at NGI for advanced testing of fluid-rock interactions, among which the triaxial-CT scanner cell and the new

shear box are presented. The triaxial-CT scanner cell (by Ergotech Ltd.) enables applying axial load (max 88 MPa), radial load (max 70 MPa) and temperature (max 140 deg. C) on the sample while simultaneously image the interior of the sample by CT-scanner. This will reveal failure mechanisms, micro cracking and localization of shear bands. A drawing of the current isotropic pressure cell made of carbon-fiber which is transparent to X-ray is shown in Fig. 6 (left).

The designed Direct Shear Box (by MTS) handles intact or naturally fractured rock specimens with the dimensions of 150×150×300 mm, provides max normal force of 500 kN, max shear force of 250 kN and max shear displacement of 100 mm (Fig. 6 right). It can be applied for i) determining the direct shear strength, friction and deformation behavior (creep) of rocks at high stress, and ii) measuring conductivity of fractures during normal loading and shearing at high stress.

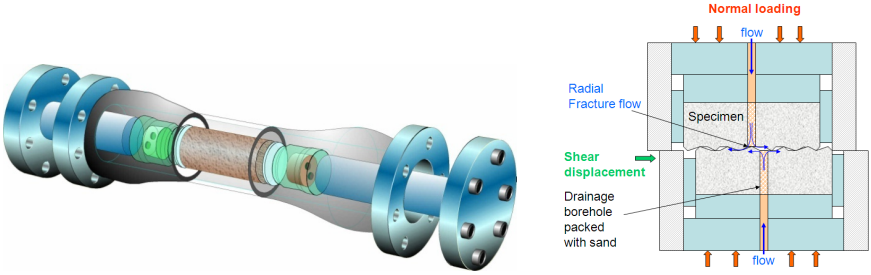

Fig. 6 Schematic drawing of the current X-ray transparent pressure cell (left) and the direct shear box (right)

References

Alemu, B.L., Aker, E., Soldal, M., Johnsen, Ø., Aagaard, P.: Effect of sub-core scale heterogeneities on acoustic and electrical properties of a reservoir rock: A CO2 flooding experiment of brine saturated sandstone in a CT-scanner. Geophysical Prospecting (in Press, 2012)

Berre, T.: Triaxial testing of soft rocks. Geotechnical Testing Journal 34, Paper IDGTJ102879 (2010)

Skurtveit, E., Aker, E., Soldal, M., Angeli, M., Wang, Z.: Experimental investigation of CO2 breakthrough and flow mechanisms in shale. Petroleum Geoscience 18, 3–15 (2012)

Wang, Z., Gelius, L.J., Kong, F.N.: Simultaneous core sample measurements of elastic properties and resistivity at reservoir conditions employing a modified triaxial cell-a feasibility study. Geophysical Prospecting 57, 1009–1026 (2009)

Voltolini, M., Wenk, H.R., Mondol, N.H., Bjørlykke, K., Jahren, J.: Anisotropy of experimentally compressed kaolinite-illite-quartz mixtures. Geophysics 74, D13–D23 (2009)

Cuisiat, F., Aker, E., Soldal, M., Kuehn, D.: Relating acoustic emission sources to rock failure around a borehole. In: 72nd WAGE Conf. & Exh., Barcelona, Spain, June 14-17 (2010)

Treated and Weathered Geomaterials

Using Shear Wave Velocity to Determine the Cementation Effect of Soft Bangkok Clay Mixed with Cement and Fly Ash

K. Piriyakul[1] and S. Pochalard[2]

[1] Department of Civil and Environmental Engineering Technology, College of Industrial Technology, King Mongkut's University of Technology North Bangkok, Thailand
keeratikanp@kmutnb.ac.th
[2] Civil Engineer, Division of Campus Buildings and Site,
Suan Dusit Rajabhat University, Thailand
sakol.poc@gmail.com

Abstract. This paper presents the using of shear wave velocity to determine the cementation effect of soft Bangkok clay mixed with cement and fly ash. The Bangkok clay is mixed with 20 % of the Portland cement type 1 by weight of dry soil and varied the replacement of fly ash 10, 15, 20, 25 and 30 % by weight of cement. Then, these samples were cured to 7, 14, 28 and 90 days respectively and performed the bender element and unconfined compression test. From the results, the research found that the undrained shear strength and the shear wave velocity increased with increasing the curing time. The undrained shear strength data of 15 % of fly ash type F were maximum values and in good agreement with the result of no fly ash. In the similar ways, the shear wave velocity results of 15-20 % of fly ash type F were higher than the result of no fly ash in the long term. The relationship between the shear wave velocity and the undrained shear strength was $V_s = 243.38(S_u/P_a)^{0.305}$ and in good agreement with the field data.

1 Introduction

The research has developed a new technique to determine the cementation effect of Bangkok clay mixed with cement and fly ash by using shear wave velocity as described in Dyvik & Madshus (1985). The shear wave is generated and received by piezoelectric transducers placed at opposite ends of the soil specimen. The shear wave velocity, V_s, is calculated from the tip to tip distance, L, between the two transducers and the time required, t, by the shear wave to cover this distance as shown in Equation 1.

$$V_s = L/t \tag{1}$$

L. Laloui and A. Ferrari (Eds.): Multiphysical Testing of Soils and Shales, SSGG, pp. 311–316.
springerlink.com

2 Bender Element Test

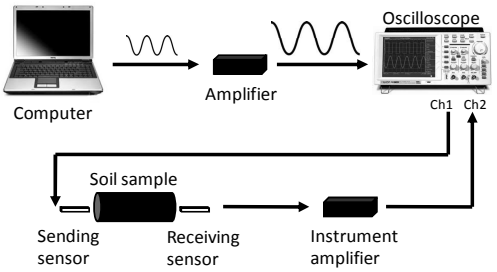

Fig. 1 Schematic of shear wave measurement and associated electronics

Figure 1 shows the schematic test set-up. A personal computer generates a signal through a sound card with 5V peak to peak as suggested by Mohsin & Airey (2003). This signal is amplified to 40V peak to peak. An oscilloscope is used to measure the arrival time between a sending signal and a receiving signal. A voltage pulse is applied to the sending sensor, this causes it to produce a shear wave. When the shear wave reaches the other end of the soil sample, distortion of the receiving sensor produces another voltage pulse. The receiving sensor is directly connected to the oscilloscope to compare the difference in time between the sending and the receiving signals. The shear wave velocity measurements are usually performed with frequencies ranging between 2 to 12 kHz, at strains estimated to be less than 0.0001 %. At low frequencies, signals can be influenced by a near-field effect. At high frequencies, the receiving signal is very weak and difficult to interpret. In most cases, signals are averaged 32 times in order to get a clear signal. The measurement of shear wave velocity in soil sample by means of piezoelectric ceramic sensors is clearly described by Brignoli et al. (1996).

3 Bangkok Clay Material

The soft Bangkok clay at 10-12 m depth is sampled for this research. The engineering properties are found that the specific gravity is 2.72, the natural water content is 66.3%, the mass density is 1,470 kg/m^3 and the liquid limit is 88%. 60 experiment soft Bangkok clay samples are prepared at the liquid limit by mixing 20% by weight of Portland cement Type 1 and varying the replacement fly ash of 0, 10, 15, 20, 25 and 30%. This research uses the fly ash Type F from Mae Moh Lignite Power Plant in Lampang. Then, these samples are cured 7, 14, 28 and 90 days in order to perform the bender element test and the unconfined compression test.

4 Experimental Results

Figure 2a showed the undrained shear strength, S_u, versus the percent replacement of fly ash. From the experimental results, the research found that the optimum percent replacement of fly ash was 15%. In the similar ways, Figure 2b showed the shear wave velocity, V_s, versus the percent replacement of fly ash. From the experimental results, the research found that the optimum percent replacement of fly ash was about 15-20%. From the 90 days results, the V_s of 20% replacement of fly ash were maximum data which reports the long term behaviour of fly ash and cement mixed.

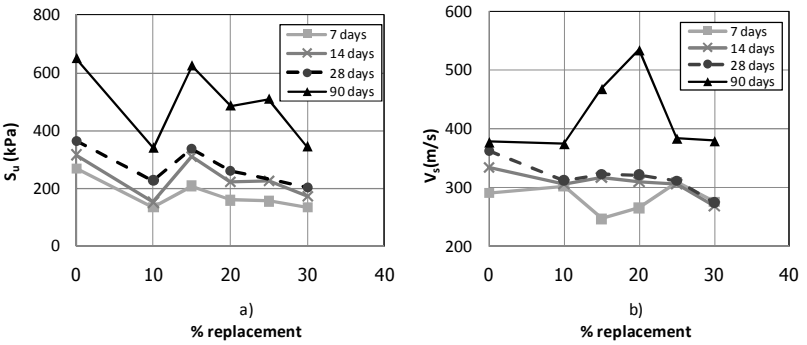

Fig. 2 a) S_u and b) V_s versus the % replacement of fly ash

Figure 3 showed the undrained shear strength, S_u, versus the time in logarithmic scale. From the experimental results, the S_u increased with increasing the curing time. Figure 3c showed the results of 15% replacement of fly ash were almost the same as the result of 0% replacement of fly ash as seen in Figure 3a. In the similar ways, Figure 4 showed the shear wave velocity, V_s, versus the time in logarithmic scale. From the experimental results, the V_s also increased with increasing the curing time. The results of 15% (see Figure 4c) and 20% (see Figure 4d) replacement of fly ash were higher than the result of 0% replacement of fly ash (see Figure 4a) which reports the long term behaviour of fly ash and cement mixed. But the results of 25% (see Figure 4e) and 30% (see Figure 4f) replacement of fly ash were lower than the result of 0% replacement of fly ash.

Likitlersuang & Kyaw (2010) studied the relationship between the shear wave velocity and the undrained shear strength as shown in Equation 2.

$$V_s = A\,(S_u/P_a)^{\,n} \tag{2}$$

Where A is the coefficient reflecting the material. n is the coefficient reflecting the behavior when subjected to the force. P_a is the atmospheric pressure (100 kPa).

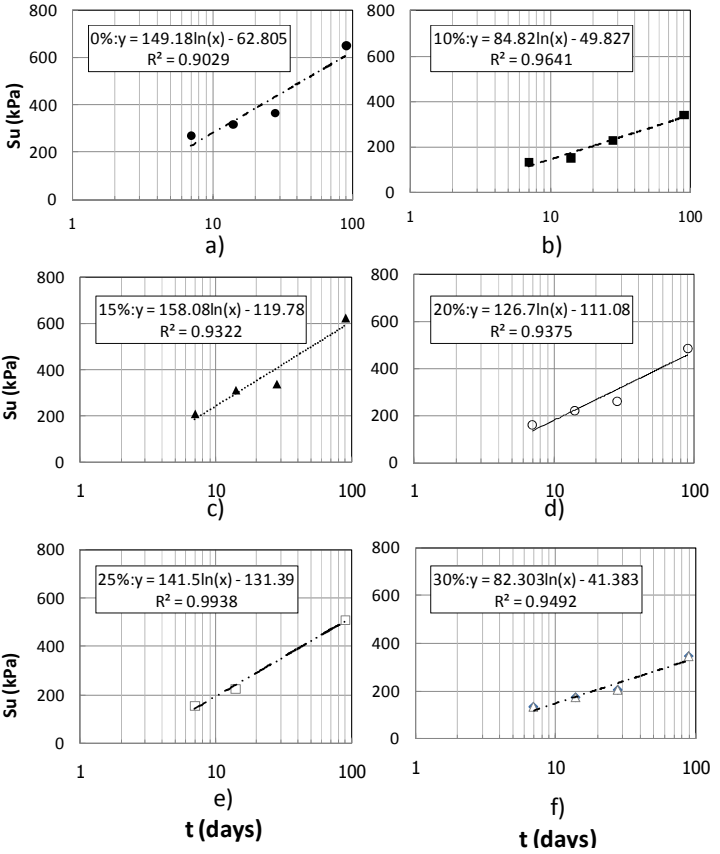

Fig. 3 The undrained shear strength, S_u, versus time, t, of the % replacement of fly ash a) 0% b) 10% c) 15% d) 20% e) 25% and f) 30%

Figure 5 showed the relationship between the shear wave velocity and the undrained shear strength and found that A = 243.38 and n = 0.305, corresponding to the field test data of Likitlersuang & Kyaw (2010). They performed the multichannel analysis of surface waves method (MASW) and found A = 187.42 and n = 0.372. Also, they did the Down-hole method and found A = 227.93 and n = 0.510 as shown in Table 1.

Table 1 Field test data of Bangkok clay formation after Likitlersuang & Kyaw (2010)

Method	**A**	**n**
MASW	187.42	0.372
Down-hole	227.93	0.510

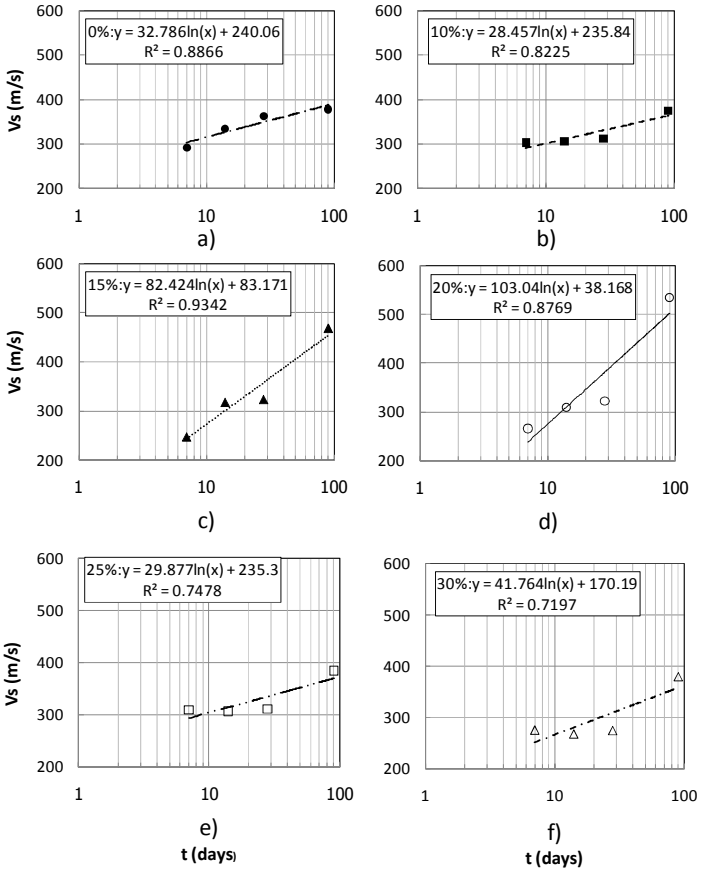

Fig. 4 The shear wave velocity, V_s, versus time, t, of the % replacement of fly ash a) 0% b) 10% c) 15% d) 20% e) 25% and f) 30%

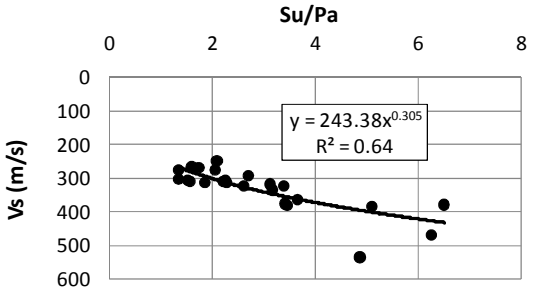

Fig. 5 V_s versus S_u/P_a

5 Conclusions

The research can conclude the cementation effect of soft Bangkok clay mixed with the 20% of Portland cement type 1 and the fly ash type F replacement of 0, 10, 15, 20, 25 and 30% by using the shear wave velocity as follows;

- The undrained shear strength and the shear wave velocity increased with increasing the curing time.
- The undrained shear strength data of 15% fly ash replacement were maximum values and in good agreement with the results of no fly ash.
- The shear wave velocity data of 15-20% fly ash replacement were higher values than the results of no fly ash in the long term.
- The relationship between the shear wave velocity and the undrained shear strength was $V_s = 243.38(S_u/P_a)^{0.305}$ and in good agreement with the field test data of Likitlersuang & Kyaw (2010).

Acknowledgement. The author is grateful to the scientific research fund for publication on Scopus database of the College of Industrial Technology, King Mongkut's University of Technology North Bangkok (KMUTNB).

References

Brignoli, E.G.M., Gotti, M., Stokoe, K.H.: Measurement of shear waves in laboratory specimens by means of piezoelectric transducers. Geotechnical Testing Journal 19, 384–397 (1996)

Dyvik, R., Madshus, C.: Laboratory measurement of G_{max} using bender elements. The ASCE Annual Convention, Detroi, pp. 186–196 (1985)

Kramer, S.L.: Geotechnical Earthquake Engineering. Prentice-Hall International Series. Prentice Hall, Upper Saddle (1996)

Mohsin, A.K.M., Airey, D.W.: Automating G_{max} measurement in triaxial tests. In: The Pre-failure Deformation Characteristics of Geomaterials, Lyon, pp. 73–80 (2003)

Likitlersuang, S., Kyaw, K.: A Unified Correlation for Shear Wave Velocity of Bangkok Subsoil. In: The 17th Southeast Asian Geotechnical Conference, Taipei, Taiwan, May 10-13, pp. 431–435 (2010)

Settlement Calculation and Back-Analysis of Soil Properties for a Test Embankment on a Soft Clay Ground Improved by PVD and Vacuum-Assisted Preloading at a Site in Vung Tau, Viet Nam

Nguyen Duy Quang[1] and Su Minh Dang[2]

[1] Saga University, Department of Civil Engineering, Saga, Japan
[2] Minho University, Portugal
eng.dang@gmail.com

Abstract. Application of vacuum assisted preloading is helpful when a considerable load is required to meet the desired rate of settlement and an increase in the undrained shear strength in a relative short time. To facilitate the vacuum propagation, vertical drains are usually employed in conjunction. A pilot test was carried out at a land reclamation project to study the effect of ground improved by vacuum combined with PVD and surcharge preloading on the rate of consolidation of a soft clay at the site of Saigon International Terminals Vietnam (SITV) in Ba Ria-Vung Tau Province, Viet Nam. Theorectical analysis were conducted to interpret the field measurements of pore pressure and settlement, and consolidation parameters were back－calculated. The degree of consolidation estimated from the settlement is higher than that obtained from the pore-pressure dissipation measurement. The coefficient of consolidation back－calculated from the settlement is slightly larger than that obtained from the pore-pressure measurement. Furthermore, undrained shear strength was back– calculated and compared with those obtained from soil investigation after treatment.

1 Introduction

The prefabricated vertical drain preloading with embankment was modified by combining with vacuum pressure to decrease the associated instability. Vacuum consolidation preloads the soil by reducing the pore pressure while maintaining constant total stress instead of increasing the total stress. The effective stress is increased due to the reduced pore pressure in the soil mass. The net effect is an additional surcharge ensuring early attainment of the required settlement and an increased shear strength resulting in increased embankment stability. Hence, the vacuum preloading technique can diminish large quantity of fill material as well as minimize instability problem.

L. Laloui and A. Ferrari (Eds.): Multiphysical Testing of Soils and Shales, SSGG, pp. 317–322.
springerlink.com

The full-scale field test confirmed the effectiveness of the prediction and monitoring methods, such as comparison of the degree of consolidation using pore-pressure measurement and settlement measurement, and comparison of the actual increase in shear strength with predicted values. The full-scale test embankments was constructed in stages on a subsoil improved by PVDs combined with vacuum surcharge preloading at the SITV project site, southern of Viet Nam.

2 Soil Conditions and Properties

The generalized soil profile and soil properties are shown in Fig. 1. The soil profile is relatively uniform, consisting of a 2 m thick weathered crust overlying very soft to soft clay approximately 10 m thick. Underlying the soft clay is a medium clay layer about 7 m thick followed by a sand layer which is in turn underlain by a layer of hard clay.

3 Pilot Test Construction and Instrumentations

The test embankment of trapezoidal shape has the size of 85 x 73 x 251m in plan dimensions and a final height of 4.1m as shown in Fig. 2a. Organic soil was removed at +2.5m Chart Datum, then backfilled sand at +3.5m CD and drainage fill at +4.1m CD, where the PVDs were installed. The final platform elevation was +5.7m CD. The design load on sand cushion consist of a vacuum pressure of 80kPa, and a height of surcharge of 2.5m. The PVDs were installed to a depth of 16 ~ 20m on a triangular pattern with 1.2m spacing. The size of PVD is 100mm length and 5mm width. The duration of vacuum preloading was about 4 months.

A field monitoring program was established to monitor surface and subsurface settlements, lateral movements, and excess pore pressures. Several settlement plates, one inclinometer, and piezometers were installed. The extensometers were installed in the center of the test embankment. The extensometers and the piezometers were installed at every 3m vertical interval. The piezometers were installed between the PVDs. Inclinometers are placed along the boundary of the soft ground treatment project, the bottom of which was embedded 3.0m bellow the top of firm ground during consolidation of foundation. The groundwater level is measured by observation well, which is placed in the center of each vacuum and surcharge combined preloading zone. The master plan showing the embankment instrumentation is plotted in Fig. 2b.

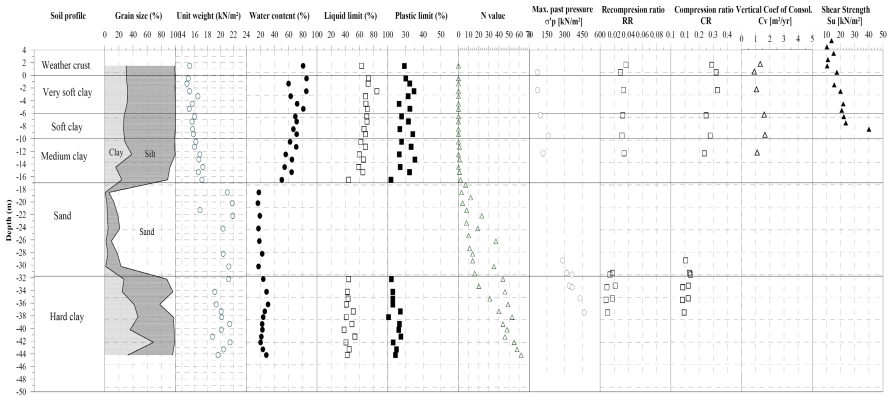

Fig. 1 Physical and mechanical properties

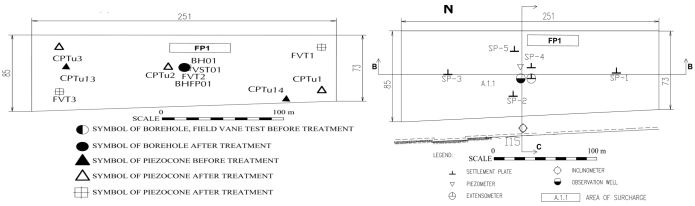

Fig. 2a&2b Locations of boreholes and layout of installation of field instrumentations

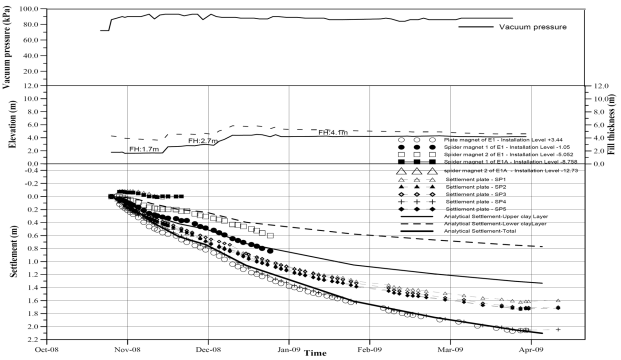

Fig. 3 Comparison of settlement between analytical results and monitoring data

4 Estimation of Settlements

4.1 Asaoka's Method (Asaoka, 1978)

The Asaoka's method (Asaoka, 1978) is based on settlement observation, in which earlier observations are used to predict the ultimate primary settlement. Asaoka

showed that one-dimensional consolidation settlements at certain time intervals (Δt) could be described as a first order approximation:

$$S_n = \beta_0 + \beta_1 . S_{n-1} \tag{1}$$

Where: S_1, S_2, …, S_n are settlements observations, S_n denotes the settlement at time tn, $\Delta t = (t_n - t_{n-1})$ is time interval. The ultimate primary settlement is considered to be reached when $S_n = S_{n-1}$ and can be calculated by the following:

$$S_{ult} = \frac{\beta_0}{1 - \beta_1} \tag{2}$$

4.2 Pore Pressure-Based Method (Chu and Yan, 2005)

Another possibility of assessing the degree of consolidation is based on pore water pressure measurements (Chu and Yan, 2005). The average degree of consolidation can be calculated as

$$U_{avg} = 1 - \frac{\int [u_t(z) - u_s] dz}{\int [u_0(z) + \Delta\sigma - u_s] dz} \tag{3}$$

$$u_s(z) = \gamma_w z - s \tag{4}$$

where u_0 (z) is initial pore water pressure at depth z; $\Delta\sigma$ is the stress increment due to surcharge at a given depth; u_t (z) is pore water pressure at depth z and at time t; u_s (z) is suction line; γ_w is unit weight of water; s is suction applied.

The calculated settlements versus time are plotted in comparison with the measured values as shown in Fig. 3. The degree of consolidation of the clay layers below the test embankments was calculated both from pore-pressure and settlement measurements. If the compression ratio is assumed to be constant, then the degree of consolidation can be obtained from the measured pore pressures. The corresponding values of the degree of consolidation can also be obtained from the measured settlements. Table 01 compares the calculated degrees of consolidation from various methods.

The degree of consolidation obtained from pore pressures (U_P) is consistently less than that from settlements (U_S). These problems have also been observed by Bergado et. al (2002) and Bo et. al (2003). The possible reasons for these differences may be as follows: involved uncertainties in the prediction of ultimate settlement, such as measurements of initial settlements or effect of measurements by secondary compression. Secondly, piezometers were installed between two vertical drains in soil layers. Pore water pressure at this location will be the maximum and will gradually decrease towards vertical drain. Any misalignment in the piezometer vertically will lead to different measurements.

Table 1 Comparison of average degree of consolidation (U_a) and horizontal coefficient of consolidation (c_h) from settlement and pore pressure data

		Field measurements	
		From settlement	From pore pressure
	Analytical method	Asaoka's method	
U_a (%)	84%	87.2%	74.6%
c_h (m^2/yrs)		2.17	2.03

5 Back-Analysis of Soil Parameter

5.1 Increase Undrained Shear Strength

Changes in undrained shear strength can also be estimated from the following equations based on field settlement data (Stamatopoulos and Kotzias, 1985):

$$\Delta S_u = \left(\frac{1 + w_n G}{0.434 C_c} \right) S_u \frac{\delta}{h} \tag{5}$$

where S_u, ΔS_u are the original and change of undrained shear strength; w_n, Δw_n are the original and change of natural water content; G is the special gravity of soil grains, C_c is the coefficient of compressibility, δ is the settlement under preloading, and h is the thickness of compressible soils.

The increase in undrained shear strength, S_u, was also obtained from piezocone penetration tests as follows:

$$S_u = \frac{q_t - \sigma_{vo}}{N_{kt}} \tag{6}$$

where q_t, is the corrected cone resistance; σ_{vo} is the total overburden stress, N_{kt} is the cone factor (N_{kt} = 12 for soft clay in this area).

The increase of shear strength can be estimated from the SHANSEP technique. In this project, the SHANSEP equation can be obtained from field vane shear tests, oedometer and Constant Rate of Strain (CRS) tests as follows:

$$\frac{S_u}{\sigma'_{vo}} = 0.215 * OCR^{0.805} \tag{7}$$

The predicted increases in undrained shear strengths are indicated by "solid lines" in Fig. 4a. The corrected undrained shear strengths measured by field vane shear tests before and after treatment are also plotted by "dotted lines". As seen in Fig. 4a, there is an excellent agreement between the measured and predicted data with regards to the increase in undrained shear strength due to preconsolidation and drainage. Furthermore, cone resistance, q_c measured by piezocone tests in before and after treatment are also plotted for comparison in Fig. 4b. The results indicate that the shear strengths increase about 75% and from 34% to 72% for the cone resistance.

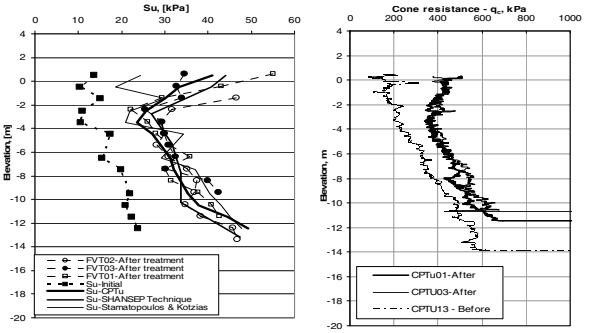

Fig. 4a&4b Undrained shear strength and cone resistance before and after treatment

6 Conclusions

Based on the test results, the following conclusions can be drawn: (1) The estimated and measured settlements are within an error of 3 ~ 6%, which are considered to be acceptable. (2) The average degree of consolidation was assessed based on both settlement and pore pressure data. The results indicated that the average degree of consolidation estimated from the settlement data was higher than that estimated from the pore water pressure data. (3) There is a good agreement between the measured and predicted undrained shear strength profiles after vacuum-assisted preloading based on SHANSEP technique and results from the piezocone penetration tests. The results indicates that the shear strength increase with 75% and from 34% to 72% for the cone resistance. (4) The c_h values deduced from field settlement were slightly higher than those estimated from field pore-pressure back-analysis.

References

Asaoka, A.: Observational procedure of settlement prediction. Soils and Foundations 18(4), 87–101 (1978)

Bergado, D.T., Balasubramaniam, A.S., Jonathan Fannin, R., Holtz, R.D.: Prefabricated vertical drains in soft Bangkok clay: A case study of the new Bangkok International Airport project. Canadian Geotechnical Journal 18(39), 304–315 (2002)

Bo, M.W., Chu, J., Low, B.K., Choa, V.: Soil improvement; Prefabricated vertical drain techniques, p. 341. Thomson Learning, Singapore (2003)

Chu, J., Yan, S.W.: Estimation of degree of consolidation for vacuum preloading projects. International Journal of Geomechanics, ASCE 5(2), 158–165 (2005)

Stamatopoulos, Kotzias, P.C.: Soil improvement by preloading, pp. 155–167. John Wiley and Sons, N.Y. (1985)

Evaluation of Geotechnical Properties and Liquefaction Behavior of Cohesive Subgrade Soil Stabilized with Fly Ash, Gypsum and Lime

Saad Farhan Ibrahim

Civil, Environmental and Geodetic Engineering Department,
Ohio State University,
Columbus, Ohio, USA
drsaadfarhan@yahooo.com

Abstract. This paper is an investigation to evaluate the stabilization of silty clay subgrade (A-6) brought from Ohio State-United States .Atterberg limits standard proctor compaction, unconfined compression, triaxial, consolidation and swelling tests, in addition to liquefaction tests were carried out on subgrade mixed with 5% fly ash, 5% gypsum, 10% fly ash, 10% gypsum and 10% fly ash mixed with 5% lime.

It is concluded that the soil that stabilized with 10% fly ash and 5% lime improving the stiffness, compressibility and shear strength characteristics as well as it shows withstanding against liquefaction by reaching high value of normalized principal stress when reaching to critical built up of pore water pressure which lead to the fact that a liquefied condition could not possibly develop in the mixture. Many correlation equations obtained to evaluate the stiffness of stabilized soil.

1 Introduction

Soil stabilization may be defined as the alteration of one or more soil properties to improve the engineering characteristics and performance of a soil. There are many techniques for soil stabilization, including compaction, dewatering and by adding material to the soil. There a number of materials that can be used individually, or mixed with other materials, to achieve soil stabilization (Reuben, 2003; Tuncer, et al. 1991; Little, 1995).

AASHTO classification noticed that A-7-6 and A-6 soils rarely have adequate strength and durability for use as a subgrade material under pavements. Liquefaction denotes a condition where, during the course of cyclic stress applications, the residual pore water pressure on completion of any full stress cycle become equal to the applied confining pressure, which leads to liquefaction [Seed, et al.1975].

L. Laloui and A. Ferrari (Eds.): Multiphysical Testing of Soils and Shales, SSGG, pp. 323–329.
springerlink.com

2 Materials, Test Procedures

2.1 Lime Stabilization

Lime stabilization of subgrade soils can significantly improve the engineering properties of weak subgrade (National Lime Association, 2001; Transportation Research Board, 1987).

2.2 Fly Ash Stabilization and Flue Gas Desulfurization Gypsum

The fly ash used in this study is class F while the FGD gypsum (see Table 1). It has low cohesion but high angle of friction [Kirch, 2011]

Table 1 Typical FGD gypsum and fly ash properties (American Electric Power)

Specific Gravity	Gypsum	Fly Ash
	2.27	2.16
In situe Void Ratio	o.73	o.72
In situ Moisture Content	8.0%	O.25%
Maximum Dry Density	88.6 pcf	L.O.I=2.34%
Optimum Moisture Content	19.8%	-
Cohesion	4.7ksf	-
Angle of Friction	40.5^{o}	-

The FGD gradation curve has 100% passing sieve # 200 with the majority particle sizes ranging from 0.35millimeters to 0.85 millimeters (Am. Electric Power, 2008)

2.3 The Soil Used in the Study

Test sample mixtures were prepared with Fly Ash contents of 0% and 5%, and Gypsum contents of 5% and 10% and with 10% Fly Ash mixed with 5% Lime to get six different mixtures based on typical pavement subgrade stabilization procedures.

3 Experimental Study

Laboratory tests were performed according to the appropriate AASHTO or ASTM standards. Table 2, 3 shows the properties of the subgrade soil before and after stabilized was prepared at optimum content according AASHTO T99.

Table 2 Classification and engineering properties of used soil

Soil Type		Gs	L.L.	PI	#200 Finer	Sand %	Silt %	Clay %	O.M.C %	Max. Dry Density kN/m^3
AASHTO	USCS									
A-6	CL	2.72	24.5	13.3	69.19	29	48	23	12.65	20.83

General Subgrade Rating Fair to Poor (L.L=Liquid limit), PI(Plasticity Index)

4 Results and Discussions

4.1 Classification Tests

Tables 2&3 summarize the results of physical properties of untreated A6 and each stabilized soil. The liquid limit decrease and the plastic limit first decrease and increase slowly with increases in the amount of stabilization agents in each content. The plasticity index was reduced by about 20% with an increase of the additives.

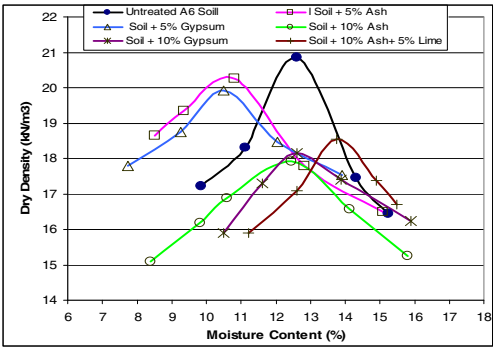

Fig. 1 Moisture contents vs. dry density for untreated A6 soil with stabilized additives

4.2 Swelling Characteristics

The free swell tests results performed in accordance with ASTM D 4546 were given in Figure 4 recorded after 30Days for each mixture .it is noticed that the increase in Ash and lime content reduced the amount of free swell.

4.3 Shear Strength Characteristics

4.3.1 Unconfined Compression Strength

The test was then conducted in accordance with ASTM D2166 -1992, up to failure or 20% strain under a constant strain rate of 1.2 mm/min.After stress was plotted against strain (Figure 5), While Figure 6 shows the values of unconfined

compression strength of each specimens from each mixture after curing period of 1, 7,and 60 days, from the results it can be concluded that the soil stabilized with 10%Ash mixed with 5% Lime posses the high compressive strength specifically after a curing period of 60 days. Close results by Wolfe et al 2010.

Table 3 Classification and engineering properties of stabilized soil

AASHTO Classification	MIX I A-6	MIX II A-6 +5% Ash	MIX III A-6 +5% Gypsum	MIX IV A-6 + 10% Ash	MIX V A-6 +10% Gypsum	MIX VI A-6 +10% Ash +5% Lime
Unified Soil Classification	CL	CL	CL	CL	CL	CL
Specific Gravity(Gs)	2.72	2.72	2.72	2.72	2.72	2.72
Maximum Dry Density (kN/m^3)	20.83	20.25	19.92	17.91	18.15	18.55
Optimum Moisture Content (%)	12.65	10.80	9.22	12.45	12.59	13.75
Liquid Limit (%)	24.56	20.65	17.4	15.7	16..32	16.8
Plastic Limit (%)	11.24	8.33	12.5	6.3	10.30	10.7
Plasticity Index (%)	13.32	12.32	4.9	9.4	4.02	6.1

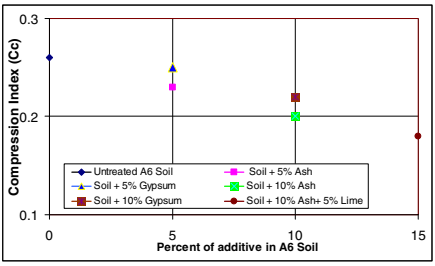

Fig. 2 Variation of Compression Index for Untreated A6 Soil with stabilized additives

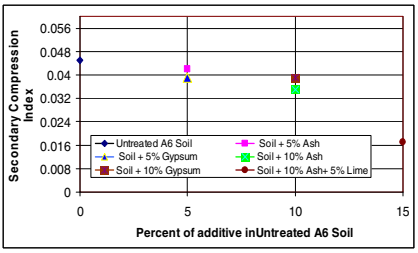

Fig. 3 Variation of Secondary Index for Untreated A6 Soil with stabilized additives

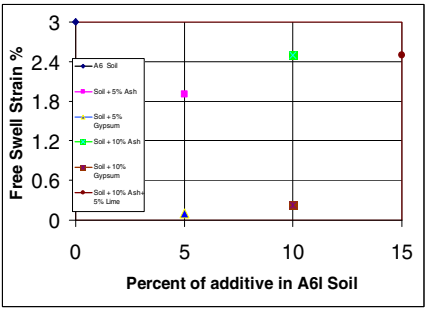

Fig. 4 Variation of percent of free swell for untreated A6 Soil with stabilized additives

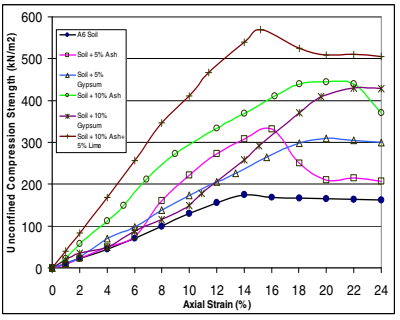

Fig. 5 Variation of unconfined shear strength for untreated A6 Soil with stabilized additives

4.3.2 Consolidated Undrained Compression Triaxial (CU)

It can be clearly seen from figures 7,8,and 9 that addition of 10%Ash to 5%lime for soil used as subgrade increases both undrained shear strength and angle of friction , continuing increasing after curing period of 7,30 days.

4.3.3 Evaluation of Stiffness Test Results

A multiple regression analysis was applied and studying of the relationship between stiffness parameters and Fly Ash percent with Time confirmed by Sezer2004, the following relationship could be adopted to evaluate shear parameters of stabilized soil with Fly Ash

$\Phi_{cu} = 17.00 + 0.51$ Ash Content % + 0.1 t (days)
$C_u = 60.00 + 10.0$ * Ash Content % + 2.0 t (days)

These equations could be used as reference values for roads Engineers.

4.4 Evaluation of Liquefaction

The liquefaction tests according (ASTM D- 5311-92) carried out for each mixture. Figure 10 shows sample of the test results. While Figure 11 shows the Normalized principal stress difference ($\acute{O}_d/2\acute{O}_c$), it could be noticed that the soil stabilized with Ash and Lime got the higher ability to resist liquefaction phenomenon while the natural soil and soil stabilized with gypsum appears not good results.

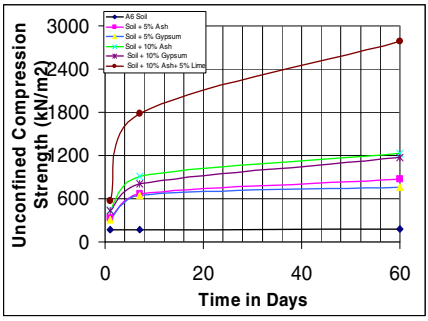

Fig. 6 Variation of unconfined shear strength with time for untreated A6 Soil with stabilized additives

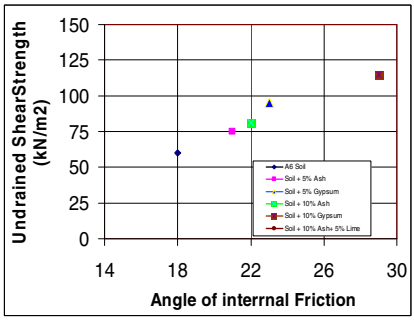

Fig. 7 Variation of shear strength stiffness for untreated A6 Soil with stabilized additives

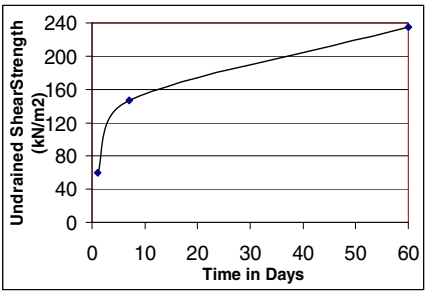

Fig. 8 Variation of undrained shear strength with curing time for Untreated A6 Soil stabilized with Ash and Lime

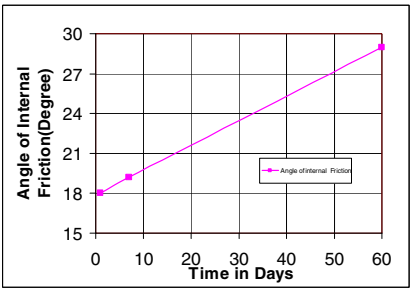

Fig. 9 Variation of angle of friction with curing time for Untreated A6 Soil stabilized with Ash and Lime

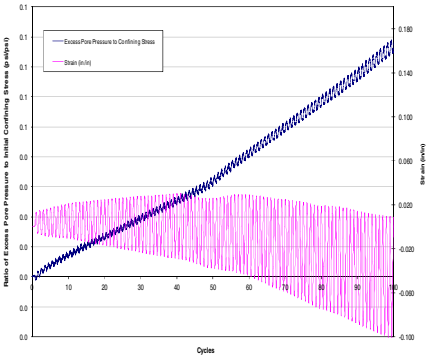

Fig. 10 Liquefaction test results of A6 soil treated with Fly Ash and Lime

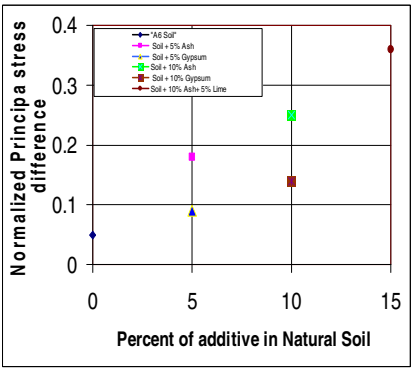

Fig. 11 Normalized principal difference obtained from liquefaction test for untreated A6 Soil with stabilized additives

5 Conclusions

Evaluation of Soil stabilized with by products additive were well studied and the following conclusions were drawn:

1. The Soil stabilized with 10% Fly Ash and 5% Lime shows a considerable improvement in compressibility, Hydraulic Conductivity, Shear Strength Characteristics.
2. Empirical formulas were concluded to evaluate the undrained shear strength and the internal angle of friction with percent of Fly Ash content with time in days.
3. From the properties investigated in this study, it could be concluded that A-6 subgrade clay soil can be used as subgrade clayey soil after mixing with Fly Ash and Lime.

4. Liquefaction condition didn't show conflict values and could be not recommended in study the possibility of acceptance of clay subgrade in site.
5. It should announce the essential of taking into consideration the time of curing required by the stabilized soil for obtaining suitable results.
6. A lime-fly ash combination is welcomed in the industry because the combination is more economical and may obtain the desired strength and modulus.
7. It is quite obvious that soil stabilized with 10%Ash mixed with 5 % Lime shows good ability to withstand higher stress before failure.

References

American Electric Power, Civil Laboratory. August 1, Test Report for Consolidated-Undrained Triaxial Compression Test – ASTM D 4767. Project: Cardinal FGD Landfill. Report Prepared for American Electric Power ASTM Standard, 2003, 2006 and 2007 (2008)

Kirch, J.P.: Potential Use of Gas Desulfurization Gypsum in a Flowable Grout for Remining of Abandoned Coal Mines, M.Sc Thesis, Department of Civil and Environmental Engineering and Geodetic Science The Ohio State University (2011)

Little, D.N.: Handbook for Stabilization of Pavement Subgrades and Base Courses with Lime, National Lime Association, Kendall/Hunt Pub. (1995)

National Lime Association, 2006, Lime Stabilization Construction Manual, Bulletin 326, 1991(2006)

Karol, R.H.: Chemical Grouting and Soil Stabilization, 3rd edn., Revised and Expanded, arcel Dekker, INC. (2003)

Seed, B.H., Arango, I., Chan, C.K.: Evaluation of Soil Liquefaction Potential During Earthquake, Report No.75-28, College of Engineering, University of California (October 1975)

Sezer, A., Inan, G., Ramyar, K.: Utilization of a very High fly ash for improvement of Izmir Clay. Building and Environmental 41(2), 150–155 (2006)

Solanki, P., Naji, K.: Engineering Properties and Moisture Susceptibility of Silty Clay Stabilized with Lime, Class C Fly Ash, and Cement Kiln, ASCE (December 2009)

Wolfe, W.E., Butalia, T.S., Walker, H., Weaver, N., Baker, R.: FGD By-Product Utilization at Ohio Coal Mine Sites: Past, Present, and Future. The Ohio State University. Technical Report CDO/D-07-06, July 1 (2010)

Experimental Methodology for Chemo-Mechanical Weathering of Calcarenites

M.O. Ciantia[1], R. Castellanza[2], C. di Prisco[1], and T. Hueckel[3]

[1] Politecnico di Milano, Piazza L. da Vinci 32, 20133, Milano, Italia
ciantia@stru.polimi.it, cdiprisc@stru.polimi.it
[2] Università degli Studi Milano Bicocca, Piazza della Scienza, Milano, Italia
riccardo.castellanza@unimib.it
[3] Duke University, Hudson Hall, Durham, NC 27708
hueckel@duke.edu

Abstract. Calcarenite is a soft rock strongly affected by weathering processes that markedly reduce the mechanical rock properties with time. As a consequence, cliffs and underground cavities formed in calcaernites are frequently affected by intense erosion and instabilities. The field and laboratory experimental results mainly show three peculiarities of calcarenite mechanical behavior: a) a marked and instantaneous reduction in strength, up to 60% of the dry initial value, when water fills the pores of the rock; b) a slow reduction in strength after saturation; c) progressive weakening of the material during wetting and drying cycles. In the present work we concentrate on the long term effect of water on calcarenite. In this context, an experimental procedure necessary for the calibration of a strain hardening-chemical softening elasto-plastic constitutive model is presented. Suitably designed tests under controlled "weathering" conditions were performed in order to define the critical variables that can physically explain the variety of phenomena occurring in the material.

1 Introduction

Formations of calcarenite are very common in many regions of Mediterranean shores. They are affected by weathering processes induced by a chemo-mechanical degradation of the rock mass in contact with sea water. Along the coastline large caves formed under human settlement areas present situations were a risk analysis is fundamental, as is the case of "Grotta Palazzese" (Fig. 1). A series of pressing question arise: what portions of the shore can become mechanically unstable, how fast is the process and how the mitigation measures can be designed. To answer these questions, the authors propose to follow a continuum approach. A strain hardening chemical softening elasto-plastic constitutive model is used to describe the porous bonded soft rock subject to weathering (Fig. 2).

L. Laloui and A. Ferrari (Eds.): Multiphysical Testing of Soils and Shales, SSGG, pp. 331–336.
springerlink.com

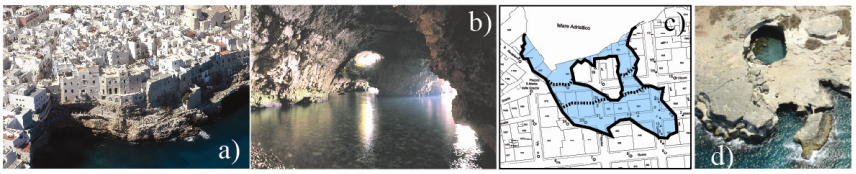

Fig. 1 The effect of water on calcarenite in a marine environment. (a) air view of Polignano a Mare, (b-c) the cavern "Grotta Palazzese", (d) Collapsed cave near Bari.

The constitutive model illustrated hereafter is inspired by the approaches proposed by Hueckel (1992), Nova et al (2003) and Hu and Hueckel, (2007). Important modifications to the chemical softening function are proposed here by linking it to the chemical dissolution rate equations of calcium carbonate. In particular, the mechanical behaviour of intact Apulian calcarenites has already been studied by Lagioia & Nova (1995). These authors introduced the first version of the mechanical model by disregarding the chemo-coupling. Nova et al. (2003) introduced a damage mechanism driven by the chemical dissolution using a phenomenological approach. Here the authors modify the chemo-softening rule by assigning a specific physical meaning to the chemical state variable hence introducing a one-way chemo-mechanical coupling.

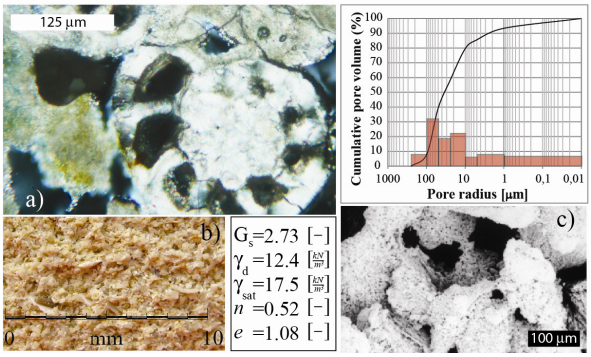

Fig. 2 Microstructure of calcarenite: (a) microscope view of a thin section, (b) naked eye view of the rock and (c) SEM image of the bonded grains. The graph shows the pore size distribution of an Apulian calcarenite.

The experimental test results obtained by the authors show that the normalized dissolved mass is a chemical variable controlling the damage of calcarenite. To calibrate the previously mentioned constitutive model, specific tests have been designed. The key point for a successful calibration is to perform tests where the chemo-mechanical phenomena are uncoupled. On the other hand, the validation requires the lab tests where the behaviour is coupled. These two phases are presented in the following section after a brief outline of the chemical governing equations and the presentation of the new chemical softening function.

2 Critical Variables of Weathering of Calcarenite

To identify the variables to be correlated in the experimental studies, the principal mechanisms governing the phenomena accounted for have to be postulated beforehand. In the case of chemical damage, a crucial role is played by the dissolved mass and as according to the fundamental rules of chemistry; the mass changes are controlled by the kinetics equation. The kinetics of dissolution of calcite, which is the dominating mineral of calcarenite, has been intensively studied in the last decades. The rate at which calcium carbonate dissociates and falls into solution is directly proportional to the area of the interface between the two phases (Sjöberg, 1976) and to the pH of the fluid in acidic conditions (Sjöberg, 1985). The rate of calcite dissolution with water as expressed through calcium carbonate mass change rate per unit water volume in $g\ cm^{-3}s^{-1}$, reads

$$\begin{cases} \dfrac{dM_{CaCO_3}}{dt} = -k_b A \mathrm{M}^m \left\{ C - \left[Ca^{2+} \right]^{\frac{1}{2}} \left[CO_3^{2-} \right]^{\frac{1}{2}} \right\} & \text{for } 7.5<\text{pH}<14 \\ \dfrac{dM_{CaCO_3}}{dt} = -k_a A \mathrm{M}^m \left[\mathrm{H}^+ \right] & \text{for } 2<\text{pH}<7.5 \end{cases}$$

where k_b and k_a are apparent rate constants ($cm\ s^{-1}$) for neutral and acidic pH conditions, respectively. A is the calcite surface area in cm^2per unit reacting volume assumed as a constant, M^m is the molecular mass of calcium carbonate in *g/mol* and C is a constant expressing the limit condition at chemical equilibrium. In this work ionic concentrations are expressed in mol/cm^3 and therefore C is in mol/cm^3. The accumulated relative mass removal of calcium carbonate from the solid (or reaction progress) is defined as

$$\xi = \frac{\Delta M}{M^0} = \frac{M^0 - M}{M^0}$$

where M^0 is the initial calcite mass per unit reacting fluid volume. Therefore, substituting the rate equation in the time derivative of the reaction progress variable, the rate of relative dissolved mass results

$$\begin{cases} \dot{\xi} = k_b A \dfrac{\mathrm{M}^m}{M^0} \left\{ C - \left[Ca^{2+} \right]^{\frac{1}{2}} \left[CO_3^{2-} \right]^{\frac{1}{2}} \right\} & \text{for } 7.5 \le \text{pH}<14 \\ \dot{\xi} = k_a A \dfrac{\mathrm{M}^m}{M^0} \left[\mathrm{H}^+ \right] & \text{for } 2<\text{pH}<7.5 \end{cases}$$

ξ is constrained by the inequalities: $0 \le \xi \le 1$, as proposed by De Groot (1966). When $\xi = 1$, the reaction is completed, that is all the calcium carbonate is removed from the material. The rate equation in acid conditions is necessary because the rates in basic solutions are so slow that it is very hard to obtain experimental data, while in acid solutions the experiments can be carried out in a reasonable time.

As was mentioned above, the plasticity theory is extended in order to capture the dissolution mechanism. It is reasonable to think that the strength of the material is proportional to the mass forming the structure. Model wise this translates in a shrinking of the yield locus for an increasing dissolved mass. As is shown in Fig. 3 the chemical softening function can be determined directly from the experiments. More details of the constitutive model are found in Nova et al, 2003. The chemical softening function is postulated as,

$$Y(\xi) = \exp(-R_c \xi)$$

where Y is the chemical softening function and R_c is a material constant. This affects the shrinkage of the yield locus, as the hardening variables p_s, p_m , p_t. are assumed to depend on Y, as is suggested in Fig. 3.

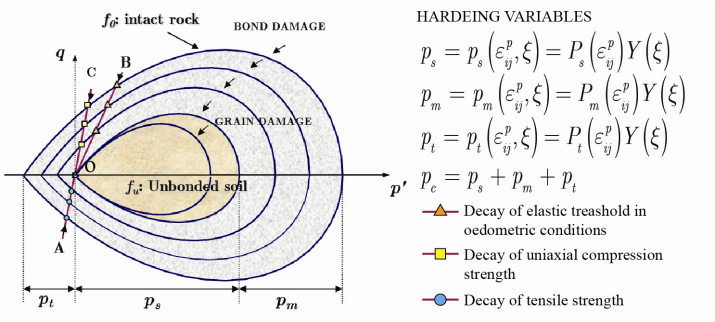

Fig. 3 Evolution of hardening variables due to chemical damage

3 Multiphysical Weathering Tests and Model Simulations

To calibrate the chemical softening function Y the material was immersed in acid and with time the pH, ΔM (change in mass) and, via an oedometric compression test, the elastic limit threshold (defining the size of the yield locus) were measured (Fig. 4). Mercury intrusion porosimetry was used to calculate the specific surface area. By assuming the reacting surface to be constant throughout the process and by integrating the incremental relationship between $\dot{\xi}$ and pH, from Fig.4d k_a can be calibrated. By fitting the experimental curve of Fig.4e constant R_c results. In contrast with what proposed by Ciantia & Hueckel 2013, here the increase in reacting surface area due to micro-cracks is neglected According to this strategy, the comparison between experimental data and modelling simulations of Fig.4f becomes a validation of the approach.

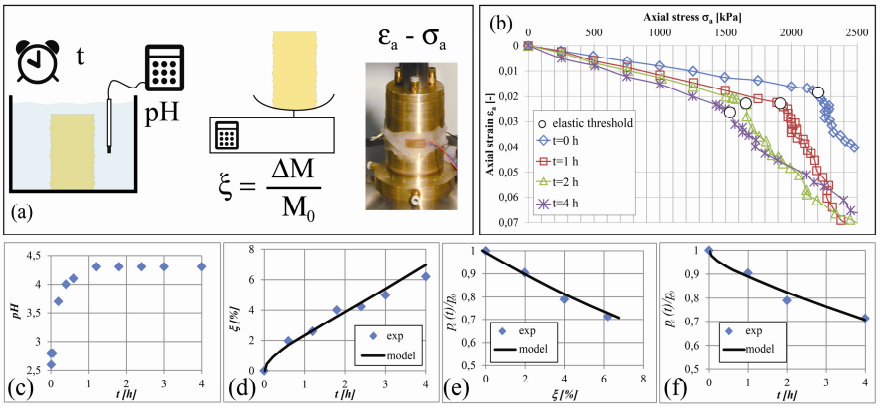

Fig. 4 Experimental set up and results and chemical softening function calibration.

Once the chemical softening function is calibrated here below a full coupled problem is analyzed: during this second experimental test, the rock is initially loaded under oedometric conditions up to 90% of its elastic limit and, subsequently, an acid flux (pH=2.8) is imposed through the specimen under a constant vertical load (Fig. 5a). The chemical damage causes the material to yield and with time plastic deformation accumulates. In this test, the vertical deformation, the radial stress and the pH of the outflowing fluid are measured. Fig. 5b shows the experimental and numerical stress paths together with the yield surface and plastic potential evolution, Fig. 5c presents the evolution of the hardening variables and Fig. 5d-c the numerical and experimental evolution of radial stress and axial strain respectively.

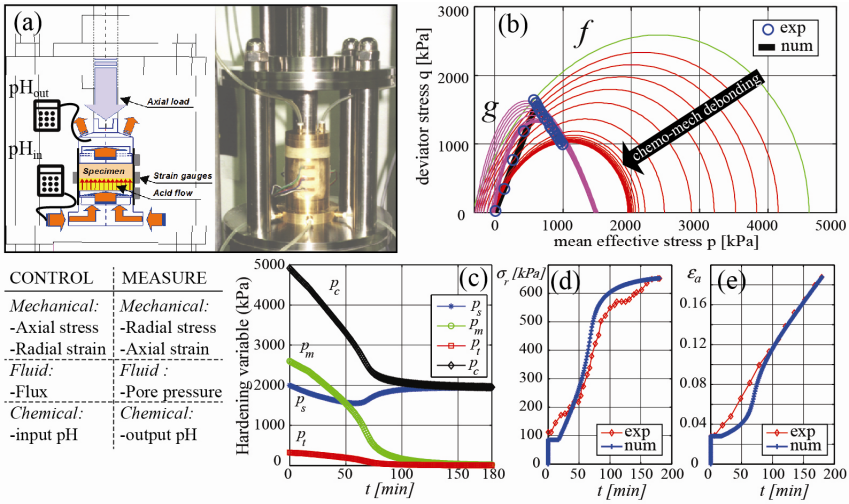

Fig. 5 (a) Weathering testing device (Castellanza & Nova, 2004), experimental results and model predictions (b,d,e), evolution of hardening variables (c).

4 Conclusions

This work illustrates a successful strategy for accounting for chemical damage by starting from the kinetics of chemical dissolution of calcite. By introducing the dissolved mass as a new state variable, in an already conceived advanced elasto-plastic constitutive model, the chemical softening is reproduced. As a consequence, time to failure becomes a physically based parameter of the degradation process at any scale, including that concerning deterioration of coastal structures. The reactive area is assumed as constant. This assumption makes it justified to neglect the effect of mechanical damage on the chemical process evolution.

References

Castellanza, R., Nova, R.: Oedometric Tests on Artificially Weathered Carbonatic Soft Rocks. Journal of Geotechnical and Geoenvironmental Engineering ASCE 130(7), 728–739 (2004)

Ciantia, M.O., Hueckel, T.: Weathering of stressed submerged calcarenites: chemo-mechanical coupling mechanisms. Submitted to. Géotechnique. Paper for Symposium in Print 2013, number: SIP 13-P-024 (2013)

De Groot, S.R.: Termodynamics of irriversible processes. North Holland, Amsterdam (1966)

Hu, L.B., Hueckel, T.: Coupled chemo-mechanics of intergranular contact: Toward a three-scale model. Computers and Geotechnics 34, 306–327 (2007)

Hueckel, T.: Water–mineral interaction in hydro-mechanics of clays exposed to environmental loads: a mixture theory approach. Can. Geotechn. J. 29, 1071–1086 (1992)

Lagioia, R., Nova, R.: An experimental and theoretical study of the behaviour of a calcarenite in triaxial compression. Géotechnique 45(4), 633–648 (1995)

Nova, R., Castellanza, R., Tamagnini, C.: A constitutive model for bonded geomaterials subject to mechanical and or chemical degradation. Int. J. Num. Anal. Meth. Geomech. 27(9), 705–732 (2003)

Sjöberg, E.L.: A fundamental equation for calcite dissolution kinetics. Geochim. Cosmochim. Acta 40, 441–447 (1976)

Sjöberg, E.L., Rickard, D.T.: Temperature dependence of calcite dissolution kinetics between 1 and 62 °C at pH 2.7 to 8.8 in aqueus solutions. Geochim. Cosmochim. Acta 48, 485 (1984)

Author Index